ERCOFTAC
European Research Community On Flow, Turbulence And Combustion

Politecnico di Torino

European Drag Reduction and Flow Control Meeting – EDRFCM 2024

10th - 13th September 2024

Castello del Valentino
Turin (Torino), Italy

BOOK OF ABSTRACTS

ERCOFTAC
European Drag Reduction and Flow Control Meeting – EDRFCM 2024 **(Revised and updated on 01-9-2024)**

Tuesday 10th September

Coffee	**10:10-10:40**		
Welcome	**10:40-10:50**		
Session 1.2	**10:50-12:30**	**Riblets**	
Daniel	Chung	APPLICATION OF THE VISCOUS VORTEX MODEL TO RIBLETS, SLIP/TRANSPIRATION SURFACES AND OPPOSITION CONTROL	1
Alessandro	Mazzara	EFFECT OF THE RIBLETS ON THE CONVECTIVE HEAT TRANSFER COEFFICIENT OF A TURBULENT BOUNDARY LAYER ON A FLAT PLATE	2
Stefano	Cipelli	SINUSOIDAL RIBLETS FOR TURBULENT DRAG REDUCTION	3
Gioacchino	Cafiero	UNIFORM MOMENTUM ZONES IN TURBULENT BOUNDARY LAYERS OVER SINUSOIDAL RIBLETS	4
Felipe	Alves Portela	ON THE FLOW STRUCTURE IN THE VICINITY OF SINUSOIDAL RIBLETS IN A TURBULENT CHANNEL FLOW	5
Lunch	**12:30-14:00**		
Session 1.3	**14:00-15:40**	**Boundary-layer Control**	
Giulio	Foggi Rota	TURBULENCE AND STRUCTURAL DYNAMICS IN FLEXIBLE CANOPY FLOWS	6
Daniel	Burnet	BOUNDARY LAYER CONTROL OF HEAT TRANSFER BY AN EFFUSION FILM	7
Francesco	Scarano	EFFECT OF FREESTREAM TURBULENCE ON A SPATIALLY DEVELOPING TURBULENT BOUNDARY LAYER SUBJECTED TO MODERATE ADVERSE PRESSURE GRADIENT	8
Min Jae	Kang	DRAG REDUCTION OF A DOWNSTREAM CYLINDER WITH A FLEXIBLE FIN IN THE WAKE GENERATED BY AN UPSTREAM CYLINDER	59
Abdelrahman	Hassanein	LARGE-SCALE ENERGY ATTENUATION OF WALL-BOUNDED TURBULENCE WITH AN INNER-SCALED HELMHOLTZ RESONATOR	10
Tea break	**15:40-16:10**		
Session 1.4	**16:10-17:50**	**Spanwise-wall Forcing**	
Davide	Gatti	NUMERICAL STUDY OF TURUBLENT SKIN-FRICTION DRAG REDUCTION VIA SPANWISE FORCING AT LARGE VALUES OF REYNOLDS NUMBER	11
Max	Knoop	SPATIAL MODIFICATION OF TURBULENCE BY STEADY SQUARE-WAVE SPANWISE WALL FORCING	12
Niccolò	Berizzi	DIRECT NUMERICAL SIMULATIONS OF A TRANSONIC AIRFOIL WITH SPANWISE FORCING FOR DRAG REDUCTION	13
Marco	Castelletti	SPANWISE WALL OSCILLATION IN A DAMPED CHANNEL FLOW FOR TURBULENT DRAG REDUCTION	14
Federica	Gattere	ON THE OPTIMAL PERIOD OF SPANWISE FORCING FOR TURBULENT DRAG REDUCTION	15

Welcome Reception	**17:50-19:30**	Castello del Valentino Sala delle Colonne

Wednesday 11th September

Session 2.1	**9:00-10:20**	**Aerodynamic Flow Control**	
Ari	Glezer	CIRCULATION CONTROL OF A 2-D WING	16
Si-Yuan	Feng	EFFECT OF A PERIODIC GUST ON THE AERODYNAMIC CHARACTERISTICS OF NACA0012 AIRFOIL	17
Yaxing	Wang	LEADING-EDGE BUMP ON IMPROVEMENTS OF AERODYNAMIC LOADS OF A VERTICAL TAIL	18
Xianyang	Jiang	DRAG REDUCTION FOR HEAVY ROAD VEHICLES WITH REAR FLAPS	19
Coffee break	**10:20-10:50**		
Session 2.2	**10:50-12:30**	**Active Flow Control**	
Pierre	Ricco	TURBULENT DRAG REDUCTION BY PASSIVELY ROTATING DISCS	20
Mathieu	Tocquer	MASS ENTRAINMENT ANALYSIS OF THE CONTROLLED TURBULENT SEPARATION USING SWEEPING JET ACTUATORS	21
Deepak	Ramswamy	SEPARATION CONTROL WITH SPANWISE-INCLINED MICRO JETS	22
Pierre Louis	Spychala	DEVELOPMENT AND VALIDATION OF AN HYBRID JET FLOW CONTROL ACTUATOR	23
~~Isabella~~	~~Fumarola~~	~~INFLUENCE OF TRAVELLING SURFACE WAVES TO A TURBULENT BOUNDARY LAYER AT HIGH REYNOLDS NUMBER~~	~~24~~
Lunch	**12:30-14:00**		
Session 2.3	**14:00-15:40**	**Data-driven Flow Control 1**	
Yusuke	Yugeta	AUTOMATIC EXPLORATION OF COST FUNCTION FOR SUBOPTIMAL CONTROL OF TURBULENT FLOW BY MACHINE LEARNING	25
Chengwei	Xia	ACTIVE FLOW CONTROL OF DRAG REDUCTION USING DATA-ENABLED PREDICTIVE CONTROL	26
Pol	Suarez Morales	MULTI-AGENT REINFORCEMENT-LEARNING CONTROL FOR A 3D CYLINDER AT ReD = 3900	27
Carlos	Villa Sanmiguel	LSTM-BASED PREDICTIVE MODELLING FOR ACTIVE FLOW CONTROL OF A WAKE	28
Stefano	Discetti	DRAG REDUCTION WITH SELF-TUNING MODEL PREDICTIVE CONTROL	29
Tea break	**15:40-16:10**		
Session 2.4	**16:10-17:50**	**Plasma Flow Control**	
Sergey	Leonov	SUPERSONIC FLOW CONTROL IN DUCTS AND OVER COMPRESSION RAMPS BY Q-DC DISCHARGE	30

Jacopo	Serpieri	CROSSWISE AND WALL-NORMAL PLASMA JETS IN A TURBULENT CHANNEL FLOW	31
Olga	Azarova	SOME APPROACHES TO CONTROLLING HIGH-SPEED FLOWS USING REMOTE AND SURFACE PLASMA ENERGY DEPOSITION	32
Lucas	Schneeberger	PLASMA ACTUATORS FOR DRAG REDUCTION ON HEAVY GROUND VEHICLES	33
Gabriele	Salomone	AI-DRIVEN REAL-TIME CONTROL OF TOLLMIEN-SCHLICHTING WAVES ON A FLAT PLATE	34

Visits CdV **18:00-19:00**

Thursday 12th September

Session 3.1 **9:00-10:20** **Wall Turbulence Control**

Julio	Soria	2C-2D PIV/PTV MEASUREMENTS OF HIGH REYNOLDS NUMBER TURBULENT CHANNEL FLOW WITH WALL-NORMAL RESOLUTION OF 0.6 VISCOUS LENGTH	35
Giulio	Dacome	TOWARDS ADAPTIVE CONTROL OF WALL-BOUNDED TURBULENCE	36
Antonio	Cuellar	EFFECT OF THE WALL-SENSOR AVAILABILITY ON THE FLOW FIELD ESTIMATION WITH 3D-GANS IN TURBULENT WALL-BOUNDED FLOWS	37
Jochen	Kriegseis	TURBULENT CHANNEL FLOW – A MEASUREMENT TECHNIQUE COMPARISON	38

Coffee break **10:20-10:50**

Session 3.2 **10:50-12:30** **Passive Flow Control**

Gennadi	Voropaiev	INTERACTION OF TURBULENT BOUNDARY LAYER WITH VISCOELASTIC COATING	39
Marie	Koseki	THE ROLE OF ROUGHNESS IN TURBULENT CHANNEL FLOWS OVER ELASTIC WALLS	40
Ricardo	Garcia-Mayoral	TURBULENT DRAG REDUCTION BY FIBROUS PERMEABLE SUBSTRATES	41
Luca	Boscagli	TRANSITION CONTROL OF HYPERSONIC BOUNDARY LAYER VIA NON-UNIFORM WALL TEMPERATURE	47
Carola	Schmidt	GLOBAL FRICTION OF HETEROGENEOUS ROUGH SURFACES	43

Lunch **12:30-14:00**

Session 3.3 **14:00-15:40** **Laminar Flow Control**

Antonios-Lykourgos	Synodinos	ON THE INTERACTION OF STATIONARY CROSSFLOW INSTABILITIES WITH A WALL-MOUNTED PHONONIC CRYSTAL	44
Gaspare	Li Causi	OPTIMAL LAMINAR FLOW CONTROL	45
Haodong	Zhu	EXPERIMENTAL INVESTIGATION OF EARLY STAGE OF TURBULENT SPOTS	46
Angelo	Paduano	AN AERODYNAMIC DESCRIPTION OF THE FLOW FIELD OVER A LINER WITH GRAZING FLOW	42
Juan	Franco	INFLUENCE OF SHALLOW GAPS ON COMPRESSIBLE BOUNDARY-LAYER TRANSITION	48

Tea break **15:40-16:10**

Session 3.4 **16:10-17:30** **Blowing and Suction**

Georg	Fahland	PIV MEASUREMENTS ON A WING WITH UNIFORM BLOWING	49
Annika	Frede	PARAMETRIC STUDY OF HOMOGENEOUS BLOWING AND SUCTION ON THE TRANSONIC AIRFOIL RAE2822	50
Xiaonan	Chen	A BAYESIAN OPTIMIZATION FRAMEWORK FOR OPTIMIZING GLOBAL SKIN-FRICTION DRAG REDUCTION VIA WALL BLOWING	51
Qi-Ming	Wang	EFFECT OF SYNTHETIC JET ON MULTI-ELEMENT AIRFOIL LIFT ENHANCEMENT	64

Banquet **19:30** Restaurant "Capodoglio_Murazzi"

Friday 13th September

Session 4.1 **9:00-10:20** **Flow Separation Control**

Ahmed	Abed-Meraim	CHARACTERIZATION OF THE WAKE OF A ROAD VEHICLE TO IMPROVE AERODYNAMIC PERFORMANCES	52
Jia-xin	Liu	WAKE ASYMMETRY BEHIND A WALL-MOUNTED HEMISPHERE	53
Yekaterina	Goodwin	CONTROL OF FLOW SEPARATION VIA CORIOLIS ACCELERATION IN FLAPPING FLIGHT	54
Yongxiang	Wu	TURBULENT BOUNDARY LAYER SEPARATION CONTROL USING MICRO ROTATING CYLINDRICAL VORTEX GENERATORS	55

Coffee break **10:20-10:50**

Session 4.2 **10:50-12:30** **Turbulent Drag Reduction**

Emanuele	Gallorini	THE STATE OF TURBULENCE IN A PIPE FLOW WITH DRAG REDUCTION	56
Lukas	Brandfellner	ONSET OF POLYMERIC DRAG REDUCTION AT DIFFERENT REYNOLDS AND WEISENBERG NUMBERS	57
Jonathan	Tay Chien Ming	STUDY OF DRAG REDUCTION CAPABILITY OF MACROSCALE CORRUGATED SURFACE IN TURBULENT CHANNEL FLOW	58
Zahir	Hussain	THEORETICAL AND EXPERIMENTAL STUDIES OF BOUNDARY LAYER FLOW OVER BROAD ROTATING CONES IN AXIAL FLOW	9
Shaiful Hakim	Bin Mohamed Noor	A PARTICLE IMAGE VELOCIMETRY STUDY OF AERODYNAMICALLY-SHAPED VORTEX GENERATOR IN ZERO PRESSURE GRADIENT BOUNDARY LAYER	60

Lunch **12:30-14:00**

Session 4.3 **14:00-15:00** **Data-driven Flow Control 2**

Giorgio	Cavallazzi	DEEP REINFORCEMENT LEARNING FOR LOW-SPEED STREAKS CONTROL IN TURBULENT FLOWS	61
Enrico	Saccaggi	BAYESIAN OPTIMIZATION OF AN OPPOSITION CONTROL STRATEGY IN A FULLY TURBULENT CHANNEL FLOW	62
Enrico	Amico	BLUFF BODY WAKE CONTROLLED WITH DEEP REINFORCEMENT LEARNING	63

Farewell **15:00**

Tea break **15:00-15:30**

Visit PoliTO labs **16:00 PM** Those interested, please write to Jacopo.Serpieri@Polito.it

1

ERCOFTAC
European Drag Reduction and Flow Control Meeting – EDRFCM 2024
September 10$^{\text{th}}$–13$^{\text{th}}$, 2024, Turin, Italy

APPLICATION OF THE VISCOUS VORTEX MODEL TO RIBLETS, SLIP/TRANSPIRATION SURFACES AND OPPOSITION CONTROL

Jeremy Wong, Christopher J. Camobreco
Department of Mechanical Engineering, University of Melbourne, Victoria 3010, Australia

Ricardo García-Mayoral
Department of Engineering, University of Cambridge, Cambridge CB2 1PZ, UK

Nicholas Hutchins, Daniel Chung
Department of Mechanical Engineering, University of Melbourne, Victoria 3010, Australia

INTRODUCTION

The viscous vortex model of Wong *et al.* [1] was recently developed to accurately predict the optimal riblet drag performance, without the need of expensive direct numerical simulations (DNSs) or experiments. The model calculates the near-wall response below a quasi-streamwise vortex, governed by the steady, two-dimensional Stokes equations. This abstract outlines the development of the model and expands its application to slip/transpiration surfaces and opposition control. While the protrusion height model is able to predict skin-friction drag reduction for riblets and slip/transpiration surfaces [2, 3], following methods previously advanced by Luchini [4, 5], it is formally valid only for vanishingly small riblets and small slip/transpiration velocities. Thus, the predictions of the protrusion height model become inaccurate for larger riblets (and slip/transpiration surfaces with larger slip/transpiration velocities [3]). Here, we show that the viscous vortex model accurately predicts the virtual origin for turbulence, and thereby the drag reduction, for optimally sized riblets, slip/transpiration surfaces, and opposition control, for reasonable control parameters.

THE VIRTUAL ORIGIN FRAMEWORK

Many drag reduction technologies do not alter the turbulent flow, besides wall-normal displacements of the mean flow (virtual origin: ℓ_U^+) and turbulence (ℓ_T^+), and thus satisfy [3, 4]

$$-\Delta U^+ \approx \ell_U^+ - \ell_T^+, \tag{1}$$

where ΔU^+ is a log-layer measure of the drag change. Here, the '+' superscript denotes normalisation with friction velocity u_τ and kinematic viscosity ν. The drag reduction is then given by $DR \sim -(2C_{f0})^{1/2}\Delta U^+$ [6], where C_{f0} is the skin-friction coefficient of a baseline smooth wall. The relation (1) applies for riblets up to their optimal size [1] and for some slip/transpiration and opposition-controlled surfaces [3].

THE PROTRUSION HEIGHT MODEL

Luchini [5, 4] advanced a method of predicting ΔU^+ for riblets using viscous (Stokes) flow,

$$-\Delta U^+ \approx h_\parallel^+ - h_\perp^+ = (h_\parallel/\ell_g - h_\perp/\ell_g)\ell_g^+, \tag{2}$$

where $h_\parallel$ and $h_\perp$ are the Stokes-flow protrusion heights that locate the virtual origins perceived by streamwise and spanwise motions, respectively, and ℓ_g^+ is the riblet size characterised by the square root of the groove cross-sectional area [2]. The protrusion heights scaled by the riblet size ($h_\parallel/\ell_g$, $h_\perp/\ell_g$) can be routinely obtained from Stokes-flow calculations for a given riblet shape [7, 2], and their difference ($h_\parallel/\ell_g - h_\perp/\ell_g$) expresses the effect of riblet shape on the drag performance. In the limit of vanishingly small sizes ($\ell_g^+ \to 0$), it has been shown that $\ell_U^+ \to h_\parallel^+$ and $\ell_T^+ \to h_\perp^+$ [1]. At non-vanishing sizes, $\ell_U^+ \approx h_\parallel^+$ still holds for streamwise-aligned riblets, however $h_\perp^+$ departs from ℓ_T^+ with increasing size, leading to riblet-shape-dependent inaccuracies in the protrusion height model. For example, extrapolating (2) to the optimal size overpredicts the drag reduction, with optimal DNS-measured ΔU_{opt}^+ up to 40% smaller than predicted (figure 1a).

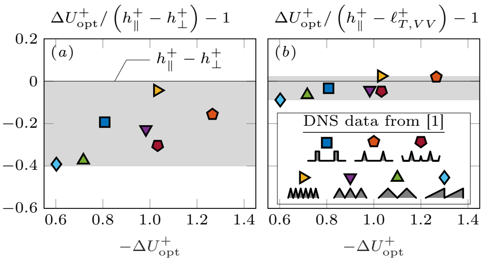

Figure 1: A comparison of optimal riblet drag predictions. (a) Extrapolated protrusion height model (2). (b) Present viscous vortex model (4). Legend inset.

THE VISCOUS VORTEX MODEL

The viscous vortex model predicts ℓ_T^+ *a priori* by explicitly modelling the effect on the quasi-streamwise vortices near the wall. This modelling was motivated by observations that the turbulence virtual origin ℓ_T^+ is not set by (the virtual origin of) the spanwise velocity alone, with the wall-normal velocity (transpiration) also playing a key role [3]. The calculation of $h_\perp^+$ neglects transpiration at the riblet crest plane, leading to the discrepancy $\ell_T^+ \neq h_\perp^+$, where transpiration refers to the spanwise-varying wall-normal flow in the cross plane, predominantly induced by quasi-streamwise vortices. Transpiration at the riblet crest plane allows the quasi-streamwise vortices to penetrate deeper within riblet grooves, which deepens the

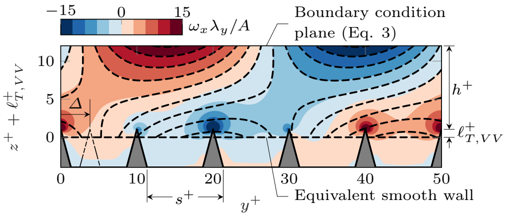

Figure 2: Contours of the streamwise vorticity field ω_x within the viscous vortex model domain.

turbulence virtual origin ℓ_T^+ as the riblet size increases.

The riblets are embedded in the viscous vortex model domain, as shown in figure 2. Here, a streamwise (x) uniform two-component flow is calculated in the cross (yz) plane, as governed by the steady Stokes equations $-(1/\rho)\boldsymbol{\nabla} p + \nu\nabla^2\boldsymbol{v} = 0$ and $\nabla \cdot \boldsymbol{v} = 0$, where p is the pressure, ρ the density, and y and z the spanwise and wall-normal directions, respectively, with corresponding velocities $\boldsymbol{v} = \{v, w\}$. Thus far, this is the same setup as for calculating $h_\perp^+$ [5]. However, instead of a spanwise-homogeneous upper boundary condition (i.e. an infinitely large scale velocity, or equally, a vanishingly small riblet), a model of a vortex is prescribed through the upper boundary condition, with a given scale (wavelength) and intensities (amplitudes)

$$w|_{z=h} = -A\sin\left(\beta y\right), \qquad v|_{z=h} = -B\sin\left(\beta y + \mathit{\Phi}\right). \qquad (3)$$

Here, transpiration effects at the crest are readily incorporated through (3), as is crucial to accurately predict ℓ_T^+ [3]. The amplitudes (A and B), phase difference ($\mathit{\Phi}$), model domain height measured from the riblet crest (h) and the period (β) that is related to the spanwise wavelength λ_y ($\beta = 2\pi/\lambda_y$) are all set based on either observations or measurements of smooth-wall flows. Jiménez *et al.* [8] noted that the spanwise wavelength of a vortex is $\lambda_y^+ \approx 50$, having observed the peak in the wall-normal velocity spectral density at $\lambda_y^+ \approx 50$ and $\lambda_x^+ \approx 300$, aligning closely with the signature of a quasi-streamwise vortex. Furthermore, windowed Fourier analysis of DNS cross-flow velocities above a smooth wall provided $B/A \approx 1.4$ at $z^+ = h^+ \approx 12$ [1]. The phase difference selected ($\mathit{\Phi} \approx 0.31\pi$) provided more accurate predictions of ℓ_T^+ than $\mathit{\Phi} \approx 0.5\pi$, as suggested by continuity. Having defined the cross-flow velocities at the upper boundary, the steady Stokes equations are solved for v and w, with a no-slip smooth or riblet wall, and spanwise periodicity (figure 2). Then, to model the unpinned nature of quasi-streamwise vortices above riblets [1], the Stokes field is uniformly averaged across spanwise shifts of the riblet wall $\mathit{\Delta}$ between $0 \leq \mathit{\Delta} \leq s$, where s is the riblet spacing (figure 2 inset). The resulting $\ell_{T,VV}^+$ is computed by negatively offsetting the domain height by a guessed value of $\ell_{T,VV}^+$, and iterating on this value until the local minimum of the r.m.s. streamwise vorticity ω_x' matches with that above the equivalent smooth wall (at $z^+ + \ell_{T,VV}^+ \approx 5$). The drag prediction of the viscous vortex model

$$-\Delta U_{VV}^+ = h_\parallel^+ - \ell_{T,VV}^+, \qquad (4)$$

is then obtained, and agrees well with the DNS-measured ΔU^+ up to the riblet optimum size (figure 1*b*). This accuracy leads the viscous vortex model to be well suited for shape-optimisation and performance degradation studies of riblets, without needing to run DNS.

Predictions of $\ell_{T,VV}^+$ for slip/transpiration surfaces and opposition control are obtained in an almost identical fashion, with the no-slip riblet textures replaced by the appropriate homogeneous wall boundary conditions. For slip/transpiration surfaces, the boundary conditions at the wall ($z^+ = 0$) are $v|_{z^+=0} = \ell_y \partial v/\partial z|_{z^+=0}$ and $w|_{z^+=0} = \ell_z \partial w/\partial z|_{z^+=0}$, where ℓ_y and ℓ_z are the prescribed spanwise slip and transpiration lengths, respectively. For opposition control, the boundary conditions are instead $v|_{z^+=0} = 0$ and $w|_{z^+=0} = -A_d w|_{z^+=z_d^+}$ where A_d is the amplitude ratio and z_d^+ the detection plane height. Figure 3 compares $\ell_{T,VV}^+$ (lines) and the DNS-measured ℓ_T^+ (markers) for slip/transpiration surfaces and opposition control. In figure 3(*a*), the DNS data (markers) of [3] agree well with the viscous vortex model for a range of slip lengths, at least up to $\ell_T^+ \approx 4$. Similarly, for opposition control, the viscous vortex model (lines) accurately predicts $\ell_T^+ = \Delta U^+$ from the DNSs of [9] (markers) for detection plane heights up to $z_d^+ \approx 5$ and amplitude ratios $A_d \leq 1$, with some discrepancies for larger $z_d^+ \approx 10$ (note the viscous vortex domain height is $h^+ = 12$). Agreement with DNS shows that smooth-wall-like turbulence persists across these surfaces, and their wall-normal shifts ℓ_T^+ can be predicted using steady Stokes flow.

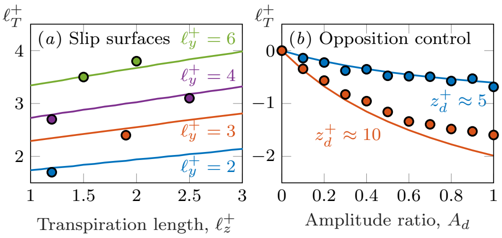

Figure 3: Viscous vortex model compared to DNSs of (*a*) slip [3] and (*b*) opposition control [9]. Solid lines are viscous vortex model predictions and markers are DNS data, where colours represent the inset slip length ℓ_y^+ or detection plane height z_d^+.

REFERENCES

[1] J. Wong, C. J. Camobreco, R. García-Mayoral, N. Hutchins, and D. Chung. *J. Fluid Mech.*, 978:A18, 2024.

[2] R. García-Mayoral and J. Jiménez. *J. Fluid Mech.*, 678:317–347, 2011.

[3] J. Ibrahim, G. Gómez-de-Segura, D. Chung, and R. García-Mayoral. *J. Fluid Mech.*, 915:A56, 2021.

[4] P. Luchini. In *Comput. Methods Appl. Sci. '96*, pages 466–470. 1996.

[5] P. Luchini, F. Manzo, and A. Pozzi. *J. Fluid Mech.*, 228:87–109, 1991.

[6] P. R. Spalart and J. D. McLean. *Phil. Trans. R. Soc. A.*, 369:1556–1569, 2011.

[7] D. W. Bechert, M. Bruse, W. Hage, J. G. T. Van Der Hoeven, and G. Hoppe. *J. Fluid Mech.*, 338:59–87, 1997.

[8] J. Jiménez, J.C. del Álamo, and O Flores. *J. Fluid Mech.*, 505:179–199, 2004.

[9] Y.M. Chung and T. Talha. *Phys. Fluids*, 23(2):025102, 02 2011.

2

ERCOFTAC
European Drag Reduction and Flow Control Meeting – EDRFCM 2024
September 10$^{\text{th}}$–13$^{\text{th}}$, 2024, Turin, Italy

EFFECT OF THE RIBLETS ON THE CONVECTIVE HEAT TRANSFER COEFFICIENT OF A TURBULENT BOUNDARY LAYER ON A FLAT PLATE

A. Mazzara, G. Paolillo
Dipartimento di Ingegneria Industriale Sezione Aerospaziale, Università di Napoli Federico II, 80125, Napoli, Italy

G. Cafiero
Dipartimento di Ingegneria Meccanica e Aerospaziale, Politecnico di Torino, 10129 Turin, Italy

C.S. Greco, T. Astarita, G. Cardone
Dipartimento di Ingegneria Industriale Sezione Aerospaziale, Università di Napoli Federico II, 80125, Napoli, Italy

ABSTRACT

Since the early 1970s, reducing skin friction drag has been a recurring research topic in the aeronautical industry. This is largely due to the constant rise in fuel prices and the growing need to decrease atmospheric pollutants [1][2][3]. One technique that has been developed and extensively studied over the years is the use of riblets.

They proved to be an effective technique for reducing skin friction in turbulent boundary layers [4][5].The mechanism through which riblets operate is not entirely clear. According to Gallagher and Thomas [6], riblets may be effective because they increase the height of the viscous sublayer. Bacher and Smith [7] emphasized the role of counter-rotating streamwise vortices and suggested that riblets reduce the momentum exchange properties of these structures. Choi [8] believed there are several mechanisms involved, but the main responsible of the turbulent skin friction production is the spatial structure of the near-wall burst. What he suggested is that the presence of the riblets halves the duration of the near-wall burst and increases its frequency. Additionally, the average spacing between the vortex pairs over the riblets surface is greater than that over a smooth surface.

Various geometries were tested in wind tunnels, showing drag reductions of up to 10% relative to a flat plate [9]. To achieve properties that lie between those of triangular and blade shapes, a parabolic cross-sectional shape was selected in this case. Furthermore, the parabolic riblets are not merely aligned with the flow direction; they feature a sinusoidal pattern in the streamwise direction [10].

Several methods exist to measure the friction drag and they include direct approaches using load cells or skin friction balances, as well as indirect methods such as the 2D boundary layer Momentum Integral (MI), oil flow visualization, reconstruction of flow field patterns using hot wire anemometry, and optical techniques like Particle Image Velocimetry (PIV) and InfraRed Thermography (IRT).

In particular, these latter approaches are advantageous for their non-intrusive nature. Infrared Thermography (IRT) could be used for studying various aspects of thermo-fluid dynamics, including convective heat flux on the wall and the behavior of surface flow patterns [11]. Indeed, the heat transfer behavior within the boundary layer undergoes significant changes based on whether the flow regime is laminar or turbulent.

In the present work, the Reynolds analogy is considered to estimate the skin friction coefficient on sinusoidal riblets, through the measurement of the convective heat transfer coefficient. The experiments were carried out in a closed loop open-vein vertical wind tunnel (Figure 1.1) with a test section measuring approximately 0.60 m x 0.9 m x 1.3 m. The free-stream turbulence level, measured through hot-wire anemometry, was less than 0.1%.

An MDF flat plate, characterized by a rounded leading edge, is positioned vertically at zero angle of attack along the centre line of the test section. This plate includes a hollow section measuring 260 mm x 260 mm to accommodate the riblets plate. The riblets plate, made of plexiglass, is heated via a Printed Circuit Board (PCB) powered by a power supply. For thermal imaging, a FLIR T650sc IR camera is utilized, offering a resolution of 640 × 480 pixels and sensitivity ranging from 7.5 to 13 μm. The camera operates at an acquisition frequency of 30 Hz; the spatial resolution is about 2 pixels/mm. As for the riblets geometry, the height of the grooves is $h = 210\ \mu m$ whilst the spacing between two adjacent grooves is $s = 300\ \mu m$, thus leading to a h/s ratio equal to 0.7; the sinusoidal pattern is characterized by a wavelength $\lambda = 19.2\ mm$ and a semi-amplitude $a = 0.15\ mm$.

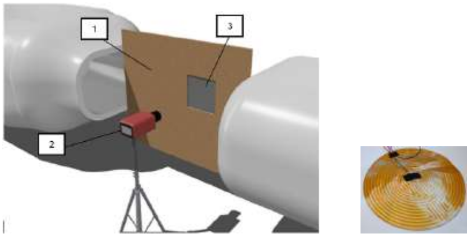

(a) (b)

Figure 1.1: (a) Experimental setup representation: (1) MDF plate, (2) Infrared Camera, (3) riblets plate. (b) Printed Circuit Board

The experiments begin with the wind tunnel operating prior to the start of camera acquisition. The plexiglass plate undergoes approximately two minutes of heating provided by the PCB to ensure an uniform temperature distribution and the PCB is switched off only after the IR camera starts acquiring. By considering the plexiglass solid wall semi-infinite (from the thermal point of view), with uniform initial temperature T_{wi} and subjected to a constant convective heat flux (expressed as the Newton's law with constant convective heat transfer coefficient h and constant reference temperature T_r, i.e. the adiabatic wall temperature), the analytical one-dimensional solution can be used:

$$\theta = \frac{T - T_{wi}}{T_r - T_{wi}} = erfc(\xi) - exp(Bi_x + \beta^2)erfc(\xi + \beta) \quad (1.1)$$

where T is the slab temperature at a certain depth x and:

$$\xi = x/2\sqrt{\alpha t} \quad \beta = h\sqrt{t/\rho ck} \quad Bi_x = hx/k \quad (1.2)$$

with α, ρ, c and k being respectively the thermal diffusivity coefficient, the mass density, the specific heat and the thermal conductivity of the solid wall. To determine the convective heat transfer coefficient, a least-squares fitting method is applied and to improve the accuracy, an additional correction term beyond equation 1.1 is considered. This correction term accounts for the radiative heat flux emitted by the plate and modifies the analytical solution, for $x = 0$ (i.e. on the wall surface), as follows:

$$\theta = exp(\beta^2)erfc(\beta) - \frac{q_r}{h(T_r - T_{wi})} \quad (1.3)$$

q_r is estimated through the Stefan-Boltzmann law, $q_r = \sigma(T_w^4 - T_r^4)$, being $\sigma = 5.67 \cdot 10^{-8}\ Wm^{-2}K^{-4}$ the well-known Stefan-Boltzmann constant. The results of this procedure are shown in the Figure 1.2 where a comparison between a plexiglass smooth flat plate and the riblets plate for a freestream velocity equal to $20\,m/s$ is reported.

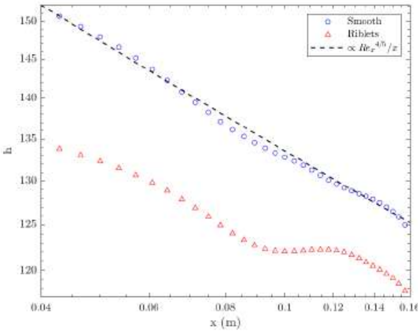

Figure 1.2: Comparison of the mean value of the convective heat transfer coefficient between the riblets plate and a smooth flat plate. The dashed line refers to a semi-empirical correlation provided by Incropera et al [12] in the case of a constant heat flux.

It can be seen that the presence of the riblets, in these conditions, causes a convective heat transfer coefficient reduction of about 8.5% with respect to the smooth case. Such a reduction is evaluated by averaging in both the streamwise and spanwise directions on the plate surface. In addition, the reduction in terms of the convective heat transfer coefficient is the same as that of the Stanton number, St, as it is defined as:

$$St = \frac{h}{\rho_f V c_p} \quad (1.4)$$

where ρ_f is the fluid mass density, V is the fluid velocity and c_p is the fluid specific heat capacity at constant pressure. Consequently, for the Reynolds analogy [13], this reduction is also the same as that of the skin friction, C_f.

REFERENCES

[1] Bushnell D. Turbulent drag reduction for external flows. In *21st Aerospace Sciences Meeting*, page 227, 1983.

[2] Hirschel E.H., Thiede P., and F. Monnoyer. Turbulence management: Application aspects. *In AGARD*, 1989.

[3] Thomas A.S.W. Aircraft drag reduction technology. *AGARD CP-365*, 11:1–20, 1984.

[4] Viswanath P.R. Aircraft viscous drag reduction using riblets. *Progress in Aerospace Sciences*, 38(6-7):571–600, 2002.

[5] García-Mayoral R. and Jiménez J. Drag reduction by riblets. *Philosophical transactions of the Royal society A: Mathematical, physical and engineering Sciences*, 369(1940):1412–1427, 2011.

[6] Gallagher J. and Thomas A. Turbulent boundary layer characteristics over streamwise grooves. In *2nd Applied aerodynamics conference*, page 2185, 1984.

[7] Bacher E.V. and Smith C. A combined visualization-anemometry study of the turbulent drag reducing mechanisms of triangular micro-groove surface modifications. In *Shear Flow Control Conference*, page 548, 1985.

[8] Choi K.S. Near-wall structure of a turbulent boundary layer with riblets. *Journal of fluid mechanics*, 208:417–458, 1989.

[9] Walsh M. and Lindemann A. Optimization and application of riblets for turbulent drag reduction. In *22nd aerospace sciences meeting*, page 347, 1984.

[10] Cafiero G. and Iuso G. Drag reduction in a turbulent boundary layer with sinusoidal riblets. *Experimental Thermal and Fluid Science*, 139:110723, 2022.

[11] Carlomagno G.M. and Cardone G. Infrared thermography for convective heat transfer measurements. *Experiments in fluids*, 49:1187–1218, 2010.

[12] Incropera F.P., DeWitt D.P., Bergman T.L., Lavine A.S., et al. *Fundamentals of heat and mass transfer*, volume 6. Wiley New York, 1996.

[13] Eckert E.R.G. and Drake Jr R.M. Analysis of heat and mass transfer. 1987.

3

ERCOFTAC
European Drag Reduction and Flow Control Meeting – EDRFCM 2024
September 10$^{\text{th}}$–13$^{\text{th}}$, 2024, Turin, Italy

SINUSOIDAL RIBLETS FOR TURBULENT DRAG REDUCTION

S. Cipelli
Institute of Fluid Mechanics, Karlsruhe Institute of Technology, 76131 Karlsruhe, Germany

M. Quadrio, F. Gattere
Department of Aerospace Science and Technologies, Politecnico di Milano, 20156 Milan, Italy

A. Chiarini
Complex Fluids and Flows Unit, Okinawa Institute of Science and Technology, 904-0495 Okinawa, Japan

P. Luchini
Dipartimento di Ingegneria Industriale, Università di Salerno, 84084 Fisciano, Italy

D. Gatti
Institute of Fluid Mechanics, Karlsruhe Institute of Technology, 76131 Karlsruhe, Germany

MOTIVATION

Drag reduction strategies can be classified into two main categories: active and passive. Active techniques typically involve wall movements, either in the spanwise or wall-normal direction, which can achieve significant drag reduction, up to 50% at low Reynolds numbers. However, their industrial application is constrained by substantial power consumption required for wall movement, and more critically, by the technical challenges associated with the physical implementation of the control mechanisms. In contrast, passive techniques, although offering smaller gains in terms of friction reduction, require only modifications to the wall geometry, making them easier to integrate into the aeronautical industry.

This work specifically focuses on riblets, a groovy type of surface geometry belonging to the passive category. Riblets typically achieve a friction drag reduction of $5 \div 10\%$ compared to a smooth surface. The underlying physical mechanism for drag reduction with riblets is well understood and can be attributed to a viscous differential effect of the wall on parallel and cross-flow, resulting in a difference between two virtual origins [5] $\Delta h = h_\parallel - h_\perp$, known as the parallel ($h_\parallel$) and perpendicular ($h_\perp$) protrusion heights. These quantities depend solely on the cross-section shape, as they are always non-dimensionalized with the square root of the groove cross-section area l_g. The two virtual origins indicate the position of a flat wall capable of producing the same average velocity profiles in the two directions; when the parallel origin is below the perpendicular one, the wall geometry impedes the cross flow more than the longitudinal flow, leading to drag reduction. In turbulent flows, this mechanism fully describes riblet behavior in the viscous regime, where riblets are extremely small, as the Re_τ-independent roughness function ΔU^+, used to quantify drag, is given by $\Delta U^+ = h_\perp^+ - h_\parallel^+$ [4]. For riblets of increasing dimensions, [2] showed that the concept of protrusion heights for parallel and transverse flow must be generalized to virtual origins for streamwise (l_U^+) and turbulent (l_T^+) flows, as drag reduction is generally quantified as $\Delta U^+ = l_T^+ - l_U^+$. While the virtual origin for mean flow (l_U^+) can always be related to the parallel protrusion height ($h_\parallel^+$), the origin for turbulence is a priori unknown and aligns with that of transverse flow only for a limited range of small l_g^+ values, necessitating evaluation through numerical or physical experiments for larger riblets. For straight riblets, following the observations from [1] regarding the position of maximum drag reduction occurring at approximately $l_g^+ = 11$, it is theoretically possible to derive a universal roughness function by accounting for Δh. This implies that viscous calculations aimed at estimating the protrusion heights should be sufficient to approximately characterize the drag reduction curve of a given geometry.

The aim of this work, however, is to test riblets with crests whose spanwise position varies sinusoidally along the longitudinal direction. The idea is to induce spanwise motions in the near-wall flow that mimic those typical of active control techniques, such as spanwise forcing [6]. By doing so, we aim to combine the virtual origin effect characteristic of straight riblets with the drag-reducing benefits of spanwise forcing techniques, exploring a potential enhancement of the performance of straight riblets.

METHOD

The described geometries are investigated through Direct Numerical Simulations (DNS) in a periodic channel with dimensions of $(7.5\,\delta,\, 3.75\,\delta,\, 2\,\delta)$ in the streamwise, spanwise, and wall-normal directions, respectively, being δ the channel half height. The spatial discretization employs second-order finite differences, and the timestep is advanced through a third-order Runge-Kutta scheme. The geometry is represented using an immersed boundary method (IBM). Riblets are present on both walls, and the friction Reynolds number is $Re_\tau = 200$. Statistics are averaged over 400 $t\,\delta/u_\tau$ time units.

Typically, extremely fine grid spacings are required near the riblet tips to ensure proper flow discretization. However, in this study, we use a uniform grid in the near-wall region where the minimum grid spacing never falls below 0.5 plus-units. This is achievable due to the correction of the IBM with local Stokes and Laplace solutions near the edges. This method, introduced by [3] and previously presented at EDRFCM 2022, allows for the simulation of full channel flows with riblets on a smooth-wall-like grid, maintaining the computational cost around 40 thousand CPU-hours for most configurations.

The simulated geometries include triangular riblets with a

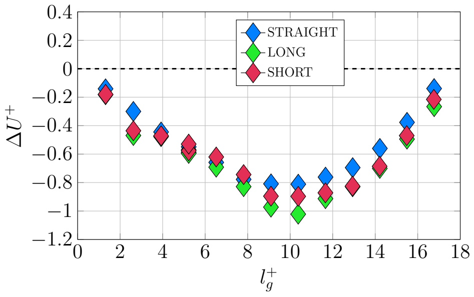

Figure 1: A summary of the ΔU^+ values obtained for all simulations as a function of the riblets size l_g^+. The three labels indicate the straight riblets configuration and the two sinusoidal configurations, namely "LONG" and "SHORT".

60° tip angle spanning the entire drag-reducing regime, from $l_g^+ \approx 1.5$ to $l_g^+ \approx 16.5$. We present results for both straight and sinusoidal riblets, where the sinusoidal waves are defined by two additional parameters: the wavelength λ_x^+ and the maximum inclination with respect to the x-direction β_{max}. The simulated sinusoidal geometries are characterized by (λ_x^+, β_{max}) = (1500, 2°) and (250, 12°), labeled as "LONG" and "SHORT" due to their different wavelengths. We calculate l_T^+ by overlapping the ribbed and smooth wall Reynolds shear stress profiles in the near-wall region, considering the total shear stress at the turbulence origin in the evaluation of u_τ. Then, all mean velocity profiles are shifted in the wall-normal direction to share the same virtual origin for turbulence. The vertical displacement between these aligned profiles corresponds precisely to ΔU^+. The virtual origin for turbulence is finally calculated as $l_U^+ = l_T^+ - \Delta U^+$.

RESULTS

An overview of the simulations results is given in Figure 1, where the drag reduction is evaluated in terms of shift of the roughness function ΔU^+. Results demonstrate the successful retrieval of drag reduction curves for all geometries, with minor discrepancies observed for sinusoidal riblets at very low l_g^+ values (also visible in Figure 2). These discrepancies are likely due to insufficient resolution for such small geometries. While straight riblets achieve a ΔU^+ value around 0.8 for $l_g^+ \approx 10$, both considered sinusoidal geometries surpass this value. Specifically, the "LONG" geometry achieves $\Delta U^+ \approx 1.0$, indicating an improvement of approximately 25% compared to the straight configuration. Notably, the peaks in the drag reduction curve for sinusoidal geometries occur at larger riblet sizes, suggesting that sinusoidal riblets can extend the viscous regime to higher l_g^+ values.

Further insights can be gained by examining the mean flow and turbulence virtual origins. In alignment with the earlier discussion, in Figure 2, we observe that the curves for $l_U/h_\parallel$ and $l_T/h_\perp$ exhibit the expected behavior: the value for l_U consistently matches the parallel protrusion height, while l_T deviates from $h_\perp$ as the riblet size increases. As mentioned earlier we note that for the sinusoidal cases the ratio $l_T/h_\perp$ remains constant over a broader range of l_g^+ compared to straight riblets. This suggests that sinusoidal riblets may extend the viscous behavior for larger dimensions, potentially delaying the occurrence of phenomena such as Kelvin-Helmholtz instabilities and secondary motions. Future results will determine whether this behavior persists at higher Reynolds numbers and if these observations hold true for different cross-section shapes and/or different sinusoidal waves.

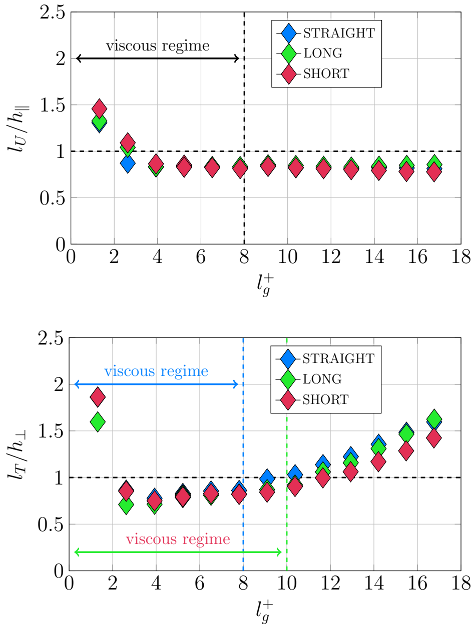

Figure 2: A comparison of virtual origins for the mean flow (l_U) and turbulence (l_T) to these of the longitudinal ($h_\parallel$) and transverse ($h_\perp$) flows, plotted as functions of the riblets size l_g^+.

REFERENCES

[1] R. Garcia-Mayoral and J. Jiménez. Hydrodynamic stability and the breakdown of the viscous regime over riblets. *J. Fluid. Mech.*, 678:317–347, 2011.

[2] J. I. Ibrahim, G. Gomez-de Segura, D. Chung, and R. Garcia-Mayoral. The smooth-wall-like behaviour of turbulence over drag-altering surfaces: a unifying virtual-origin framework. *Journal of Fluid Mechanics*, 915:A56, 2021.

[3] P. Luchini. A deferred correction multigrid algorithm based on a new smoother for the Navier–Stokes equations. *Journal of Computational Physics*, 92:349–368, 1991.

[4] P. Luchini. Reducing the turbulent skin friction. In Desideri et al., editor, *Computational Methods in Applied Sciences 1996*. Wiley, 1996.

[5] P. Luchini, F. Manzo, and A. Pozzi. Resistance of a grooved surface to parallel flow and cross-flow. *Journal of Fluid Mechanics*, 228:87–109, 1991.

[6] M. Quadrio and P. Ricco. Critical assessment of turbulent drag reduction through spanwise wall oscillation. *J. Fluid Mech.*, 521:251–271, 2004.

4

ERCOFTAC
European Drag Reduction and Flow Control Meeting – EDRFCM 2024
September 10th–13th, 2024, Turin, Italy

UNIFORM MOMENTUM ZONES IN TURBULENT BOUNDARY LAYERS OVER SINUSOIDAL RIBLETS

G. Cafiero[1] E. Amico[1], J. Serpieri[1] & G. Iuso[1]
[1]Department of Mechanical and Aerospace Engineering, Politecnico di Torino, 10129 Turin, Italy

INTRODUCTION

The interruption of the turbulence self-sustained cycle leads to the suppression of the exchange of momentum between the outer and inner regions of the boundary layer, and as such to the reduction of the turbulent fluxes near the wall, in turn promoting an attenuation of the skin friction drag. Understanding the scaling, interaction/generation and the role of coherent motions, i.e. regions of uniform momentum, in the turbulence production and dissipation has been at the very core of the research in wall bounded flows [11]. Understanding how to model the coherent motions and their link with the structures that can be detected in a turbulent boundary layer, such as haripins and packets of structures has also driven a large body of research [2, 7].

It has been demonstrated that a large portion of the turbulent kinetic energy in wall bounded turbulence is carried by these coherent motions [6]. Furthermore, they exchange momentum and affect smaller turbulence scales by interacting with the flow through the intense shear layers that generate at their edges.

Flow conditioning and control approaches aimed at reducing the skin friction drag are typically responsible for a modification of the structure of the turbulent boundary layer, and as such, it is expected that they can interact with the coherent motions that populate a boundary layer. It is therefore of interest to understand how they are affected by a given manipulation of the surface aimed at reducing the drag.

Sinusoidal riblets have been proposed as an alternative solution that could join the benefits of straight riblets with the spanwise-induced motion of the wall oscillation [9, 10, 3]. The sinusoidal riblets are obtained by considering grooves modulated by a stream-wise sine wave. [4] experimentally demonstrated that sinusoidal riblets cater for values of drag reduction as large as 10%, with an enhancement of about 3% when compared with straight riblets.

While the effect on the skin friction drag is very well assessed and investigated in the literature, no consensus has been reached on how the riblet surface affects the uniform momentum zones (UMZs). Even less so, the effect of sinusoidal riblets has not been investigated on the organization of the UMZs in a turbulent boundary layer.

EXPERIMENTAL SETUP

The experiments were performed in an open circuit wind tunnel at Politecnico di Torino, and the experimental setup is similar to the one used in [4, 3] and schematically represented in figure 1. Four plates were investigated: a flat plate, a riblet plate with longitudinal grooves (RLONG), and two riblet plates with sinusoidal grooves (RS1 and RS2). Each tested plate has a square shape, with a side of 258 mm and a thickness of 10 mm. This leads to a small gap between the edge of the tested plate and the flat plate. A labyrinth seal was mounted underneath the plate to avoid leaks through the tested inserts and the fixed flat plate.

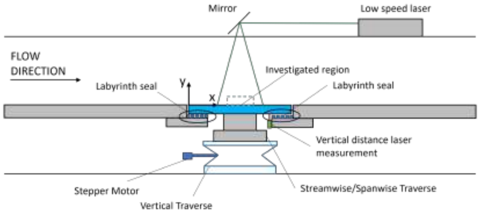

Figure 1: Schematic representation of the test section with detail of the removable plate. The track of the laser sheet, indicated in green, is not to scale.

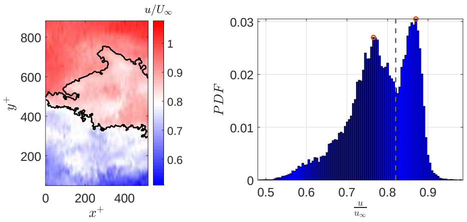

(a) (b)

Figure 2: Identification of UMZs in a generic instantaneous velocity field; (a) normalized streamwise velocity u/U_∞ in the streamwise-wall normal plane. Zones with uniform streamwise velocity are marked by black lines; (b) pdf of the normalized streamwise velocity u/U_∞.

The three riblet plates are characterized by the same groove profile, having a parabolic shape. The height of the groove is $h = 210$ μm whilst the spacing between two grooves is $s = 300$ μm, thus resulting in a $h/s = 0.7$. The two sinusoidal riblets are characterized by the same wavelength $\lambda = 19.2$ mm, thus leading to at least 13 wavelengths on the tested plate; conversely, two different values of the amplitude a are considered, with $a = 0.15$ mm in the RS1 and $a = 0.6$ mm in the RS2 case, respectively.

RESULTS

The UMZs are large-scale structures of regions of flow with roughly the same velocity magnitude. [1] hypothesised that the observed UMZs are caused by the presence of highly organised hairpin-like structures that form packets. Under these assumptions, it is possible to observe an increase in the number of UMZs (N_{UMZ}) with increasing Reynolds number as

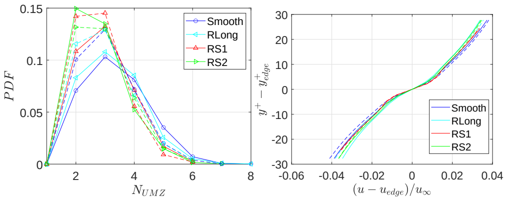

(a) (b)

Figure 3: a) Pdf of the number of UMZs detected in the turbulent boundary layer for the Smooth, RLong, RS1 and RS2 cases, at two values of the Reynolds number, $Re_\theta = 2900$ (continuous line) and $Re_\theta = 3900$ (dashed line).

the range of scales increases. As a consequence, when comparing with investigations at higher values of the Reynolds number, it is expected a higher mean value of UMZs. A histogram-based approach was implemented to determine the UMZs, following the approaches proposed by [5, 7]. Figure 2a shows a representative instantaneous realization of the flow field with colourmap of the streamwise velocity normalized with the freestream U_∞, and with overlaid black isolines indicating the edges of the UMZs. In the present investigation, the streamwise extent of the window used to determine the UMZ is set to 520 wall units for all the cases. Furthermore, regions of the flow at $y^+ < 50$ are also excluded from the analysis, as well as the non-turbulent region of the flow [8], i.e. beyond the turbulent/non-turbulent interface.

The velocity vectors that simultaneously satisfy the previous constraints are used to produce the pdf of the streamwise velocity component, which is then subdivided into 100 bins. Figure 2b shows two clear peaks, that can be associated with the modal velocities of the UMZs. A UMZ is identified as the midpoint between two consecutive values of the modal velocity, and as such leads to two UMZs in the example reported in Fig. 2.

For fixed Reynolds number, Fig. 3 shows that the number of uniform momentum zones reduces in the RS cases. More specifically, the Smooth and the RLong cases are typically characterized by quite similar behaviour, with a peak of the pdf occurring at $N_{UMZ} = 3$. The corresponding sinusoidal cases, instead, feature a reduction in the number of UMZs. Following the perspective proposed by [1], this can be interpreted as an attenuation of the coherent structures arising in the turbulent boundary layer and wall-normal momentum transfer, owing to the weakening of the internal shear layers that arise at the edges of the UMZs. From a more global perspective, another possible interpretation of the result is a homogenization of the momentum when the flow is manipulated via sinusoidal riblets, associated with the reduction of the UMZ.

It is also interesting to investigate the effect of the riblet geometry on the conditionally averaged velocity profiles calculated across the innermost UMZ. The fact that the UMZ is a relevant feature of the flow field is confirmed by the fact that there is a velocity jump, denoted by a different slope of the velocity profile. The results show that the riblet geometry is associated with a reduced velocity jump across the UMZ. This can be linked with an attenuation of the structures that has been demonstrated when comparing the riblet geometry with the smooth wall [3]. The presentation will focus on the link between the attenuation of the UMZs and the coherent structures that are generated in the turbulent boundary layer, when manipulated with sinusoidal geometries.

ACKNOWLEDGEMENTS

This study was carried out within the GREENER project – funded by the European Union – Next Generation EU within the PRIN 2022 program (D.D. 104 - 02/02/2022 Ministero dell'Universita e della Ricerca). This paper reflects only the authors' views and opinions, and the Ministry cannot be considered responsible for them.

REFERENCES

[1] R. J. Adrian, C. D. Meinhart, and C. D. Tomkins. Vortex organization in the outer region of the turbulent boundary layer. *Journal of Fluid Mechanics*, 422:1–54, 2000.

[2] Ronald J. Adrian. Hairpin vortex organization in wall turbulence. *Physics of Fluids*, 19(4):041301, 04 2007.

[3] G. Cafiero, E. Amico, and G. Iuso. Manipulation of a turbulent boundary layer using sinusoidal riblets. *Journal of Fluid Mechanics*, 984:A59, 2024.

[4] G. Cafiero and G. Iuso. Drag reduction in a turbulent boundary layer with sinusoidal riblets. *Experimental Thermal and Fluid Science*, 139:110723, 2022.

[5] C. M. de Silva, N. Hutchins, and I. Marusic. Uniform momentum zones in turbulent boundary layers. *Journal of Fluid Mechanics*, 786:309–331, 2016.

[6] B. Ganapathisubramani, E. K. Longmire, and I. Marusic. Characteristics of vortex packets in turbulent boundary layers. *Journal of Fluid Mechanics*, 478:35–46, 3 2003.

[7] M. Gul, G. E. Elsinga, and J. Westerweel. Internal shear layers and edges of uniform momentum zones in a turbulent pipe flow. *Journal of Fluid Mechanics*, 901:A10, 2020.

[8] W. Li, D. Roggenkamp, V. Paakkari, M. Klaas, J. Soria, and W. Schröder. Analysis of a drag reduced flat plate turbulent boundary layer via uniform momentum zones. *Aerospace Science and Technology*, 96:105552, 2020.

[9] Y. Peet and P. Sagaut. Theoretical prediction of turbulent skin friction on geometrically complex surfaces. *Physics of Fluids*, 21(10), 2009.

[10] M. Sasamori, O. Iihama, H. Mamori, K. Iwamoto, and A. Murata. Parametric Study on a Sinusoidal Riblet for Drag Reduction by Direct Numerical Simulation. *Flow, Turbulence and Combustion*, 99(1):47–69, 2017.

[11] A. J. Smits, B. J. McKeon, and I. Marusic. High–reynolds number wall turbulence. *Annual Review of Fluid Mechanics*, 43(Volume 43, 2011):353–375, 2011.

5

ERCOFTAC
European Drag Reduction and Flow Control Meeting – EDRFCM 2024
September 10$^{\text{th}}$–13$^{\text{th}}$, 2024, Turin, Italy

ON THE FLOW STRUCTURE IN THE VICINITY OF SINUSOIDAL RIBLETS IN A TURBULENT CHANNEL FLOW

F. A. Portela[1], E. Amico[2], G. Iuso[2], A. Busse[3] & G. Cafiero[2]
[1]Laboratoire de Mecanique des Fluides et d'Acoustique, Ecole Centrale de Lyon, France
[2]Department of Mechanical and Aerospace Engineering, Politecnico di Torino, 10129 Turin, Italy
[3]James Watt School of Engineering, University of Glasgow, UK

INTRODUCTION

Passive strategies for drag reduction in wall-bounded flows often involve tampering with the near-wall flow structures through modifications in the surface texture. The addition of riblets (or grooves) aligned with the mean-flow direction is arguably one of the most popular of such strategies [4, 6]. To some extent, however, riblets are often regarded as an academic exercise due to being strongly influenced by the flow direction and the relatively small values of drag reduction when deployed at scale. These limitations can be partly alleviated by modifying the stream-wise structure of the riblet.

This work builds on recent experiments by [3, 2] showing how sinusoidal riblets (riblets modulated by a stream-wise wave) can outperform classical riblets yielding larger values of drag reduction. Nevertheless, the inherent limitations of the experiments did not allow the authors to elucidate the undergoing physics in the vicinity of the groove. In this contribution, we use direct numerical simulation (DNS) data obtained at a friction Reynolds number $Re_\tau = 540$ to investigate the local flow structure near sinusoidal riblets.

NUMERICAL SETUP

The incompressible Navier-Stokes equations were solved in a doubly periodic channel of half-height δ, using second-order finite differences on a staggered grid for spatial derivatives and second-order Adams-Bashforth method for the time integration. The friction Reynolds number of $Re_\tau = 540$ is imposed through the constant driving force in the stream-wise direction. The no-slip and impermeability conditions at the riblets are imposed following an iterative version of an embedded boundary method described in [1]. As that method requires a Fourier representation of the surface, the riblets are inherently smoothed at the tip; this effect is minimised by retaining over half the wavenumbers in the span-wise direction.

A symmetric configuration of the channel is adopted with riblets on mirrored both the top and bottom walls, such that their mid-planes are 2δ apart. The two surfaces are offset by half the domain size along the homogeneous directions with respect to each other so as to minimise blockage effects. The grids used are uniformly discretised in the homogeneous directions with spacings of $\sim 3\delta_\nu$ and $0.4\delta_\nu$ in the stream- and span-wise directions, respectively. Along the wall-normal direction, a uniform spacing of $0.5\delta_\nu$ is used below the riblets' crests, the grid is then stretched using a hyperbolic tangent function yielding a maximum spacing of $\sim 4\delta_\nu$. For this grid, a time step of $4\times10^{-5}\delta/u_\tau$ led to numerically stable solutions.

RESULTS AND DISCUSSION

The stream-wise velocity profile and the stream-wise-wall-normal velocity component of the Reynolds shear stress tensor are plotted in figure 1 (a) and (b), respectively, as a function of the wall-normal location. The profiles are plotted for various locations across the groove, with the blue line indicating the centreline, the red line at the tip and the magenta line indicating the spatial averaged profile.

The $\overline{u}^+$ and $-\overline{u'w'}^+$ profiles are shifted to account for the effect of the rough wall, as suggested by [5]. In particular, the profiles are shifted to match the origin of the turbulence production, resulting in $|\Delta z^+| \approx 6.5$. The resulting velocity profiles show an upward shift, which corresponds to a value of the Hama function $\Delta U^+ \approx 0.6$, in agreement with the drag reduction effects of the riblets identified in the turbulent boundary layer experiments of [3].

The stream-wise-wall-normal component of the Reynolds shear stress tensor shows a significant variability depending on the location across the groove. In particular, at the tip, the $\overline{-u'w'}^+$ profile changes sign, thus leading to a region of the flow with negative turbulence production.

Shifting the focus to the spatial organization of the flow field, it is possible to see that, similar to the case of stream-wise-aligned riblets, mean-flow vortical structures aligned with the stream-wise direction develop just above the riblets tip [6]. In the present case, we observe that the wavy nature of the riblets causes the strength of these structures to alternate in phase with the riblet waviness itself, as shown in figure 2. These flow structures are associated with spatial inhomogeneity in the near-wall mean flow which can not only interfere with the turbulence but have drag-inducing/reducing effects, both of which can be analysed with our data.

It is possible to infer that the stream-wise aligned flow structures are those responsible for the local organization of the Reynolds shear stresses, which are found to be responsible for the negative turbulence production, and as such weaken the turbulence feeding the mean flow.

REFERENCES

[1] A. Busse, M. Lützner, and N. D. Sandham. Direct numerical simulation of turbulent flow over a rough surface based on a surface scan. *Computers & Fluids*, 116:129 – 147, 2015.

[2] G. Cafiero, E. Amico, and G. Iuso. Manipulation of a turbulent boundary layer using sinusoidal riblets. *Journal of Fluid Mechanics*, 984:A59, 2024.

[3] G. Cafiero and G. Iuso. Drag reduction in a turbulent

boundary layer with sinusoidal riblets. *Experimental Thermal and Fluid Science*, 139:110723, 2022.

[4] R. García-Mayoral and J. Jiménez. Drag reduction by riblets. *Philosophical Transactions of the Royal Society A: Mathematical, Physical and Engineering Sciences*, 369(1940):1412–1427, 2011.

[5] G. Gomez-de Segura and R. Garcia-Mayoral. Turbulent drag reduction by anisotropic permeable substrates–analysis and direct numerical simulations. *Journal of Fluid Mechanics*, 875:124–172, 2019.

[6] D. Modesti, S. Endrikat, N. Hutchins, and D. Chung. Dispersive stresses in turbulent flow over riblets. *Journal of Fluid Mechanics*, 917:A55, 2021.

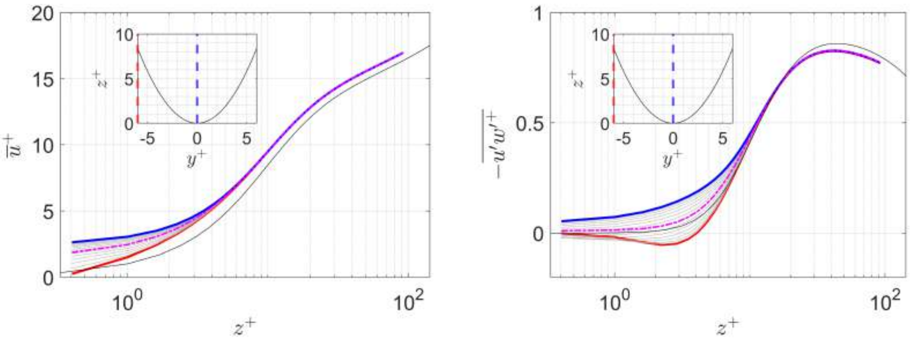

(a) (b)

Figure 1: Mean stream-wise velocity (a) and stream-wise-wall normal component of the Reynolds shear stress tensor (b) at different locations across the groove for the sinusoidal riblet case. The data are shifted according to the procedure proposed by [5].

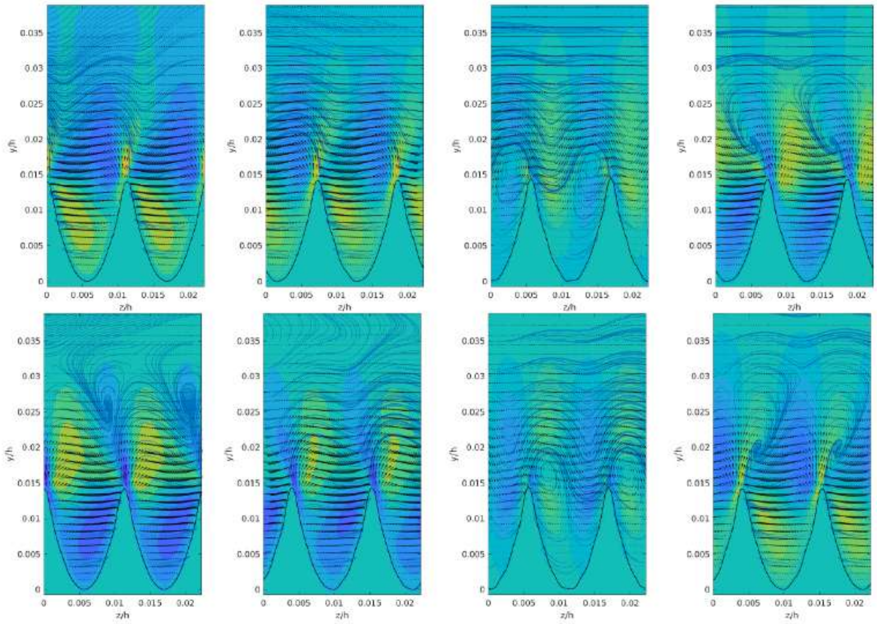

Figure 2: Averaged flow field (on the $y-z$ plane) at 8 evenly spaced locations along a stream-wise period of the riblets. The colours show the stream-wise component of vorticity, the arrows and streamlines are obtained from the span-wise and wall-normal mean velocities.

6

ERCOFTAC
European Drag Reduction and Flow Control Meeting – EDRFCM 2024
September 10^{th}–13^{th}, 2024, Turin, Italy

TURBULENCE AND STRUCTURAL DYNAMICS IN FLEXIBLE CANOPY FLOWS

G. Foggi Rota[§*]

A. Monti[§,†]

S. Olivieri[§,‡]

M. E. Rosti[§]

[§]Complex Fluids and Flows Unit, Okinawa Institute of Science and Technology Graduate University (OIST), 1919-1
Tancha, Onna, Okinawa 904-0495, Japan

INTRODUCTION

Canopy flows, common in nature [2], occur when a wall-bounded flow interacts with numerous slender objects protruding from a surface (like the flexible filments in figure 1), such as trees in forests or plants in fields. These obstacles significantly alter surface wind dynamics, enhancing turbulence and mixing, thus affecting surface ozone levels and seed dispersal. In water, marine currents frequently interact with seagrass meadows and different animal furs are associated to different swimming performances. Anatomically, ciliated surfaces in the bronchial epithelium and intestinal villi facilitate mucus transport and nutrient absorption, respectively. The study of canopy flows is thus motivated by their ubiquity and critical functions. Engineering applications include meta-surfaces for microfluidics and submerged canopies for coastal protection, due to their ability to attenuate waves and reduce sediment movement. Understanding canopy flow dynamics offers insights into natural phenomena and supports innovative engineering solutions.

In this work we employ direct numerical simulations (*DNS*) to investigate turbulent fluid motion and flexible filament dynamics within a dense submerged canopy, focusing on the effect of the filament flapping on canopy drag. At the meeting, building on top of our investigation [4], we will provide detailed characterisations of the flow above and within the canopy, compare these with experimental measurements, and assess the impact of variations in the filament density. Additionally, we will characterise the individual motion of the filaments in the canopy and reconcile it with the picture we previously drew for a single isolated filament [3].

METHODS

We employ our well tested *DNS* solver *Fujin* (`https://groups.oist.jp/cffu/code`) to simulate the turbulent flow of an incompressible fluid in an open channel, bounded from below by a no-slip wall covered by a dense canopy, and from the top by a free-slip surface. *Fujin* tackles the Navier-Stokes equations in primitive variables, sampling them on a staggered cartesian grid and adopting second order central finite differences. It resorts to a projection-correction scheme, solving the Poisson equation for the pressure with an efficient decomposition library (*2decomp*) coupled to an in-place spectral solver based on the Fourier's series method. The motion of the flexible filaments is modelled solving an extended version of the distributed-Lagrange-multiplier/fictitious-domain (*DLM/FD*) formulation of the continuum equations: a generalisation of the Euler-Bernoulli beam model allowing for finite deflections, but retaining the inextensibility constraint. We follow an approach like that of Huang et al. [5], coupling the fluid and the structure at their interface through a no-slip boundary condition enforced by the force distribution computed with a Lagrangian immersed boundary method (*IBM*).

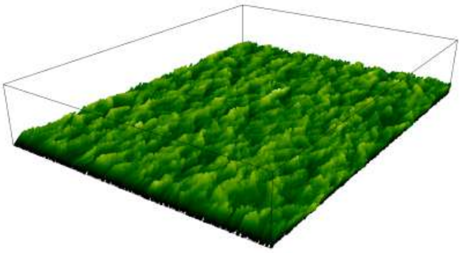

Figure 1: Computational domain with the fluid region and flexible filaments, coloured from dark to light green with their elevation.

RESULTS

Our study covers various Cauchy numbers, $Ca \in \{0, 10, 25, 50, 100\}$, indicating the ratio between the fluid deforming force and the filament elastic restoring force, at a fixed value of the bulk Reynolds number based on the domain height, $Re_b = 5000$. Increased filament flexibility reduces the canopy frontal area, yielding a weaker drag discontinuity at the canopy tip and less intense velocity fluctuations. Consequently, the canopy drag decreases with increasing flexibility (aligning with the available experimental results). Saturation is attained once the fully deflected filaments pile one on top of the other, parallel to the wall. Furthermore, the turbulent kinetic energy spectra within the canopy confirm the *spectral short-cut* mechanism [2], while a regular energy cascade is observed above the canopy tip. Increased filament flexibility enhances velocity fluctuations within the canopy, but reduces them outside due to the weakening of the shear layer.

---

[*] **Email for correspondence:** Giulio.FoggiRota@oist.jp

[†] Currently at: Centre for Maritime Research and Experimentation, STO—NATO, 19126, La Spezia, Italy

[‡] Currently at: Universidad Carlos III de Madrid, Leganés, 28911, Madrid, Spain

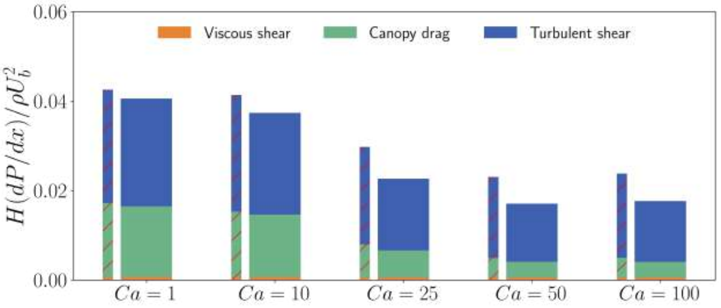

Figure 2: Shear stress balance contributions integrated across the wall normal direction for frozen canopy cases at different Ca values. Flexible case results are shown as thinner red-hatched bars.

Within the canopy, turbulence is quasi-2D near the bottom wall, becoming isotropic between the inner inflection point and the virtual origin of the outer flow. A strongly anisotropic state is attained approaching the canopy tip, and the flow exhibits a behaviour consistent with what observed in conventional channel flows moving above it, thus supporting outer similarity arguments [1]. Turbulence inside the canopy appears to be sustained by intense events generated in the outer flow, induced by the structures populating the close proximity of the shear layer, with only the strongest sweeps penetrating the canopy due to filament obstruction. On the other hand, ejections are less obstructed by the filaments and thus dominate the inner-outer flow interactions.

In a flexible canopy, the motion of the filaments is tightly coupled to the large scale coherent fluctuations of the turbulent flow [6]; in turn, the flow is affected by the flapping motion of the filaments along with their wakes at significantly smaller scales, due to the *spectral short-cut* mechanism. To assess the consequences of this complex fluid-structure interaction we inhibit it, "freezing" the flexible canopy in one of its instantaneous configurations, and we compare the flow attained above such peculiar rigid canopy to the flow developed above its flexible counterpart. We repeat the comparison for all the non-zero values of Ca in this study. The macroscopic effect of freezing the flexible canopy in its instantaneous configuration, despite the increased average velocity difference between the filaments and the fluid, is a reduction of its total drag (which nevertheless remains higher then in an open channel at $Re_b = 5000$ without the canopy). As visible in figure 2, the driving pressure gradient $\mathrm{d}P/\mathrm{d}x$ is reduced with respect to all the flexible canopy cases, reported for reference as thinner vertical bars highlighted with a red hatched fill. $\mathrm{d}P/\mathrm{d}x$ is made dimensionless with the channel height H, the fluid density ρ, and the bulk velocity U_b. The viscous shear contribution remains small and constant, while the canopy drag is slightly depleted. The most significant reduction is undergone by the turbulent shear, which is therefore almost completely responsible for the depletion of drag compared to the flexible cases. Indeed, the decrease of the driving pressure gradient is accompanied by a reduction in all the Reynolds stress components across the channel height, attributed to a diminished energy input into small-scale turbulence and a more effective obstruction of intense vertical interactions by the frozen filaments.

Consistently with our previous work on the flapping states of a clamped flexible fiber in wall turbulence [3], also here we observe two regimes of motion for the filaments: one dominated by their structural natural response and one by turbulence. At the transition between the two, resonance occurs. Furthermore, in the turbulence dominated regime, all the filaments exhibit the same dominant flapping frequency dictated by the largest flow structures regardless of the filament structural parameters, once again supporting the outcome of our precursory study. Yet, in the canopy, an increase in the filament density prompts the dominance of the natural response, as the filaments shield each other and are less deflected by the mean flow.

OUTLOOK

Here we have assessed how the flapping motion of the flexible filaments affects the total canopy drag, yet such flapping might have a non negligible effect also on the turbulent mixing, which is the topic of an upcoming investigation. Our results also pave the way towards the simulation of realistic scenarios, constituted by more accurate plant models. At the meeting we will further characterise the dynamics of the structure and of the fluid, providing insights to develop accurate turbulence models for RANS and LES simulations without resolving the flow at the filament scale.

REFERENCES

[1] Z. Chen and R. García-Mayoral. Examination of outer-layer similarity in wall turbulence over obstructing surfaces. *J. Fluid Mech.*, 973:A31, 2023.

[2] J. Finnigan. Turbulence in Plant Canopies. *Annu. Rev. Fluid Mech.*, 32(1):519–571, 2000.

[3] G. Foggi Rota, M. Koseki, R. Agrawal, S. Olivieri, and M. E. Rosti. Forced and natural dynamics of a clamped flexible fiber in wall turbulence. *Phys. Rev. Fluids*, 9(1):L012601, 2024.

[4] G. Foggi Rota, A. Monti, S. Olivieri, and M. E. Rosti. Dynamics and fluid-structure interaction in turbulent flows within and above flexible canopies. *J. Fluid Mech.*, *accepted*, 2024.

[5] W. X. Huang, S. J. Shin, and H. J. Sung. Simulation of flexible filaments in a uniform flow by the immersed boundary method. *J. Comput. Phys.*, 226(2):2206–2228, 2007.

[6] A. Monti, S. Olivieri, and M. E. Rosti. Collective dynamics of dense hairy surfaces in turbulent flow. *Sci. Rep.*, 13(1):5184, 2023.

 # 7

ERCOFTAC
European Drag Reduction and Flow Control Meeting – EDRFCM 2024
September 10th–13th, 2024, Turin, Italy

BOUNDARY LAYER CONTROL OF HEAT TRANSFER BY AN EFFUSION FILM

D. Burnett
Aeronautics, Imperial College London, SW7 2AZ London, United Kingdom

J. F. Morrison
Aeronautics, Imperial College London, SW7 2AZ London, United Kingdom

INTRODUCTION

To raise the maximum cycle temperature in gas turbine engines for increased thermal efficiency, a greater understanding of the mixing processes and mechanisms between the cooler film and hotter freestream must be obtained. A lack of this currently leads to excessive coolant use in real turbine designs and the concomitant efficiency penalties [2]. The experiments presented here aim to address this issue, where the geometry of a turbine blade is idealised in a large-scale facility with a canonical upstream boundary layer. The large perturbation to the boundary layer from the effusion film causes misalignment between the directions of the heat and momentum flux, leading to poor heat transfer predictions in RANS models [3]. A goal of the current experiments is to quantify this difference.

EXPERIMENTAL SETUP AND METHOD

A diagram of the effusion plate in depicted in figure 1. The temperature difference between the effused fluid and upstream boundary layer is small, such that temperature can be treated as a passive scalar. High resolution 3-component velocity profiles for a range of film-freestream velocity ratios ($VR = U_e/U_\infty < 0.4$) were acquired with Laser Doppler Anemometry (LDA). This enables greater understanding of the near-wall behaviour of the boundary layer and the turbulence generation mechanisms, which will both influence heat transfer into the surface. The wall-normal profiles were obtained at a streamwise distance of $x/D = 37.5$, $x/\delta \approx 3$ from the beginning of the effusion panel, at two spanwise locations: behind a column of holes, and in the centre between two columns of holes, as indicated in the inset of the figure plots. Oil Film Interferometry (OFI) measurements were taken at a streamwise distance of $x/\delta \approx 0.45$ behind the effusion panel, to provide skin friction coefficient measurements independent of the highly perturbed velocity profiles. The trends of these results are compared to skin friction estimates from the LDA velocity profiles, through linear sublayer fitting for $y^+ < 5$. The heat and momentum flux distributions were characterised through simultaneous x-wire and cold-wire measurements at the same locations as the LDA measurements.

RESULTS AND DISCUSSION

Figure 2 shows the normalised skin friction coefficient results obtained from OFI and the LDA velocity profiles. The magnitude of the values cannot be compared, due to difference in the streamwise location, but trends observed with changing velocity ratio are consistent between cases. They show a reduction in skin friction with the addition of blowing. On the hole centreline, a much greater decrease is observed, with c_f decreasing with increasing VR, until $VR \approx 0.2$, where it begins to plateau. On the hole centreline, c_f is approximately constant.

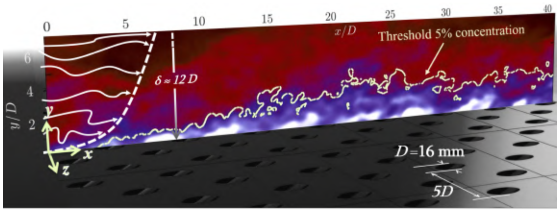

Figure 1: Schematic illustrating the mixing of effused fluid from the effusion panel with the incoming turbulent boundary layer [1].

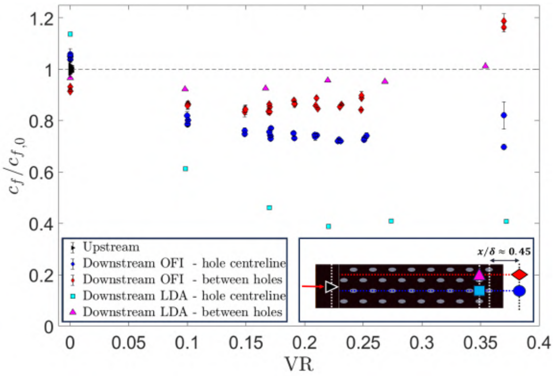

Figure 2: Comparison of skin friction coefficient results acquired from OFI and the LDA profiles, at a range of velocity ratios, normalised by the skin friction coefficient of the upstream boundary layer. The inset (bottom right) indicates the locations of the respective measurements.

Figure 3 shows the acquired mean velocity profiles, where large departures from canonical behaviour beyond $y^+ \approx 10$ are clearly observed. On the hole centreline, profiles show an increase in inner scaled streamwise velocity with increasing VR until $VR \approx 0.22$, where the trend starts to reverse. Beyond this velocity ratio, the profiles start to show two plateaus (at $y^+ \approx 20$, $y^+ \approx 100$), which become distinctly apparent at $VR = 0.37$, which indicates the bulk of the effusion film lifting from the surface. In these regions, a strong upwash is observed in the vertical velocity profiles (not shown). For the between holes cases, a plateau is also observed at $y^+ \approx 100$, which is accompanied by a negative

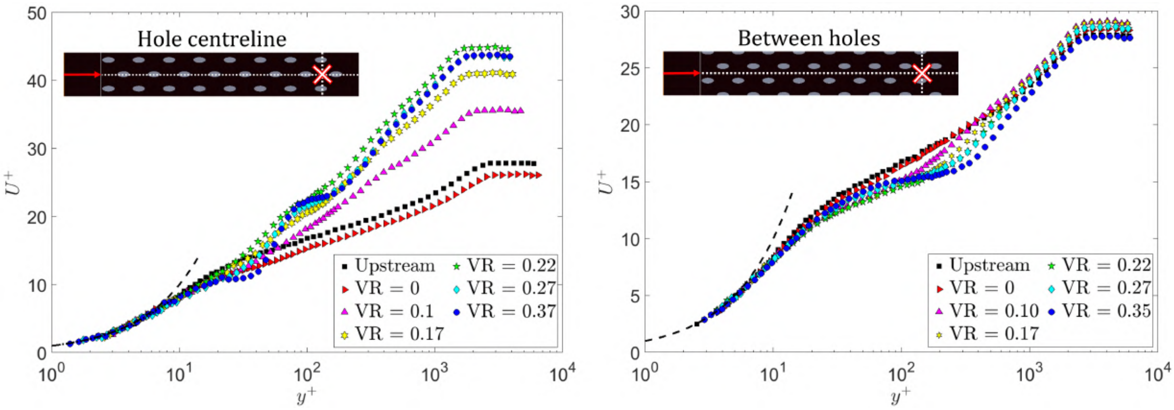

Figure 3: Wall-normal profiles of the mean streamwise velocity, scaled on inner variables, at variety of velocity ratios.

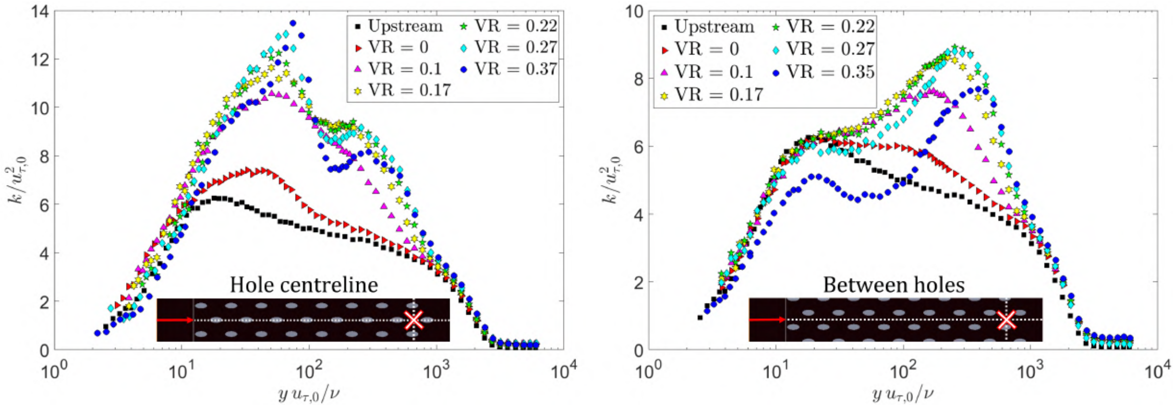

Figure 4: Wall-normal profiles of the turbulent kinetic energy, normalised by the upstream friction velocity, at variety of velocity ratios.

peak in the wall-normal mean velocity at a similar location. This suggests the formation of contra-rotating vortices either side of the jets that promote film lift-off. This jet-in-crossflow type phenomenon has been well documented in literature for film cooling flows at high velocity ratios ($VR > 1$), and conjectured to be the dominant mechanism in film lift-off [4], but not associated with lower velocity ratios. The inflection points in the velocity profiles also correspond to lift-off in the temperature profiles. At these locations, large deviations in the Reynolds analogy are observed and the Turbulent Prandtl number becomes negative.

Figure 4 shows profiles of turbulent kinetic energy. On the hole centreline, a significant increase in turbulence is observed in the near wall region, with a peak located at approximately $y\,u_{\tau,0}/\nu \approx 80$. The magnitude and wall-normal distance of the peak increases with increasing VR. Profiles of the production, $\overline{uv}\,\partial U/\partial y$ (not shown), indicate that this is likely a streamwise shear dominated interaction. An outer peak also begins to form at $VR \approx 0.22$, likely associated with the film-freestream shear layer. It moves further from the wall with increasing VR, where mean shear rate is lower, and reduces in magnitude. Beyond this velocity ratio, the near-wall turbulence was observed to become dominated by spanwise fluctuations, as opposed to streamwise.

For the profiles located between holes, an outer peak in a similar location was observed, with the same trends as described above. The 'inner' peak appears as a shoulder with similar magnitude to the upstream case. At $VR = 0.35$, an attenuation of the inner peak is observed. Basley et al. [1] observed a significant reduction in the modulation of smaller near-wall structures by large scale outer structures at a similar velocity ratio, when compared to lower velocity ratios or no-blowing cases, which could explain this observation.

REFERENCES

[1] Jérémy Basley, Kevin Gouder, and Jonathan F. Morrison. Mixing and large-scale modulation of a turbulent boundary layer perturbed by an effusion film. In *12th International Symposium on Turbulence and Shear Flow Phenomena (TSFP12)*.

[2] Je-Chin Han. Fundamental gas turbine heat transfer. *Journal of Thermal Science and Engineering Applications*, 5(2), 2013. 021007.

[3] Richard D. Sandberg and Vittorio Michelassi. Fluid dynamics of axial turbomachinery: Blade- and stage-level simulations and models. *Annual review of fluid mechanics*, 54(1):255–285, 2022. USDOE.

[4] Jing-Zhou Zhang, Shengchang Zhang, Chun-hua Wang, and Xiao-Ming Tan. Recent advances in film cooling enhancement: A review. *Chinese Journal of Aeronautics*, 33:1119–1136, 2020.

 # 8

ERCOFTAC
European Drag Reduction and Flow Control Meeting – EDRFCM 2024
September 10^{th}–13^{th}, 2024, Turin, Italy

EFFECT OF FREESTREAM TURBULENCE ON A SPATIALLY DEVELOPING TURBULENT BOUNDARY LAYER SUBJECTED TO MODERATE ADVERSE PRESSURE GRADIENT

Francesco Scarano
DIMEAS, Politecnico of Turin, ZIP 10129 Turin, Italy

Tomek Jaroslawski
Center for Turbulence Research, Stanford University, 94305 Stanford, US
Département Multi-physique pour l'énergétique, ONERA Toulouse, 31000, Toulouse, France

INTRODUCTION

Turbulent boundary layers (TBLs) experiencing adverse pressure gradients (APGs) are more industrially relevant compared to zero pressure gradients (ZPGs). However, limited knowledge exists regarding the impact of elevated freestream turbulence (FST) on TBLs with moderate APGs. While extensive research has investigated the influence of FST on canonical ZPG turbulent boundary layers, there remains a notable gap in understanding the impact of elevated FST on TBLs subject to moderate APGs, particularly in non-equilibrium developing flows and over real airfoils rather than idealized flat plates with imposed pressure gradients. In ZPG TBLs subjected to freestream turbulence (FST), pivotal investigations were undertaken by [5, 4], utilizing two distinct passive grids in a wind tunnel study, with the boundary layer measured over a flat plate. They examined a maximum T_u ($u'/U_{\inf}$) of 5.8%. [3] investigated the impact of freestream turbulence on turbulent boundary layers at relatively low Reynolds numbers, $500 < Re_\theta < 2500$. Two passive grids were employed to induce FST with turbulence intensities up to 7%. Results indicated that skin friction was influenced by both Reynolds number and freestream turbulence intensity. Similarly, [2] demonstrated an increase in skin friction with FST in turbulent boundary layers for $1000 < Re_\theta < 7000$. In a subsequent analysis [1], the influence of FST on the turbulent boundary layer profile shape was examined. While the logarithmic region remained relatively unaffected by freestream turbulence, the presence of the wake was strongly dependent on FST levels.

Compared to ZPG TBLs, adverse pressure gradients (APGs) induce notable alterations in turbulent statistics. Previous studies have identified a secondary peak in production located in the outer region of the boundary layer. This peak enables significant diffusion of turbulent energy towards the wall, resulting in amplified normal stresses near the wall [7].

EXPERIMENTAL SETUP

The experimental campaign has been conducted in the ONERA Toulouse TRIN 2 subsonic wind tunnel. A sketch of the experimental setup is reported in figure 1. The test model is a NACA 0015 aerofoil. Varying the angle of attack (2 and 4°) adjusted the pressure gradient, and hotwire anemometry measured boundary layer properties at different chordwise positions ($x/c = 0.400$–0.625, with $\beta = \delta^*/\tau_0 dP/dx = 0.3$-$1.2$). The FST level was increased using static grids, resulting in levels ranging from 0.15 to 6%. The chord-based Reynolds number was kept constant at around 250,000 for all configurations.

The boundary layer surveys were obtained using constant temperature hot-wire anemometry using a Dantec Dynamics Streamline Pro system with a 90C10 module and a 55P15 boundary-layer probe.

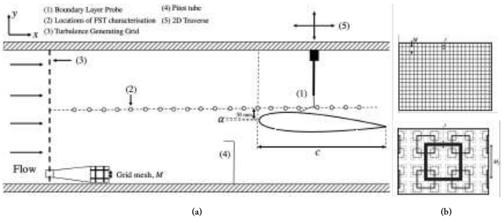

Figure 1: Sketch of the experimental setup

The free-stream turbulence development along the aerfoil is detailed in figures 2 (a) and in 2 (b) the spectrum of the free-stream turbulence is reported.

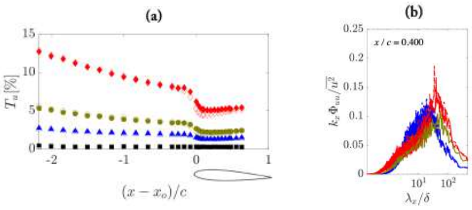

Figure 2: Free-stream turbulence evolution along the profile (a), spectral content of the FST at a fixed streamwise postion.

PRELIMINARY RESULTS

In figure 3 the mean and variance velocity profiles are reported at iso streamwise position for $AOA = 4°$. The wake increases due to the APG but it decreases due to FST (as previously reported in the literature). The occurrence of an outer peak already present for the low T_u (due to the APG) is further enhanced by the FST. The inner peak increases.

The FST increases the boundary layer thickness and reduces the shape factor as reported in figure 4.

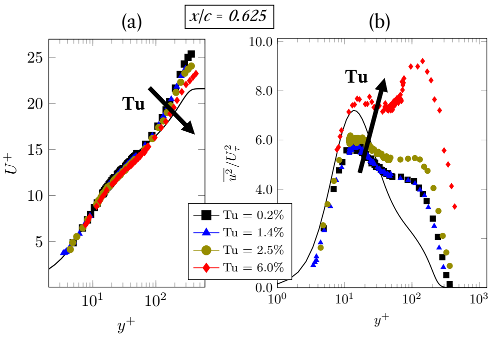

Figure 3: Non-dimensional velocity and standard deviation profiles at $x/c = 0.625$ for the four values of turbulence intensities for $AOA = 4°$. The arrow indicates the turbulence intensity increase.

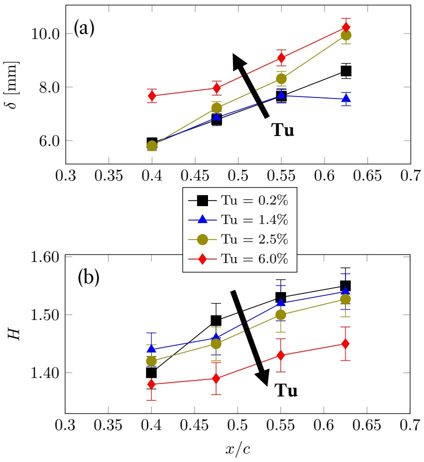

Figure 4: Streamwise evolution of the boundary layer parameters for $AOA = 4°$ and different Turbulence intensities, (a) boundary layer thickness, (b) shape factor, (c) momentum thickness based Reynolds number.

The skin friction coefficient, obtained with the fitting method proposed by [6], is reported in figure 5. The friction coefficient for an APG diminishes with respect to a ZPG condition (Coles-Fernholz relation for smooth, ZPG turbulent boundary layer reported in solid line). However the friction coefficient increases when increasing the FST approaching the ZPG value for the highest FST.

The variance profiles have been separated in small and large scales contributions. The threshold chosen is $\lambda_x = 8\delta$ to better isolate the effect of the FST (whose spectral content is reported in figure 2 (b)). As depicted in figure 6, the large scales due to the turbulence penetrate into the near wall region and are responsible for the near wall peak increase, reported in figure 3 (b) and the skin friction increase. This penetration is further enhanced by the APG (not shown here).

The current results suggest that any flow-control strategy in industrially relevant application (namely in presence of FST and APG) should address the large-scale structures even at low Reynolds number.

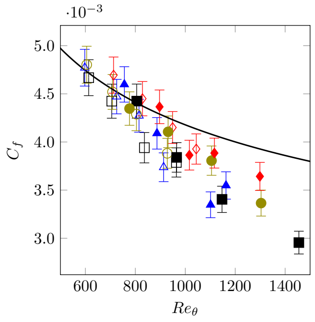

Figure 5: Skin friction coefficient as function of momentum thickness Reynolds number.

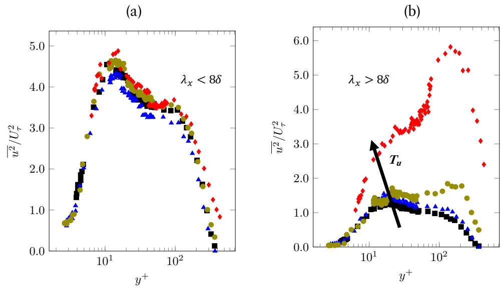

Figure 6: Variance decomposition based on a wavelength threshold of 8δ.

REFERENCES

[1] MF Blair. Influence of free-stream turbulence on turbulent boundary layer heat transfer and mean profile development, part ii—analysis of results. 1983.

[2] MF Blair. Influence of free-stream turbulence on turbulent boundary layer heat transfer and mean profile development, part i—experimental data. 1983.

[3] IP Castro. Effects of free stream turbulence on low reynolds number boundary layers. 1984.

[4] PE Hancock and P Bradshaw. Turbulence structure of a boundary layer beneath a turbulent free stream. *Journal of Fluid Mechanics*, 205:45–76, 1989.

[5] Philip Ernest Hancock and P Bradshaw. The effect of free-stream turbulence on turbulent boundary layers. 1983.

[6] Eduardo Rodríguez-López, Paul J. K. Bruce, and Oliver R. H. Buxton. A robust post-processing method to determine skin friction in turbulent boundary layers from the velocity profile. *Experiments in Fluids*, 56(4):68, April 2015.

[7] Ricardo Vinuesa, Seyed M Hosseini, Ardeshir Hanifi, Dan S Henningson, and Philipp Schlatter. Pressure-gradient turbulent boundary layers developing around a wing section. *Flow, turbulence and combustion*, 99:613–641, 2017.

 # 9

ERCOFTAC
European Drag Reduction and Flow Control Meeting – EDRFCM 2024
September 10$^{\text{th}}$–13$^{\text{th}}$, 2024, Turin, Italy

THEORETICAL AND EXPERIMENTAL STUDIES OF BOUNDARY LAYER FLOW OVER BROAD ROTATING CONES IN AXIAL FLOW

Z. Hussain
School of Engineering, University of Leicester, Leicester, UK

S. Tambe
Department of Aerospace Engineering, Indian Institute of Science, Bangalore, India

INTRODUCTION

In this study, a theoretical and computational solution for analysing the stability of rotating boundary layers is applied to the flow over a broad rotating cone in axial flow, for the first time. The investigation includes a direct comparison with experiments conducted via infrared thermography (IRT) and particle image velocimetry (PIV) techniques. The mean flow field is perturbed leading to disturbance equations, and both are solved via a robust spectral numerical method employing Chebyshev polynomials.

In the aerospace industry, this problem depicts flow over rotating machinery components at the leading edge of a turbofan. Laminar-turbulent transition within the boundary layer can result in significant drag increases, which negatively impacts fuel efficiency, energy consumption and noise generation.

Delaying transition to turbulence can counteract these effects and controlling the primary instability may be one route to achieving this. Ultimately, real-time control of the governing input parameters, in this case rotational speed, oncoming flow and surface curvature, for such a problem may lead to future design improvements and potential cost savings.

However, other related control mechanisms have also been investigated for this geometry, in particular, the effects of organised roughness on the non-stationary modes of the flow instability, and the current study will report on these.

Current results are discussed in terms of existing experimental data and neutral stability curves for broad-angled rotating cones, which are susceptible to the crossflow instability observed for flow over a rotating disk, and this instability is visualised in terms of co-rotating spiral vortices.

Importantly, favourable comparisons are obtained with the experimental results, in particular with regards to the critical Reynolds number and critical location of onset of the most dangerous mode for the governing crossflow instability, as illustrated in Figs. 1 and 2.

FIGURES

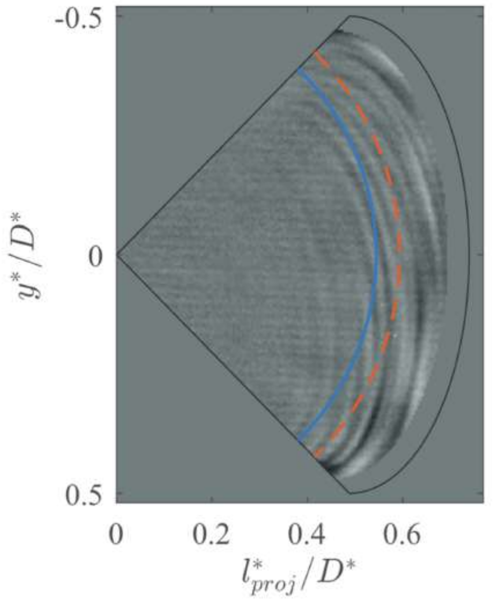

Figure 1: Instantaneous thermal footprints in the camera plane of the spiral vortices on a rotating broad cone of half-angle $\psi = 45°$.

REFERENCES

[1] Garrett, S.J., Hussain, Z. & Stephen, S.O. (2010): Boundary-layer transition on broad cones rotating in an imposed axial flow, *AIAA J.*, **48**, No. 6.

[2] Hussain, Z., Garrett, S.J., Stephen, S.O. & Griffiths, P.T. (2016): The centrifugal instability of the boundary layer on a rotating cone in an enforced axial flow, *J. Fluid Mech.*, **788**, 70–94.

[3] Unadkat, J. & Hussain, Z. (2020): On the stability of boundary-layer flow over a rotating cone in an enforced axial free stream, *Proceedings of the ISROMAC 18.*

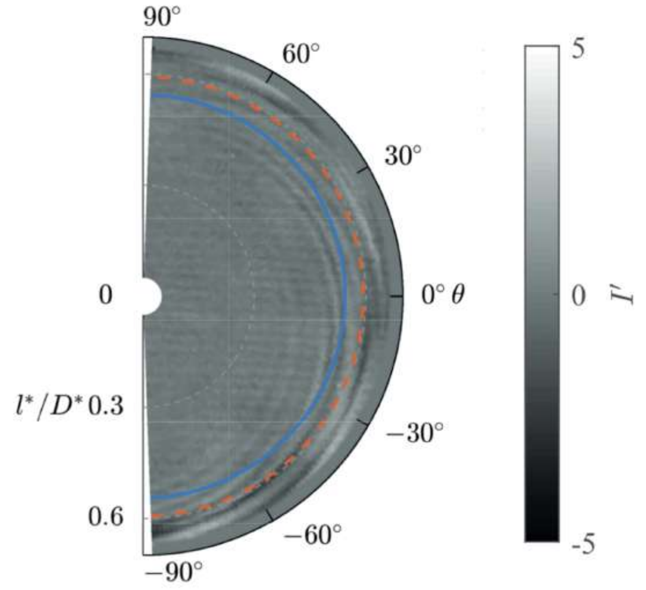

Figure 2: Instantaneous thermal footprints on the unwrapped cone surface of the spiral vortices on a rotating broad cone of half-angle $\psi = 45°$.

10

ERCOFTAC
European Drag Reduction and Flow Control Meeting – EDRFCM 2024
September 10$^{\text{th}}$–13$^{\text{th}}$, 2024, Turin, Italy

LARGE-SCALE ENERGY ATTENUATION OF WALL-BOUNDED TURBULENCE WITH AN INNER-SCALED HELMHOLTZ RESONATOR

A.H. Hassanein, **D. Modesti**, **F. Scarano**, **W.J. Baars**
Faculty of Aerospace Engineering, Delft University of Technology, 2629 HS Delft, The Netherlands

INTRODUCTION

For over four decades, a considerable research effort has been devoted to the study of turbulent skin-friction drag and control methods for mitigating this drag [2]. In this work, we present an appealing passive method with the prospect of controlling wall-bounded turbulence. Helmholtz resonators (HR) show potential in manipulating wall-bounded turbulence as they can be frequency-tuned to the temporal scales of velocity fluctuations within wall-bounded turbulence [5, 4]. Dacome et al. [3] explored the interaction between a single miniature Helmholtz resonator and a grazing Turbulent Boundary Layer (TBL) flow, through varying independently its inner-scaled orifice diameter, as well as its inner-scaled resonance frequency. They revealed that behind the resonator, an amplification of the streamwise velocity fluctuations appeared at a scale close to the one of resonance. This resonance-induced amplification co-existed with a notable decrease in large-scale energy. Particularly, the changes in the spectral energy content of the flow became more pronounced when the natural frequency of the HR aligned with the peak frequency of the wall-pressure spectrum. The objective of this study is to explain the physical mechanism responsible for large-scale energy attenuation. For this purpose, spatio-temporal data is required to assess the interaction of the incoming velocity fluctuations and fluctuations associated with the resonator response, on a per-frequency basis. For acquiring these data, experiments have been conducted using time-resolved particle image velocimetry (TR-PIV).

LAYOUT OF EXPERIMENTS

Experiments were conducted in a low-speed open-return wind tunnel facility (W-tunnel) comprising a zero-pressure gradient development section for a TBL flow. Details of the facility are described by Baars et al. [1]. Flow conditions and TBL parameters of the nominal boundary layer flow at 3.17 m downstream from the leading-edge are summarized in Table 1.

U_∞ (m/s)	Re_τ	δ (mm)	l_v (μm)	U_τ (m/s)
15.0	2300	72.0	30.3	0.52

Table 1: Nominal TBL parameters.

A single HR was embedded in the spanwise-center of the bottom wall at a distance of 3.17 m from the leading edge. The diameter of the orifice was $d^+ = 60$ and the considered natural frequency was tuned to match one-to-one with the peak of the wall pressure spectrum, which is known to reside at $\lambda_p^+ \approx 250$ ($f_p^+ \approx 1/25$) and to be invariant with Re_τ as shown in the literature [6].

Time-resolved planar velocity fields were measured with high-speed PIV. Illumination was provided with a Quantronix Darwin Duo-527 Nd:YLF laser (2x25 mJ @ 1 kHz). The thickness of the laser sheet was kept to 1 mm. Imaging was performed using a Photron FASTCAM SA1.1, comprising a 12-bit sensor of 1024×1024 px^2 at 5.4 kHz, and a 20 μm pixel size. A Nikon lens with a 200 mm focal length was utilized, set to an aperture $f\#$ of 4. Additionally, a teleconverter was employed to double the optical magnification, reaching a value of 1. The acquisition frequency was set to 14.94 kHz, and the corresponding sensor resolution was 750×512 px^2. In total, 6 sets of 14400 consecutive images were acquired uninterruptedly (resulting in 6×14400 images per measurement case: the baseline boundary layer and the resonator case). A photo of the TR-PIV setup, alongside a schematic of the resonator and field-of-view (FOV), are shown in fig. 1. DaVis 10.2 software was used for system synchronization, image acquisition, and PIV processing. Cross-correlations of the time-resolved recordings were carried out using the sliding sum of correlations technique [7] with a length of 4 frames. The PIV parameters are summarised in Table 2.

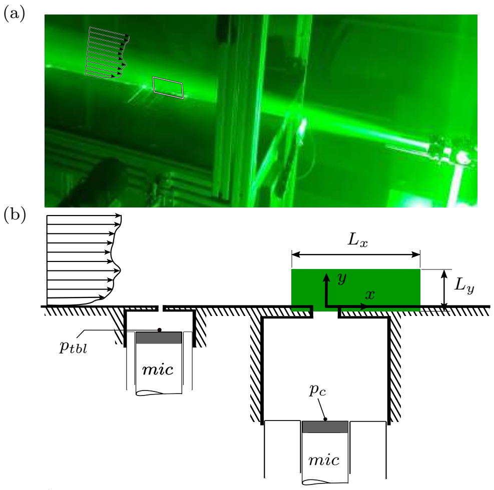

Figure 1: (a) Photograph of the TR-PIV setup. (b) Schematic of the HR under grazing flow, including the pinhole-mounted microphone located upstream, as well as an indication of the fluctuating pressure measurements, p_{tbl} and p_c.

RESULTS

Availability of time-resolved velocity fluctuations allows for a detailed inspection of how the resonator alters the spectral energy content of the TBL flow. The energy spectrogram of

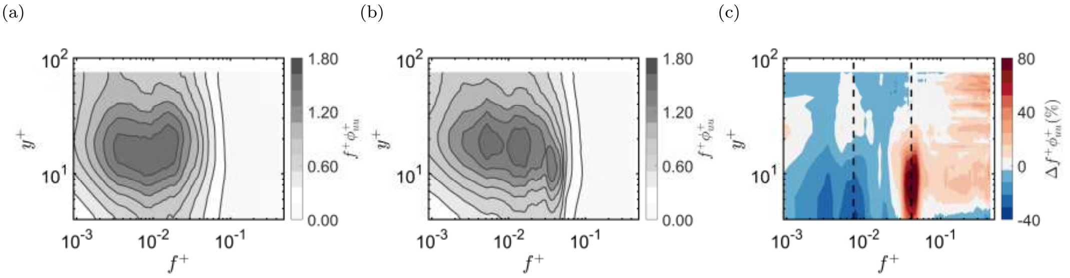

Figure 2: (a,b) Premultiplied energy spectrogram of the streamwise velocity fluctuations, $f^+\phi^+_{uu}$ at $x^+ = 100$, for (a) the baseline TBL and (b) the embedded Helmholtz resonator case. (c) Percentage difference between the premultiplied energy spectrograms presented in sub-figures (a) and (b). A positive (red) value indicates a larger energy content in the case of the embedded Helmholtz resonator.

Field of view	$14 \times 9.5\ mm^2$
Image resolution	$53.7\ px/mm$
Interrogation window	$24 \times 6\ px^2$
Processing technique	Sliding sum of correlation
Overlap	75%
Vector pitch	0.056mm, $2l_v$
Measurement rate	$14.94\ kHz$

Table 2: PIV measurement parameters.

the baseline boundary layer flow is shown in fig. 2a, with alongside in fig. 2b the altered spectrogram downstream of the HR, at $x^+ = 100$. In both of these spectrograms, one can observe that the inner peak is well-captured with the TR-PIV at the location $(y^+; f^+) \approx (15; 0.01)$.

To highlight changes in the spectrograms, the percentage difference between the contours in fig. 2a and fig. 2b is plotted in fig. 2c. There is an observable narrow-band increase in the streamwise velocity fluctuations around the resonator's natural frequency. This region of increased energy is confined to a wall-normal location of approximately $y^+ = 30$ at this downstream location, and reaches up to 60% in intensification. In addition, the resonator amplifies the energy of smaller scales (i.e., higher frequencies) at super resonance, up to 20%. Furthermore, a broader band of energy attenuation is observed at larger scales up to 40%, resulting in a significant depletion of energy within the spectral-inner peak.

DISCUSSION AND FULL CONTRIBUTION

The resonator's frequency alignment with the peak-frequency of the wall-pressure spectrum results in the excitation of scales near and above resonance while attenuating the energy of sub-resonant scales. This phenomenon is attributed to the local impedance at the resonator's orifice. In the full conference contribution it will be highlighted that the attenuation of large-scale energy resides within the near-wall region beyond a distance of $x^+ = 300$ downstream of the resonator (beyond our field-of-view). Concurrently, intensified smaller resonance-scales recover relatively quickly, at roughly $x^+ = 200$, to the level of the baseline case.

The phenomenon by which the resonance scales are intensified and the large-scales are suppressed is attributed to the local impedance condition that is established at the resonator's orifice. Temporal evolution of the velocity fluctuation fields at different scales are presented in support of our hypothesis. By disrupting the inner-spectral peak of the streamwise velocity fluctuations and diminishing the energy of the larger structure's footprint near the wall, Helmholtz resonators placed at frequencies near the peak-frequency of the wall-pressure spectrum demonstrate potential scalability with friction Reynolds number and applicability in the construction of control surfaces for skin-friction drag manipulation.

REFERENCES

[1] W. J. Baars, G. Dacome, and M. Lee. Reynolds-number scaling of wall-pressure–velocity correlations in wall-bounded turbulence. *J. Fluid Mech.*, 981:A15, 2024.

[2] T.C. Corke, Y. Guezennec, and H.M. Nagib. Modification in drag of turbulent boundary layers resulting from manipulation of large-scale structures. Technical report, NASA, 1981.

[3] G. Dacome, R. Siebols, and W. J. Baars. Inner-scaled Helmholtz resonators with grazing turbulent boundary layer flow. *arXiv preprint arXiv:2308.07776*, 2023.

[4] K. P. Flynn and R. L. Panton. The interaction of Helmholtz resonators in a row when excited by a turbulent boundary layer. *J. Acoust. Soc. Am.*, 87(4):1482–1488, 1990.

[5] K. P. Flynn, R. L. Panton, and D. G. Bogard. Effect of Helmholtz resonators on boundary-layer turbulence. *AIAA J.*, 28(11):1857–1858, 1990.

[6] R. L. Panton, M. Lee, and R. D. Moser. Correlation of pressure fluctuations in turbulent wall layers. *Phys. Rev. Fluids*, 2(9):094604, 2017.

[7] A. Sciacchitano, F. Scarano, and B. Wieneke. Multi-frame pyramid correlation for time-resolved PIV. *Exp. Fluids*, 53(4):1087–1105, 2012.

11

ERCOFTAC
European Drag Reduction and Flow Control Meeting – EDRFCM 2024
September 10th–13th, 2024, Turin, Italy

NUMERICAL STUDY OF TURUBLENT SKIN-FRICTION DRAG REDUCTION VIA SPANWISE FORCING AT LARGE VALUES OF REYNOLDS NUMBER

D. Gatti
Institute of Fluid Mechanics, Karlsruhe Institute of Technology, 76135 Karlsruhe, Germany

M. Quadrio, F. Gattere
Department of Aerospace Science and Technology, Politecnico di Milano, 20156 Milano, Italy

A. Chiarini
Complex Fluids and Flows Unit, Okinawa Institute of Science and Technology, 904-0495 Okinawa, Japan

S. Pirozzoli
Department of Mechanics and Aerospace Engineering, Univeristà La Sapienza, 00185 Roma, Italy

INTRODUCTION

Transverse near-wall forcing as a means to mitigate skin-friction drag in turbulent flows has gathered significant attention, owing to its potential for substantial environmental and economic benefits [10]. Beginning with the seminal work on spanwise wall oscillations by Jung *et al.* [4], three decades of research efforts led to important progress; however, several crucial factors still hinder the deployment of spanwise forcing to industrial settings. One of the major challenges concerns the diminishing efficacy of drag reduction with increasing Reynolds numbers Re, as industrial scenarios are often characterised by a large value of Re.

In the present work, we address the Reynolds-dependence of skin-friction drag reduction induced by streamwise-traveling waves of spanwise wall velocity (StTW) [9], thanks to their large potential for drag reduction at small energy expenditure. With StTW the following wall velocity distribution is imposed:

$$w_w(x,t) = A \sin(\kappa x - \omega t) \ , \tag{1}$$

where w_w is the spanwise (z) velocity component at the wall, A is the maximum wall velocity and thus a measure of the amplitude of the spanwise forcing, κ is the streamwise wavenumber, ω is the angular frequency, and x and t are the streamwise coordinate and time, respectively.

While extremely important, the studies that addressed the Re-effect on the drag reduction potential of StTW so far suffer from some limitations. The numerical study by Gatti & Quadrio [2] is comprehensive but has been performed in computational domains of reduced size, with only few validations in regular domain sizes limited up to a friction Reynolds number based on the friction velocity of the unmodified channel of $Re_{\tau_0} = 1000$. Rouhi *et al.* [11] extended the parametric study of StTW to $Re_{\tau_0} = 4000$ but employed large eddy simulations (LES) and domain sizes marginally larger than those by Gatti & Quadrio [2]. Marusic *et al.* [5] and Chandran *et al.* [1] observed for the first time that the drag reduction potential can increase with Re but based their evidence on a comparison between high-Re experimental data and lower-Re LES data.

METHOD

A new high-fidelity direct numerical simulation (DNS) dataset of turbulent open-channel flows is produced to study the effect of the Reynolds number up to $Re_{\tau_0} = 6000$ on the reduction of turbulent drag achieved by StTW, enforced as wall boundary condition for the spanwise velocity component after equation (1). The database is designed to be high-fidelity, exploits the same method throughout the Re range and employs computational domains of regular size. Thus, it circumvents the main shortcomings of previous studies.

Re_b	Re_{τ_0}	N_{cases}	$N_x \times N_y \times N_z$	Symbol
20000	994.4	71	2304 × 165 × 1536	▲
43650	2002.2	71	4608 × 265 × 3072	▼
68600	3009.0	7	6912 × 355 × 4608	♦
148000	6010.1	3	13312 × 591 × 9216	●

Table 1: Details of the direct numerical simulations of open channel flows modified by StTW, grouped in sets of N_{cases} simulations performed at a constant value of bulk Reynolds number $Re_b = U_b h/\nu$. Re_{τ_0} is the friction Reynolds number in the reference uncontrolled channel at the same Re_b; N_x, N_y and N_z are the number of grid points in the direction indicated by the subscript. The last column indicates the color and symbol employed in the following figures to represent each set of simulations.

The open channel flow is essentially half a channel flow with a symmetry boundary condition at the centreplane, and is chosen here to halve the computational cost without affecting the drag reduction results. The computer code used for the DNS is based on the classic fractional step method with second-order finite differences on a staggered grid [3, 6].

Four sets of simulations, whose details are listed in table 1, are run at prescribed values of bulk Reynolds number $Re_b = U_b h/\nu$, by enforcing the bulk velocity U_b as described in [8]. Each set comprises one reference simulation, in which the wall is fixed, and a variable number of cases with StTW applied at different values of $\{A, \kappa, \omega\}$. In the following, we will refer to each simulation set via its (nominal) value of Re_{τ_0}. Figure 1 shows the portion of the $\{\kappa^+, \omega^+\}$-space spanned in the present study. We consider only $A^+ = 5$, value at which StTW achieve the maximal net power saving. Here the superscipt + indicates viscous units defined with the reference friction velocity u_{τ_0}, as opposed to $*$, used to indicate the same units yet defined with the actual friction velocity u_τ.

All DNS are carried out in a box with $L_x = 6\pi h$ and $L_z = 2\pi h$, which is larger than what has been adopted by [11] at similar values of Re and sufficient to accommodate large-scale turbulent structures, as shown by a comparison with results from [12]. The mesh resolution for these cases is designed based on the criteria discussed by [7].

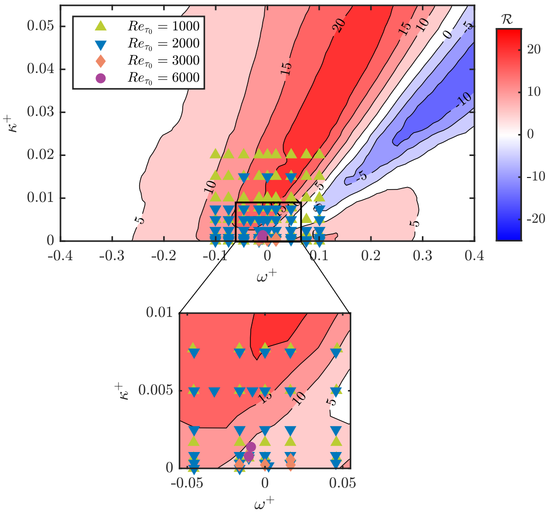

Figure 1: Portion of the parameter space spanned in the present study overlaid to the drag reduction map by [2] computed at $A^+ = 5$. Each symbol corresponds to a single simulation performed at the Reynolds number encoded by its shape, as described by the legend. All simulations are performed at $A^+ = 5$.

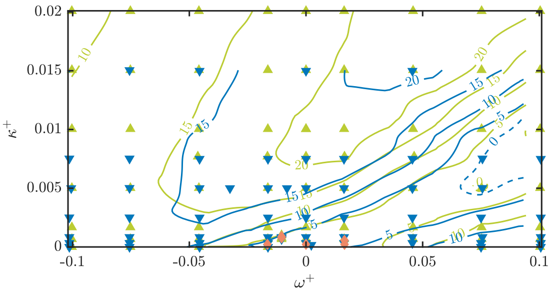

Figure 2: Maps of $\mathcal{R}$ as a function of the angular frequency ω^+ and wavenumber κ^+ of the forcing at $Re_{\tau_0} = 1000$ (——) and $Re_{\tau_0} = 2000$ (——). The symbols are colored after table 1 and show the parameters of each simulation underlying the map interpolation shown in the figure.

RESULTS

Figure 2 shows the percent drag reduction $\mathcal{R} = 1 - c_f / c_{f_0}$, defined as the relative control-induced change of skin-friction coefficient at $Re_{\tau_0} = 1000$ and $Re_{\tau_0} = 2000$. As predicted by the model proposed by Gatti & Quadrio [2], $\mathcal{R}$ is observed to decrease within the statistical uncertainty as Re increases. The maximum value of drag reduction at $Re_{\tau_0} = 2000$ is achieved at larger values of κ^+ compared to the lower value of Re.

Gatti & Quadrio [2] showed that the drag reduction effect by spanwise forcing becomes in fact constant with Re, provided it is not expressed via $\mathcal{R}$, that is *per se* a Re-dependent quantity, but through the Reynolds number-invariant parameter ΔB^*. This quantity, which expresses the main effect of StTW to induce a change ΔB^* of the additive constant in the logarithmic law for the mean velocity profile, is shown in figure 3. The figure clearly shows only minor changes of ΔB^* between the two Reynolds number considered above, confirming that at these values of Re, $\mathcal{R}$ decreases with Re itself.

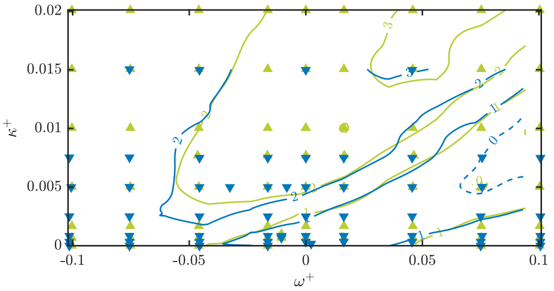

Figure 3: Maps of ΔB^* as a function of the angular frequency ω^+ and wavenumber κ^+ of the forcing at $Re_{\tau_0} = 1000$ (——) and $Re_{\tau_0} = 2000$ (——). Symbols as is figure 2. Contour lines are placed every unity with dashed lines indicating $\Delta B^* = 0$

At the conference, we will discuss the database in its entirety, including results up to $Re_{\tau_0} = 6000$ both in terms of drag reduction and net power saving.

REFERENCES

[1] D. Chandran, A. Zampiron, A. Rouhi, M.K. Fu, D. Wine, B. Holloway, A.J. Smits, and I. Marusic. Turbulent drag reduction by spanwise wall forcing. Part 2: High-Reynolds-number experiments. *J. Fluid Mech.*, 968:A7, 2023.

[2] D. Gatti and M. Quadrio. Reynolds-number dependence of turbulent skin-friction drag reduction induced by spanwise forcing. *J. Fluid Mech.*, 802:553–58, 2016.

[3] Francis H. Harlow and J. Eddie Welch. Numerical Calculation of Time-Dependent Viscous Incompressible Flow of Fluid with Free Surface. *Phys. Fluids*, 8(12):2182–2189, December 1965.

[4] W.J. Jung, N. Mangiavacchi, and R. Akhavan. Suppression of turbulence in wall-bounded flows by high-frequency spanwise oscillations. *Phys. Fluids A*, 4 (8):1605–1607, 1992.

[5] I. Marusic, D. Chandran, A. Rouhi, M.K. Fu, D. Wine, B. Holloway, D. Chung, and A.J. Smits. An energy-efficient pathway to turbulent drag reduction. *Nat Commun*, 12(1):5805, 2021.

[6] P. Orlandi. *Fluid Flow Phenomena: A Numerical Toolkit*. Kluwer Academic Publishers, 2006.

[7] S. Pirozzoli and P. Orlandi. Natural grid stretching for DNS of wall-bounded flows. *J. Comp. Phys.*, 439:110408, August 2021.

[8] M. Quadrio, B. Frohnapfel, and Y. Hasegawa. Does the choice of the forcing term affect flow statistics in DNS of turbulent channel flow? *Eur. J. Mech. B / Fluids*, 55:286–293, 2016.

[9] M. Quadrio, P. Ricco, and C. Viotti. Streamwise-traveling waves of spanwise wall velocity for turbulent drag reduction. *J. Fluid Mech.*, 627:161–178, 2009.

[10] P. Ricco, M. Skote, and M. A. Leschziner. A review of turbulent skin-friction drag reduction by near-wall transverse forcing. *Prog. Aero. Sci.*, 123:100713, 2021.

[11] A. Rouhi, M. K. Fu, D. Chandran, A. Zampiron, A. J. Smits, and I. Marusic. Turbulent drag reduction by spanwise wall forcing. Part 1: Large-eddy simulations. *J . Fluid Mech.*, 268:A6, March 2023.

[12] Jie Yao, Xi Chen, and Fazle Hussain. Direct numerical simulation of turbulent open channel flows at moderately high Reynolds numbers. *J. Fluid Mech.*, 953:A19, December 2022.

ERCOFTAC
European Drag Reduction and Flow Control Meeting – EDRFCM 2024
September 10$^{\text{th}}$–13$^{\text{th}}$, 2024, Turin, Italy

SPATIAL MODIFICATION OF TURBULENCE BY STEADY SQUARE-WAVE SPANWISE WALL FORCING

Max W. Knoop
Faculty of Aerospace Engineering, Delft University of Technology, 2629HS Delft, The Netherlands

Rahul Deshpande
Department of Mechanical Engineering, University of Melbourne, Parkville, VIC 3010, Australia

Ferry F.J. Schrijer
Faculty of Aerospace Engineering, Delft University of Technology, 2629HS Delft, The Netherlands

Bas W. van Oudheusden
Faculty of Aerospace Engineering, Delft University of Technology, 2629HS Delft, The Netherlands

INTRODUCTION

We experimentally investigate standing wave (SW) forcing of a turbulent boundary layer (TBL) through transverse wall motion, to assess its potential for skin friction drag reduction (DR). This choice for studying steady SW forcing is motivated by the relatively sparse attention devoted to understanding the efficacy of this mechanism at high Reynolds numbers, compared to oscillating wall and travelling wave forcing [1]. The reference configuration for this approach is one where the forcing is imposed as a spatially distributed sinusoidal spanwise wall velocity [2]:

$$W_w(x) = A\sin\left(\frac{2\pi}{\lambda_x}x\right), \tag{1}$$

where A is the spanwise velocity amplitude and λ_x the streamwise wavelength of actuation. The coordinates of the x, y, and z denote the streamwise, wall-normal, and spanwise directions, respectively, with corresponding velocity components U, V, and W. Viscous scaling with the superscript '+' is based on the non-actuated friction velocity $u_{\tau 0}$. This abstract presents a novel experimental actuator that relies on steady forcing by a series of spanwise running belts, of which a preliminary version was recently presented by Knoop et al. [3].

EXPERIMENTAL SETUP

The experimental setup, depicted in fig. 1 (a), comprises an array of 48 streamwise-spaced belts that can be activated to run in alternating spanwise directions, thereby creating a spatial square-wave forcing. This choice was justified by the DR efficacy of non-sinusoidal forcing as discussed previously by Cimarelli et al. [4]. The belts are 15 mm wide with a 2 mm streamwise separation, resulting in a length $l_S = 17$ mm of one "belt-element", while the number of elements in one waveform is denoted by S. To realise a flush actuation surface, the belts are embedded in an aluminium surface plate with 50 µm tolerances. The setup is tested in a zero pressure gradient TBL at 2.35 m downstream of the tripping location. Flow conditions are: $U_\infty = 5$ m/s, with boundary layer characteristics: $\delta = 70.3$ mm, $u_{\tau 0} = 0.21$ m/s, and $Re_\tau = 957$. A three-camera planar PIV experiment was performed in the streamwise-wall-normal ($x - y$) plane, as schematically shown in Fig. 1(b), to capture the upstream portion and eight belts over the actuation surface.

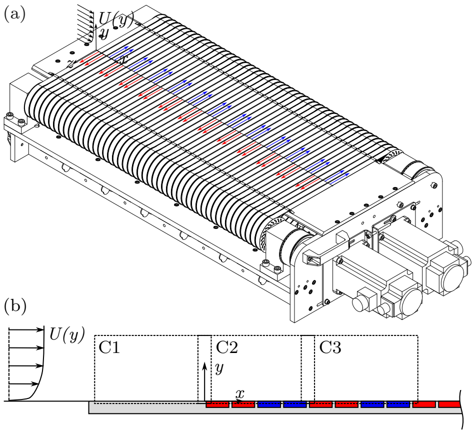

Figure 1: Schematics of (a) the experimental apparatus and (b) the PIV experiment. Coloured arrows and belts indicate their respective positive (red) and negative (blue) W_w.

RESULTS

In contrast to previous channel flow direct numerical simulations, the current experimental setup offers a unique opportunity to investigate the streamwise transients associated with turbulence modification. A belt configuration is selected where the waveform comprises four belt elements (i.e. $S = 4$). This results in a viscous wavelength $\lambda_x^+ = 943$, in the order of the optimum found in the literature [2], with an actuation amplitude of $A^+ = 12$.

We first consider the spatial evolution of the mean streamwise velocity profiles, presented in fig. 2. Profiles are sampled on every other belt (i.e., belts 1, 3, 5, 7), spatially averaged over the 1 mm central region. These profiles clearly reflect a DR, signified by the upward shift of the logarithmic layer. A monotonically increasing trend with x is evident, and a short transient can be observed, asymptoting beyond belt 4 (i.e., one actuation phase) to achieve a DR = 33%. This finding contrasts the 2-3 actuation periods found by Agostini et al. [5]. We conjecture the shorter transient is attributed to the "stronger" efficacy of square-wave over sinusoidal forc-

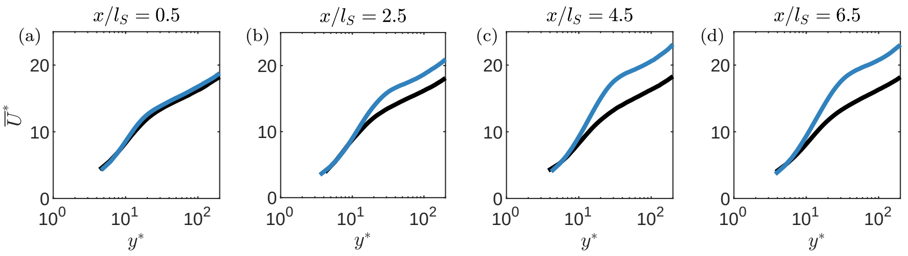

Figure 2: Spatial evolution of the mean velocity profile the non-actuated case (black) and actuated at $\lambda_x^+ = 943$, $A^+ = 12$ (blue). Note that scaling is performed in this case with the friction velocity u_τ of the individual cases, indicated by a superscript '*'.

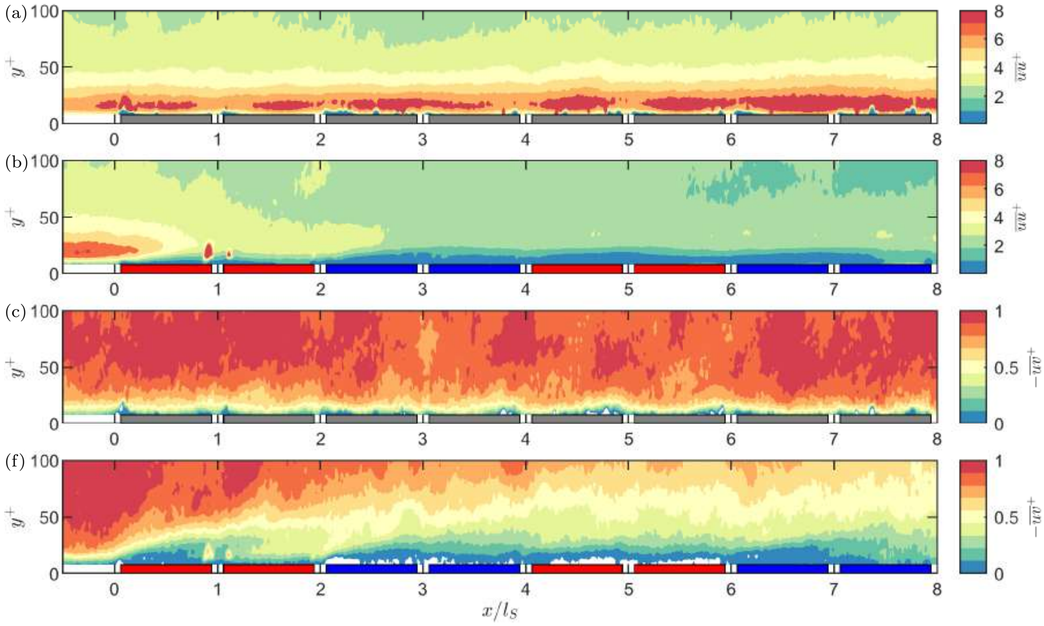

Figure 3: $x - y$ contours of the second-order statistics (a,b) $\overline{uu}^+$ and (c,d) $-\overline{uv}^+$, for the (a,c) non-actuated and (b,d) actuated case. Shaded areas indicate belts and their spanwise velocity: grey $W_w^+ = 0$, red $W_w^+ = 12$, and blue $W_w^+ = -12$.

ing [4]. A similar picture emerges when we consider the second-order statistics in fig. 3. The forcing strongly attenuates the streamwise normal stress, attaining a quasi-steady energy state within one wavelength. A pronounced phase-wise dependence of turbulence modification can be observed for the Reynolds shear stress, which is attenuated from the wall. In addition to the near-wall modification, a more gradual transient can be observed in the attenuation into the logarithmic layer.

REFERENCES

[1] P. Ricco, M. Skote, and M. A Leschziner. A review of turbulent skin-friction drag reduction by near-wall transverse forcing. *Prog. Aerosp. Sci.*, 123:100713, 2021. doi:10.1016/j.paerosci.2021.100713.

[2] C. Viotti, M. Quadrio, and P. Luchini. Streamwise oscillation of spanwise velocity at the wall of a channel for turbulent drag reduction. *Phys. Fluids*, 21, 2009. doi:10.1063/1.3266945.

[3] Max W. Knoop, Friso H. Hartog, Ferdinand F. J. Schrijer, Olaf W. G. van Campenhout, Michiel van Nesselrooij, and Bas W. van Oudheusden. Experimental assessment of square-wave spatial spanwise forcing of a turbulent boundary layer. *Experiments in Fluids*, 65(5):65, 2024. doi:10.1007/s00348-024-03799-9.

[4] A. Cimarelli, B. Frohnapfel, Y. Hasegawa, E. De Angelis, and M. Quadrio. Prediction of turbulence control for arbitrary periodic spanwise wall movement. *Phys. Fluids*, 25 (7):075102, 2013. doi:10.1063/1.4813807.

[5] L. Agostini, E. Touber, and M. A. Leschziner. Spanwise oscillatory wall motion in channel flow: drag-reduction mechanisms inferred from dns-predicted phase-wise property variations at $Re_\tau = 1000$. *J. Fluid Mech.*, 743: 606–635, 2014. doi:10.1017/jfm.2014.40.

ERCOFTAC
European Drag Reduction and Flow Control Meeting – EDRFCM 2024
September 10^{th}–13^{th}, 2024, Turin, Italy

DIRECT NUMERICAL SIMULATIONS OF A TRANSONIC AIRFOIL WITH SPANWISE FORCING FOR DRAG REDUCTION

Niccoló Berizzi
Department of Aerospace Science and Technologies, Politecnico di Milano, 20156 Milano, Italy

Davide Gatti
Institute of Fluid Mechanics, Karlsruhe Institute of Technology, 76131 Karlsruhe, Germany

Sergio Pirozzoli
Dipartimento di Meccanica e Ingegneria Aerospaziale, La Sapienza Università di Roma, 00184 Roma, Italy

Giulio Soldati
Dipartimento di Meccanica e Ingegneria Aerospaziale, La Sapienza Universitá di Roma, 00184 Roma, Italy

Maurizio Quadrio
Department of Aerospace Science and Technologies, Politecnico di Milano, 20156 Milano, Italy

ABSTRACT

Spanwise forcing at the wall in the form of streamwise-travelling waves is applied to the suction side of a transonic wing to reduce its aerodynamic drag. The study, carried out with direct numerical simulations (DNS), extends our previous results [2], also presented at the last EDRFCM in Paris, and shows that shifting the shock wave downstream is key to enhancing the global aerodynamic efficiency and to reducing the overall drag. An extensive parameter study discusses analogies and differences with the incompressible plane case, provides quantitative metrics for the effectiveness of the forcing, and for the first time describes how the interaction between the shock wave and the turbulent boundary layer is modified by the control. It is found that, when the suction-side shock is delayed, the size of the ensuing separation correlates well with the reduction in skin friction. Moreover, the observation of the transient after the sudden application of control brings to light the key physical effects of the control.

BACKGROUND

The potential of spanwise forcing for reducing turbulent skin-friction drag in aeronautical application has received so far little attention: despite the large drag reduction rates predicted by DNS in plane incompressible plane channel and pipe flow [5], so far few studies explored realistic flows featuring non-planar geometries and compressibility effects. At EDRFCM 2022 we presented [3, 2] the first DNS of spanwise forcing via streamwise-travelling waves (StTW) of spanwise velocity [4] applied on a transonic wing with a shock on the suction side. Changes in position and intensity of the shock alters the aerodynamic performances of the wing significantly. In particular, the aerodynamic efficiency of the profile was improved. We estimated a 9% net reduction of the total aerodynamic drag on an entire aircraft when the angle of attack is reduced to retrieve the original lift. This seminal work only tested two quite similar configurations, whose control parameters were deduced from incompressible information; the extent and position of the surface area where the forcing is applied were just guessed. Moreover, an in-depth analysis of the physics behind the control-induced changes to the flow was lacking. The present work extends our previous study by addressing two goals. The first one is to explore the parameter space of the forcing variables together with the position and extent of the controlled region, such that analogies with the incompressible plane channel flow can be identified and discussed in terms of drag reduction and power budget. The second goal, instead, lies in understanding the link between control parameters and flow physics, to arrive at the description of how the streamwise-travelling waves, and the forcing in general, affect the complex physics of the shock/turbulent boundary layer interaction.

NUMERICAL METHODS

This work consists in DNS of the airflow around a transonic wing slab. The section profile is a supercritical airfoil, and the flow field is discretized with a mesh consisting of 536×10^6 grid points and complying with the requirements for fully-resolved turbulent scales. The compressible Navier–Stokes equations for a calorically perfect gas are solved with a second-order, energy-consistent finite-volumes numerical code [1]; the inflow is laminar, and turbulence is tripped numerically at 10% of the chord downstream of the leading edge on both sides of the wing. The flow features steady conditions of Mach number $Ma_\infty = 0.7$, chord-based Reynolds number $Re_\infty = 3 \times 10^5$, and angle of attack $\alpha = 4°$, the latter corresponding to the angle of maximum aerodynamic efficiency of the wing. Flow control is applied on a portion of the suction side of the wing, and is achieved via StTW, an active technique in which the spanwise velocity component at the wall evolves according to:

$$W_w(x,t) = A \sin\left(\kappa_x x - \omega t\right)$$

where A is the forcing amplitude, and κ_x, ω are the spatial and temporal frequencies of the forcing, respectively. Two additional control parameters are represented by the beginning and end position of the actuated surface on the suction side of the wing (x_b, x_e, respectively). One simulation reproduces the reference uncontrolled scenario, while the space of the parameters is explored via 26 DNS in which all the control variables are modified at a constant angle of attack. Two additional simulations reproduce a controlled and an uncontrolled scenario at a reduced angle of attack ($\alpha = 3.45°$).

RESULTS

The aerodynamic coefficients of the airfoil are modified as a consequence of the changes in the wall stresses induced by the application of StTW. The aerodynamic efficiency is defined as $E = C_L/C_D$, where C_L, C_D are the lift and drag coefficients, respectively. The percentage changes of these variables, together with the one of the pitching moment $C_{m,TE}$ at the trailing edge, are plotted in Figure 1. E generally increases by approximately 10%, with the exception of one case, where StTW cause drag increase and efficiency decrease. Interestingly, the drag coefficient of the wing changes little as a consequence of the friction-reducing control, and sometimes even increases ($\Delta C_D > 0$). Clearly, changes in the efficiency are primarily related to enhanced values of C_L; the same can be observed for the pitching moment with respect to the trailing edge ($C_{m,TE}$), which is mostly built on normal stresses.

These changes descend from the shift of the shock towards the trailing edge; a second effect is its intensification, which consequently affects the shock/turbulent boundary layer interaction. This has major consequences on the flow. Figure 2 shows a detail of the friction coefficient C_f in the region of its local minimum. When StTW are effective, a major decrease of C_f is observed before the shock. The increased adverse longitudinal pressure gradient is however transmitted without changes across the boundary layer, and the slower near-wall flow becomes more prone to separation. The curves are colored according to the skin-friction drag reduction $\Delta C_f = 1 - C_f/C_{f,0}$ extracted at $x/c = 0.4$ on the suction side of the wing (the '0' subscript denoting the reference uncontrolled simulation), and show that cases with small ΔC_f have minimal or no separation. One drag-increasing case, instead, presents a globally increased friction coefficient. A comparison with data from the incompressible channel flow confirms that StTW yield analogous effects on C_f on the transonic wing. We found that, when present, the size of the separated region correlates well with ΔC_f. Furthermore, from the analysis of the temporal transients ensuing after the activation of control, we deduced that the presence of recirculation is a consequence of the modified position of the shock, and not a direct effect of the application of StTW.

Deciding position and extent of the actuated portion of the suction side represents a non-trivial problem, where the increase in aerodynamic efficiency should be maximized by limiting as much as possible the power consumption of the forcing. We tested different configurations changing x_b, x_e, and found that withdrawing the control from the post-shock region has positive consequences, while delaying the beginning of the actuation has detrimental effects on the performances of the wing.

With the two simulations performed at $\alpha = 3.45°$, a reduced incidence chosen for the controlled wing to produce the same lift of the reference wing, we estimated a total reduction in the aerodynamic drag of a full aircraft equal to 12.5%. This is a huge figure, and its value has to be appreciated also in view of the negligible power cost when compared to the power required for cruise fight.

At the Meeting, we will also compare StTW as applied to the plane channel flow and to the transonic wing, as a function of the control input. We will provide a first description of how the classical transonic shock wave/turbulent boundary layer interaction is altered by the control, and how the topology of the shock system is affected by the reduced levels of friction brought about by the spanwise forcing.

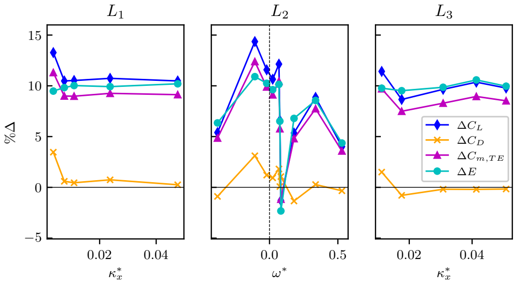

Figure 1: Percentage changes of lift, drag, trailing edge pitching moment and aerodynamic efficiency.

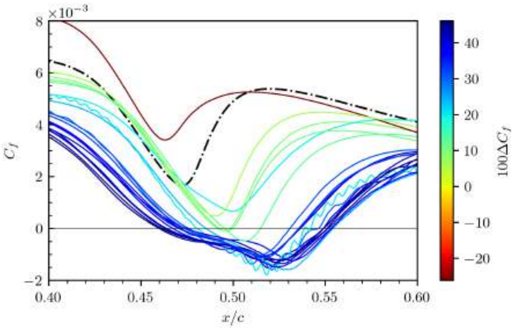

Figure 2: Friction coefficient C_f: zoom at its local minimum on the suction side. The dashed line is the reference uncontrolled case. The value of ΔC_f is encoded in the line color.

REFERENCES

[1] A. Memmolo, M. Bernardini, and S. Pirozzoli. Scrutiny of buffet mechanisms in transonic flow. *Int. J. Numer. Meth. Fluids*, 28(5):1031–1046, 2018.

[2] M. Quadrio, A. Chiarini, J. Banchetti, D. Gatti, A. Memmolo, and S. Pirozzoli. Drag reduction on a transonic airfoil. *J. Fluid. Mech.*, 942:R2, 1–10, 2022.

[3] M. Quadrio, A. Chiarini, D. Gatti, J. Banchetti, A. Memmolo, and S. Pirozzoli. Drag reduction on a transonic wing. In *20th EDRFCM*, Paris, 2022.

[4] M. Quadrio, P. Ricco, and C. Viotti. Streamwise-traveling waves of spanwise wall velocity for turbulent drag reduction. *J. Fluid Mech.*, 627:161–178, 2009.

[5] P. Ricco, M. Skote, and M. A. Leschziner. A review of turbulent skin-friction drag reduction by near-wall transverse forcing. *Prog. Aero. Sci.*, 123:100713, 2021.

14

ERCOFTAC
European Drag Reduction and Flow Control Meeting – EDRFCM 2024
September 10^{th}–13^{th}, 2024, Turin, Italy

SPANWISE WALL OSCILLATION IN A DAMPED CHANNEL FLOW FOR TURBULENT DRAG REDUCTION

M. Castelletti, E. Gallorini, M. Quadrio
Department of Aerospace Sciences and Technologies, Politecnico di Milano, via La Masa 34, 20156 Milano, Italy

INTRODUCTION

Turbulent skin friction drag reduction is a longstanding objective in fluid mechanics research. Over the years, various flow control techniques, both active and passive, as well as open-loop or closed-loop, have emerged. Among all the possible techniques, the oscillating wall (OW) stands out for its effectiveness. OW is an active method that is capable of positive net energy savings. Moreover it is conceptually simple as requires no feedback from the flow.

With OW, the wall moves periodically, with period T, in the spanwise direction according to $w_w(t) = A\cos(\omega t)$, where w_w is the spanwise velocity at the wall, A the oscillation amplitude and $\omega = 2\pi/T$ the oscillation frequency. This wall oscillation is able to create the so-called Stokes layer, whose interaction with the near wall turbulence reduces friction drag.

There is broad consensus that an optimal oscillation period exists which maximizes drag reduction. For simulations at constant flow rate, this optimal period is $T^+_{opt} \approx 100$, when scaled with the viscous units of the uncontrolled flow. However there is no shared view to interpret this optimal value and the drag reduction mechanism in general. However, several ideas regarding the working mechanism of the OW technique suggest that turbulent structures may play a central role. For instance, the optimal period may be linked to characteristic timescales of near-wall turbulence. T^+_{opt} could be related to a convective time scale derived from the ratio between the typical length of near-wall streaks and their convection velocity. In an unmodified channel flow, these values are approximately $\lambda^+_x = O(10^3)$ and $U^+_{conv} = O(10)$ at a location consistent with the location of the streaks. This would result in $T^+_{opt} \approx \lambda^+_x/U^+_{conv} \approx 100$. Whether or not the coincidence of this time scale with the optimum forcing period is physically significant remains an open question [5]. This time scale is obviously not the only option, several others are possible, for instance [1] calculated the streak amplification time and tried to relate it to the optimal period of the forcing.

In this work, we take inspiration from the work by [2], where the longest turbulence structures in a turbulent channel flow were artificially damped to understand the importance of long streaks in near-wall turbulence dynamics. The OW technique is applied here to a damped channel flow, characterized by an altered turbulence in terms of length scales and time scales, in an attempt to elucidate the role of near wall turbulence time scales in the working mechanism of the OW.

METHODS

We consider DNS of a channel flow at $Re_b = U_b h/\nu = 10000$, where U_b is the bulk velocity, h half the height of the channel and ν the kinematic viscosity. This corresponds to $Re_\tau = u_\tau h/\nu \approx 550$ for the unmodified and unforced case, where u_τ is the friction velocity. In the following x, y and z represent respectively the streamwise, wall-normal and spanwise directions, while u, v, w represent the corresponding velocity components. The employed code solves the Navier–Stokes equations in the $v-\omega_y$ formulation, employing Fourier expansion in the homogeneous directions x and z and compact finite differences in y.

To damp the system a filter, similar to the one employed in [2], is used. At each time step, the filter explicitly zeroes all the Fourier modes of the wall-normal vorticity, $\hat{\omega}_y$, characterized by a streamwise wavelength above a threshold $\lambda_{x,f}$ as

$$\hat{\omega}_y(k_x, y, k_z) = \hat{\omega}_y(k_x, y, k_z)F(y) \quad \forall k_z, \quad k_x < 2\pi/\lambda_{x,f} \quad (1)$$

where $F(y)$ is a function that is either 0 or 1 and allows to control the y location where the damping is applied.

The OW technique is applied in comparative form to the reference damped/undamped case: the oscillation amplitude is kept fixed at $A^+ = 12$, while the oscillation period is varied from $T^+ = 25$ to $T^+ = 200$. Two different sets of experiments of damped turbulence are performed. In one case, only the near-wall flow is damped, i.e. $F(y) = 0$ for $y^+ < 60$ and $F(y) = 1$ otherwise. In the other, only the outer flow is damped. The specific wall distance $y^+ = 60$ is chosen after [3], who showed that below $y^+ = 60$ wall turbulence survives autonomously. Multiple simulations are performed by varying the parameter $\lambda_{x,f}$ in (1), e.g. by filtering modes with different wavelengths. The obtained modified turbulence is then characterized via relevant time scales for the streamwise velocity component u. In particular, following [4], we compute the space-time autocorrelation function to extract the typical Eulerian and Lagrangian time scales of the flow at the y position where the streamwisse velocity fluctuations are most intense. These two time scales will be referred respectively as $T^{+,E}_u$ and $T^{+,L}_u$, these will be always expressed in + units but the superscript will be dropped in the following for clarity. T^E_u and T^L_u can be interpreted respectively as the time a turbulent structure take to completely pass over a fixed point and as the life-time of a turbulent structure itself.

Since damping by itself reduces the turbulent friction, it is important to point out that the superscript + indicates, as usual, scaling in viscous units computed with the friction velocity of the case without OW, and additionally that the friction velocity is the one of the damped simulation itself.

RESULTS

One reference undamped simulation was carried out, while six damped simulations without OW were performed, three cases filtered near the wall and the remaining three far from the wall. Table 1 summarizes all the results for the reference simulations in terms of Re_τ and time scales. It reports also the value of $\lambda_{x,f}$ for the damped simulations. Ref indicates the reference undamped simulation, I-2, I-3 and I-4 are the simulations where the inner flow at $y^+ < 60$ is damped, and $\lambda_{x,f}$ is chosen to damp the second, third and fourth longitudinal wavenumber. Correspondingly, O-2, O-3 and O-4 are the simulations where the outer flow is damped.

	$\lambda_{x,f}/h$	$\lambda^+_{x,f}$	Re_τ	T_u^E	T_u^L
Ref	-	-	545	20.9	80.8
I-2	3.14	1624	517	6.2	28.7
I-3	2.09	1043	498	4.9	24.2
I-4	1.57	742	473	4.0	20.3
O-2	3.14	1494	476	15.7	51.6
O-3	2.09	913	437	15.7	51.6
O-4	1.57	602	384	13.6	46.0

Table 1: Results in terms of Re_τ and time scales for all the seven reference simulations. Ref is the reference undamped simulation. For the reference damped simulations I-2, I-3, I-4 (filtered near the wall) and O-2, O-3, O-4 (filtered far from the wall) also the value of the threshold $\lambda_{x,f}$ is reported.

As expected [2], increasing the number of damped modes, i.e. reducing $\lambda_{x,f}$, leads to a reduction of Re_τ, yet all cases remain fully turbulent. Damping far from the wall results in a lower Re_τ compared to damping near the wall. This can be explained by the greater volume damped if the filter is applied far from the wall.

Calculated values for of T_u^E and T_u^L for the reference flow are in accordance with [4]. Damping has a significant effect on the time scales: T_u^E and T_u^L are reduced, especially for the inner damping. Indeed, directly filtering the near-wall region reduces the streamwise extent of near wall turbulent structures, that must be shorter than $\lambda^+_{x,f}$, which immediately translates in a decrease of T_u^E for the inner damping. Instead, outer damping shows a minor effect on the time scales.

Moving on to the application of the OW, Figure 1 plots the results of the small parameter studies carried out for each of the seven cases discussed above, in terms of the percentage drag reduction $DR\%$ obtained at various oscillation periods T^+. $DR\%$ is defined as $DR\% = 100\frac{C_{f_0}-C_f}{C_{f_0}}$, where C_{f_0} is the skin friction coefficient of the reference simulation and C_f is the one of the forced simulation.

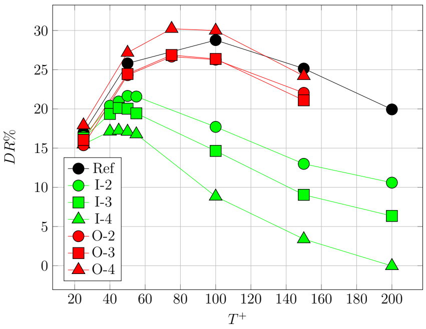

Figure 1: $DR\%$ as a function of the forcing period T^+.

The optimal forcing period T^+_{opt}, as visible from Figure 1, shifts towards smaller periods, if the reference simulation is damped. As expected, for the undamped case $T^+_{opt} \approx 100$. The inner damping decreases it to $T^+_{opt} \approx 50$, while outer damping yields $T^+_{opt} \approx 80$. Another relevant change is the maximum $DR\%$ attainable. Compared to the undamped case, $DR\%_{max}$ is always smaller for inner damping, as part of the drag reduction margin is already taken away from the damping. Differently, with outer damping $DR\%_{max}$ tends to increase. This may be linked to a Reynolds effects, as the decrease in Re_τ causes the OW to become more effective.

The shift of T^+_{opt} towards shorter periods may be linked to the decrease in the time scales of turbulent structure near the wall. As shown in Figure 2 there is a general trend of decreasing of T^+_{opt} accompanied by a reduction in both Lagrangian and Eulerian time scales.

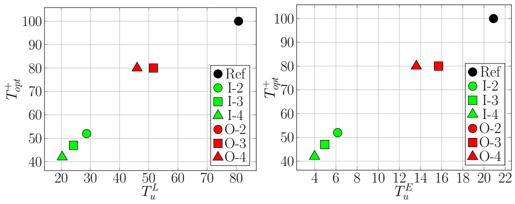

Figure 2: Left: trend of T^+_{opt} against the Lagrangian time scale T_u^L. Right: trend of T^+_{opt} against the Eulerian T_u^E. O-2 and O-3 markers are superimposed.

As illustrated in Figure 3, this trend does not follow a linear pattern. The ratio between T^+_{opt} and the time scales increases as the life scale decreases, suggesting that faster dynamics of near-wall turbulence require a slower control.

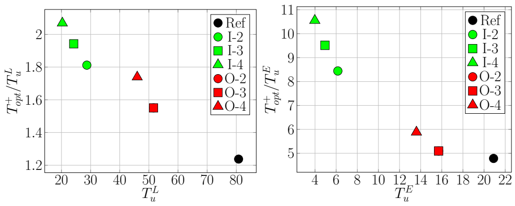

Figure 3: Left: trend of T^+_{opt}/T_u^L against the Lagrangian time scale T_u^L. Right: trend of T^+_{opt}/T_u^E against the Eulerian time scale T_u^E. O-2 and O-3 markers are superimposed.

Further research is ongoing to clarify the physical relevance of the presented patterns and whether one time scale (Lagrangian or Eulerian) prevails over the other.

REFERENCES

[1] O. Blesbois, S. I. Chernyshenko, E. Touber, and M. A. Leschziner. Pattern prediction by linear analysis of turbulent flow with drag reduction by wall oscillation. *Journal of Fluid Mechanics*, 724:607–641, 2013.

[2] J. Jiménez. The streaks of wall-bounded turbulence need not be long. *Journal of Fluid Mechanics*, 945:R3, 2022.

[3] J. Jiménez and A. Pinelli. The autonomous cycle of near-wall turbulence. *J. Fluid Mech.*, 389:335–359, 1999.

[4] M. Quadrio and P. Luchini. Integral time-space scales in turbulent wall flows. *Phys. Fluids*, 15(8):2219–2227, 2003.

[5] E. Touber and M.A. Leschziner. Near-wall streak modification by spanwise oscillatory wall motion and drag-reduction mechanisms. *J. Fluid Mech.*, 693:150–200, 2012.

15

ERCOFTAC
European Drag Reduction and Flow Control Meeting – EDRFCM 2024
September 10th–13th, 2024, Turin, Italy

ON THE OPTIMAL PERIOD OF SPANWISE FORCING FOR TURBULENT DRAG REDUCTION

F. Gattere
Department of Aerospace Science and Technologies, Politecnico di Milano, 20156 Milan, Italy

A. Chiarini
Complex Fluids and Flows Unit, Okinawa Institute of Science and Technology, 904-0495 Okinawa, Japan

M. Castelletti, M.Quadrio
Department of Aerospace Science and Technologies, Politecnico di Milano, 20156 Milan, Italy

INTRODUCTION

Efforts to reduce turbulent skin-friction drag are important for both environmental and economic reasons. Various methods have been proposed over the years, and among these, techniques that use active predetermined wall-based actuation without feedback are particularly noteworthy for their simplicity and effectiveness.

This study examines spanwise forcing [3], which has been proven effective at high Reynolds and Mach numbers and offers significant energy savings. The simplest and earliest variant of spanwise forcing is the spanwise oscillation of a plane wall [2]. Although the spatially uniform oscillation is not among the most efficient implementations, it is considered here as the prototypical form of spanwise forcing, because its working principle is shared by the other variants. The wall periodically oscillates in the spanwise direction as a function of time t according to a prescribed harmonic law

$$w_w(t) = A \sin\left(\frac{2\pi}{T} t\right), \tag{1}$$

where w_w is the spanwise velocity component of the wall (the other components are set to zero), and A and T indicate the amplitude and period of the oscillation.

The harmonic oscillation of the wall generates a spanwise cross-flow that is periodic after space- and phase-averaging, and that superimposes to and interacts with the turbulent flow. The phase-averaged spanwise flow coincides (small deviations are present for large T) with the analytical laminar solution $w_{SL}(y,t)$ of the second Stokes problem, hereafter referred to as the Stokes layer or SL, which reads:

$$w_{SL}(y,t) = A \exp\left(-\frac{y}{\delta}\right) \sin\left(\frac{2\pi}{T} t - \frac{y}{\delta}\right), \tag{2}$$

where δ is the SL thickness and y the wall-normal coordinate. Since the maximum amplitude A of the wall oscillation only appears as a multiplicative factor because of the linearity of the governing equations, the SL is shaped by the remaining two parameters T and δ. These two quantities are not independent, and once T is set, δ is determined as a function of T and the fluid kinematic viscosity by

$$\delta = \delta_{SL}(T,\nu) \equiv \sqrt{\frac{\nu T}{\pi}}, \tag{3}$$

where the SL thickness δ defined above is the wall distance where the maximum spanwise velocity during the oscillation reduces to $A\ \exp(-1)$.

Starting from the early numerical studies of [2] and [1], the available evidence indicate that there is an optimal oscillation period T_{opt}, which corresponds to an optimal Stokes Layer thickness $\delta_{opt} = \delta_{SL}(T_{opt}, \nu)$, for which drag reduction is maximized. There is general agreement that $T^+_{opt} \approx 100$, corresponding to a penetration depth of the SL of $\delta^+_{opt} \approx 5.7$.

Despite the evidence, there is no consensus on the physical interpretation of these optimal values which can be understood in more than one way. For instance, T_{opt} can be directly linked to other time scales in the flow, such as the characteristic lifetime of near-wall coherent structures. Additionally, due to the flow's convective nature, T_{opt} can be translated into a longitudinal length scale through a convection velocity. Furthermore, within the Stokes layer, the optimal period also defines the maximum lateral displacement of the moving wall, $D_{max} = AT$, which is another potentially significant length scale of the flow. The optimal period might also be seen as determining the optimal penetration depth δ_{opt} of the Stokes layer via equation 3, representing a diffusion length scale in the wall-normal direction and a measure of the near-wall mean spanwise shear. Our inability to distinguish among these various interpretations reflects our current limited understanding of the overall drag reduction mechanism associated with the oscillating wall setup.

The objective of this work is to advance this understanding by clarifying the significance of the (T_{opt}, δ_{opt}) optimum. Based on DNS, we move beyond the traditional concept of the oscillating wall and remove the constraint $\delta = \delta_{SL}(T,\nu)$: we explore the complete (T,δ) two-dimensional space of parameters and investigate the role of T and δ separately. In other words, instead of imposing the harmonic spanwise oscillation of the wall to generate the SL, we enforce a mean spanwise velocity profile of the form (2) at each time step, and vary δ and T independently.

METHODS

Direct numerical simulations (DNS) of the turbulent flow in an indefinite plane channel are carried out, to study the effect of the Stokes layer generated by the sinusoidal oscillations of the walls after its period T and thickness δ are decoupled. We remove the link (3) between T and δ_{SL} that exists when a true Stokes layer is created by the oscillation of the wall. An extended Stokes layer profile (ESL)

$$\langle w \rangle_h(y,t;\delta,T) = A \exp\left(-\frac{y}{\delta}\right) \sin\left(\frac{2\pi}{T} t - \frac{y}{\delta}\right) \tag{4}$$

is indeed enforced directly at each time step; the operator $\langle \cdot \rangle_h$ indicates spatial averaging along the homogeneous directions. While enforcing an arbitrary profile $\langle w \rangle_h(y,t)$ may suggest that the present numerical experiments are mere thought experiments that are possible with DNS only, it should be remarked that our procedure is equivalent to solving the Navier–Stokes equations with the boundary condition (1) and an additional volume forcing that is practically zero whenever the extended

Stokes layer (4) reduces to the standard Stokes layer. We measure that the two techniques almost provide the same results in terms of $\mathcal{R}$, with a small deviation only at large T (see figure 1, where for $T^+ = 200$ the relative discrepancy is of 6%); the ESL always provides a smaller $\mathcal{R}$ compared to the true SL. Here we define $\mathcal{R} = 100 \times (C_{f0} - C_f)/C_{f,0}$ with $C_{f,0}$ and C_f the skin friction coefficient of the uncontrolled and controlled case, respectively. The simulations are carried out at the bulk Reynolds number $Re_b = U_b h/\nu = 7000$ for all cases, which corresponds to a friction Reynolds number of $Re_\tau = u_\tau h/\nu \approx 400$ in the unforced case. The oscillating period is varied in the $10 \le T^+ \le 200$ range, while δ varies between $2 \le \delta^+ \le 20$. The amplitude of the forcing is set to $A^+ = 12$.

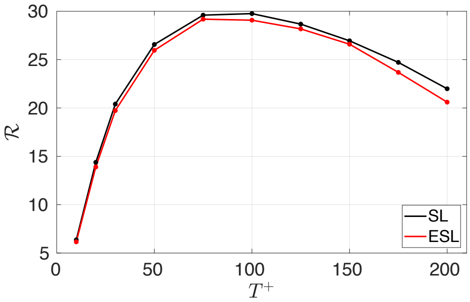

Figure 1: Drag reduction versus oscillation period for the oscillating wall (black) and the present approach with $\delta = \delta_{SL}$ (red).

RESULTS

Figure 2 shows that, once δ and T are made independent, the maximum drag reduction on the SL line is not particularly meaningful in view of the global $\mathcal{R}$ map. Along the SL line, a maximum $\mathcal{R}$ of $\approx 30\%$, shown by the black symbol, is indeed found at $(T^+_{opt}, \delta^+) \approx (100, 5.7)$, but the position of the actual maximum in the two-dimensional plane is larger and quite far from it. Indeed, the global maximum drag reduction obtained with the ESL is $\mathcal{R}_{max} \approx 40\%$, found for $(T^+, \delta^+) \approx (30, 14)$; see the red symbol in figure 2. Hence, the maximum drag reduction is significantly larger than that on the SL line, and is obtained by decreasing the oscillating period from $T^+ = 100$ to $T^+ = 30$, while at the same time increasing the SL thickness from $\delta^+ = 5.7$ to $\delta^+ = 14$. Note that, when moving along the SL line, it is impossible to change T and δ in opposite directions. The $\mathcal{R}$ map can be divided into different regions according to the behaviour of the drag reduction at varying parameters T and δ. The area of the global optimum is quite broad, spanning the region of $20 \le T^+ \le 50$ and $8 \le \delta^+ \le 14$; the values of δ correspond to the position of the buffer layer, where the near-wall cycle takes place, suggesting that the maximum $\mathcal{R}$ is gained for the ESL effectively interacting with the near-wall coherent structures of the wall. Where δ is very small the spanwise motion is confined in the viscous sublayer where the turbulent activity is weak. Similarly, for small oscillating periods $\mathcal{R}$ is relatively small and independent on δ since the oscillating period is too small compared to the flow time scales, and the resulting oscillating motion and the incoming flow are decoupled. As T increases above $T^+ > 30$, the local optimum thickness δ^+ moves towards smaller values, suggesting that with longer oscillating period the ESL is more effective when its influence remains confined closer to the wall. For large T, $\mathcal{R}$ degrades quickly at large δ. A possible explanation of the suboptimal $\mathcal{R}$ is the spanwise instantaneous velocity field being quite different from the laminar ESL due to the slow period of oscillation and large δ significantly interacting with the underling turbulence.

We conclude that the values $T^+ \approx 100$ and $\delta^+ \approx 6$ do not possess a special meaning and they are the optimum when we are constrained by the control actuator to lie on the black line of figure 2; instead designing a control which allows to decouple T and δ is able to provide a much higher $\mathcal{R}$.

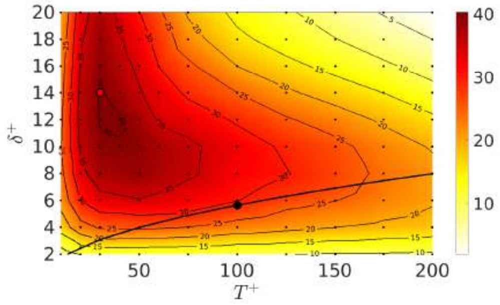

Figure 2: Drag reduction map in the (T, δ) space of parameters. The black thick line indicates the $\delta = \delta_{SL}$ constraint. The red dot identifies the point of maximum drag reduction, whereas the black dot indicates the maximum along the line $\delta = \delta_{SL}(T)$. The small black dots indicate each point of the dataset.

The drag reduction potential of the present control needs to be put in perspective accounting for both benefits, i.e. $\mathcal{R}$ and costs, i.e. energy spent to enforce the control. P_c is the control power required to create the ESL, when neglecting the losses of the actuation device. It is expressed as a fraction of the pumping power needed to maintain a constant flow rate. We measure that the power is a function of δ only, once A is fixed: the larger δ, the smaller P_c.

To compare benefits and costs of the control we define the net energy saving rate $P_{net} = \mathcal{R} - P_c$. For this A the oscillating wall leads to a negative P_{net} for all T, meaning that at $Re_\tau = 400$ the cost of the actuation overcomes the actual savings. The ESL, instead, guarantees the possibility of positive net benefits for some (T, δ) pairs, as the region of large $\mathcal{R}$ corresponds to the region of relatively small P_c due to the large δ. For $(T^+, \delta^+) = (30, 20)$ we measure a non-negligible positive $P_{net} \approx 17\%$, which is noteworthy when compared to the negative net balance of the oscillating wall at this value of A, whose maximum is $P_{net} \approx -30\%$. Also, note that in this work we are considering the simplest variant of the spanwise forcing.

The positive net power saving obtained when T and δ are decoupled paves the way for the implementation of alternative actuators able to enforce any velocity profile to the flow field in order to get the maximum net benefit. The control law does not need to be the result of the choice of the actuator as in the case of the wall oscillation, but more conveniently the actuator can be designed to induce the desired control law to the flow field. The profile of the resultant velocity is not constrained to follow the law of Eq.(4) anymore and a body force leading to a velocity profile able to target the mechanism which induces the reduction of drag can be designed.

REFERENCES

[1] A. Baron and M. Quadrio. Turbulent drag reduction by spanwise wall oscillations. *Applied Scientific Research*, 55:311–326, 1996.

[2] W.J. Jung, N. Mangiavacchi, and R. Akhavan. Suppression of turbulence in wall-bounded flows by high-frequency spanwise oscillations. *Phys. Fluids A*, 4 (8):1605–1607, 1992.

[3] P. Ricco, M. Skote, and M. A. Leschziner. A review of turbulent skin-friction drag reduction by near-wall transverse forcing. *Progress in Aerospace Sciences*, 123:100713, 2021.

 # 16

ERCOFTAC
European Drag Reduction and Flow Control Meeting – EDRFCM 2024
September 10th–13th, 2024, Turin, Italy

CIRCULATION CONTROL OF A 2-D WING

Bojan Vukasinovic
Woodruff School of Mechanical Engineering, Georgia Institute of Technology, Atlanta, GA 30332, USA

Robert Funk
Aerospace, Transportation & Advanced Systems Laboratory Georgia Tech Research Institute ATAS, Smyrna, GA 30080

Ari Glezer
Woodruff School of Mechanical Engineering, Georgia Institute of Technology, Atlanta, GA 30332, USA

INTRODUCTION

Circulation control of aircraft wings by using nominally 2-D surface wall jets and the Coanda effect on lifting and the control surfaces can effect remarkable changes in aerodynamic performance has been known since the 1930s (e.g. Metral, 1939). The art of such Coanda-based circulation control has been investigated extensively, perhaps most notably by Englar and his co-workers (e.g., 2000, 2003, 2006). While the earlier work has utilized almost exclusively 2-D wall jets, recent circulation control investigations at Georgia Tech demonstrated the utility of arrays of unsteady, 3-D fluidically-oscillating wall jets.

2- AND 3-D CIRCULATION CONTROL

In the present investigations, the center segment of a 2-D wing model used by Englar (2006, $c = 46$ cm) and having a quarter cylinder trailing edge ($R = 1.3$ cm) is integrated with interchangeable inserts of 2-D Coanda jets or arrays of N fluidically oscillating jets (Figure 1). The aerodynamic loads are measured at cross flow speeds of $v_\infty = 35$ m/s ($Re_c = 4.7 \cdot 10^5$). Earlier investigations demonstrated that discrete fluidically oscillating Coanda jets can deliver the same total thrust as the 2-D jets but at lower mass flow rates. The performance of these 2-D and 3-D wall jets is depicted by their jet momentum coefficient $\hat{C}_\mu = T/(q \cdot S)$ based on the *measured jet thrust T* and the jet mass flow rate coefficient $C_q = \dot{m}_j/(\rho_\infty v_\infty S)$ relative to cross flow mass flow rate through the wing's actuated planform area *S*. The investigations used two existing configurations of 2-D steady wall jets having a nominal jet orifice areas denoted A_o and $0.82A_o$. Two arrays of 29 and 14 equally-spaced, fluidically-oscillating jets FO1 and FO2 (Figure 1a) were used for comparison whose orifice areas were $A_{FO1} = 0.34A_o$ and $A_{FO2} = 0.29A_o$.

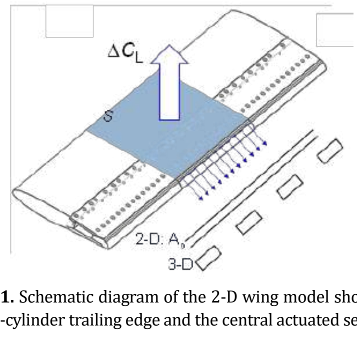

Figure 1. Schematic diagram of the 2-D wing model showing the quarter-cylinder trailing edge and the central actuated segment.

The aerodynamic performance of the 3-D Coanda jets at the trailing edge of the airfoil is compared with the 2-D jets in Figures 2a and b in terms of the respective variations of the induced lift increment (relative to the baseline wing) ΔC_L with each of $\hat{C}_\mu$ and C_q, at $Re = 4.7 \cdot 10^5$ (ΔC_L is normalized by the active spanwise area of the wing). The data for both the 2-D (areas A_o and $0.85A_o$) and 3-D ($A_{FO1} = 0.34A_o$ and $A_{FO2} = 0.29A_o$) Coanda jets are shown for $\hat{C}_\mu < 0.2$ and $C_q < 0.01$. The data in Figure 2a are shown at $\alpha = -5^o$, 0^o, and 5^o and for each actuator configuration exhibit a nearly- **Figure**

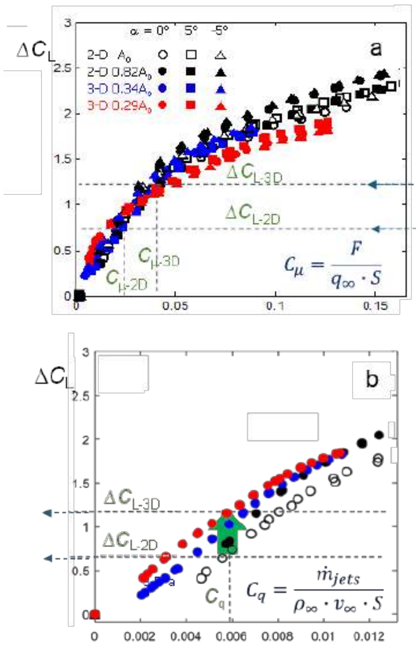

Figure 2. Variation of induced lift increment ΔC_L with jet momentum (a) and with flow rate coefficients (b) for the 2-D jets (areas A_o and $0.82A_o$), and the 3-D jets $A_{FO1} = 0.34A_o$ and $A_{FO2} = 0.29A_o$, $\alpha = 5°$, 0°, and 5°.

linear variation of ΔC_{L} with $\hat{C}_\mu$ in two distinct rates below and above $\hat{C}_\mu \approx 0.06$. This change in the rate of variation of ΔC_{L} with $\hat{C}_\mu$ was observed by a number of earlier investigators (e.g., Jones, 2005, Radespiel et al., 2016) who argued that it results from transition from boundary layer (BL) to circulation control. As shown in Figure 2a, while for $\hat{C}_\mu < 0.06$ all wall jets yield nearly identical performance, for $\hat{C}_\mu > 0.06$ the linear rates of increase of ΔC_{L} with $\hat{C}_\mu$ are almost identical and they are offset by some constants. This indicates that each of these wall jets reaches a different upper limit of its BL (or separation) control on the Coanda surface and the increase in circulation or lift thereafter is manifested primarily by turning of the outer flow over the Coanda surface.

The variation of ΔC_{L} with C_{q} in Figure 2b (for clarity only at $\alpha = 0^{o}$) shows that unlike Figure 2a, the transitions between BL and circulation control regimes occurs at different levels of C_{q}, and the rates of change of ΔC_{L} with C_{q} for the 2- and 3-D actuation within the BL regime are not the same. The difference in the effectiveness of the 3-D Coanda jets relative to the 2-D jets is demonstrated by *considering their performances at the same* $C_q = 0.6\%$ as marked in Figure 2b. The corresponding induced ΔC_{L} increments are $\Delta C_{\mathrm{L\text{-}2D}} = 0.75$ and $\Delta C_{\mathrm{L\text{-}3D}} = 1.2$ which as shown in Figure 2a are realized at $\hat{C}_{\mu\ \mathrm{-2D}} = 0.025$ $\hat{C}_{\mu\ \mathrm{-3D}} = 0.035$, respectively (the mass flow rate yields 40% *higher* $C_{\square\mathrm{-3D}}$). Therefore, the *3-D Coanda jets effects about 60% higher lift increment relative to the 2-D configuration*. These data indicate that the geometry and dimensions of the 3-D Coanda jets can be optimized over a broad operating range by taking into account flow losses and compressibility effects.

The effects of the 2- and 3-D trailing edge circulation control on the drag increments ΔC_{D} relative to the corresponding baseline levels in the absence of actuation are compared in Figure 3. The variation with $\hat{C}_\mu$ of the drag increments associated with the 2-D jets $\Delta C_{\mathrm{D\text{-}2D}}$ exhibits similar trends to ΔC_{L} in Figure 2a, but their respective rates of change increase significantly with α. For example, at $\hat{C}_\mu = 0.1$ $\Delta C_{\mathrm{D\text{-}2D}} = 0.094$ at $\alpha = 0^{o}$, increases by about 45% (to 0.135) and decreases by about 33% (to 0.062) at $\alpha = +5^{o}$ and -5^{o}, respectively. While $\Delta C_{\mathrm{D\text{-}2D}}$ continues to increase with $\hat{C}_\mu$ at $\alpha = 0^{o}$ and 5^{o}, at $\alpha = -5^{o}$ $\Delta C_{\mathrm{D\text{-}2D}}$ asymptotes to about 0.067 while the corresponding lift increment (Figure 2a) continues to increase.

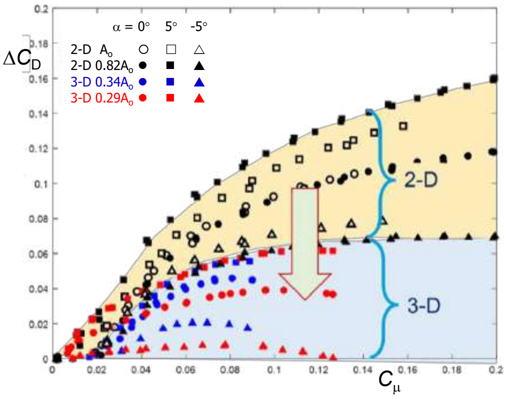

Figure 3. Variation of induced drag increment the actuation jet momentum coefficient for the 2-D jets (A_o and $0.82A_o$), and 3-D jets FO1 ($A_{\mathrm{FO1}} = 0.34A_{\mathrm{o}}$ and $A_{\mathrm{FO2}} = 0.29A_{\mathrm{o}}$) jets for angles of attack $\alpha = -5°, 0°$, and $5°$.

Perhaps the most salient feature of the data in Figure 3 is that within the range of operation of the 3-D jets in the present investigations ($\hat{C}_\mu < 0.126$ *for C3D-2), the drag increments induced by their actuation for a given* $\hat{C}_\mu$ *are significantly lower than the corresponding increments induced by the 2-D jets.* For example, for C3D-2 at $\hat{C}_\mu = 0.1$ $\Delta C_{\mathrm{D\text{-}3D}} = 0.01$, 0.039, and 0.062 at $\alpha = -5^{o}$, 0^{o} and $+5^{o}$, respectively and the corresponding $\Delta C_{\mathrm{D\text{-}2D}}$ are about 54%, 58%, and 62% *higher*. As a result, the ratios of the actuation induced lift and drag increments for the 2-D (C2D-2) and 3-D (C3D-2) actuations at $\alpha = 0^{o}$ and $\hat{C}_\mu = 0.1$ are about 21 and 43, respectively indicating that *the 3-D actuation at the same momentum coefficient is significantly more efficient.*

The reductions in induced drag by 3-D actuation is attributed to the interaction of the cross flow with the discrete fluidically oscillating wall jets over the Conada surface that gives rise to the formation of surface-bound array of counter-rotating streamwise vorticity concentrations (e.g., DeSalvo et al., 2016, 2020) and will be discussed in the presentation.

REFERENCES

[1] DeSalvo, M. E., Gissen, A. N.,Whalen, E. A., and Glezer A. "High-Lift Performance Enhancement of a Simple Flap using Aerodynamic Flow Control," 2016-3306, 2016.

[2] DeSalvo, M., Whalen, E. and Glezer, A., “High-Lift Performance Enhancement Using Active Flow Control,” AIAA Journal, Vol. 58 (10), pp. 4228-4242, 2020.

[3] Jones, G. S., “Pneumatic flap performance for a 2d circulation control airfoil, steady and pulsed,”*Proceedings of the 2004 NASA/ONR Circulation Control Workshop, Part 2*, 2005.

[4] Radespiel, R., Heinze, W., and Bertsch, L., “High-Lift Research for Future Transport Aircraft,” 66th Deutschen Luft-und Raumfahrtkongress, September 5 – 7, Munich, 2017.

[5] Metral, A. R., “On the Phenomenon of Fluid Veins and their Application, the Coanda Effect,” AF Translation, F-TS-786-RE, 1939.

[6] Englar, R. J., “Circulation Control Pneumatic Aerodynamics: Blown Force and Moment Augmentation and Modification; Past, Present and Future,” AIAA Paper 2000-2541, AIAA Fluids 2000 Meeting, Denver, CO, June 19-22, 2000.

[7] Englar R. J., “Overview of Circulation Control Pneumatic Aerodynamics: Blown Force and Moment Augmentation and Modification as Applied Primarily to Fixed-Wing Aircraft,” Applications of Circulation Control Technologies, R. D. Joslin and G. S. Jones Eds, Progress In Astronautics and Aeronautics, Volume 214, 2006.

17

ERCOFTAC
European Drag Reduction and Flow Control Meeting – EDRFCM 2024
September 10$^{\text{th}}$–13$^{\text{th}}$, 2024, Turin, Italy

EFFECT OF A PERIODIC GUST ON THE AERODYNAMIC CHARACTERISTICS OF NACA0012 AIRFOIL

Si-Yuan Feng
Fluid Mechanics Key Laboratory of Education Ministry, Beihang University, Beijing 100191, China

Xi He
Fluid Mechanics Key Laboratory of Education Ministry, Beihang University, Beijing 100191, China

Jin-Jun Wang
Fluid Mechanics Key Laboratory of Education Ministry, Beihang University, Beijing 100191, China

INTRODUCTION

Gusts are ubiquitous occurrences of unsteady flow in aviation. The impact of gusts on airplane safety and comfort has received wide attention [2, 1]. Therefore, many works on gust encounters have been conducted over the past several decades, mainly based on the potential flow theory [6, 3, 7].

Recently, micro air vehicles (MAVs) have developed rapidly and may operate in complex flight environments at low Reynolds numbers [5]. More attention has been paid to the possible flow separation and vortex structures in such an environment [4].

This paper presents a wind tunnel experiment on the effect of gusts on the aerodynamic characteristics of NACA0012 airfoil at different angles of attack. The mechanism behind the lift enhancement and the lift fluctuation increment around the stall is revealed.

EXPERIMENTAL SETUP

The experiment was carried out in the low-speed wind tunnel at Beihang University, whose test section has a cross-section of 430 mm (width) × 500 mm (height) and a total length of 5 m. The experimental setup is shown in figure 1. A pair of NACA0015 airfoils pitching sinusoidally in-phase is installed upstream of the experimental section to generate a periodic vertical gust with a frequency of 4 Hz. In the empty flow field, the peak-to-peak gust angle is 6.5°. A NACA0012 airfoil with a chord length of 120mm and a span length of 440mm was adopted as the experimental model. Under the free flow velocity of 7.5 m/s in the experiment, the Reynolds number based on the chord length was $Re = 6.0 \times 10^4$.

The velocity field of the gust was acquired by two-dimensional time-resolved PIV measurement with the sampling frequency of image pairs of 800 Hz at the airfoil mid-span. A Beamtech Vlite-Hi-527-30 high-speed double-pulsed laser illuminated the desired plane, and a Pco.dimax HS4 high-speed CMOS camera was adopted to capture image pairs. A MicroVec Micropulse-725 synchronizer was employed to realize the synchronous measurement of the force and the flow field by coinciding with the starting time of the two samples.

RESULTS

The aerodynamic characteristics of the airfoil under the gusty inflow are shown in figure 2. Compared with the steady inflow, the time-averaged lift coefficient increases significantly. The stall Angle of attack delay from 10° to 14°, and the maximum lift coefficient increases by over 30% from 0.70 to 0.94. On the other hand, the fluctuation of the lift coefficient increases as well. Around the stall angle of attack particularly, the standard deviation of the lift coefficient increases significantly by over 60% compared with Sears theory, in the range of 11° ∼ 15°.

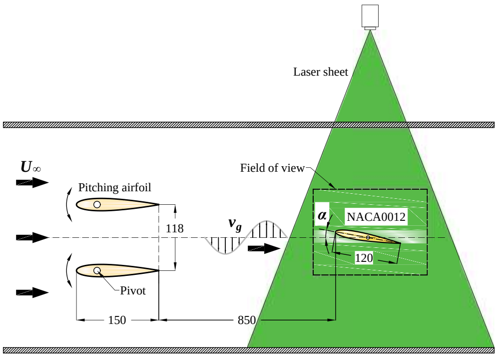

Figure 1: Schematic diagram of the experiment.

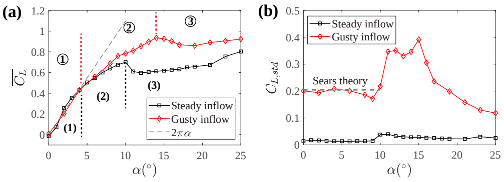

Figure 2: (a) Time-averaged and (b) standard deviation values of lift coefficient varied with angle of attack.

Figure 3 shows the time-averaged velocity field at $\alpha = 13^\circ$. Under the gusty inflow, the flow remains attached to the lifting surface, while it is in a large separation state for the steady inflow, indicating that the gust disturbance can suppress the flow separation effectively.

Near the stall angle of attack, the flow alternates between attached and separation periodically, and the lift coefficient has two peaks in a cycle, as shown in figure 4. With increased gust angle and velocity above the airfoil, the lift coefficient

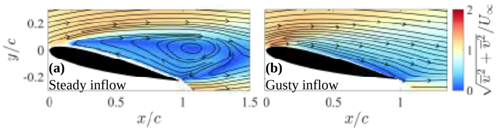

Figure 3: Time-averaged velocity fields at $\alpha = 13°$ under (a) steady inflow and (b) gusty inflow.

gradually increases and reaches the first peak (i). Then, the leading-edge separation occurs, and the leading-edge vortex is generated (ii). The lift coefficient reaches the second peak as the leading-edge vortex develops (iii). Subsequently, the leading-edge vortex shed (iv). Finally, as the gust angle decreases, the flow gradually returns to the attached flow from the leading edge to the tailing edge (v). When the flow is just restored to the attached flow, the velocity above the airfoil remains low; therefore, the minimum lift coefficient is obtained (vi). Since the high values of the two peaks and the low value of the minimum, the fluctuation of the lift coefficient increases significantly.

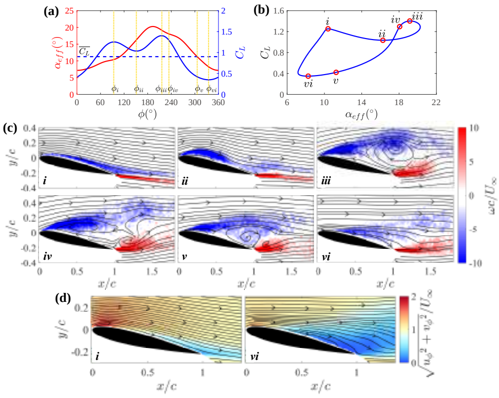

Figure 4: Periodic evolution of (a),(b) gust angle and lift coefficient, (c) vorticity fields, and (d) velocity fields at $\alpha = 13°$ under gusty inflow.

REFERENCES

[1] Federal Aviation Administration Advisory Circular 25.341-1. Dynamic gust loads, 2014.

[2] European Aviation Safety Agency. Certification specifications for normal, utility, aerobatic, and commuter category aeroplanes cs23 amendment 3, 2012.

[3] H. M. Atassi. The sears problem for a lifting airfoil revisited - new results. *Journal of Fluid Mechanics*, 141:109–122, 1984.

[4] A. R. Jones and O. Cetiner. Overview of unsteady aerodynamic response of rigid wings in gust encounters. *AIAA Journal*, 59(2):731–736, 2021.

[5] A. Mohamed, S. Watkins, M. V. OL, and A. R. Jones. Flight-relevant gusts: Computation-derived guidelines for micro air vehicle ground test unsteady aerodynamics. *Journal of Aircraft*, 58(3):693–699, 2021.

[6] W. R. Sears. Some aspects of non-stationary airfoil theory and its practical application. *Journal of the Aeronautical Sciences*, 8(3):104–108, 1941.

[7] N. J. Wei, J. Kissing, T. T. B. Wester, S. Wegt, K. Schiffmann, S. Jakirlic, M. Hölling, J. Peinke, and C. Tropea. Insights into the periodic gust response of airfoils. *Journal of Fluid Mechanics*, 876:237–263, 2019.

18

ERCOFTAC
European Drag Reduction and Flow Control Meeting – EDRFCM 2024
September 10th–13th, 2024, Turin, Italy

Leading-edge Bump on Improvements of Aerodynamic Loads of a Vertical Tail

Y. X. Wang, M. J. Muhammad, K.-S. Choi
Faculty of Engineering, University of Nottingham, NG7 2RD, Nottingham, UK

INTRODUCTION

Leading-edge bump is a type of passive flow control device modified from leading edge undulations. The initial Leading-edge modifications in the form of tubercles or undulations were originated from humpback whale flipper. The specific protuberant structure on flipper's leading edge has been widely recognised to be responsible for its excellent turning manoeuvres [1]. A model with tubercles was firstly tested [2] in a wind tunnel and showed the maximum lift increase and delays of the stall angle. Other experimental and CFD results on the tubercles on aerofoils and 3D wings showed different levels of control effects [3-6]. Some of these results on swept wing models did not show beneficial effects at all probably due to the complexity of the 3D flow structures, especially at large angles of attack, where flow are fully separated. We present a study, by experiments and LES simulations, of a single leading edge bump flow control effects on a swept wing in the form of a vertical tail model. This study is a part of the EU Clean Sky2 TailSurf project.

METHODOLOGY

The effects of leading-edge undulations were studied by wind tunnel tests on a vertical tail mode, which has a swept and tapered shape with a rudder at its trailing edge. The model was designed in modular structures with exchangeable leading-edge part for implementing different undulation flow control devices. A variety of leading-edge undulations were designed and tested including single and multiple undulations, dog teeth with protruding and recessing configurations. The results showed that a single protruding undulation (bump) produced the most significant effects on side-force enhancement. The optimum spanwise location of this single protruding bump was then further investigated in the wind tunnel study. The bump location and its geometry were fed into the LES simulations, where computations were carried out on the baseline model (smooth leading edge) and the model with a leading-edge bump. The flow field structures, pressure distributions, turbulent kinetic energy, streamline patterns and were compared to reveal the control mechanism of the bump.

EXPERIMENTAL SET-UP and CFD SIMULATIONS

The experiments were conducted in a low-speed, open-return wind tunnel at the University of Nottingham. The wind tunnel has a test section of 0.9 × 0.9 × 1.5 m, where the freestream velocity was set to 10 m/s. The test model was installed (see Fig. 1) in the centre of the test section, 0.56 m downstream from the inlet, where the turbulence intensity was increased to 4% by setting a turbulence-generating grid at the end of the contraction section to increase the effective Reynolds number.

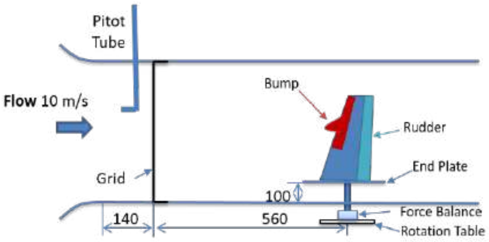

Figure 1: Schematic of the vertical tail model with a leading edge bump mounted inside the wind tunnel.

The vertical tail model has a swept wing shape with a root chord length of 0.322 m, tip chord length of 0.148 m and span length of 0.4 m, as shown in Fig. 1. The mean aerodynamic chord (MAC) was 0.246 m and the leading edge swept angle was 32°. The aspect ratio is 1.7 with a span of 0.4 m. The model was vertically mounted on a turntable over the wind tunnel floor through a rotation shaft mounted on a three-component strain gauge load cell for aerodynamic force measurements. The model has an exchangeable leading edge insert to implement the leading edge undulations. This insert has a size of 20% of local chord in streamwise and 65% of the model span in spanwise. The insert and the main model have a crenellated interface to secure the mounting of the bump. The bump has peak-to-peak amplitude of 12% of the tip chord and its spanwise wavelength is 29% of the tip chord [7].

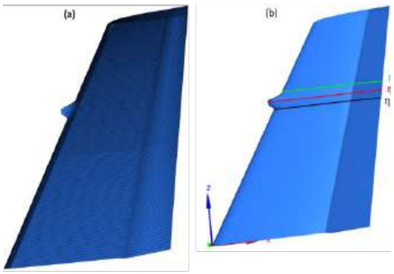

Figure 2: Mesh of the single bump model (a) and the spanwise sections where detailed comparisons were made with that of baseline case without bump (b).

It was found in experiments that the protruding single bump performed best among these tested undulations. This single bump geometry and location were then used to generate mesh for the CFD simulations as shown in Fig. 2. The structured mesh has nodes of Nx × Ny × Nz = 670 × 100 × 150 in the streamwise (x), wall-normal (y) and spanwise (z) directions with finer mesh clustered around the bump to have enough resolution to account for small flow structures produced by bump. The LES with Wall-Adapting Local Eddy-viscosity (WALE) model was used for the baseline and bump flow simulations. The LES simulation was run at the sideslip angle of 8° with a rudder deflection angle of 30°, where single bump experimental results showed significant benefit of control on the aerodynamic loads.

RESULTS AND DISCUSSIONS

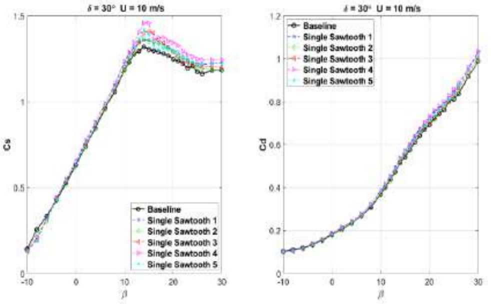

Figure 3: Comparison of baseline and single protruding tooth (bump) loads of the model at rudder deflection angle of 30° and Re = 0.17×10^6.

Among the tested leading-edge modifications, including undulation (sinusoidal) teeth, dog teeth, a single protruding undulation (bump) produced the most significant effects on side-force enhancement. The aerodynamic loads of a single bump at five spanwise positions were shown in Fig. 3. The bump lower-edges were located at 92% (No. 1), 83% (No. 2), 75% (No. 3), 67% (No. 4) and 58% (No. 5) of the model span. All the bumps have favorable effects to increase side-force to different levels. The maximum increments are from 2.8% to 10.6% at rudder angles of 30°. For other rudder angles of 0° and 15° the increments are from 4.3% to 8.5% and from 4.5% to 8.0%. Among these bumps, the No. 4 tooth with its lower edge located at 67% of the model span is outstanding by producing the largest side-force increases at all rudder deflections.

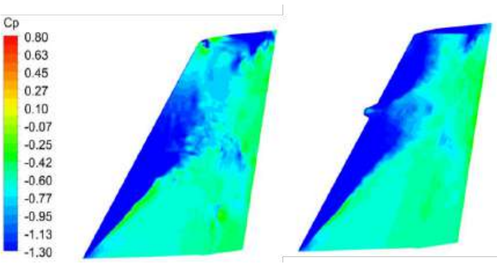

Figure 4: Comparison of Cp on the model suction side of LES simulation.

The CFD simulation results of baseline and this bump were shown in Fig 4, where Cp distributions over the suction side of the model surface are compared. The bump generated larger suction area, and hence produced more side force as expected. The streamwise vorticity contours of the baseline and bump cases at the lower trough, peak and upper trough spanwise sections were shown in Fig. 5. Apparently, the flow separated region and wake were significantly reduced by the bump control.

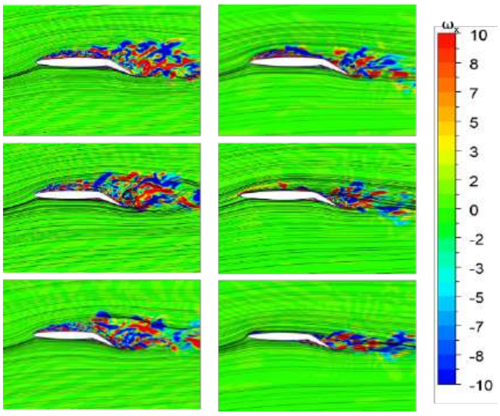

Figure 5: Comparison of streamwise vorticity contours. Left column for the baseline case and right column for the bump case. Top is at the lower trough section, middle is at the peak section and the bottom is at the upper trough section.

ACKNOWLEDGEMENTS

The present study was financially supported by Clean Sky 2 Joint Undertaking (JU) under grant agreement number 864290.

REFERENCES

[1] Fish, F. E., & Lauder, G. V. (2006). Passive and active flow control by swimming fishes and mammals. Annual Review of Fluid Mechanics, 38, 193-224.

[2] Miklosovic, D. S., Murray, M. M., Howle, L. E., & Fish, F. E. (2004). Leading-edge tubercles delay stall on humpback whale flippers. Physics of Fluids, 16(5), L39-L42.

[3] Bolzon, M. D., Kelso, R. M., & Arjomandi, M. (2016). Tubercles and their applications. Journal of Aerospace Engineering, 29(1), 04015013-1.

[4] Bolzon, M. D., Kelso, R. M., & Arjomandi, M. (2017). Force Measurements and Wake Surveys of a Swept Tubercled Wing. Journal of Aerospace Engineering, 30(3), 04016085-1.

[5] Custodio, D., Henoch, C. W., & Johari, H. (2015). Aerodynamic Characteristics of Finite Span Wings with Leading-Edge Protuberances. AIAA Journal, 53(7), 1878-1893.

[6] Wei, Z. Y., New, T. H., & Cui, Y. D. (2018). Aerodynamic Performance and Surface Flow Structures of Leading-Edge Tubercled Tapered Swept-Back Wings. AIAA Journal, 56(1), 423-431.

[7] Kim, J.-H., Choi, K.-S., Lacagnina, G., Chaitanya, P., Joseph, P., Hasheminejad, S. M., Pei Chong, T., Shahab, M. F., Omidyeganeh, M., & Pinelli, A. (2022). Aerodynamic and Aeroacoustic Optimization of Leading-Edge Undulation of a NACA 65(12)-10 Airfoil. AIAA Journal, 60(4), 2342-23.

19

ERCOFTAC
European Drag Reduction and Flow Control Meeting – EDRFCM 2024
September 10$^{\mathrm{th}}$–13$^{\mathrm{th}}$, 2024, Turin, Italy

DRAG REDUCTION FOR HEAVY ROAD VEHICLES WITH REAR FLAPS

X. Jiang, J. Zhang, M. Weissenbacher, I. Fumarola and G. Rigas
Department of Aeronautics, Imperial College London, SW7 2AZ London, UK

INTRODUCTION

Enhancing fuel efficiency and reducing air pollution in heavy road vehicles crucially depend on addressing the challenge of reducing aerodynamic drag [1]. For example, trucks transported the majority of freight across the UK in 2022, contributing to 20% of all domestic transport CO_2 emissions in the UK in 2021 [2].

The aerodynamic drag of trucks is dominated by the pressure difference between their frontal area and wake regions. Several flow motions identified in the wake of canonical Ahmed body geometries, such as bi-stable wake motions, vortex shedding, and bubble pumping, are related to aerodynamic drag [5, 6]. Active and passive flow control techniques are commonly used to tame wake dynamics and decrease the flow separation zone at the end of trucks. Adding flaps has been found to be one effective way to control the wake [4].

Coherent structures play a crucial role in turbulent separation and wakes [3], therefore, exploring their connection to drag reduction can enhance the development of effective control strategies. However, the impact of flaps on coherent flow structures in the wake zone and their contribution to pressure recovery and drag reduction is not well understood, especially in experiments or complex geometries. In this study, we experimentally investigate the role of flaps on coherent flow structures and mean flow quantities under various conditions, including yaw and rolling road scenarios.

EXPERIMENTAL SETUP

The experiment was conducted in the 10' × 5' National Wind Tunnel Facility at Imperial College London. The wind tunnel was equipped with a rolling road, traverse, and full boundary layer control. The flow speed was set to $U_\infty = 8.4$ m/s, with turbulence intensity less than 0.25%.

The truck model used was a scaled model (1:14) of a MAN TGX trailer. The cross-section of the model is 193 mm x 180 mm. It was mounted in the lower section (3.04 m x 1.52 m x 20 m) of the wind tunnel above a moving floor. The floor moving speed was set to be the same as the wind speed in the rolling road scenario. The truck was lifted 5 mm away from the floor, hanging on the support beams (see figure 1a), allowing its relative angle to the free-stream flow direction (yaw angle α) to be adjusted and the force induced by the wind to be measured. As shown in figure 1(a), the load cell was mounted below the yaw plate with their relative positions finely tuned. The load cell used was an ATI Gamma-IP68, which can measure force in three orthogonal directions (F_x, F_y, F_z) and three corresponding torques. The transducer is able to measure F_x and F_y within 65 N with an uncertainty below 1%.

The pressure was measured using a 64-channel digital pressure scanner (Chell μDAQ2-64DTC). It was connected to 36 pressure taps at the rear plate of the truck and to 18 taps at the side walls via a tubing system. Four flaps were mounted at the rear of the truck, precisely controlled by four motors (RMD-L-50005 for the left and right, RMD-L-4005 for the top and bottom). The chord length was 30 mm for the straight flap. Both straight and non-uniform flaps were explored in the experiment.

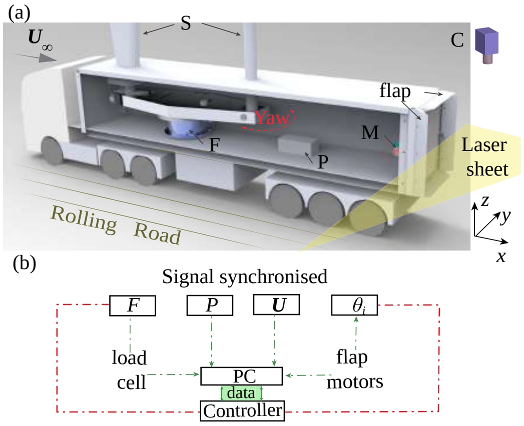

Figure 1: (a) Experimental setups in a wind tunnel; (b) diagram of data flow in the experiment. P: pressure scanner; F: load cell; M: flap motors; C: camera; S: support beams.

Particle image velocimetry (PIV) was performed to measure the wake downstream of the rear plate. The field of view was set in the middle of the rear plate, with the high-speed camera viewing from the roof of the wind tunnel. The 2D PIV measurement was conducted at 200 Hz using double-pulse mode. The trigger of the imaging system is synchronised with the start of pressure and force measurements. The diagram of data flow is shown in figure 1(b).

RESULTS

A comparison between the averaged (approximately 2500 frames) streamwise velocity contours with flaps mounted at 0° and with flaps removed is shown in figure 2(a) and (b). It shows that the wake region becomes a triangular zone behind the truck when using the flaps. The low momentum zone in (b) has a sharper convergent angle and a modified bubble area. For the yaw scenario, a similar comparison is shown in figure 2(c) and (d). When the flaps were mounted, they were parallel to the truck body (yawed to the right). Due to the yaw effect, the bubble zone is more asymmetric than in the straight scenario. The bubble zone with the flap on is observed to be confined closer to the truck and is inclined towards the right flap.

Figure 3 shows the Power Spectral Density (PSD) for the

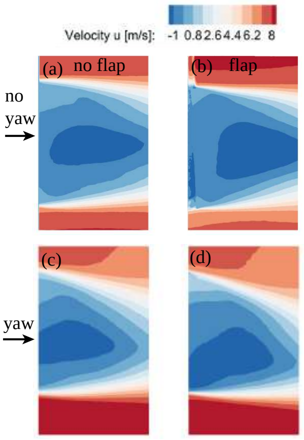

Figure 2: Comparison of streamwise velocity contour based on PIV measurement. (a) no yaw, no flap; (b) no yaw, with 4 flaps; (c) no flap, yaw at 5°; (d) 4 flaps, yaw at 5°.

four cases shown above based on the anti-symmetric pressure $(\bar{P}_l(t) - \bar{P}_r(t))$ at the rear base. Here, $\bar{P}_l(t)$ represents the average of 18 pressure measurements on the left part of the rear plate, while $\bar{P}_r(t)$ represents the average of 18 pressure measurements on the right. There are two main modes for all cases, $St \approx 0.1$ and $St \approx 0.2$ related to anti-symmetric coherent vortex shedding. The results demonstrate that with 4 flaps, the PSD is greatly reduced, especially for the yaw case, and the flaps successfully suppress the coherent oscillations in the near wake.

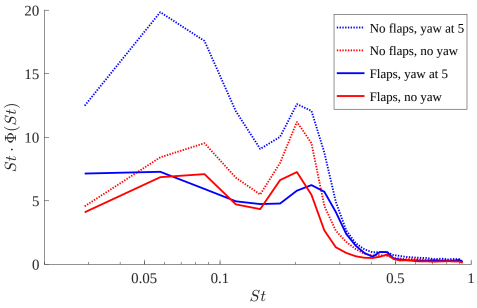

Figure 3: Comparison of Power Spectral Density (PSD) based on the asymmetric pressure $(\bar{P}_l(t) - \bar{P}_r(t))$ at the rear plate.

The flap geometry and a detailed correlation between the velocity data and the pressure/force data are also analysed in this study. Though not shown here, we also investigated the rolling road effect, which is important for quantifying and characterising drag reduction strategies in realistic regimes.

Acknowledgments: This work was supported by the UKRI AI for Net Zero grant EP/Y005619/1.

REFERENCES

[1] H. Choi, J. Lee, and H. Park. Aerodynamics of heavy vehicles. *Annu. Rev. Fluid Mech.*, 46:441–468, 2014.

[2] Department for Transport. Future of freight: long-term plan. Technical report, 2022.

[3] M. Gad-El-Hak. Coherent structures and flow control: genesis and prospect. *Bulletin of the Polish Academy of Sciences Technical Sciences*, 67:411–444, 2019.

[4] A. E. Giannenas, S. Laizet, and G. Rigas. Harmonic forcing of a laminar bluff body wake with rear pitching flaps. *J. Fluid Mech.*, 945:A5, 2022.

[5] M. Grandemange, M. Gohlke, and O. Cadot. Turbulent wake past a three-dimensional blunt body. Part 1. Global modes and bi-stability. *J. Fluid Mech.*, 722:51–84, 2013.

[6] R. Volpe, P. Devinant, and A. Kourta. Experimental characterization of the unsteady natural wake of the full-scale square back Ahmed body: flow bi-stability and spectral analysis. *Exp. Fluids*, 56:99, 2015.

20

ERCOFTAC
European Drag Reduction and Flow Control Meeting – EDRFCM 2024
September 10$^{\text{th}}$–13$^{\text{th}}$, 2024, Turin, Italy

TURBULENT DRAG REDUCTION BY PASSIVELY ROTATING DISCS

Pierre Ricco
Department of Mechanical Engineering, University of Sheffield, S1 3JD Sheffield, UK

Paolo Olivucci
Institute of Fluid Mechanics, Technische Universität Braunschweig, 38108 Braunschweig, Germany

Daniel Wise
Institute of High Performance Computing, Singapore 138632, Republic of Singapore

INTRODUCTION

We present the main results of our paper Olivucci *et al.*, *J. Fluid Mech.* (2021) [2]. A turbulent channel flow modified by the motion of discs that are free to rotate under the action of wall turbulence is studied numerically. The Navier-Stokes equations are coupled nonlinearly with the dynamical equation of the disc motion, which synthesizes the fluid-flow boundary conditions and is driven by the torque exerted by the wall-shear stress. We consider discs that are fully exposed to the fluid and discs for which only half of the surface interfaces the fluid. The disc motion is thwarted by the fluid torque in the housing cavity and by the torque of the ball bearing that supports the disc. For the full discs, no drag reduction occurs because of the small angular velocities. The most energetic disc response occurs for disc diameters that are comparable with the spanwise spacing of the low-speed streaks. A perturbation analysis for small disc-tip velocities reveals that the two-way nonlinear coupling has an intense attenuating effect on the disc response. The reduced-order results show excellent agreement with the nonlinear results for large diameters. The half discs rotate with a finite angular velocity, leading to large reduction of the turbulence activity and of the skin-friction drag over the spinning portion of the discs, while the maximum drag reduction over the entire walls is 5.6%. The dependence of the drag reduction on the wall-slip velocity and the spatial distribution of the wall-shear stress qualitatively match results based on the only available experimental data.

NUMERICAL PROCEDURES

Figure 1 shows the schematics of the flows we have studied. An incompressible turbulent flow between parallel flat walls fitted with spinning discs is investigated. The flat discs, flush-mounted on the walls, are free to rotate under the viscous action of the turbulent channel flow. No motors are used to move the disc and therefore these drag reduction techniques are passive. The turbulent channel flow with the freely-rotating discs is studied via direct numerical simulation. The open-source code Incompact3D is used to simulate the flows [1] and all flows are at a Reynolds number 4200, based on the maximum laminar Poiseuille velocity at the same mass flow rate and the half channel height.

The velocity is null over the stationary portions of the walls, while it coincides with the local disc velocity when the fluid passes over a disc. The boundary conditions are time dependent because they are determined by the rigid-body dynamics of the discs, driven by the instantaneous wall-shear stresses exerted by the wall turbulence on the surfaces of the discs. The system dynamics is therefore ruled by a two-way coupling between the fluid and freely-rotating discs. The detailed description of this coupling is presented in our paper Olivucci *et al.*, *J. Fluid Mech.* (2021) [2]. Two configurations are considered: a full-disc layout where two coaxial discs, one on each wall, are fully exposed to the viscous action of the turbulent flow, and an arrangements of rows and columns of half discs, for which only the right half of the discs is wetted by the fluid.

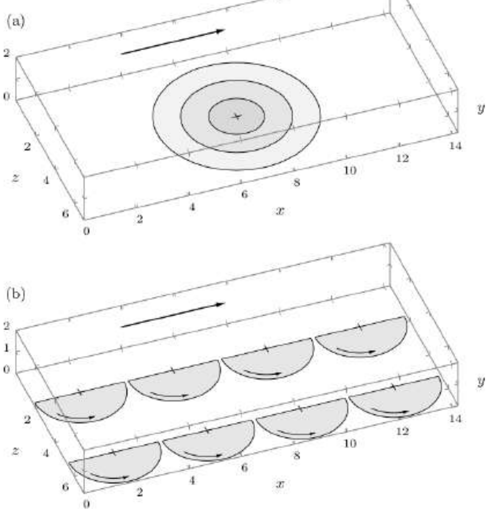

Figure 1: Schematic of a) the single freely-rotating disc of increasing diameter and b) the rows and columns of half discs.

RESULTS FOR THE FULL DISCS

For all the diameters tested, the discs oscillate randomly around $W = 0$, where W is the tip velocity of the discs. The variance of W is larger at small diameters, the oscillations of the disc becoming less intense as the diameter increases. Because of the small angular displacements, no drag reduction occurs on the disc surface. As for other moving-wall drag-reduction techniques, a minimal value of the wall velocity, about $W^+ = 1$, is required for the wall turbulence to be af-

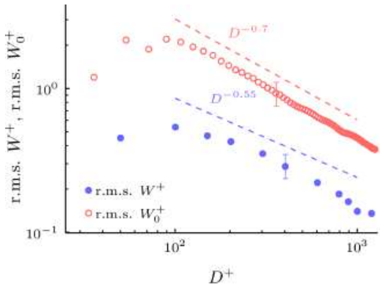

Figure 2: Root-mean-square values of the disc-tip velocities W^+ in the coupled case and W_0^+ in the uncoupled case as functions of the disc diameter. The blue full circles denote the coupled-dynamics data and the red empty circles symbols denote the uncoupled-dynamics data.

fected by the wall motion and to experience drag reduction. If the wall displacement is too small, the viscous effects are confined in a very thin layer because the wall-normal momentum diffusion from the wall is limited. In the freely-rotating case, W_{rms} is always smaller than the estimated minimal displacement and it is therefore expected that the skin-friction drag is unaffected.

Figure 2 shows the values of W_{rms}. The blue symbols denote the coupled-dynamics results and the red symbols denote the uncoupled-dynamics results, discussed in Olivucci *et al.*, *J. Fluid Mech.* (2021) [2]. In the range $D^+<100$, W_{rms} grows with the disc diameter. The maximum W_{rms} occurs for $D^+=100$, which is comparable with the characteristic spanwise spacing of the low-speed streaks. For larger diameters, in the $100<D^+<900$ range, W_{rms} decreases as $D^{-0.55}$ when the diameter grows. An optimum occurs because, for very small D, the torque is too small to exert the required power to move the discs, while for large discs, the inertia of the disc thwarts the action of the torque.

RESULTS FOR THE HALF DISCS

The main difference from the full discs is the finite average disc velocity due to the driving action of the mean turbulent flow. Once the new fully-developed regime is established, the disc inertia can be neglected because the mean disc-tip velocity $\overline{W}$ of the half disc is determined by the steady-state balance between the fluid torque and the frictional housing torques. We define a streamwise slip velocity $U_{s,d}$, averaged over the moving disc surface. In the best performing configurations, the highest $\overline{W}^+$ values are obtained and the drag-reduction margins over the disc surfaces are $\mathcal{R}_d = 20\%$ and $\mathcal{R}_d = 14\%$.

Figure 3 shows the drag-reduction margin as a function of the slip velocity. The drag-reduction level $\mathcal{R}_d$ is positively correlated to $U^+_{s,d}$. As the slip velocity increases, the drag-reduction margin over the entire wall, $\mathcal{R}$, first increases linearly and then levels off at higher disc velocities. On the stationary wall region (amounting to 63% of the total wall area) neither drag reduction nor drag increase is measured for $U^+_{s,d} \approx 1$, while a 3% drag increase is observed for $U^+_{s,d} \approx 2$. When the $\mathcal{R}_d$ on the rotating half disc increases by 6%, the non-negligible level of drag increase on the rest of the wall surface causes the global drag reduction $\mathcal{R}$ to only grow by about 0.6%.

Figure 4 show the wall-shear stress reduction as a function of x and z. A non-homogeneous spatial distribution along both the x and z directions is shown. The drag-reduction margin increases moving away from the centreline because the local streamwise slip velocity grows as the right side of the disc is approached. The maximum wall-shear-stress reduction occurs over the lower part of the rotating disc, while the maximum drag increase occurs in a region that is narrow in the spanwise direction, near the centreline, and upstream of the disc centre.

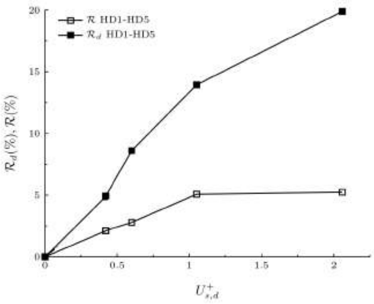

Figure 3: Drag-reduction margins $\mathcal{R}_d$ (averaged over the disc surface) and $\mathcal{R}$ (over the entire channel walls) as functions of the slip velocity $U^+_{s,d}$.

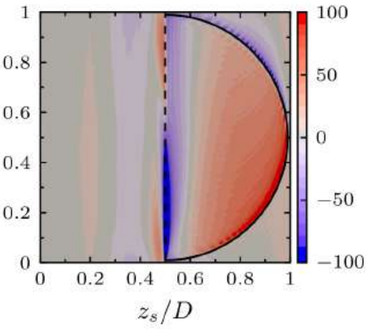

Figure 4: Wall-shear stress reduction as a function of x and z for a high drag-reduction case.

This increase of wall friction might be an effect of the modelled discontinuity at the centreline. As the slip velocity doubles, the drag-increase region on the disc surface and near the centreline becomes wider and more intense. The drag-reduction margin also grows, especially near the disc tip. The improvement of drag reduction as the disc spins faster is more relevant than the increase of drag. These two contrasting effects are the reason why the drag-reduction margin over the disc surface does not double as does the disc-tip velocity, as shown in figure 3.

REFERENCES

[1] S. Laizet and N. Li. Incompact3d: A powerful tool to tackle turbulence problems with up to $\mathcal{O}(10^5)$ computational cores. *Int. J. Num. Meth. Fluids*, 67:1735–1757, 2011.

[2] P. Olivucci, D. Wise, and P. Ricco. Reduction of turbulent skin-friction drag by passively rotating discs. *J. Fluid Mech.*, 923:A8, 2021.

 # 21

ERCOFTAC
European Drag Reduction and Flow Control Meeting – EDRFCM 2024
September 10th–13th, 2024, Turin, Italy

MASS ENTRAINMENT ANALYSIS OF THE CONTROLLED TURBULENT SEPARATION USING SWEEPING JET ACTUATORS

M. Tocquer
Univ. Orléans, INSA-CVL, PRISME UR 4229, F45072, France

C. Raibaudo
Univ. Orléans, INSA-CVL, PRISME UR 4229, F45072, France

A. Kourta
Univ. Orléans, INSA-CVL, PRISME UR 4229, F45072, France

INTRODUCTION

Flow separation concerns many practical aerodynamic configurations and has an impact on aerodynamic performance losses. Consequently, controlling separation using flow control strategies has garnered particular interest. Over the past decades, active control (such as fluidic actuators [3] or oscillators) has proven highly promising results, due to its ability to adapt to changing flow conditions. However, to substantially influence aerodynamics, these actuators must operate at high frequency ranges and inject significant momentum [1].

Sweeping jets (SWJs) have demonstrated promising results in achieving active flow control with high oscillation frequency and significant momentum injection. These characteristics are obtained using the Coanda effect on the internal part of the SWJ, without moving parts. SWJs have been applied for control purposes in several automotive and aeronautic applications [2, 4], improving aerodynamic performance.

However, the interaction between the flow generated by the SWJ and the controlled flow, as well as the mechanisms that lead to effective separation control, are not well understood. The present study aims at characterising the mitigation of the separation caused by a canonical ramp using sweeping jets. We will focus here on the effect of the control on the recirculation length, the mean drag and the mass entrainment through the turbulent non-turbulent interface (TNTI).

EXPERIMENTAL SETUP

SWJs are employed to mitigate the turbulent separation over a canonical ramp. A rounded SWJ with an outlet throat of 3 mm is used in this study. It produces a high momentum injection with high frequency. Results on the characterisation of the SWJ used in this work are detailed in previous studies [6].

The ramp with a height of $h = 30$ mm and a slope of $\beta = 25°$ is located in the S2 Eiffel open wind tunnel of the PRISME Laboratory in Orléans. The flow over a ramp is managed by eight SWJs, along the spanwise at the leading edge of the ramp, which are pitched on the ramp at an angle of 30°, 45°, and 90°. The geometry of the ramp is identical to that which Stella et al. [5] examined in their study and is presented in Fig. 1. 103 wall pressure sensors (500 Hz) are placed on the ramp. They are coupled with a planar PIV in the centerline of the ramp for a 30° actuation angle. The PIV plane covers the entire range of the separation. The freestream velocity is set to $U_\infty = 20\ m.s^{-1}$. Seven different inlet pressures are tested to highlight the efficiency of the SWJ to control the separation over the ramp ($P_0 = 0; 1; 3; 5; 13; 15; 18$ kPa).

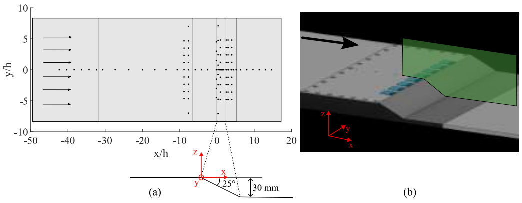

Figure 1: Experimental setup. (a) Distribution of the pressure along the ramp. (b) PIV plan on the ramp geometry with implemented SWJs.

EFFECT OF THE SWJ ON MEAN QUANTITIES

In order to state the effectiveness of the SWJ to control separated flows, the pressure drag coefficient C_D is estimated by integrating and projecting on the streamwise axes the wall pressure coefficient C_P.

$$C_D = -\int_{ramp} C_P cos(\beta) dl \tag{1}$$

Figure 2a shows the evolution of the drag coefficient with the momentum coefficient C_μ for the three actuation angles tested. In this study, the momentum coefficient is given by:

$$C_\mu = \frac{\rho_{jet} U_{jet}^2 A_{jet}}{\frac{1}{2}\rho_\infty U_\infty^2 h w_{ramp}} \tag{2}$$

with U_{jet}, ρ_{jet}, and A_{jet} being the jet velocity, the jet density, and the total exit area of the actuators, respectively. U_∞, ρ_∞, and w_{ramp} are the velocity, the density of the main flow, and the width of the ramp.

With an actuation angle of 90°, the drag coefficient increases with the momentum injection (Fig. 2a). For the other two angles of actuation (30° and 45°), the drag coefficient is decreased by the control. For the highest momentum injection net thrust is even produced $C_\mu \geq 6$ %. The recirculation length of the 30° actuation angle is estimated from the PIV (Fig. 2b). For high momentum injection where thrust is generated ($C_\mu \geq 6$ %), the recirculation is fully suppressed. At lower momentum injection, the recirculation length is reduced

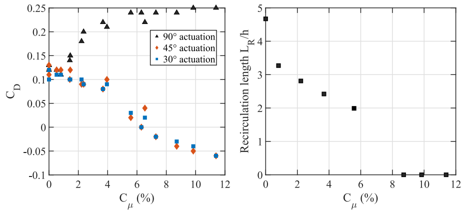

(a) (b)

Figure 2: Effect of control on mean properties. (a) Pressure drag coefficient C_D for different angles of actuation. (b) Recirculation length L_R for a 30° angle of actuation.

by up to 58%. The reduction of the recirculation on the ramp induces an increase of aerodynamic performances.

MASS ENTRAINMENT ANALYSIS

As observed previously, the control has an important effect on the turbulent non-turbulent interface (TNTI), where the entrainment mechanism is of primary importance. The TNTI is defined using a streamwise velocity contour calculated with uniform momentum zone. To study the mass entrainment induced by the control, a mass budget is performed on a domain containing the turbulent separation and its associated shear layer. The domain is presented in Fig. 3 and is bounded by the wall, the TNTI and the leading edge of the ramp. The last boundary, the oulet, is varied along the streamwise direction. The mass budget is defined in incompressible flow using the following equation:

$$div(\vec{U^*}) = 0 \Rightarrow \int_{in} \vec{U^*}.\vec{n}_{in} dl^* + \int_{wall} \vec{U^*}.\vec{n}_{wall} dl^* + \int_{out} \vec{U^*}.\vec{n}_{out} dl^* + \int_{TNTI} \vec{U^*}.\vec{n}_{TNTI} dl^* = 0 \quad (3)$$

where * represents normalised quantities using the main flow properties.

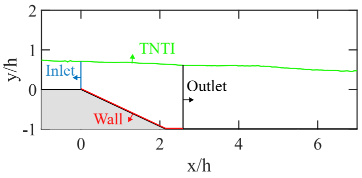

Figure 3: Mass budget calculation

Fig. 4a and Fig. 4b present the results of the normalised mass budget for the baseflow and for a momentum injection of $C_\mu = 2.22$ %. It is clearly visible that the control has a direct effect on the entrainment. For the control case, the entrained mass through the TNTI is highly increased (multiplied by 1.9 at the end of the control domain). It is also triggered earlier over the ramp in the controlled case and begins at $x/h = 0$ compared to $x/h = 2.5$ for the baseflow. The increase in mass that goes through the TNTI leads to an increase in the turbulent stresses inside the separated shear layer. The streamwise normal stress and the shear stress are multiplied by 2 in the controlled case, as presented in Tab. 1. Thus, the turbulent kinetic energy is increased, and the mixing between the upper part of the shear layer (high momentum) and the recirculation zone (low momentum) is enhanced.

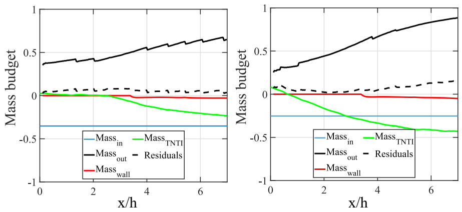

(a) (b)

Figure 4: Mass budget on the ramp. Normalise mass budget for the baseflow (a) and $C_\mu = 2.22$ % (b).

Table 1: Maximum of Reynolds stresses for the baseflow and $C_\mu = 2.22$ % inside the turbulent shear layer.

	Baseflow	$C_\mu = 2.22$ %
max($\lvert\overline{u'u'}/U_\infty^2\rvert$)	0.0469	0.1057
max($\lvert\overline{u'v'}/U_\infty^2\rvert$)	0.0169	0.0366
max($\lvert\overline{v'v'}/U_\infty^2\rvert$)	0.0247	0.0394

CONCLUSION

In this study, SWJs are employed to mitigate the turbulent separation that occurs over a canonical ramp. It is shown that the control increases the mass entrainment through the TNTI, which intensifies the turbulent stresses in the shear layer and improves the mixing between high momentum flow over the shear layer and low momentum flow in the recirculation region. The present mechanism induces a reduction in the recirculation length, which leads to a decrease in the drag on the ramp.

The mechanism proposed in this work raises some questions that will be addressed in future work. For example, the possible scaling of the mass entrainment with the injected mass by the SWJ. To go deeper in the analysis, momentum budget using pressure reconstruction is considered. Control on more realistic geometries like airfoils is also considered to verify the proposed mechanism.

REFERENCES

[1] L. N. Cattafesta and M. Sheplak. *Annual Review of Fluid Mechanics*, 43(1):247–272, 2011.

[2] R. E. Childs, P. M. Stremel, L. K. Kushner, J. T. Heineck, and B. L. Storms. In *54th AIAA Aerospace Sciences Meeting*, San Diego, California, USA, 2016. American Institute of Aeronautics and Astronautics.

[3] C. Raibaudo, M. Stanislas, and F. Kerhervé. *Flow, Turbulence and Combustion*, 98(4):1039–1063, 2017.

[4] H. J. Schmidt, R. Woszidlo, C. N. Nayeri, and C. O. Paschereit. *Experiments in Fluids*, 58(8):106, 2017.

[5] F. Stella, N. Mazellier, and A. Kourta. *Journal of Fluid Mechanics*, 826:851–887, 2017.

[6] M. Tocquer, C. Raibaudo, and A. Kourta. In *58th 3AF International Conference on Applied Aerodynamics*, Orléans, France, 2024. Association Aéronautique et Astronautique de France.

ERCOFTAC
European Drag Reduction and Flow Control Meeting – EDRFCM 2024
September 10th–13th, 2024, Turin, Italy

SEPARATION CONTROL WITH SPANWISE-INCLINED MICRO JETS

D.P. Ramaswamy, R. Sebastian and A-.M.Schreyer
Institute of Aerodynamics and Chair of Fluid Mechanics, RWTH Aachen University, 52062 Aachen, Germany

INTRODUCTION

Shock-wave / boundary-layer interactions (SWBLIs) are an ubiquitous flow phenomenon in high-speed aerospace applications. A strong shock wave imposes a large adverse pressure gradient and can lead to large-scale separation of the flow. Such separated flows are detrimental and can lead to highly unsteady thermal and pressure loading, inlet instabilities, and total pressure loss, amongst others. Furthermore, the low-frequency unsteadiness of the shock/separation bubble system [1] can induce significant structural vibrations and accelerate material fatigue. Therefore, proper control of this interaction is essential.

A suitable control strategy is the application of air-jet vortex generators (AJVGs), where streamwise vortices are introduced by small jets injected into the boundary layer. These streamwise vortices redistribute the momentum within the boundary layer and make it more resistant to separation. The effectiveness of AJVGs, however, depends on several air-jet geometrical and flow parameters. To understand the parameters and mechanisms, we studied the structures induced by spanwise-inclined jets in a supersonic crossflow (JiSC) and their influence on compression-ramp interactions, for various AJVG configurations. Selected configurations at Mach 7.2 were also simulated. Numerical and experimental tools were employed to understand the spatio-temporal evolution of flow dynamics comprehensively. A summary of the main results will be presented here.

Numerical investigations of jets injected into a Mach 2.5 supersonic crossflow (JiSC) were carried out with large-eddy simulations (LESs) for several single-jet and jet-array configurations using the in-house finite volume solver m-AIA (formerly, ZFS). Furthermore, focusing-schlieren, oil-flow visualisations and particle image velocimetry (PIV) were employed to study the impact of jet-induced structures on a fully-separated SWBLI induced by a 24^o compression-expansion corner.

STEADY SPANWISE-INCLINED JETS IN CROSSFLOW

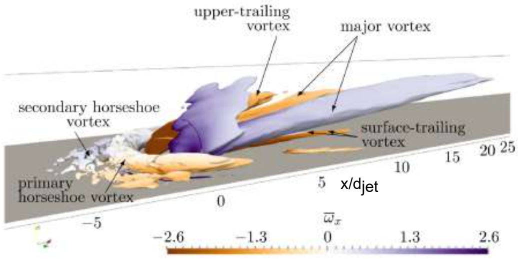

Figure 1: Isosurface of Q-criterion with Q = 0.07 [6]

The flow topology of a spanwise-inclined single JiSC at Mach 2.5, representative of a single AJVG, is similar to perpendicularly-injected jets and mechanical micro-vortex generators (MVGs): it includes a major counter-rotating vortex pair (CVP), mostly responsible for the control effect, and secondary upper- and surface-trailing vortices. Nevertheless, due to the spanwise-inclined injection, the crossflow is largely diverged along the injection direction, and crossflow on the side opposite to the direction of injection interacts with the jet wake. As a result, a strongly asymmetric ensemble of vortices is generated; it remains intact and close to the surface for a long downstream distance [6]. The strong major CVP enhances the momentum redistribution within the boundary layer, which makes the flow less prone to separation.

For control purposes, AJVGs are usually arranged in rows of multiple devices. For single-row arrays of steady, spanwise-inclined jets with spacing $7d_{jet} - 11d_{jet}$ (d_{jet} is the injection-pipe diameter), interactions among the asymmetric adjacent CVPs enhance the transfer of momentum to the near-wall region, thus making the boundary-layer more resistant to separation [7]. Additionally, the jet/crossflow interactions strengthen with the injection pressure (p^{pl}) before saturating for $p^{pl} \geq 25p_{\infty}$. However, upon saturation, larger p^{pl} deteriorate control effectiveness by causing stronger blockage to the crossflow and larger momentum influx, giving rise to a secondary flow along the direction of injection [5].

A strong interplay thus exists between jet spacing and injection pressure. For both, intermediate values allow for optimal jet/jet interactions, whereas too-weak interactions reduce the mixing and control effect, and too-strong interactions hinder the full formation of the major CVP [7, 5].

Additional LESs performed across different flow regimes [8] show that the ratio of injection-pressure-to-freestream-pressure (p^{pl}/p_{∞}) is a suitable parameter to characterize and compare jet/crossflow interactions across supersonic and hypersonic flow regimes. Furthermore, a boundary-layer-to-jet-diameter ratio of $\delta/d_{jet} \approx 10$ is recommended for control applications, as it delays the lift-off of major vortices.

SEPARATION CONTROL USING STEADY JET ARRAYS

In tandem with the numerical investigations, we analysed configurations of spanwise-inclined AJVGs on a 24^o compression-ramp interaction experimentally at Mach 2.52, to study their separation control behaviour. Effectively configured AJVGs can shrink the total separation length by nearly 25%, the separated area by as much as $\sim 57\%$ and can mitigate turbulence amplification across the SBLIs by nearly $\sim 40\%$ [2]. However, the control effectiveness depends on several AJVG parameters.

As witnessed in the LES, the jet-to-jet spacing (D) in AJVG arrays has a strong influence. For very small jet spacings

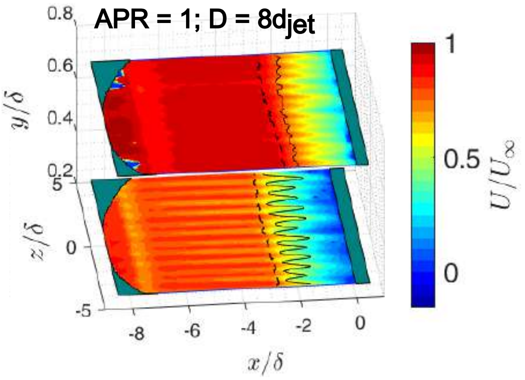

Figure 2: Mean velocity profiles from PIV at $y = 0.24\delta$ and $y = 0.69\delta$ for an effectively configured AJVG arrray [3]

($D \approx 4 - 6d_{jet}$), the jets are very close to each other and incite vortex interactions to adverse strength. Consequently, the jet-induced coherent structures break down and cause an increase in separation. On the other hand, at very large jet spacings ($D \sim 25d_{jet}$), the jets do not interact and the jet arrays display characteristics equivalent to a spanwise series of single jets in crossflow. At moderate jet-to-jet spacings ($D = 8d_{jet}$; see Fig. 2), the most favourable control effectiveness is achieved, with a reduction in both the separation length and area; these effects are brought about by the formation of stable, interacting, streamwise-elongated coherent jet-induced vortices and the associated momentum transfer [2].

A similar mechanism occurs when changing the air-jet injection pressure ratio (APR $= p^{pl}/p_o$, where p^{pl} is the stagnation pressure in the jet-plenum and p_o is the stagnation pressure of the freestream) for a fixed jet spacing. Jets injected with APR ≤ 0.20 display characteristics similar to single jets in crossflow. For APR ≥ 1.8, the individual bow shocks merge and strongly obstructs the crossflow. At intermediate values of injection pressure ($0.80 \lessapprox$ APR $\lessapprox 1.5$), the control effectiveness is favourable with $25\%-32\%$ reduction in total separation length. The injection pressure and jet/jet spacing thus show an interplay when affecting the separation-control effectiveness of AJVGs [5].

Also the jet-orifice shape has an influence on the control effectiveness. Investigations performed on elliptical AJVGs with the same hydraulic diameter [3] as the equivalent circular case show that elliptical AJVGs achieve a 45% improved separation control effectiveness, due to stronger streamwise vortices that are able to penetrate $\sim 25\%$ deeper into the boundary layer. Stronger streamwise vortices are also induced by jet injection via pipes that are $\sim 8d_{jet}$ long, in comparison to shorter pipes [4]. This length ensures fuller velocity profiles within the jet-injection pipe, thus improving the induced streamwise vorticity and consequently, the separation-control effectiveness.

CONTROL OF SWBLIS USING UNSTEADY JET ARRAYS

To explore the potential of AJVGs for fully active control, we compared the jet/jet interactions and control effect of forced (cases LFreInj, MFreInj, HFreInj) and unforced (case StdyInj) spanwise-inclined AJVGs on the aforementioned SWBLI using LESs. The overall mean flow topology is very similar. The total mean separation length (L_{sep}) is not affected by the forcing (see Fig. 3), indicating that unforced AJVGs are sufficient when reducing the extent of the separation region is the objective, as they are easier to implement and less complex than forced AJVGs. However, a dynamic mode decomposition (DMD) analysis revealed that bow-shock oscillation, flow modulation and vortices due to jet/jet interactions strongly influence the dynamics of the SWBLI. While the overall dynamic behaviour of the SWBLI remains similar, which indicates that SWBLI is a robust phenomenon, forcing of the jets alters the characteristic frequencies of these DMD modes. As a result, certain frequencies dominate and alter the shock and bubble motion. The characteristic frequency of SWBLI can be shifted up to $St_{L_{sep}} \approx 0.1$, which can be of interest when the SWBLI frequency equals a structural resonance frequency.

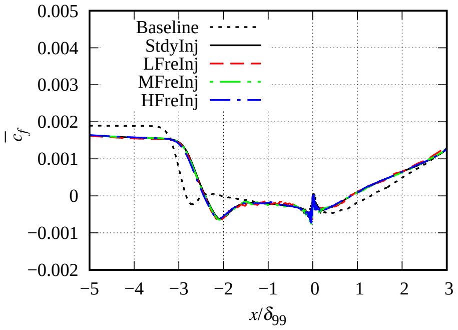

Figure 3: Skin-friction distribution of forced & unforced cases.

ACKNOWLEDGMENTS

This research was funded by the DFG within the framework of the Emmy Noether Programme (project number 326485414). Computing resources were provided by the High-Performance Computing Center Stuttgart (HLRS) within a Large-Scale Project of the Gauss Center for Supercomputing (GCS).

REFERENCES

[1] N. T. Clemens and V. Narayanaswamy. *Annual Review of Fluid Mechanics*, 46(1):469–492, 2014.

[2] D. P. Ramaswamy and A.-M. Schreyer. *AIAA Journal*, 59(3):927–939, 2021.

[3] D. P. Ramaswamy and A.-M. Schreyer. *Experiments in Fluids*, 64(5), 2023.

[4] R. Ramaswamy, D. P. Sebastian and A.-M. Schreyer. *Physical Review Fluids*, 8(11), 2023.

[5] R. Sebastian, D. P. Ramaswamy, and A.-M. Schreyer. *AIAA Journal*, 61(9):3833–3847, 2023.

[6] R. Sebastian and A.-M. Schreyer. *European Journal of Mechanics - B/Fluids*, 94:299–313, 2022.

[7] R. Sebastian and A.-M. Schreyer. *Journal of Fluid Mechanics*, 946, 2022.

[8] R. Sebastian and A.-M. Schreyer. *Aerospace Science and Technology*, 147:109033, 2024.

 # 23

ERCOFTAC
European Drag Reduction and Flow Control Meeting – EDRFCM 2024
September 10th–13th, 2024, Turin, Italy

DEVELOPMENT AND VALIDATION OF AN HYBRID JET FLOW CONTROL ACTUATOR

P.L. Spychala, P. Joseph, J. Delva, A. Dazin
Univ. Lille, CNRS, ONERA, Arts et Métiers ParisTech, Centrale Lille, Laboratoire de Mécanique des Fluides de Lille - Kampé de Fériet, 59000, Lille, France

INTRODUCTION

In the field of separated flow control, a significant technological leap was achieved by transitioning from continuous blowing to periodic perturbations [3]. This permitted to reduce the mass of fluid required to control the flow while keeping the same efficiency. Within previous studies, the two main examples of periodic blowing are (excepting sweeping jets, which are periodic in space but constant in time) pulsed jets [7] and synthetic jets [2]. However, there is only a limited amount of works that studied control techniques which do not stricly rely on pulsed or synthetic jets. Some efficient control solutions and means of interacting with the flow may therefore be unexplored. The authors would nonetheless like to underline some recent studies by Steinfurth and Weiss [6] and Haffner et al. [4] that were focused on a more pertinent use of pulsed perturbations, where adjusting the duty-cycle led to increased control performances. In both studies, time characteristics of the perturbation were tuned based on separation and reattachment timescales of the flow, which were extensively described by Darabi and Wygnanski [1]. Considering these results, the question arises as to whether further exploring the concept of combining pulsed and synthetic jets in “hybrid jets” might result in an increased control authority. These hybrid jets would consist in alternating blowing and suction with or without zero net mass flux or constant phasing. Some actuators designs aiming at producing unusual perturbations have already been reported in the literature [5]. However, none of these researches seemed to achieve as many degrees of freedom regarding the amount of time varying blowing / suction combinations as the hybrid jets developed in the present research work. Therefore, the aim of the current study is to experimentally investigate the efficiency of hybrid jets on an academic separated flow geometry.

METHODOLOGY

The hybrid actuator was designed to perform local blowing and suction, both of which independently adjustable in time and amplitude. Design criteria such as maximum forcing frequency or blowing / suction velocities were dictated by the flow geometry to be controlled, in this case a 25° backward facing ramp separated flow. The maximum expected forcing frequency and velocity based on previous research from the literature are 500 Hz and 80 m/s. The developed actuator is able to perform blowing and suction phases through a single 30×0.5 mm^2 slot, using compressed air and vacuum systems. Pulsed blowing and suction are managed by two solenoid valves, operated with a two-channels generator used to produce two square command signals, both with freely adjustable frequency and duty-cycle. Characterization of the actuator in quiescent environment was carried out using primarily hotwire velocimetry and unsteady pressure measurements (Figure 1), as well as supply pressures and blowing and suction flowrates measurements.

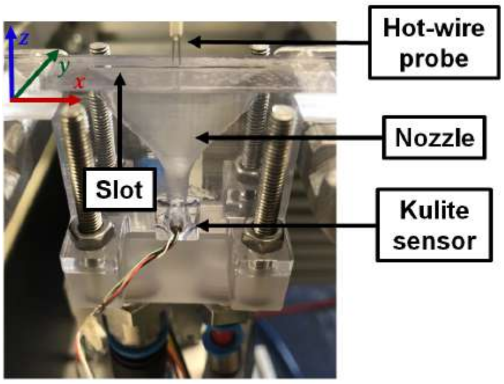

Figure 1: Experimental apparatus for characerization in quiescent environment.

RESULTS

The characterization phase demonstrated the feasibility of alternating blowing and suction using the designed apparatus. In addition, the expected maximum forcing velocity could be reached during the experiments. As a result, the control system is able to produce a wide variety of perturbations. One of the most important aspect is to be able to perform a variation of blowing duty-cycle while keeping a zero net mass actuation. This allows to generate “pseudo-synthetic perturbations”, which aim at injecting more momentum in the flow than classical synthetic jets, while retaining the zero net mass characteristic. They require adjusting the blowing velocity so that both blowing and suction flowrates remain balanced. For low forcing frequencies (Figure 2) the obtained velocity time signals matched the expected square shape and zero net mass criterion. However, an increase of forcing frequency leads to a deformed signal and limits the minimum value of exploitable blowing duty-cycle (Figure 3). This is primarily attributed to velocity transient phenomena, occurring and the beginning and end of both blowing and suction phases, and which durations become non-negligible at higher frequencies. At low blowing duty-cycles, blowing duration becomes too small, preventing both starting and stopping transients to fully exist, leading to blowing velocity being too low to ensure zero net mass actuation. These transient durations were characterized and seen to be mostly dependent on pneumatic ducts geometry (primarily length) and blowing or suction amplitude. The transients also affect synchronization between blowing and suction, which further limit the temporal parameter space of achievable perturbations. During testing, the maximum exploitable forcing frequency was identified to be close to 200 Hz, which is lower than the expected 500 Hz. It is believed that optimizing the ducting geometry of the actuator could lead to an increase of forcing frequency between 250 and 300 Hz. While this could not be tested on the prototype version discussed here, it will be applied on the wind tunnel model.

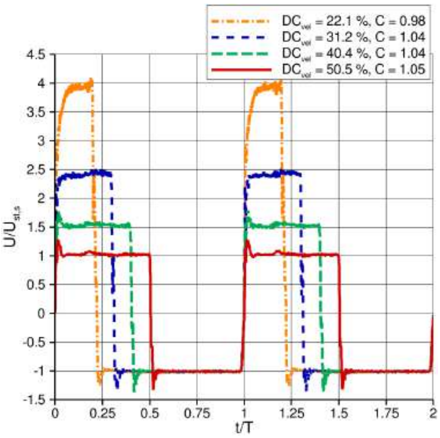

Figure 2: Example of pseudo-synthetic perturbations at a 10 Hz forcing frequency and steady state suction velocity $U_{st,s} = 38.6\ m/s$.

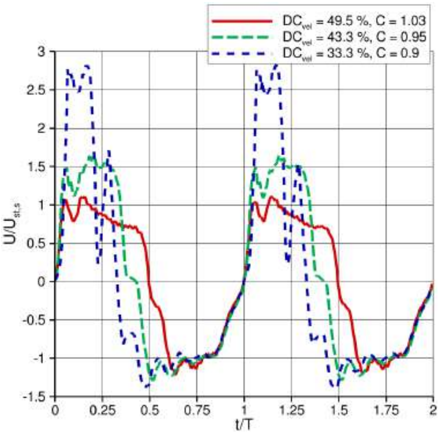

Figure 3: Example of pseudo-synthetic perturbations at a 100 Hz forcing frequency and steady state suction velocity $U_{st,s} = 38.6\ m/s$.

CONCLUSIONS AND OUTLOOKS

The practicability of an active flow control system which allow the generation of perturbations with uncorrelated temporal and amplitude aspects was demonstrated through the generation of artificial synthetic perturbations. They consisted in varying blowing duty-cycle while retaining equal flowrates for suction and blowing. The experimental work highlighted limitations in the range of achievable values of blowing duty-cycle and difficulties in balancing suction and blowing flowrates. The actuation system was further optimized in order to mitigate these limitations and is currently being integrated in a wind tunnel experiment. The flow is a ramp separation of height 30 mm and 25° slant angle controlled using an array of five slots situated upstream of the separation point (Figure 4). A combination of mean and unsteady wall pressure measurements, hotwire velocimetry and PIV will be used in order to assess the efficiency of control strategies based on pseudo-synthetic perturbations. Preliminary results are expected to be presented and discussed during the presentation.

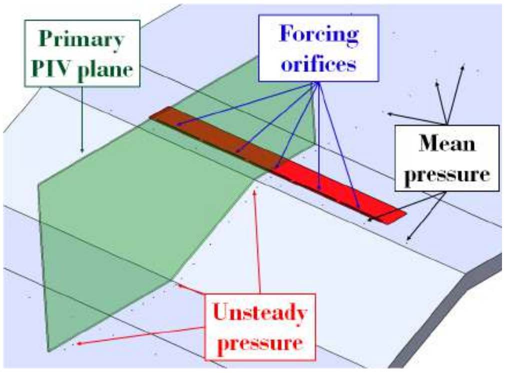

Figure 4: Detail of the wind tunnel experimental apparatus.

REFERENCES

[1] A. Darabi and I. Wygnanski. Active management of naturally separated flow over a solid surface. Part 1. The forced reattachment process. *Journal of Fluid Mechanics*, 510:105–129, July 2004.

[2] Ari Glezer and Michael Amitay. Synthetic Jets. *Annual Review of Fluid Mechanics*, 34(1):503–529, 2002.

[3] David Greenblatt and Israel J. Wygnanski. The control of flow separation by periodic excitation. *Progress in Aerospace Sciences*, 36(7):487–545, October 2000.

[4] Yann Haffner, Jacques Borée, Andreas Spohn, and Thomas Castelain. Unsteady Coanda effect and drag reduction for a turbulent wake. *Journal of Fluid Mechanics*, 899:A36, September 2020.

[5] Jozef Kordík and Zdeněk Trávníček. Non-harmonic excitation of synthetic jet actuators based on electrodynamic transducers. *International Journal of Heat and Fluid Flow*, 73:154–162, October 2018.

[6] Ben Steinfurth and Julien Weiss. Efficiency Enhancement in Active Separation Control Through Optimizing the Duty Cycle of Pulsed Jets. *AIAA Journal*, 60(12):6566–6580, 2022.

[7] Clyde Warsop, Martyn Hucker, Andrew J. Press, and Paul Dawson. Pulsed Air-jet Actuators for Flow Separation Control. *Flow, Turbulence and Combustion*, 78(3):255–281, June 2007.

ERCOFTAC
European Drag Reduction and Flow Control Meeting – EDRFCM 2024
September 10$^{\text{th}}$–13$^{\text{th}}$, 2024, Turin, Italy

AUTOMATIC EXPLORATION OF COST FUNCTION FOR SUBOPTIMAL CONTROL OF TURBULENT FLOW BY MACHINE LEARNING

Y. Yugeta
Department of Mechanical Engineering, The University of Tokyo, 7-3-1 Hongo, Bunkyo-Ku, Tokyo 113-8656, Japan

Y. Hasegawa
Institute of Industrial Science, The University of Tokyo, 4-6-1 Komaba, Meguro-Ku, Tokyo 153-8505, Japan

INTRODUCTION

Wall turbulence is a common phenomenon that can significantly impact the performances of thermo-fluid devices. Consequently, smart control of turbulence is a pivotal aspect of engineering practice, while turbulence control is challenging due to its extensive degrees of freedom, nonlinearity, chaotic nature, and multi-scale characteristics. Thus, it has been extensively studied both experimentally and numerically. Among excisting control algorithms, a few control strategies, albeit at reolaively low Reynolds numbers, have successfully relaminarize wall turbulence. One of such successful examples is the application of the optimal control theory.

Optimal and suboptimal control theory has successfully demonstrated their capability in literature. For instance, Bewley et al. [2] demonstrated that adjoint-based optimal control theory can relaminarize turbulent channel flow, and consequently achieve 60-70% drag reduction. At the same time, their algorithm requires laborious procedures to obtain the optimal control input. In contrast, suboptimal control [6] considers future dynamics of turbulence in a vanishing small time period, and allows to obtain the control input analytically, while its control performance is relatively low compared with the optimal control theory.

Optimal/suboptimal control framework is a powerful methodology, but there remains a big challenge of choosing a proper cost function. For instance, in their suboptimal control framework, Lee et al. [6] observed that setting the square of fluctuation of streamwise shear stress as a cost function did not result in drag reduction. However, setting the spanwise shear stress fluctuation as a cost function achieves comparable drag reduction to that obtained by the opposition control proposed by Choi et al [3]. In optimal control theory, once a cost function to be minimized is given, the control inputs are obtained deterministically. Although scholars generally agree that the performance of optimal control theory can be significantly affected by the setting of the cost function, it has been determined on a trial-and-error basis, and there are no general guidelines on how to set the cost function for a given objective, say, drag reduction.

In this study, we propose a method for determining a cost function for suboptimal control [6] based on genetic programming, a machine-learning method that can deal with mathematical formulas. This allows to automatically optimize the function form of a cost functional. It is shown that the present framework can rediscover the cost functionals proposed in previous studies as well as obtain new cost fnctionals which effectively reduces drag.

NUMERICAL SETUP

In this study, we perform direct numerical simulations (DNSs) of a fully developed turbulent channel flow governed by Navier-Stokes and continuity equations subject to blowing and suction on the top and bottom walls. The flow is assumed to be Newtonian and incompressible. The bulk Reynolds number is set to be $Re_b = 2U_b h/\nu = 3220$, where U_b, h, and ν are the bulk mean velocity, the channel-half height, and the kinematic viscosity of the fluid, respectively. This flow configuration corresponds to the friction Reynolds number of $Re_\tau = u_\tau h/\nu \approx 110$ in the uncontrolled flow, where u_τ is a friction velocity.

The DNSs are carried out with an open-source solver incompact3d[5] with necessary modifications for applying wall blowing and suction. We used a sixth-order compact scheme for spatial discretization. The third-order Adams-bashforth method is employed for time integration of advection terms, while Crank-Nicolson is for viscous terms. The Navier-Stokes equations and continuity equations are coupled by the fractional step method.

The streamwise, wall-normal, and spanwise coordinates are denoted by (x, y, z), while the corresponding velocity components are (u, v, w). The dimension of the computational domain is $L_x \times L_y \times L_z = 4\pi \times 2 \times 4\pi/3$ with computational grids of $N_x \times N_y \times N_z = 128 \times 129 \times 96$. We have confirmed that the present grid resolution reproduces turbulence statistics of the uncontrolled and controlled flows reported in previous literatures.

SUBOPTIMAL CONTROL

In general, a cost function for suboptimal $\mathscr{J}$ can be defined as:

$$\mathscr{J} = \frac{1}{\Delta t}\int_t^{t+\Delta t}\int_{wall}\left(\phi^2(x,z) + \mathcal{F}(x,z)\right)dSdt, \qquad (1)$$

where the spatial integral is computed over the wall, Δt is a vanishingly small time horizon, ϕ is a control input, i.e., wall blowing and suction on the walls in the present study, and $\mathcal{F}$ is a function of a physical quantity, e.g., $\mathcal{F}(x,z) = (\partial u/\partial y(x, y = 0, z))^2$. By taking a Fréchet derivative $\mathscr{D}$ concerning the control input ϕ, one can analytically derive the optimal control input as a stationary condition i.e.,$\mathscr{D}J/\mathscr{D}\phi = 0$. Readers are referred to the literature [6] for details on the derivation process.

In this study, we optimize the functional form of $\mathcal{F}$ with the following symbolic technique so as to maximize the resulting drag reduction. We include five wall measurements as variables in the cost function, i.e. streamwise/spanwise shear stresses, pressure, and its streamwise/spanwise derivatives. In short, $\mathcal{F}$ can be written as $\mathcal{F} \equiv \mathcal{F}(\partial u/\partial y, \partial w/\partial y, p, \partial p/\partial x, \partial p/\partial z)$. The reason for this choice is two-fold.

1. Literature [6] reports a significant drag reduction performance by cost functions with wall measurements ($\mathcal{F} = -(\partial w/\partial y)^2$, and $\mathcal{F} = -(\partial p/\partial z)^2$).
2. Wall shear stress and pressure are relatively easier to measure in practice compared to the velocity or the pressure away from the wall.

GENETIC PROGRAMMING

Genetic programming is a variant of the genetic algorithm, one of the most celebrated black-box optimization techniques. A genetic algorithm prepares multiple individuals represented by corresponding genes as candidates of the optimal solution. These individuals are then subjected to repeated operations, such as crossover and mutation, to explore the search space and identify the optimal solution. Those with higher fitness are more frequently selected for this process, which facilitates the optimization. Genetic programming organizes these genes in a tree structure, enabling it to optimize mathematical expressions and algorithms. For details, readers are referred to literature, for example, by Kochenderfer and Wheeler [1].

In the present study, we employed friction coefficient $-C_f$ averaged over $t^+ \in [600,\ 2400]$ as each individual's fitness. Here, $t = 0$ correponds to the onset of applying a control. All simulations are started from the same uncontrolled flow field. The negative sign is placed in front of C_f to define a quantity to be maximized, while the objective is to reduce the friction drag. Each generation contains 50 individuals(cost functions) and we iterate for ten generations, i.e., we conducted 500 DNSs to optimize the functional shape of $\mathcal{F}$. The fifty equations belonging to the first generation are randomly created.

RESULTS AND DISCUSSIONS

Figure 1 illustrates the present optimization history for ten generations. Starting with 50 random equations, the friction coefficient decreased with each generation, ultimately achieving a very high drag reduction rate of approximately 25%, which is comparable to the literature. This validates the settings and problem formulation for the present genetic programming approach toward the automatic search of the cost function.

The best cost function in terms of drag reduction obtained in the present optimization is given as follows:

$$\mathcal{J} = \frac{1}{\Delta t}\int_t^{t+\Delta t}\int_{wall}\left(\phi^2(x,z) - l\left(\frac{\partial w}{\partial y}\right)^2\right)dSdt, \qquad (2)$$

where l is a positive coefficient. This cost function (2) is the same as that first proposed by the literature [6]. In their work, the cost function was proposed base on careful considerations of turbulent statistics under the opposition control [3], while the present method rediscovers it in a purely data-driven manner.

We also obtain another cost function with a relatively large drag reduction rate of around 10%. It is given by

$$\mathcal{J} = \frac{1}{\Delta t}\int_t^{t+\Delta t}\int_{wall}\left(\phi^2(x,z) - l\frac{\partial u}{\partial y}\frac{\partial w}{\partial y}\right)dSdt, \qquad (3)$$

This is similar to that proposed by Kawagoe et al.[4], where they obtained this cost functional from resolvent analysis.

Finally, we introduce two cost functions which are newly proposed in the present study. The first one achieving a drag reduction rate of around 20% is:

$$\mathcal{J} = \frac{1}{\Delta t}\int_t^{t+\Delta t}\int_{wall}\left(\phi^2(x,z) - l\frac{\partial w}{\partial y}\frac{\partial p}{\partial z}\right)dSdt, \qquad (4)$$

This cost function combines spanwise shear stress and the spanwise pressure gradient, physical quantities that have been reported to reduce drag when used independently, while the present study finds that their combination is also effective. The second one with a drag reduction rate of around 15% is:

$$\mathcal{J} = \frac{1}{\Delta t}\int_t^{t+\Delta t}\int_{wall}\left(\phi^2(x,z) + l\frac{\partial u}{\partial y}\frac{\partial p}{\partial z}\right)dSdt, \qquad (5)$$

in which the spanwise pressure gradient is again used for constructing the control law.

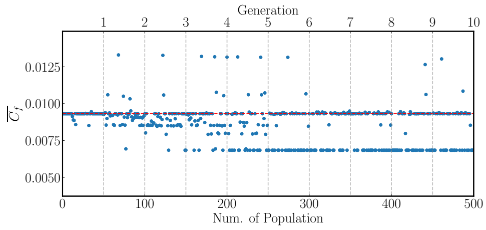

Figure 1: Optimization history of genetic programming. The horizontal axis represents the number of generations. The vertical axis depicts the time-averaged friction coefficient $\overline{C_f}(t^+ \in [600, 2400])$. Each blue dot represents each trial case and the red broken line is for the uncontrolled case.

SUMMARY

We propose a novel method for the development of a new flow control method via the automatic exploration of a cost function for optimal control. The upcoming presentation will be devoted to a comprehensive analysis of the optimization outcomes.

REFERENCES

[1] 20 Expression Optimization. In *Algorithms for optimization*. MIT Press, 2019.

[2] Thomas R. Bewley, Parviz Moin, and Roger Temam. *Journal of Fluid Mechanics*, 447:179–225, 2001.

[3] Haecheon Choi, Parviz Moin, and John Kim. *Journal of Fluid Mechanics*, 262:75–110, October 1994.

[4] Aika Kawagoe, Satoshi Nakashima, Mitul Luhar, and Koji Fukagata. *Journal of Fluid Mechanics*, 866:810–840, May 2019.

[5] Sylvain Laizet and Ning Li. *International Journal for Numerical Methods in Fluids*, 67(11):1735–1757, 2011.

[6] Changhoon Lee, John Kim, and Haecheon Choi. *Journal of Fluid Mechanics*, 358:245–258, March 1998.

26

ERCOFTAC
European Drag Reduction and Flow Control Meeting – EDRFCM 2024
September 10$^{\text{th}}$–13$^{\text{th}}$, 2024, Turin, Italy

ACTIVE FLOW CONTROL OF DRAG REDUCTION USING DATA-ENABLED PREDICTIVE CONTROL

C. Xia
Department of Aeronautics, Imperial College London, SW7 2AZ London, UK

E. C. Kerrigan
Department of Electrical and Electronic Engineering, and Department of Aeronautics, Imperial College London, SW7 2AZ London, UK

G. Rigas
Department of Aeronautics, Imperial College London, SW7 2AZ London, UK

INTRODUCTION

This work applies, for the first time, Data-enabled Predictive Control (DeePC) [2] to an active closed-loop flow control problem. The control objective is to improve the aerodynamic performance of a bluff body via drag reduction. DeePC implements a sample efficient model-free control procedure based on Willems' fundamental lemma [8] and Predictive Control [7]. Compared to other model-free optimal trajectory tracking control methods, such as Reinforcement Learning, DeePC requires fewer data samples and more interpretable hyperparameters. It also demonstrates advantages compared to system identification as it is independent of a parametric representation of the system and conveniently tackles partial observations with constraint satisfaction [2]. The technique of DeePC has been applied to various control tasks [4, 3], with several instantiations [1, 5], but awaiting explorations in flow control applications. This work applies DeePC on the flow past a two-dimensional rectangular body at $Re = 100$ via vortex shedding stabilization. The controller achieves on average 7.6% drag reduction compared with the uncontrolled scenario (51.4% with respect to the maximum drag reduction), using a minimal number of samples from the input-output time series.

METHODOLOGY

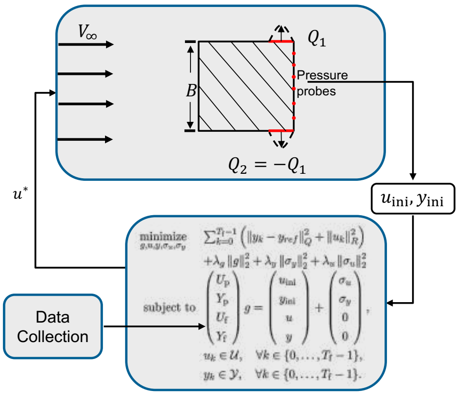

Figure 1: The DeePC active flow control framework.

DeePC is developed based on Willems' fundamental lemma [8], which states that if a controllable linear time-invariant system is persistently excited [8, 6], then all trajectories of this system can be obtained by linear combinations of the input and output signals. To implement DeePC in flow control tasks, Hankel matrices need to be built from the input/output data of the flow system. Usually, DeePC applies a sequence of random (Gaussian) inputs (with dimension m) of length T, as $u^{\text{d}} = \text{col}\left(u_1^{\text{d}}, \dots, u_T^{\text{d}}\right) \in \mathbb{R}^{Tm}$, to excite the flow system, yielding a sequence of outputs (with dimension p) $y^{\text{d}} = \text{col}\left(y_1^{\text{d}}, \dots, y_T^{\text{d}}\right) \in \mathbb{R}^{Tp}$. The Hankel matrices can be then formed as

$$\mathscr{H}(u^{\text{d}}) := \begin{pmatrix} u_1^{\text{d}} & u_2^{\text{d}} & \cdots & u_{T-T_{ini}-T_f+1}^{\text{d}} \\ u_2^{\text{d}} & u_3^{\text{d}} & \cdots & u_{T-T_{ini}-T_f+2}^{\text{d}} \\ \vdots & \vdots & \ddots & \vdots \\ u_{T_{ini}}^{\text{d}} & u_{T_{ini}+1}^{\text{d}} & \cdots & u_{T-T_f}^{\text{d}} \\ \vdots & \vdots & \ddots & \vdots \\ u_{T_{ini}+T_f}^{\text{d}} & u_{T_{ini}+T_f+1}^{\text{d}} & \cdots & u_T^{\text{d}} \end{pmatrix} := \begin{pmatrix} U_{\text{p}} \\ U_{\text{f}} \end{pmatrix}, \tag{1}$$

where the Hankel matrix $\mathscr{H}(u^{\text{d}})$ is split in to $U_p \in \mathbb{R}^{T_{ini}m \times (T-T_{ini}-T_f+1)m}$ and $U_f \in \mathbb{R}^{T_f m \times (T-T_{ini}-T_f+1)m}$ by two hyperparameters T_{ini} and T_f. The same formulation is applied to y^{d}, as $\mathscr{H}(y^d) := \begin{pmatrix} Y_{\text{p}} \\ Y_{\text{f}} \end{pmatrix}$.

With Hankel matrices $\mathscr{H}(u^{\text{d}})$ and $\mathscr{H}(y^{\text{d}})$, DeePC solves the following optimization problem in a discrete form, as

$$\begin{aligned} \underset{g,u,y,\sigma_u,\sigma_y}{\text{minimize}} \quad & \textstyle\sum_{k=0}^{T_{\text{f}}-1} \left(\|y_k - y_{ref}\|_Q^2 + \|u_k\|_R^2 \right) \\ & +\lambda_g \|g\|_2^2 + \lambda_y \|\sigma_y\|_2^2 + \lambda_u \|\sigma_u\|_2^2 \\ \text{subject to} \quad & \begin{pmatrix} U_{\text{p}} \\ Y_{\text{p}} \\ U_{\text{f}} \\ Y_{\text{f}} \end{pmatrix} g = \begin{pmatrix} u_{\text{ini}} \\ y_{\text{ini}} \\ u \\ y \end{pmatrix} + \begin{pmatrix} \sigma_u \\ \sigma_y \\ 0 \\ 0 \end{pmatrix}, \\ & u_k \in \mathcal{U}, \quad \forall k \in \{0, \dots, T_{\text{f}} - 1\}, \\ & y_k \in \mathcal{Y}, \quad \forall k \in \{0, \dots, T_{\text{f}} - 1\}, \end{aligned} \tag{2}$$

where y_k and u_k are the input-output pairs at the k^{th} step. λ_g, λ_y and λ_u are regularize parameters. σ_u and σ_y are slack variables to avoid infeasible equality constraints. u_{ini} and y_{ini}

are input-output data currently collected from the system. $\mathcal{U}$ and $\mathcal{Y}$ are the other constraint sets of inputs and outputs.

Figure 1 presents the complete framework of the DeePC active flow control technique. The flow system is a two-dimensional simulation of a uniform flow past a rectangular bluff body at $Re = 100$. 64 pressure sensors are spatial-equally placed on the downstream surface of the body and measurement y is defined as $y = \langle pres \rangle_{top} - \langle pres \rangle_{bottom}$, which represents an anti-symmetric pressure component in the vertical direction, and serves as a proxy of the vortex shedding intensity. The reference y_{ref} in Eq. 2 is set to 0 as drag reduction can be achieved by minimizing the anti-symmetric pressure fluctuation. The mass flow rate of the top jet Q_1 is chosen as control action u, and the bottom jet satisfies zero mass flow condition $Q_2 = -Q_1$. The control action and measurements are sampled every 0.5 non-dimensional time units.

In implementing DeePC, the data collection step is first conducted to obtain Hankel matrices as Eq. 1. Then, for each control loop, u_{ini} and y_{ini} are collected as initial data, and the optimization in Eq. 2 is solved to predict an optimized u^* for the next control step. The flow system will evolve under the control of u^* and generate new u_{ini} and y_{ini}, then Eq. 2 is solved again.

RESULTS

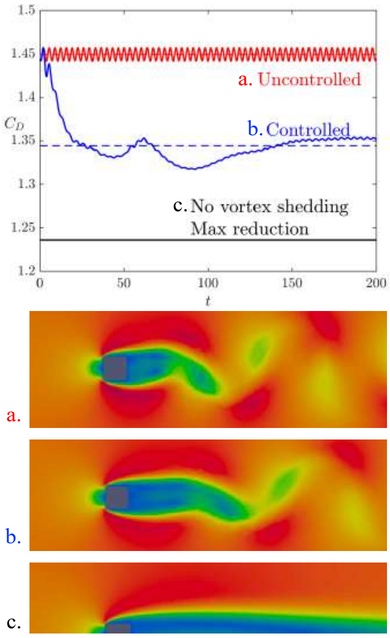

Figure 2: The top figure presents the time series (solid lines) and the time-averaged value of non-dimensional time $t \in [100, 200]$ (dashed lines) of drag coefficient C_D in three cases: a. Uncontrolled case with steady vortex shedding; b. Controlled case with DeePC; c. Flow without vortex shedding from a symmetric simulation. The bottom contours present the field of velocity magnitude of these three cases.

Figure 2 presents both the curves of drag coefficient C_D and contours of velocity magnitude for “Uncontrolled”, “Controlled” and “No vortex shedding” cases. In the “Controlled” case, DeePC is used to optimize the control action for each step and about 50% drag reduction on average is achieved with respect to the “No vortex shedding” case. The stabilization of vortex shedding and the lengthening of the recirculation area in the “Controlled” case can be both observed from the velocity contours, compared with the “Uncontrolled” scenario.

T	T_{ini}	T_f	λ_g	λ_u	λ_y
1000	150	150	1	10	500

Table 1: Hyperparameters of Eq.2 used in the controlled case. The values of T, T_{ini} and T_f correspond to lengths of data samples.

Table 1 lists the main hyperparameters used in the DeePC controller. Although these parameters have not been optimized and were tuned using trial-and-error with minimal effort, DeePC demonstrates efficacy in attenuating vortex shedding and reducing drag on the bluff body. Additionally, the primary computational requirement before control involves collecting $T = 1000$ input-output pairs. For comparison, other model-free control techniques such as Reinforcement Learning [9] usually require on the order of $O(10^5)$ input-output data to achieve a comparable level of performance.

CONCLUSIONS

This work employs DeePC for the first time in an active flow control problem aimed at drag reduction. A canonical flow past a two-dimensional rectangular bluff body has been regularized within the closed-loop system, where the DeePC controller successfully achieved 7.6% drag reduction with sample efficiency and minimal design effort. Further drag reduction could be realized by selecting different input-output pairs, redesigning the cost function and constraints or finer parameter tuning in the optimization problem.

REFERENCES

[1] J. Coulson, J. Lygeros, and F. Dorfler. *IEEE Transactions on Automatic Control*, 2021.

[2] J. Coulson, J. Lygeros, and F. Dörfler. In *2019 18th European Control Conference (ECC)*, pages 307–312. IEEE, 2019.

[3] E. Elokda, J. Coulson, P. N. Beuchat, J. Lygeros, and F. Dörfler. *International Journal of Robust and Nonlinear Control*, 31(18):8916–8936, 2021.

[4] L. Huang, J. Coulson, J. Lygeros, and F. Dörfler. In *2019 IEEE 58th Conference on Decision and Control (CDC)*, pages 8130–8135. IEEE, 2019.

[5] E. O’Dwyer, E. C. Kerrigan, P. Falugi, M. Zagorowska, and N. Shah. *IEEE Transactions on Control Systems Technology*, 31(3):1355–1365, 2023.

[6] C. De Persis and P. Tesi. In *2019 IEEE 58th Conference on Decision and Control (CDC)*, pages 873–878, 2019.

[7] J. Rawlings and D. Q. Mayne. Nob Hill Publishing, 2009.

[8] J. C. Willems, P. Rapisarda, I. Markovsky, and B. L. M. De Moor. *Systems & Control Letters*, 54(4):325–329, 2005.

[9] C. Xia, J. Zhang, E. C. Kerrigan, and G. Rigas. *Journal of Fluid Mechanics*, 981:A17, 2024.

27

ERCOFTAC
European Drag Reduction and Flow Control Meeting – EDRFCM 2024
September 10$^{\text{th}}$–13$^{\text{th}}$, 2024, Turin, Italy

MULTI-AGENT REINFORCEMENT-LEARNING CONTROL FOR A 3D CYLINDER AT $Re_D = 3900$

Pol Suárez, Fran Alcántara-Ávila
FLOW, Engineering Mechanics, KTH Royal Institute of Technology, Stockholm, Sweden

Jean Rabault
Independent researcher, Oslo, Norway

Arnau Miró
Turbulence and Aerodynamics Research Group (TUAREG), Universitat Politècnica de Catalunya (UPC), Terrassa, Spain

Bernat Font
Faculty of Mechanical Engineering, Technische Universiteit Delft, The Netherlands

Oriol Lehmkuhl
Barcelona Supercomputing Center (BSC-CNS), Barcelona, Spain

Ricardo Vinuesa
FLOW, Engineering Mechanics, KTH Royal Institute of Technology, Stockholm, Sweden

ABSTRACT

This study introduces new active-flow-control (AFC) strategies to reduce drag on a three-dimensional cylinder at a Reynolds number of $Re_D = 3900$. Using deep reinforcement learning, the cylinder, with 10 independent zero-net-mass-flux jet pairs on its top and bottom, is analyzed. The approach couples a computational-fluid-dynamics solver with a multi-agent reinforcement-learning (MARL) framework using proximal-policy-optimization. Leveraging MARL, 8% drag reduction was achieved with a mass cost two orders of magnitude lower than that of the classic method under study in this work. This advancement significantly enhances AFC in turbulent-flow regimes, which is a crucial area for industrial applications.

INTRODUCTION

Deep reinforcement learning (DRL) is effective in optimizing tasks where a controller interacts with an environment, making it ideal for many AFC scenarios. It dynamically interacts with the flow, refining action policies iteratively. The state-of-the-art on DRL for AFC applications is rapidly expanding for two-dimensional (2D) cylinders across a range of Re_D [4, 9], turbulent flows and channels [1, 2], transfer learning from 2D to three-dimensional (3D) domains [8]. Recent advancements involve DRL training directly in 3D, addressing Reynolds numbers that include transitions to three-dimensional wake instabilities, $Re_D = 100$ to 400, using MARL framework [6]. The present work constitutes the continuation of such study, challenging the training at $Re_D = 3900$. Kim & Choi (2005) [3] studied flow-control strategies for a 3D cylinder at $Re_D = 3900$, achieving 18% drag reduction with out-phase control, using sinusoidal profiles in the spanwise direction and constant blowing and suction. For their out-of-phase control, which has opposed blowing and suction on the top and bottom, we will use this setup as our controlled reference, denoting it as KC05.

METHODOLOGY

Developing flow-control strategies for fully turbulent 3D wakes around cylinders is a significant challenge for DRL. MARL setup must leverage spanwise structures to devise efficient control methods for drag reduction. We refer to Ref. [7] for recent advances in MARL-based flow control. The 3D cylinder is subjected to a constant streamwise velocity at the inlet of U_∞. The computational domain, has dimensions $(L_x/D, L_y/D, L_z/D) = (40, 25, \pi)$ with the cylinder centered at $(x/D, y/D) = (12.5, 6.25)$, where x, y, and z are the streamwise, vertical, and spanwise directions. The surfaces of the cylinder include the no-slip and no-penetration conditions. The top, bottom, and outflow surfaces of the domain box are set as zero-stress outlets. The cylinder incorporates two sets of $n_{\text{jet}} = 10$ synthetic jets positioned at the top and bottom surfaces ($\theta_0 = 90°$ or $270°$). Hence, the jet length is $L_{\text{jet}}/D \simeq 0.314$. For further details of the DRL setup, we refer to Ref. [6, 5]. The agent uses Tensorforce libraries, using the proximal-policy-optimization (PPO) algorithm, which is a policy-gradient approach based on a surrogate loss function for policy updates. The agent contains an actor-critic architecture of two hidden layers of 512 neurons. We define a streamed experience as a combination of states, actions, rewards, and the predicted next state that the agent computes, $(S, A, R, S')_{i,t}$, for each MARL environment. These streamed experiences are formed by: an action A that only controls the mass-flow rate Q; A partial observation S of 3 slices in xy-plane of 99 pressure probes and a reward, R, that focuses on the pure local drag reduction but with a lift penalty $\alpha = 0.6$ to avoid axis-switching strategies and $\beta = 0.8$ to balance the global reward:

$$R(t, i_{\text{jet}}) = K_r \left[\beta r^{\text{local}}(t, i_{\text{jet}}) + (1-\beta) r^{\text{global}}(t)\right], \quad (1)$$

$$r(t, i_{\text{jet}}) = \overline{C_{d_{\text{b}}}} - C_d(t, i_{\text{jet}}) - \alpha |C_l(t, i_{\text{jet}})|. \quad (2)$$

On the other hand, numerical simulations in computational fluid dynamics (CFD) environments are carried out by the Alya solver. A finite-element method (FEM) spatial discretization to solve direct Navier-Stokes equations. In earlier research focused on 2D cylinders, the various trainings were conducted using a single-agent reinforcement learning (SARL) setup. However, SARL is not feasible for distributed-input distributed-output (DIDO) schemes given some unsuccessful attempts of SARL in 3D contexts and given the demonstrated effectiveness of MARL in coordinating multiple actuators concurrently and training speedup. MARL takes advantage of local invariants to maximize a global reward.

RESULTS

After over 800 MARL-environment episodes, the training session concludes with a converged positive reward. The DRL-based control policy (DRL-10), deployed in deterministic mode, significantly outperforms the KC05 strategy by a factor of two orders of magnitude in terms of the ratio of mass cost per $\Delta\overline{C_d}$. However, considering the pure drag reduction ΔC_d, KC05 performs better with a reduction of -14.7% compared to -8.3% in the DRL-10. It is important to note that KC05 is significantly more invasive in the wake topology, exhibiting this peak of constant blowing or suction at $z = L_z/4$ and $3L_z/4$. As shown in Figure 1, the DRL-based control strategy unveils effective drag-reduction techniques by exploiting spanwise instabilities. These findings underscore the powerful capability of the DRL approach in identifying sophisticated flow-control strategies that surpass those derived from classical control methods. The DRL method involves a broad spectrum of possible frequencies for control (not shown here), addressing various flow-structure wavelengths observed in the wake. Moreover, when comparing the mass-flow rate spectra between $Re_D = 400$ [6] and the present $Re_D = 3900$ involves higher frequencies and richer control. More instabilities can be captured and exploited in the turbulent wake as the Reynolds number increases. In Figure 2 it can be observed that both control methods lead to an enlargement of the recirculation bubble, indicated by the yellow-colored areas where $|\overline{u}| < 0.03$. Analyzing the Reynolds stresses (not shown here), we notice a similar pattern in both the DRL-10 and KC05 scenarios. The maximum stresses are reduced by approximately 50%, and their positions shift backwards by $\approx 1D$. This behavior aligns with observed drag-reduction mechanisms typically present at lower Reynolds numbers [6]. A key advantage of MARL lies in its capacity to deploy trained agents across cylinders of different lengths and with varying numbers of actuators while maintaining consistency in the spanwise width of the jets and their corresponding pressure values as observation states. Notably, MARL training focuses on symmetries and invariant structures, a feat unattainable with SARL due to its inherent limitations. MARL facilitates cost-effective training in smaller, simplified computational domains, thus expediting the flow-control process in high-fidelity simulations. For extended details about the present $Re_D = 3900$ case we refer to Ref. [5].

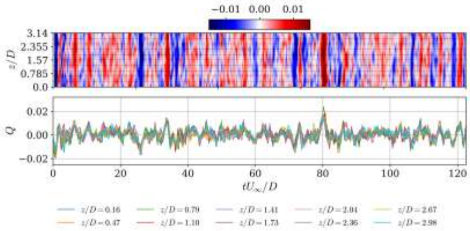

Figure 1: Mass-flow rate per unit width Q as a function of time for all jets for DRL-10 case, showing (top) spatial distribution over z/D and (bottom) individual evolutions of the various jets.

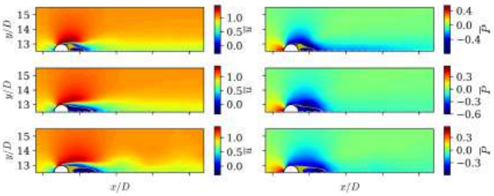

Figure 2: Time and spanwise averaged streamwise velocity field, $\overline{u}$ and pressure $\overline{p}$ fields for (top) uncontrolled, (middle) DRL-10 and (bottom) KC05. Yellow regions denote wake-stagnation points where $|\overline{u}| < 0.03$.

REFERENCES

[1] B. Font, F. Alcántara-Ávila, J. Rabault, R. Vinuesa, and O. Lehmkuhl. Active flow control of a turbulent separation bubble through deep reinforcement learning. *Journal of Physics: Conference Series*, 2753(1):012022, 2024.

[2] L. Guastoni, J. Rabault, P. Schlatter, H. Azizpour, and R. Vinuesa. Deep reinforcement learning for turbulent drag reduction in channel flows. *European Physical Journal E*, 46(4):27, 2023.

[3] J. Kim and H. Choi. Distributed forcing of flow over a circular cylinder. *Physics of Fluids*, 17(3):033103, 02 2005.

[4] F. Ren, J. Rabault, and H. Tang. Applying deep reinforcement learning to active flow control in weakly turbulent conditions. *Physics of Fluids*, 33(3), 2021.

[5] P. Suárez, F. Alcántara-Ávila, A. Miró, J. Rabault, B. Font, O. Lehmkuhl, and R. Vinuesa. Active flow control for drag reduction through multi-agent reinforcement learning on a turbulent cylinder at $Re_D = 3900$. *Preprint arXiv:2405.17655*, 2024.

[6] P. Suárez, F. Alcántara-Ávila, A. Miró, J. Rabault, B. Font, O. Lehmkuhl, and R. Vinuesa. Flow control of three-dimensional cylinders transitioning to turbulence via multi-agent reinforcement learning. *Preprint arXiv:2405.17210*, 2024.

[7] C. Vignon, J. Rabault, and R. Vinuesa. Recent advances in applying deep reinforcement learning for flow control: Perspectives and future directions. *Physics of Fluids*, 35(3), 2023.

[8] Z. Wang, D. Fan, X. Jiang, M. S. Triantafyllou, and G.E. Karniadakis. Deep reinforcement transfer learning of active control for bluff body flows at high reynolds number. *Journal of Fluid Mechanics*, 973:A32, 2023.

[9] L. Yan, Y. Li, G. Hu, W. Chen, W. Zhong, and B. R. Noack. Stabilizing the square cylinder wake using deep reinforcement learning for different jet locations. *Physics of Fluids*, 35(11):115104, 11 2023.

ERCOFTAC
European Drag Reduction and Flow Control Meeting – EDRFCM 2024
September 10$^{\mathrm{th}}$–13$^{\mathrm{th}}$, 2024, Turin, Italy

LSTM-BASED PREDICTIVE MODELLING FOR ACTIVE FLOW CONTROL OF A WAKE

A. Solera-Rico
Department of Aerospace Engineering, Universidad Carlos III de Madrid, 28911 Leganés, Spain
Sub-Directorate General of Terrestrial Systems, Spanish National Institute of Aerospace Technology (INTA), 28330, San Martin de la Vega, Spain

C. Sanmiguel Vila
Department of Aerospace Engineering, Universidad Carlos III de Madrid, 28911 Leganés, Spain
Sub-Directorate General of Terrestrial Systems, Spanish National Institute of Aerospace Technology (INTA), 28330, San Martin de la Vega, Spain

S. Discetti
Department of Aerospace Engineering, Universidad Carlos III de Madrid, 28911 Leganés, Spain

INTRODUCTION

Machine learning methods for active flow control hold significant promise in reducing aerodynamic drag across various applications [5]. To facilitate real-time operations, these algorithms must maintain a low computational cost. Achieving this balance necessitates a sufficiently compact representation in a low-dimensional space, which could be the key to optimising the compromise between prediction capability and computational efficiency. This low-dimensional space can be learned from the full flow information, as in [3], or directly obtained by a handful of sensors used as inputs [1]. In this study, we explore the use of feasible data-driven models in an optimised sensors space for active flow control in a simplified 2D truck model operating at a Reynolds number of 500.

We aim to develop a predictive, recursive model capable of predicting aerodynamic forces using as input a series of past sensor and control values. During training, we force an optimal sensor placement strategy (OSP), which seeks a balance between prediction capability and reduced number of sensors. Unlike most previous work, we only use sensors in the vehicle surface, rather than in the wake, to obtain a feasible framework that could be implemented in an experiment.

We adopt a two-step methodology to streamline the training process and improve learning efficiency, instead of relying on traditional approaches with online training. First, we generate a comprehensive dataset through random open-loop actuation sequences. This dataset is used to develop a data-driven model that predicts the relationship between pressure sensor readings, control actions and the resulting drag coefficient. This model provides a much faster environment model for offline training of control policies (for instance with reinforcement learning, RL), significantly reducing computational cost and time [1, 5]. Our results indicate that this approach, combining OSP and offline RL training, could enable significant drag reduction while maintaining computational efficiency.

Our study presents a framework for active flow control that integrates advanced sensor placement techniques and leverages offline RL training. This approach offers practical implications for real-world applications, potentially leading to significant improvements in vehicle design and performance.

METHODOLOGY

The flow environment is a 2-D direct numerical simulation (DNS) of the flow past a mid-height horizontal section of the truck model in [4], which is a rectangular bluff body of width W and length $L = 7.647W$ with rounded leading edges. The inflow velocity profile is uniform with velocity U_∞. The Reynolds number, defined as $Re = U_\infty W \nu$, is 500. The computational domain is rectangular with boundaries at (-7D, 23D) in the streamwise x direction and (-7.5D, 7.5D) in the transverse y direction. The front of the bluff body is at $x = 0$. The flow is simulated using Openfoam and the GymPrecice environment [2] as a connector with Python code. The incompressible unsteady Navier-Stokes equations are solved using a finite volume method and a hybrid mesh with a structured sub-mesh near the obstacle wall and an unstructured mesh in the far field, the mesh is shown in Figure 1.

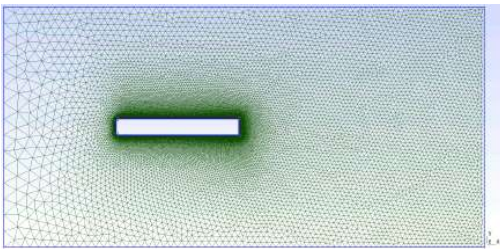

Figure 1: Mesh used for OpenFOAM simulation.

Two blowing and suction jets are placed at the two extremes of the back of the bluff body, with width $W_j = 0.05W$. The velocity profile U_j of the two jets is parabolic, with a mean jet maximum velocity of $\pm U_\infty$. A zero net mass flow condition of the two jets enforces momentum conservation, and the control action is linearly smoothed between control updates to maintain continuity. An example of the velocity field in the vicinity of the actuators is shown in Figure 2. Surface pressure measurements are defined as 25 equally spaced pressure sensors placed on the side and rear surfaces of the bluff body as shown in Figure 3.

The dataset is built by simulating 10000 convective times

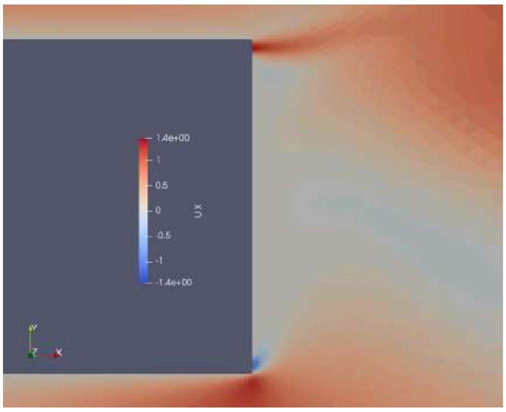

Figure 2: Velocity distribution near the jet actuators in the back surface of the obstacle.

($t_c = W/U_\infty$) with random control inputs, updated at each convective time. The pressure measurements, control actions and drag coefficient are logged to train the surrogate model. The model is based on LSTM networks and uses the previous 8 sensors and control inputs to predict the next sensors and C_D point. The last 1000 points are reserved as test data to verify generalisation.

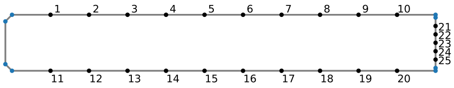

Figure 3: Schematic of sensors distribution over the vehicle.

RESULTS

Having been trained to predict only the next time step, the model can be applied recursively, starting from a true point, to propagate the prediction of the drag coefficient arbitrarily forward in time. Figure 4 shows an example of the prediction compared to true test data.

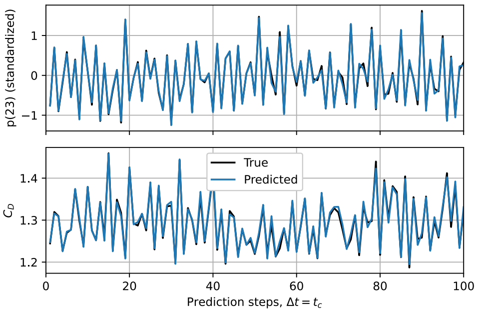

Figure 4: Sample predicted time series for one of the sensors ($p_{location_{23}}$) and C_d. Seed initial sequence not shown.

Figure 5 shows the average prediction error over all 100 time step length windows in the test data. It shows the averaged growth trend of the error over the prediction horizon, highlighting the small error obtained for prediction horizons up to 100 convective times. This prediction horizon is considered sufficient to train RL controllers or to use the model in a model predictive control framework, for example.

Once the dataset has been built and the model trained, it can be run at very low computational cost, enabling its use in real-time closed-loop predictive control applications and reducing the cost of training reinforcement learning agents. The more appropriate model has the potential to learn the underlying physics in a more sample-efficient manner than standard reinforcement learning algorithms, justifying the extra effort by reducing the expensive computational simulation time required to build the final controller.

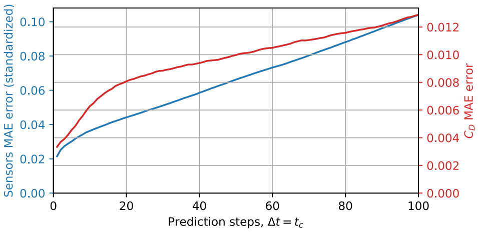

Figure 5: Averaged prediction error for sensors and drag coefficient.

ACKNOWLEDGEMENTS

This activity is part of the project ACCREDITATION (Grant No TED2021-131453B-I00), funded by MCIN/AEI/ 10.13039/501100011033 and by the European Union "NextGenerationEU/PRTR".

REFERENCES

[1] T. Déda, W. Wolf, and S. Dawson. Neural networks in feedback for flow analysis, sensor placement and control. *arXiv preprint arXiv:2308.13029*, 2023.

[2] M. Shams and A. H. Elsheikh. Gym-precice: Reinforcement learning environments for active flow control. *SoftwareX*, 23:101446, 2023.

[3] A. Solera-Rico, C. Sanmiguel Vila, M. Gómez-López, Y. Wang, A. Almashjary, S.T. Dawson, and R. Vinuesa. β-variational autoencoders and transformers for reduced-order modelling of fluid flows. *Nature Communications*, 15(1):1361, 2024.

[4] Bruce L. Storms, James C. Ross, James T. Heineck, Stephen M. Walker, David M. Driver, Gregory G. Zilliac, and Daniel P. Bencze. An experimental study of the ground transportation system (gts) model in the nasa ames 7- by 10-ft wind tunnel. Technical Memorandum NASA/TM-2001-209621, NASA Ames Research Center, 2001.

[5] Chengwei Xia, Junjie Zhang, Eric C Kerrigan, and Georgios Rigas. Active flow control for bluff body drag reduction using reinforcement learning with partial measurements. *Journal of Fluid Mechanics*, 981:A17, 2024.

 # 29

ERCOFTAC
European Drag Reduction and Flow Control Meeting – EDRFCM 2024
September 10^{th}–13^{th}, 2024, Turin, Italy

DRAG REDUCTION WITH SELF-TUNING MODEL PREDICTIVE CONTROL

L. Marra
Department of Aerospace Engineering, Universidad Carlos III de Madrid, 28914 Leganés, Spain

A. Meilán-Vila
Department of Statistics, Universidad Carlos III de Madrid, 28911 Leganés, Spain

S. Discetti
Department of Aerospace Engineering, Universidad Carlos III de Madrid, 28914 Leganés, Spain

INTRODUCTION

Model-based techniques have recently gained remarkable interest for controlling complex dynamics. Model Predictive Control (MPC) has demonstrated excellent capability in constrained highly non-linear models which are difficult to handle with traditional linear control systems. The term MPC designates a large class of control methods based on the use of a model of the system to predict future behavior and identify optimal control inputs over a recurrently shifting horizon (hence the term *receding horizon*). MPC is based on: observation of the state of the system; prediction through a model of the behavior of the system within a certain horizon; selection of the control sequence which optimizes the system behavior according to a certain cost function; advancing the system only for a short time horizon; iterating the process for the next steps.

The main advantages of MPC include, among others, straightforward implementation on constraints on state and actions, capability to handle multiple inputs/outputs (thus allowing the development of coordinated strategies), and high robustness thanks to the continuous update of the state. The main weak points reside in the technological implementation, which require fast optimization *on the fly*, identification of the plant model, and selection of the hyperparameters involved in the optimization process (state and actuation penalties, soft constraints, etc.). In this contribution, we concentrate on the last two aspects. This work aims to present a noise-robust self-tuning control framework for wake flows based on MPC and characterized by minimal user interaction.

In this work, we present a self-tunable implementation of MPC for wake flow control. Key elements of the implementation are the minimal user intervention in both plant model definition and control, and automatic adjustment to noise and control authority through Bayesian optimization. We propose an automated architecture, which self-tunes the parameters for the optimization process, and adapts to different noise conditions and/or limited state knowledge. We build upon three main pillars: identification of a compact model, discovered from system input-output data and a sparse identification of nonlinear dynamics (SINDy), following the MPC implementation of [2]; a black-box optimization via Bayesian methods [6] for hyperparameter tuning; reduction of noise effects using a local polynomial regression [LPR, 5].

METHODOLOGY

The presented application is the control of the two-dimensional viscous incompressible flow around a three-cylinder configuration, commonly referred to as fluidic pinball [1]. The three cylinders have identical diameters D. Their centers form an equilateral triangle of side $3D/2$, and are symmetrically positioned with respect to the direction of the main flow, with the leftmost vertex pointing upstream. The pinball is invested by a flow with constant uniform velocity U_∞. We denote the front, top, and bottom cylinders respectively with $1, 2, 3$. The cylinders can rotate independently with tangential velocity b^1, b^2, and b^3, respectively (with positive values for counterclockwise rotation). The three rotations are stacked into the input vector $\mathbf{b}$. The flow is solved with the two-dimensional direct numerical simulation (DNS) code [4]. The reference system is centered in the mid-point of the two downstream cylinders. The streamwise and crosswise directions are indicated respectively with x and y. The computational domain spans $(-5, 20)D \times (-5, 5)D$.

The velocity vector is $\mathbf{u} = (u, v)$. The Reynolds number is defined as $Re_D = \frac{U_\infty D}{\nu}$ (with ν being the kinematic viscosity) and set equal to $Re_D = 150$, i.e. in the chaotic regime [1]. The timescale based on the freestream velocity and the cylinder diameter is set as reference convective unit *c.u.*. The lift and drag coefficients, C_l and C_d, are obtained by normalization of the lift and drag forces with the dynamic pressure based on the density ρ and U_∞.

The objective of the control is to minimize the drag by actively tuning the rotation rate of the three cylinders. The compact model discovered by the SINDy method and used to make an online prediction is based on a state vector that includes the aerodynamic drag (C_d) and lift (C_l) coefficients, their corresponding derivatives with respect to time, and takes cylinder rotation rates b_i into account. Polynomial functions up to the second order are used. The cost function for the MPC (and its analogous one for the hyperparameter tuning with the Bayesian optimization) includes the drag coefficient reduction concerning the unperturbed wake, the variance of the lift coefficient, and terms accounting for the power input and the variability of the input over time. The reader is referred to the work by Marra et al. [3] for the complete formulation. The optimization method is a sequential quadratic programming with constraints, based on a built-in function of MATLAB. The stop criteria are set at a maximum number of iterations of 500 and a step tolerance of $1e{-6}$.

RESULTS

Figure 1 shows the results of the MPC with and without the hyperparameter tuning, at different measurement noise levels

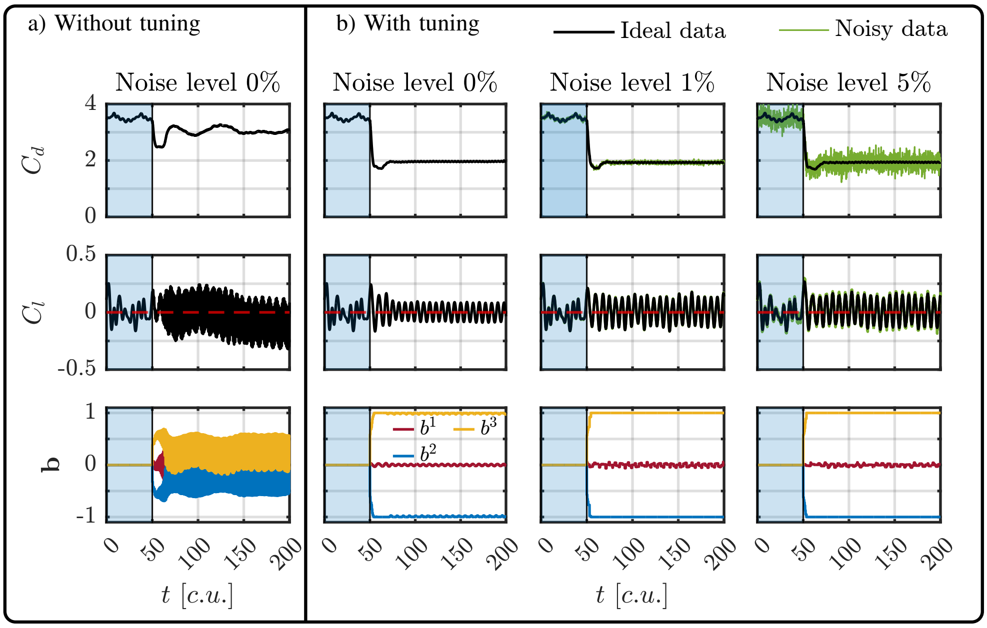

Figure 1: Time series of aerodynamic force coefficients C_d, C_l and exogenous input b^i (top to bottom row, respectively). The panels in a) show the results with all hyperparameters set to 1 (expect for the prediction control window, set to $3c.u.$). The panels in b) show the results with hyperparameter tuning and at different noise levels. LPR is used in all cases with measurement noise. Figure from [3].

(measured as the normalized standard deviation of C_d and C_l). For the baseline without tuning, all the hyperparameters are manually selected to unity, except the prediction/control window set to $3c.u.$. The control without hyperparameter tuning shows a set of undesirable features, such as large oscillations of the actuation, possibly due to insufficient penalization of the input variability. After hyperparameter tuning, the penalty weight of actuation (and actuation variability) on the rear cylinders is reduced. This allows a more vigorous boat tailing effect, which is known to drive the pinball towards wake stabilization (although not achievable here due to the hard constraints imposed on the actuation).

For data without noise, it is clear that the hyperparameter tuning can reach better performances, with lower oscillations of the C_l and an overall lower C_d. The results also show that MPC with online LPR maintains good control performances with state measures affected by noise. The rear cylinders consistently push towards saturation of the constraints to promote boat tailing. On the other hand, the lift coefficient seems to be more sensitive to measurement noise. The system finally converges on a limit cycle with slightly larger C_l oscillations in the presence of noise. Nevertheless, with LPR the control performance is only marginally degraded. A combination of hyperparameter tuning and online LPR provides a user-free robust approach for direct application of MPC in this configuration.

ACKNOWLEDGMENTS

This activity is part of the project ACCREDITATION (Grant No TED2021-131453B-I00), funded by MCIN/AEI/ 10.13039/501100011033 and by the European Union "NextGenerationEU/PRTR".

REFERENCES

[1] N. Deng, B. R. Noack, Marek M. Morzyński, and L. R. Pastur. Low-order model for successive bifurcations of the fluidic pinball. *J Fluid Mech.*, 884:A37, 2020.

[2] E. Kaiser, J. N. Kutz, and S. L. Brunton. Sparse identification of nonlinear dynamics for model predictive control in the low-data limit. *Proc. R. Soc. A.*, 474(2219):20180335, 2018.

[3] L. Marra, A. Meilán-Vila, and S. Discetti. Self-tuning model predictive control for wake flows. *J. Fluid Mech.*, 983:A26, 2024.

[4] B. R. Noack and M. Morzyński. The fluidic pinball—a toolkit for multiple-input multiple-output flow control (version 1.0). Technical report, Tech. Rep. 02/2017. Chair of Virtual Engineering, Poznan University of Technology, 2017.

[5] Q.J. Nottingham and D. F. Cook. Local linear regression for estimating time series data. *Comput. Stat. Data Anal.*, 37(2):209–217, 2001.

[6] L. Hewing K. P., Wabersich, and Marcel M. N. Zeilinger M. Menner. Learning-based model predictive control: Toward safe learning in control. *Annu. Rev. Control Robot. Auton. Syst*, 3(1):269–296, 2020.

30

ERCOFTAC
European Drag Reduction and Flow Control Meeting – EDRFCM 2024
September 10th–13th, 2024, Turin, Italy

SUPERSONIC FLOW CONTROL IN DUCTS AND OVER COMPRESSION RAMPS BY Q-DC DISCHARGE

S. Leonov
AME Department, University of Notre Dame, 46628, Notre Dame, IN, USA

INTRODUCTION

In supersonic transport systems, aerodynamic characteristics are highly dependent on several factors, such as atmospheric conditions or manoeuvres. Active flow control might increase their performance significantly especially in terms of the system response time. The problem considered in this paper is shock wave boundary layer interaction (SWBLI) control by filamentary electrical discharge in variety of geometries, including on compression surfaces, in shock-dominated duct-driven flows, or at control flaps deflected outwards.

Over the last few decades there have been a number of efforts exploring the plasma authority for supersonic flow control, including drag reduction, lift enhancement, separation zone modification, jets, cavities, flaps, etc., well considered in numerous publications [1, 2, 3]. Some works discussed a non-homogeneous plasma effect on shock wave (SW) position and pressure redistribution over a plane wall and compression ramp. In [4], the authors demonstrated effective control of oblique SW position and angle by means of electric discharge between flush-mounted electrodes installed in front of the ramp in M=2.2 airflow. A different approach for plasma-based control of a supersonic inlet was employed in [5] where the pulse-periodic arc plasma was used to control the SW reflection. Recently, several experimental efforts were performed to control the flowfield within a compression surface configuration at higher Mach numbers, M=4.5 to 7, by means of different electrical discharges, see [6-7].

This review paper observes resent works performed at the University of Notre Dame and related to SWBLI control by filamentary plasma array. The focus is on the experimental results collected in two basic geometries: plane wall and compression ramp.

BASIC EFFECT OF THE FILAMENTARY PLASMA ON SWBLI

The tests discussed here were performed at the SBR-50 supersonic blowdown wind tunnel under the following flow conditions: Mach number M = 2 and 4, stagnation temperatures T0=297-775 K, stagnation pressures P0=1.0-3.2 bar, and steady-state run time t= 0.5-2 s. The test section consists of a rectangular cross section duct of initial dimensions 76.2×76.2 mm with a 1° expansion on the top and bottom walls to compensate for boundary layer growth. In the base case, a 10° planar wedge was installed on the wall of the test section to generate a planar SW impinging on the plasma array located on the opposite wall. The plasma was generated using a quasi-DC electric discharge [8] originating from a set of high voltage electrodes arranged cross-flow and embedded in ceramic insert. The electric current connects to grounding rails placed between the HV electrodes in order to elongate the plasma filaments downstream. The electrical discharge operates in a current stabilized mode, predefined in a range of I=4-10 A at electrodes voltage Upl = 0.3-1 kV and plasma power Wpl = 1.5-4 kW per each plasma filament. The instrumentation includes multi-points pressure sensing, schlieren and camera visualization, PLIF, Mie scattering, OES, and PSP. A typical Q-DC electrical discharge image without the impinging SW in M=2 flow is shown in Fig. 1.

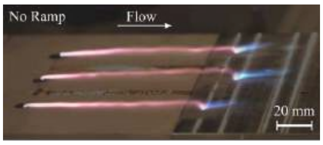

Figure 1. Q-DC discharge appearance in M=2 airflow.

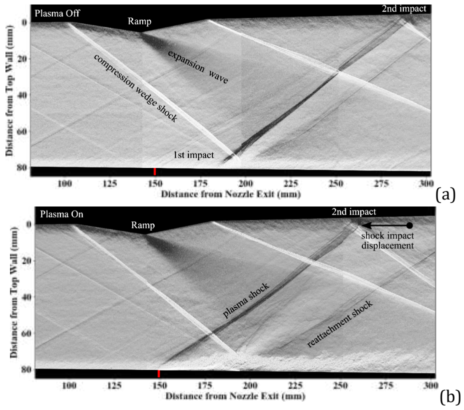

Figure 2. Schlieren images of SWBLI at plasma off (a) and on (b).

Schlieren imaging demonstrates the basic effect of plasma actuation on the flowfield structure which is observed in two key regions: (1) SW impact on the plasma array and (2) the reflection of this shock back to the upper wall. Figure 2 shows schlieren images collected prior the plasma turned on (a) and images during plasma actuation (b). Before plasma is activated, the flowfield is dominated by a series of SWs from the leading edge of the compression wedge, expansion fan from the top of the wedge, and the end SW from the ramp back wedge. After extended plasma forms over the bottom wall, the reflection of the shock is largely mitigated, and a new shock forms upstream at the location of the high voltage electrodes, see Fig. 2b. This causes upstream movement of the entire shock train. Such a shift of the SW was experimentally confirmed as far as ∆x=100 mm at M=2 and M=4 both.

SHOCK TRAIN CONTROL

When a supersonic flow is realized in ducts or limited by surfaces, such as a scramjet isolator, the flow structure can be characterized by a term “shock train” (ST): a series of compression and expansion waves caused by an adverse pressure gradient as shown in Fig. 3. In the case of scramjet isolator, changes in freestream parameters and combustion intensity result in the rapid repositioning of the ST leading to unexpected performance changes and, if the ST leading edge moves far enough upstream, unstart. ST might be actively controlled to widen the margin of engine operation, particularly at off-design conditions.

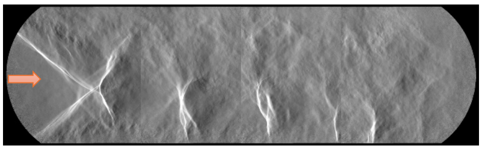

Figure 3. ST in M=2 airflow provoked by back pressure bump.

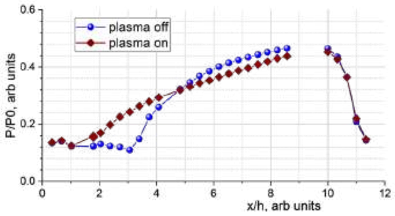

Figure 4. Wall pressure at plasma actuation of ST: h=duct height.

One of the active control approaches is to position the Q-DC plasma array upstream of the ST leading edge to reduce the duct pressure gradient and to improve overall pressure recovery. The experiments were performed in a similar to the configuration considered above conditions where the back pressure was simulated by a controlled confusor installed downstream of the test section. The effect of the plasma flow control is illustrated in Fig. 4. It was observed that the introduction of plasma to the flow anchored the ST upstream reducing the strength of the shock train on the plasma-side wall and resulted in a significantly decreased pressure gradient and an overall decrease in maximum pressure at the downstream blockage.

FLOW CONTROL OVER COMPRESSION RAMP

Another example of successful application of the Q-DC discharge for a supersonic flow control was demonstrated over the flow deflection surfaces, such as flaps or compression ramps [6]. In this case, the plasma array was placed in front of the 15° wedge simulating a flow deflection flap. At schlieren image in Fig. 5, the original position of the wedge-related SW is shown by red colour. At plasma actuation the SW moves upstream and have a reduced inclination angle.

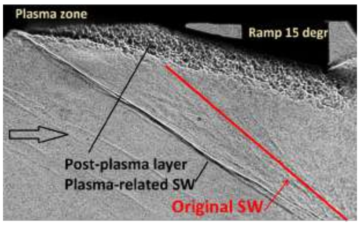

Figure 5. Control of SW position over 15° compression ramp.

Significant change in flow fields structure shown in Fig. 5 leads to pressure redistribution behind electrodes and on the flap, which is controlled by plasma power. When the plasma is turned on the pressure behind the electrodes rapidly increases. Conversely, the ramp pressure decreases up to 20% in value which leads to a reduction in the aerodynamic force/moment acting on the flap. It is important to note that the reaction time is rather short, t<0.3ms, under the conditions of the test described.

PHYSICS AND LIMITS OF STRATIFIED ENERGY EFFECT

For various conditions in M>1 flows, filamentary plasma authority has been well demonstrated. A hot plasma filament produces an extended zone of gas expansion leading to a conical SW production. With multifilamentary plasma arrays, individual SWs interfere with each other, resulting in almost planar plasma-induced SW, which is equivalent to shifting the entire shock train upstream. The physical mechanism of the plasma effect is essentially thermal: with a high local gas temperature, the plasma zone presents an array of longitudinal subsonic jets enclosed in a supersonic flow. Gas pressure is significantly redistributed resulting in pressure bump caused by an impinging SW or compression ramp is mitigated and moves upstream until reaching electrode locations. The negative x-gradient of pressure is reduced significantly due to a presence of flow reversal.

Based on the mechanism of SW-BL-plasma interaction, a simplified criterion of effective SW control was proposed [8]. The critical (minimal) plasma temperature for the triggering effect to work is a rising function of the flow Mach number. It is also concluded that the method might be especially effective for cold external flows.

CONCLUDING REMARCS

It is a paradigm-shifting concept to use plasma as an active trigger action for SW position control. In supersonic or hypersonic flows, narrow subsonic channels generated by plasma filaments are opened to allow pressure to drain into an upstream area, creating a significant pressure redistribution despite a small energy deposition relative to the flow total enthalpy.

The author would like to thank the US Air Force Office of Scientific Research (PM Dr. Gregg Abate) for funding this work, grant # FA9550-21-1-0006. Drs. S. Elliott, A. Houpt, P. Lax, Y. Watanabe, Mr. P. Andrews and Mr. L. Hahn significantly contributed to this research.

REFERENCES

[1] Bletzinger P, Ganguly B N, Van Wie D and Garscadden A 2005 *J. Phys. D: Appl. Phys.* 38 R33

[2] Poggie J, McLaughlin T and Leonov S 2015 *ONERA Aerospace Lab Journal* AL10 1

[3] Knight R 2008 *J. PROPUL. POWER* 24 1153

[4] Quan S, Bangqin C, Yonggui Y, Yiwen L and Di J 2010 *Plasma Sources Sci. Technol.* 12 708

[5] Webb N, Clifford C and Samimy M 2013 *Exp. Fluids* 54 1545.

[6] Y. Watanabe, S. Elliott, A. Firsov, A. Houpt and S. Leonov, 2019, *J. Phys. D: Appl. Phys.*, 52, 44, 444003,

[7] S. B. Leonov, I. V. Adamovich and V. R. Soloviev, 2016, *Plasma Sources Sci. Technol.*, 25, 6, 20168,.

[8] Andrews, P.; Lax, P.; Leonov, S. 2022, *Energies*, 15, 7104

31

ERCOFTAC
European Drag Reduction and Flow Control Meeting – EDRFCM 2024
September 10^{th}–13^{th}, 2024, Turin, Italy

CROSSWISE AND WALL-NORMAL PLASMA JETS IN A TURBULENT CHANNEL FLOW

J. Serpieri[1], G. Cafiero[1] & G. Iuso[1]
[1]Department of Mechanical and Aerospace Engineering, Politecnico di Torino, 10129 Turin, Italy

INTRODUCTION

Inducing a Stokes layer of flow right at the wall can reduce the skin friction drag from wall-bounded turbulent flows (e.g. [2, 3, 6]).

Plasma actuators (PAs) can induce a Stokes-like wall flow, similar to what caused by oscillating the flow-exposed surfaces along the crossflow direction, and capable of reducing the friction drag exerted by turbulent flows (e.g. [1, 8, 4]). The interest they collected is motivated by their simpler embodiment compared to mechanical, pneumatic or piezo-electric devices. Furthermore, in different configurations, they can induce stationary crosswise-directed jets [7] and also wall-normal ones similar to what was investigated by Yao et al. [9] and Iuso and Di Cicca [5]. This study investigates the effect of the two last typologies of flow control by means of arrays of PAs installed in a channel flow.

METHODOLOGY

The experimental campaign took place in a channel flow facility (0.42 m x 0.035 m x 10 m, in width, height h and length), operated at the friction Reynolds numbers of $Re_\tau = 190$.

The flow actuator hereby considered featured an array of six dielectric barrier discharge (DBD) PAs with the electrodes aligned with and extending 600 mm along the streamwise direction. The PAs considered 0.5 mm thick polyethylene terephthalate sheets as the dielectric layer. The electrodes were made with 0.35 mm thick copper tape and the isolation of the encapsulated electrodes was guaranteed by multiple layers of *Kapton* tape. Every actuator featured one exposed electrode connected to the ground and two encapsulated active electrodes, one per side of the exposed electrode, each connected to a high voltage (HV) source. The latter were four *GBS Elektronik Minipuls 4* set to deliver a 7 kHz sinusoidal signal of peak-to-peak amplitude of 8 kV.

When the HV signal was supplied to the active electrodes installed at only one side of the exposed electrode, a set of mono-directional stationary crosswise jets took place. This test case will be referred to with the ∞ symbol. When instead bot the the active electrodes received a HV signal, two oppositely-directed stationary jets where generated. These would collide somewhere at the crosswise position between two different actuators, causing an upward-directed motion. This case is here referred with the symbol 2∞.

The streamwise direction, the wall normal and the crosswise ones, are identified with x, y and z, respectively. x originates at the measured region upstream edge, y at the wall and z at the channel center-line. The velocity components along these directions are denoted with u, v, w, respectively.

Two different optical flow diagnostics experiments were set up: a xz plane PIV setup and a yz plane stereographic PIV (SPIV) setup. Both setups consisted of two *Andor Zyla* sCMOS cameras (5.5 Mpx, 16 bits) and a *Litron* double cavity laser (200 mJ/pulse, 15 Hz maximum repetition rate). The cameras were equipped with *Tokina* 100 mm macro lens with green filters and, for the SPIV setup, with Scheimpflug-condition adapters from *LaVision*. The system synchronization was guaranteed by a *National Instrument PCI-6602* board. The acquisition frequency was 15 Hz and a total of 1000 image pairs was acquired.

The PIV setup featured the two cameras placed one next to the other along the streamwise direction such to image a total field of view (FOV) extending 111.90 mm x 48.10 mm along the $x-z$ directions. This corresponds, in non-dimensional units, to 1550 x 497.40 along x^+ and $-z^+$, respectively. The illuminated plane was set at $y = 5$ mm ($y^+ = 52$). The final velocimetry resolution was 3.67 vectors/mm, i.e. 0.35 vectors per viscous length scale.

The SPIV setup investigated a domain extending 29.50 mm x 22 mm along z and y, thus 305.70 x 227.98 along $z^+ - y^+$. The plane was set at $x = 546$ mm ($x^+ = 5.67\,10^3$) from the actuator upstream edge. The velocimetry resolution was 9.26 vectors/mm (0.89 vectors per viscous length scale).

RESULTS

The performed flow actuation strongly modifies the operated flow at the wall. This can be appreciated in figure 1, where the time-averaged velocity fields are shown for the two considered control cases together with the reference uncontrolled flow. While for the latter, a rather homogeneous field is shown, for the controlled cases, a strong modulation from the operated plasma jets is observable. For the stationary crosswise forcing, the flow field appears with broad higher and lower velocity bands, slightly tilted towards the z^+ direction. For the wall-normal jets case, instead, the low velocity regions taking place at the crosswise positions in between the exposed electrodes appear much narrower and more pronounced. This is the effect of the upwelling motion of lower momentum air from the wall region caused by the colliding jets.

Turbulent flows are characterized by coherent structures. The footprint of these, in the velocity field, are regions of higher and lower velocity. As these appear elongated along the streamwise direction, they are usually referred to as "streaks". The occurrence and strength of low-speed streaks (LSS) of streamwise velocity are directly connected to larger skin friction events. As such, the performed flow actuation aims at reducing these. In figure 2, an instantaneous streamwise velocity field, for the three considered flows, is shown. The reference, unforced flow very clearly shows the occurrence of LSS. They appear rather coherent along both the streamwise and cross-wise directions. For the ∞ forcing, the LSS coherence along both directions appears reduced. High velocity regions are also more evident. Finally, for the wall-normal

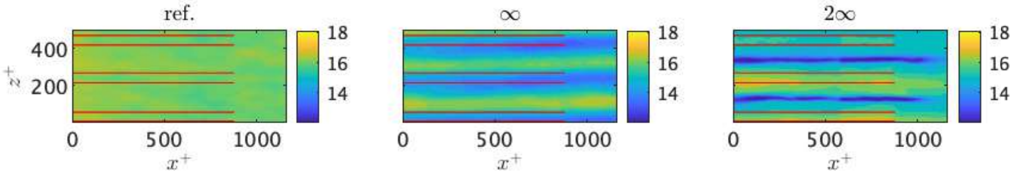

Figure 1: Time-averaged streamwise velocity fields U for the considered flow cases. The exposed electrodes are also shown with red lines.

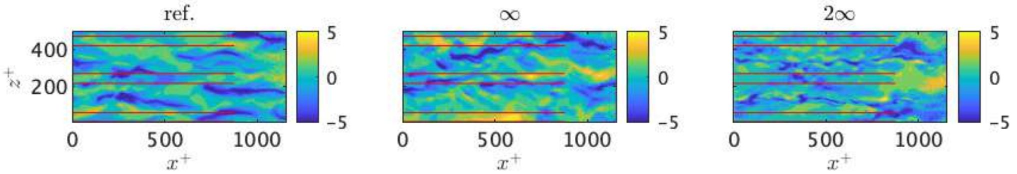

Figure 2: Instantaneous streamwise velocity fluctuations fields u' for the considered flow cases. The exposed electrodes are also shown with red lines.

forced flow, 2∞, both high and low velocity regions appear weaker and more fragmented.

The LSS features are then statistically analysed extracting connected regions of $u' < 0$, extending in the streamwise direction for at least 100 viscous length scales. The velocity fields are then conditionally averaged to derive LSS statistical features. These are shown in figure 3. Figure 3a shows that the ∞ and 2∞ forcing reduce, at the measurement plane, the velocity deficit within the LSS. Figure 3b reveals that the wall-normal vorticity ω'_y within the LSS is much reduced by all the considered forcing. The flow actuation increases the probability (pdf) of larger streaks' length L_s^+ (figure 3c) whereas, has milder effects on their average width W_s^+ (figure 3d).

The presentation will give more insight on the effect of the performed flow control on the operated flow, further discussing the flow mechanisms at play.

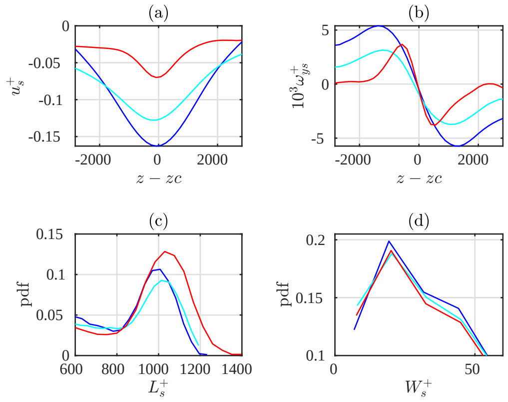

Figure 3: LSS features for the reference (blue), the ∞ (cyan) and 2∞ (red) flow cases: $u_s'^+$ (a); $10^3\,\omega_{ys}'^+$ (b); pdf of L_s^+ (c) and pdf of W_s^+ (d); z_c is the LSS center along z.

ACKNOWLEDGEMENTS

This study was carried out within the "WAll-Turbulence Active COntrol" project – funded by European Union – Next Generation EU within the PRIN 2022 PNRR program (D.D.1409 del 14/09/2022 Ministero dell'Università e della Ricerca). This manuscript reflects only the authors' views and opinions and the Ministry cannot be considered responsible for them.

REFERENCES

[1] K.-S. Choi, T. Jukes, and R. Whalley. *Philosophical Transactions of the Royal Society A: Mathematical, Physical and Engineering Sciences*, 369(1940):1443–1458, 2011.

[2] G. M. Di Cicca, G. Iuso, P. G. Spazzini, and M. Onorato. *Journal of Fluid Mechanics*, 2002.

[3] D. Gatti, A. Güttler, B. Frohnapfel, and C. Tropea. *Experiments in Fluids*, 56(5):110, 2015.

[4] M. T. Hehner, D. Gatti, P. Mattern, M. Kotsonis, and J. Kriegseis. *AIAA Journal*, 59(2):763–767, 2021.

[5] G. Iuso and G. M. Di Cicca. *Journal of Turbulence*, 2009.

[6] G. E. Karniadakis and K.-S. Choi. *Annual Review of Fluid Mechanics*, 35:45–62, 2003.

[7] J. Serpieri, M. T. Hehner, and J. Kriegseis. *Flow, Turbulence and Combustion*, 2023.

[8] R. D. Whalley and K. S. Choi. *Experiments in Fluids*, 55(8), 2014.

[9] J. Yao, X. Chen, and F. Hussain. *Journal of Fluid Mechanics*, 852(August):678–709, 2018.

32

ERCOFTAC
European Drag Reduction and Flow Control Meeting – EDRFCM 2024
September 10th–13th, 2024, Turin, Italy

SOME APPROACHES TO CONTROLLING HIGH-SPEED FLOWS USING REMOTE AND SURFACE PLASMA ENERGY DEPOSITION

O. Azarova
Department of Mathematical Modeling of Computer-Aided Design Systems,
Federal Research Center "Computer Science and Control"
of the Russian Academy of Sciences, 119333, Moscow, Russia

INTRODUCTION

Controlling the supersonic/hypersonic flow over an aerodynamic (AD) body by applying energy to the flow or to various points on the surface of the streamlined body is now a well-established field in aerospace science [1]. Numerous reviews are devoted to various aspects of this topic, from drag and aero-heating reduction [2] to the effect of plasma-induced flow separation [3] and the influence on a flow of filamentary plasma and spatially multi-component plasma structures [4].

The presented talk analyses the approaches to controlling high-speed flows and aerodynamic characteristics of an AD body using remote stratified energy sources and near surface energy supply. Special attention is paid to control the sonic boom effect during the use of stratified energy deposition.

RESULTS

New approaches have been developed to control the bow shock wave, drag and lift forces (at zero angle of attack), as well as the stability of a high-speed flow past an AD body using a thermally stratified energy deposition [5]. The possibility of initiating and damping self-sustained flow pulsations in a case of an asymmetrical energy source, influencing drag and lift forces is shown (Fig. 1 *upper*). In addition, the control of other aerodynamic characteristics of the body by changing the temperature in the layers of a thermally stratified energy source is demonstrated. The occurrence of multiple manifestations of the Richtmeyer-Meshkov instability was discovered, leading to curvature and, in some cases, almost complete disappearance of the front of the bow shock wave in the region of energy release. A new multi-vortex mechanism for the action of a stratified source on the body is described (Fig. 1 *bottom*).

A formulation of principles for high-speed flow control using thermally stratified energy deposition is presented. These principles include both unsteady and steady flow control, which provide the ability to control flow pulsations and drag/lift forces.

The results on the noise impact on the ground during flow control using thermally stratified energy sources are analysed [6]. These results showed that controlling flows with stratified energy sources does not introduce additional noise at the ground level. In a broader sense, these simulations showed that changing the surface pressure on an AD body and reducing drag do not necessarily lead to change in perceived sound level in decibels (PLdB) near the ground.

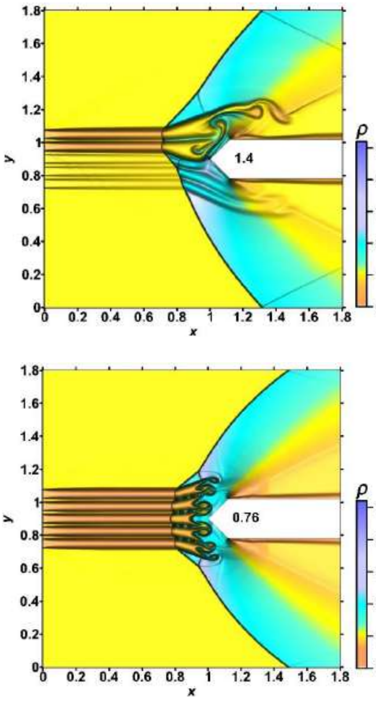

Figure 1. Fields of density for the action of asymmetrical (*upper*) and symmetric (*bottom*) thermally stratified energy sources (dimensionless time moments are indicated)

The possibility of controlling the position of a steady bow shock wave by creating a volumetric plasma region using a surface gas discharge organized on the entire front surface of the semi–cylindrical body has been demonstrated experimentally and numerically [7] (Fig. 2 *upper*). It was found that the position of the steady bow shock wave, in addition to the specific power of the gas discharge, is affected by the value of the adiabatic index in the region of plasma created by the discharge, as well as the degree of ionization and the degree of nonequilibrium of the discharge plasma. Good agreement was obtained between numerical and experimental data (Fig. 2 *bottom*). Based on studies of non-stationary processes of formation of a steady flow mode, a mechanism for the influence of the plasma region created by the discharge on the position of the bow shock wave in a steady state is formulated.

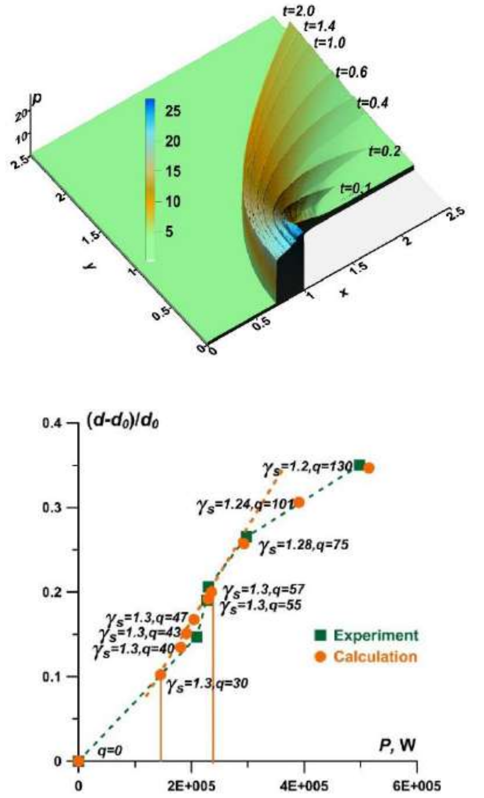

Figure 2. Dynamics of the pressure field during the establishment of a steady flow mode under the action of gas-discharge plasma (superposition of flow patterns) (*upper*). Computational and experimental data on the dependence of the relative value of the steady bow shock stand-off distance on the discharge power (*bottom*); γ_s -adiabatic index in the plasma region, *q* – specific discharge power.

The presented results have practical implications, especially in the supersonic and hypersonic context, since it has been shown that the structure and position of the bow shock wave (and consequently the characteristics of an AD body) can be precisely controlled by the considered types of energy deposition. This opens up potential advances in the field of supersonic and hypersonic flow control for a variety of applications in controlling both external and internal high-speed flows.

REFERENCES

[1] D. D. Knight. *Energy deposition for high-speed flow control*. Cambridge University Press, 2019.

[2] M. Y. M. Ahmed, N. Qin. Forebody shock control devices for drag and aero-heating reduction: A comprehensive survey with a practical perspective. *Prog. Aerosp. Sci.,* 112, 100585, 2020.

[3] S. B. Leonov, I. V. Adamovich, and V. R. Soloviev. Dynamics of near-surface electric discharges and mechanisms of their interaction with the airflow. *Plasma Sources Sci. Technol.* 25, 063001, 2016.

[4] O. A. Azarova, O. V. Kravchenko. The use of spatially multi-component plasma structures and combined energy deposition for high-speed flow control: A selective review. *Energies,* 17(7), 1632, 2024.

[5] O. A. Azarova. Basics of control of the bow shock wave, drag and lift forces, and stability in a steady supersonic flow past an AD body using permanently operating thermally stratified energy deposition. *Energies.* 15(22), 8627, 2022.

[6] O. V. Kravchenko, O. A. Azarova, and D. D. Knight. Impact of a thermally stratified energy source located in front of a pointed cylinder aerodynamic model on the pressure signatures and PLdB effect on the ground. *Applied Sciences*, 13(13), 7927, 2023.

[7] O. A. Azarova, T. A. Lapushkina, and Yu. A. Shustrov. Near-surface gas discharge effect on a supersonic flow past a cylindrically blunted body in air. *Physics of Fluids*, 34, 066117, 2022.

ERCOFTAC
European Drag Reduction and Flow Control Meeting – EDRFCM 2024
September 10^{th}–13^{th}, 2024, Turin, Italy

PLASMA ACTUATORS FOR DRAG REDUCTION ON HEAVY GROUND VEHICLES

L. Schneeberger
Department of Aerospace Engineering, Universidad Carlos III de Madrid, Leganés, Spain

A. Ianiro
Department of Aerospace Engineering, Universidad Carlos III de Madrid, Leganés, Spain

S. Discetti
Department of Aerospace Engineering, Universidad Carlos III de Madrid, Leganés, Spain

INTRODUCTION

According to European laws voted in 2019, new heavy-duty vehicles in the EU must reduce their CO_2 emissions with respect to 2005 levels by 15 % by 2025 and by 30% by 2030 [1]. In this context, active flow control is of particular interest to reduce trucks emissions, as the truck shape is largely dictated by practical constraints. Passive devices have shown effective to reduce the drag at design conditions [5, 6, 9], but they underperform outside of the design range and bring major impediments on logistical aspects.

Active flow control techniques applied to heavy transportation vehicles have shown to allow a drag reduction of up to 20% on highway-like conditions, providing 15% net power savings [7, 8]. Such results have been achieved using Coanda actuators on the base of the trailer, shortening the wake of the vehicle and therefore raising the base pressure. However, trailer owners are often not primarily interested in reducing the consumption of the truck. Instead, fleet operators have more direct influence on the tractor part of the tractor-trailer system.

Another way to enhance the aerodynamic performance of trucks is to prevent lateral separation on the cabin, as shown by Vernet et al. [10]. Fleet operators have a more direct impact on this region of the vehicle and the length limitation is not an issue. In addition, lateral separation also plays a role in the lateral force observed in asymmetric configuration (yaw angle $\neq 0°$). In this work, we investigate the effect of dielectric barrier discharge (DBD) plasma actuators located on the front vertical edges of the cabin (also known as A-pillars) on preventing separation and hence enhancing the aerodynamic performance of a standardized truck, both for drag reduction and lateral stability.

METHODOLOGY

Although less investigated than the Ahmed body [2], the Ground Transportation System (GTS) has been introduced as a generalized truck model by in Gutierrez et al. in 1996 [6]. The GTS is well-known for displaying a laminar separation bubble on both sides of the cabin, even when the incoming flow is aligned with the truck axis [9]. Together with the rear wake, the lateral separation bubbles are the main contributors to the drag on the GTS.

A scaled-down model of the GTS has been placed in the closed-loop wind tunnel of the Department of Aerospace Engineering at the University Carlos III of Madrid. The tunnel has a square test section of 40 cm x 40 cm and the model has been placed 35 cm away from the beginning of the test section, as illustrated on Figure 1. The truck has been 3D-printed in PLA and its width $w = 8.5$ cm has been selected to induce a blockage ratio below 15% when introducing yaw up to 10° in future studies. The incoming flow velocity is set at 8.0 m/s, which yields a Reynolds number $Re = 3.47 \cdot 10^5$.

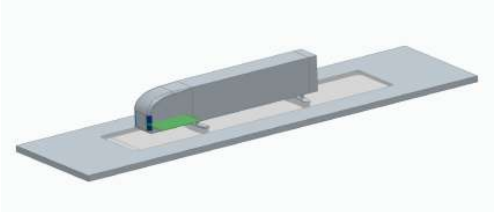

Figure 1: Sketch of the experimental setup inside the wind tunnel test section.The blue elements are the DBD plasma actuators and the green plane is the PIV plane.

The GTS has been modified with slots on the A-pillars to allow for the installation of flush-mounted DBD plasma actuators, shown in blue in Figure 1. Such actuators consists of two copper electrodes located on both sides of a dielectric. The working principle of a plasma actuator is shown in Figure 2. In our experiment the dielectric consists of a quarter-cylindrical, 1 mm thick plastic part, 3D-printed in PLA. Both plasma actuators are fed with a single Minipuls 4 pulse generator from GBS Elektronik GmbH. It produces an AC signal, oscillating at 20 kHz and with a peak amplitude of 4.44 kV.

We investigate the extent of the laminar separation bubble expected along the cabin of the GTS using planar particle image velocimetry (PIV). The horizontal measurement plane is represented by a green surface on Figure 1. It is located 5.5 cm above the wind tunnel floor. In the streamwise axis, the observation region starts 2 mm before the truck nose and extends over 135 mm downstream of it. In the spanwise axis, the PIV plane edge lies on the truck cabin and extends over 36 mm.

DEHS particles of approximately 1 µm diameter are generated with a Laskin nozzle to seed the flow. A pulsed Nd:Yag laser is used to illuminate the particles. Each of the two cavities of the laser produces a maximum pulse energy of 200 mJ. The delay between the two pulses is set to $\Delta t = 36$ µs. An Andor SCMOS camera, with 2560 x 2160 pixel sensor (6.5 µm pixel size) records the particle images. The camera is equipped with a Nikon objective with 50 mm focal length. The final spatial resolution is 18.8 pix/mm. Part of the wind tunnel floor consists of a transparent methacrylate plate, which allows the camera to be placed below the setup. The images are processed with the open software PaIRS, developed by the University of Naples ”Federico II” [3].

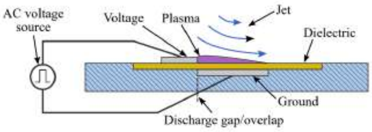

Figure 2: Functioning principle of a DBD plasma actuator. An airflow tangential to the surface is generated. Courtesy of [4].

RESULTS

Figure 3 shows the average velocity fields computed from 1,500 snapshots taken over a minute-long experiment in the wind tunnel. The velocity vectors are represented with arrows, and the color shows the velocity magnitude, according to the color bars next to the figures.

In the baseline case (Figure 3a), the flow detaches from the cab side (upper edge of the figure) after approx. $0.15w$ (the cab starts at $x/w = 0.02$). We then observe the presence of an elongated recirculation bubble that extends over $0.83w$ in length and is $0.077w$ wide.

When the plasma actuators are turned on (Figure 3b), the separation bubble is still present but its extent is reduced to $0.6w$. The width of the bubble also diminishes to approximately $0.034w$.

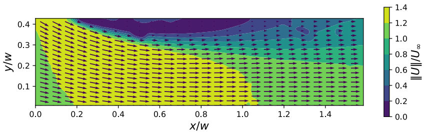

(a) No actuation

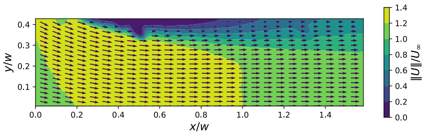

(b) Plasma actuators on

Figure 3: PIV comparison of the laminar separation bubble on the truck cabin side with and without actuation. The velocity fields are averaged over 1500 samples. The color indicates the magnitude of the velocity nondimensionalized by the free stream velocity U_∞=8 m/s. Ticks indicate the spatial coordinates as fractions of the truck width w=85 mm.

We expect this change to lead to a sensible drag reduction and even more so when the truck has a non-zero yaw angle. In the non-zero yaw case, the lateral force should also be significantly reduced. Lateral and drag force sensing results for several yaw angles will be presented during the conference.

CONCLUSION

We have demonstrated the feasibility of using plasma actuators on the A-pillars of a standardized truck model to reduce the laminar separation bubble on the cabin sides. This opens the door to more sophisticated strategies, such as controlling the actuation power on both sides depending on the yaw angle in an open-loop manner, or even including feedback. For closed-loop control, force sensing seems the easiest path to follow, but for real applications, pressure sensors appear as the preferential choice.

ACKNOWLEDGEMENTS

This activity is part of the project ACCREDITATION (Grant No TED2021-131453B-I00), funded by MCIN/AEI/ 10.13039/501100011033 and by the European Union ”NextGenerationEU/PRTR”.

REFERENCES

[1] Regulation (EU) 2019/1242 of the European Parliament and of the Council, 2019.

[2] S. Ahmed, G. Ramm, and G. Faltin. Some Salient Features Of The Time-Averaged Ground Vehicle Wake. page 840300, 1984.

[3] T. Astarita and G. Paolillo. PAIRS: a free software application for robust and accurate digital particle image velocimetry. In *75th Annual Meeting of the APS Division of Fluid Dynamics*, Indianapolis, Indiana, USA, 2022. Bulletin of the American Physical Society.

[4] R. Castellanos. *Convective heat transfer control in turbulent boundary layers*. PhD thesis, Universidad Carlos III de Madrid, Leganés, 2022.

[5] R. J. Englar. Advanced Aerodynamic Devices to Improve the Performance, Economics, Handling and Safety of Heavy Vehicles. pages 2001–01–2072, 2001.

[6] W. T. Gutierrez, B. Hassan, R. H. Croll, and W. H. Rutledge. Aerodynamics Overview of the Ground Transportation Systems (GTS) Project for Heavy Vehicle Drag Reduction. page 960906, Detroit, Michigan, 1996.

[7] J. Pfeiffer and R. King. Robust control of drag and lateral dynamic response for road vehicles exposed to cross-wind gusts. *Exp Fluids*, 59(3):45, 2018.

[8] R. Semaan, P. Oswald, G. Y. Cornejo Maceda, and B. R. Noack. Aerodynamic optimization of a generic light truck under unsteady conditions using gradient-enriched machine learning control. *Exp Fluids*, 64(3):59, 2023.

[9] B. L. Storms, J. T. Heineck, S. M. Walker, D. M. Driver, and G. G. Zilliac. An Experimental Study of the Ground Transportation System (GTS) Model in the NASA Ames 7- by 10-Ft Wind Tunnel. Technical Memorandum TM-2001-209621, NASA, Ames Research Center, Moffett Field, California, 2001.

[10] J. A. Vernet, R. Örlü, D. Söderblom, P. Elofsson, and P. H. Alfredsson. Plasma Streamwise Vortex Generators for Flow Separation Control on Trucks: A Proof-of-concept Experiment. *Flow Turbulence Combust*, 100(4):1101–1109, 2018.

 # 34

ERCOFTAC
European Drag Reduction and Flow Control Meeting – EDRFCM 2024
September 10^{th}–13^{th}, 2024, Turin, Italy

AI-DRIVEN REAL-TIME CONTROL OF TOLLMIEN-SCHLICHTING WAVES ON A FLAT PLATE

G. Salomone, C.S. Greco
Department of Industrial Engineering, Università degli Studi di Napoli "Federico II", 80125 Naples, Italy

B. Mohammadikalakoo, N.A.K. Doan, M. Kotsonis
Faculty of Aerospace Engineering, Delft University of Technology, Kluyverweg 1, Delft 2629HS, The Netherlands

INTRODUCTION

The present work focuses on the suppression of Tollmien-Schlichting waves in an incompressible boundary layer developing on a flat plate by means of a Dielectric Discharge Barrier (DBD) Plasma Actuator as a Real Time Active Flow Control (AFC) device, driven by two Artificial Intelligence based techniques: Particle Swarm Optimization (PSO) and Single Step Deep Reinforcement Learning (SDRL).

PSO, introduced by Kennedy and Eberhart [1], is a technique based on swarm intelligence that can be used to find an optimal solution to a problem by updating a population of candidate solutions (individuals) based on a metrics of relative quality (reward or loss function) in an iterative procedure.

SDRL is a policy-based optimization technique where the intelligent agent uses a policy network to represent the density function of the next iteration's evaluations [2]. It can be seen as a degenerative deep reinforcement learning algorithm in which single-step episodes are enough due to the state-independent optimal policy of the neural networks.

Drag reduction by delaying the transition in an incompressible boundary layer flow and the use of DBD as a control device are well assessed topics in Flow control [3, 4, 5]. Although Artificial Intelligence techniques found some application in numerical research [6, 7, 8], its application in real word experimental conditions has not been deeply investigated yet. The aim of the present research is to assess how PSO and SDRL perform in tuning the AFC control parameters to find an optimum control state, i.e. an optimum Finite Impulse Response (FIR) filter that, applied to a pressure reference signal, generates an optimum control output signal.

SETUP

Experiments take place in the A-Tunnel of the Low-speed Wind Tunnel Laboratory of TU Delft.

The whole setup is summarized in Figure 1. The tested model consists of a 950 mm x 495 mm Aluminium plate that hosts a 430 mm x 210 mm PMMA insertion. Six GRAS 46BE 1/4" CCP Free-field standard microphones with a threaded head are screwed from the back side of the insertion plate and they read pressure data thanks to 0.3 mm holes on the front surface. The microphones have a nominal sensitivity of 3.6 mV/Pa and are equally spaced from 0.4 m to 0.65 m from the flat plate leading edge. The signals collected by the microphones located at 0.4 m and 0.55 m from the flat plate leading edge are then filtered by using a bandpass Infinite Impulse Response (IIR) filter with a bandwith of 150 Hz centered about the frequency of the generated TS and used in the algorithms as reference ($x(k)$) and error ($e(k)$), respectively.

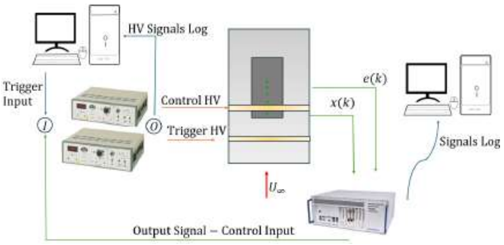

Figure 1: Setup for the AFC

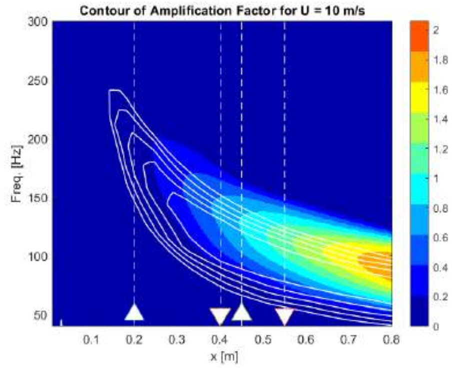

Figure 2: Map of N factor output by LST; White lines: isovalues of growth rate ($-\alpha_i$); Markers: Locations of DBD actuators(upright triangles) and sensors(inverted triangles)

A DBD Plasma actuator made with two layers of 50 μm thick Kapton and a 30 μm thick layer of copper is employed to trigger TS waves at frequencies for which Linear Stability Theory (LST) expects a sufficient growth up to the region where the sensors are placed (Figure 2). The connector of the copper layer is connected to the High Voltage output cable of a TREK 20/20C High Voltage amplifier while Aluminium plate serves as grounded electrode.

The DBD is operated remotely on a computer workstation where the driving signal is generated by LabView software and sent to the amplifier via a Digital/Analog converter.

A second DBD Plasma Actuator is used to trigger the "control" TS waves. The trigger and control DBD actuators are placed 0.2 m and 0.45 m from the flat plate leading edge, respectively.

With regards to the PSO, the algorithm is fully implemented in Simulink Real-Time and is run on a Speedgoat Performance target machine. The individuals are a set of constants that constitute a FIR filter for the reference signal $x(k)$ to output a filtered $y(k)$ signal. In turn, the modulation of this signal with a high frequency carrier signal is sent to the amplifier that then enables the controller DBD by supplying voltage to the copper electrodes, creating a strong electric field and forming ion-electrons pairs that act as momentum source in the presence of the electric field.

The target machine is connected via Ethernet to a developing computer where the Simulink Real-Time model is implemented and where data are logged in real time thanks to the Simulation Data Inspector feature. With regards to the SDRL, individuals are generated with a script running on the developing machine and the Simulink Real-Time model is only used to deploy actuation and to save individuals performances in the time horizon.

PRELIMINARY RESULTS

Preliminary results concern open-loop control that narrows down the range of voltage levels that are effective in suppressing TS waves and that highlights the effect of relative phase between the signals fed to the DBDs. Results displayed in Figure 3 refer to conditions reported in Table 1 while swept variables are the amplitude of the control signal and the relative phase between the two sinusoidals.

Table 1: Open loop: Properties of trigger and control signals

Property	Run Open Loop 1.1
Freesteam Velocity	10 m/s
Trigger Type	Sine
Trigger Amplitude	5.5 $kVpp$
Trigger Frequency	125 Hz
Control Type	Carrier Modulation
Control Frequency	125 Hz
Carrier Frequency	1000 Hz

For the closed loop, Figure 4 shows that PSO is able to make population converge to a FIR filter that generates an action that effectively reduces the rms of the error signal. In the algorithm, as reported in Table 2, the metrics of quality of an individual is set as the reduction of the rms of the error signal with respect to the uncontrolled case.

Table 2: Closed loop: Properties of trigger and algorithm

Freesteam Velocity	10 m/s
Trigger Type	Modulation with Duty Cycle
AC Signal Amplitude	5.5 $kVpp$
AC Signal Frequency	1000 Hz
Duty Cycle	50 %
Modulating Signal Frequency	125 Hz
Episode Time	0.5 s
Looping Frequency	10 kHz
Fitness	$(rms_0 - rms)/rms_0$

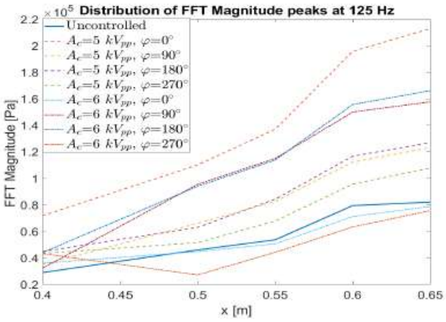

Figure 3: Open loop control: Spatial distribution of FFT magnitude peaks of the microphones signals by varying Control Signal Amplitude (A_c) and Trigger/Control sinusoidals relative phase (φ)

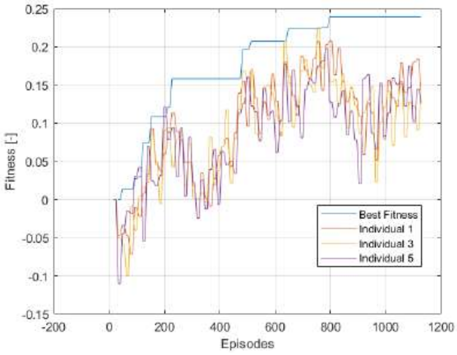

Figure 4: Closed loop control:Non-dimensional reduction of rms of error signal v. Episodes

REFERENCES

[1] Kennedy, J. and Eberhart, R. In *Proceedings of ICNN'95 - International Conference on Neural Networks*, volume 4, pages 1942–1948 vol.4, 1995.

[2] Viquerat, J. and Duvigneau, R. and Meliga, P. and Kuhnle, A. and Hachem, E. *Neural Computing and Applications*, 35(1):449–467, 2023.

[3] Corke, T.C., Enloe, C.L., Wilkinson, S.P. . *Annual Review of Fluid Mechanics*, 42:505–529, 2010.

[4] Kotsonis, M., Giepman R.,Hulshoff, S., Veldhuis, L. *AIAA journal*, 51:2353–2364, 2013.

[5] Kotsonis, M., Shukla R. K., Probsting, S. *International Journal of Flow Control*, 7, 2015.

[6] Ghraieb, H., Viquerat, J., Larcher, A., Meliga, P., Hachem, E. *Physical Review Fluids*, 6(5):053902, 2021.

[7] Ghraieb, H., Viquerat, J., Larcher, A., Meliga, P., Hachem, E. *AIP Advances*, 12(8):085108, 2022.

[8] Mohammadikalakoo, B., Kotsonis. M, Doan, N. A. K. In *Proceedings of the TSFP13*, Montreal, Canada, 2024.

35

ERCOFTAC
European Drag Reduction and Flow Control Meeting – EDRFCM 2024
September 10^{th}–13^{th}, 2024, Turin, Italy

2C-2D PIV/PTV MEASUREMENTS OF HIGH REYNOLDS NUMBER TURBULENT CHANNEL FLOW WITH WALL-NORMAL RESOLUTION OF 0.6 VISCOUS LENGTH

B. Sun
Laboratory for Turbulence Research in Aerospace & Combustion (LTRAC), Department of Mechanical and Aerospace Engineering, Monash University (Clayton Campus), VIC 3800, Australia

C. Atkinson
Laboratory for Turbulence Research in Aerospace & Combustion (LTRAC), Department of Mechanical and Aerospace Engineering, Monash University (Clayton Campus), VIC 3800, Australia

J. Soria
Laboratory for Turbulence Research in Aerospace & Combustion (LTRAC), Department of Mechanical and Aerospace Engineering, Monash University (Clayton Campus), VIC 3800, Australia

INTRODUCTION

Fully-developed turbulent channel flow is a canonical wall-bounded turbulent shear flow that is significant because it is a base for studies on how surface roughness and drag reduction strategies affect the drag in wall-bounded turbulent flows. The fully developed channel flow is statistically homogeneous in both the spanwise and streamwise directions, resulting in no spatial growth in the flow direction. Nevertheless, experimental studies of turbulent channel flow are less common compared to other canonical flow configurations like turbulent boundary layer and fully developed pipe flow, partially due to the required larger footprint of the experimental facility that produces fully developed channel flow [2]. To maintain nominally two-dimensional flow in the channel centreline, the experimental facility requires a high aspect ratio, leading to an order of magnitude larger cross-sectional area in comparison to a turbulent pipe experiment with the same Reynolds number[3]. The high spatial resolution PIV measurement in the channel centreline also presents some complexities in the experiment. This paper presents a two-component, two-dimensional hybrid particle image/tracking velocimetry (2C-2D PIV/PTV) for the turbulent channel flow investigations that overcomes these obstacles for a high spatial resolution measurement required in studies on how surface roughness and drag reduction strategies affect the drag in wall-bounded turbulent flows.

EXPERIMENTAL METHODOLOGY

The experiment was conducted in the LTRAC high-speed water channel. The test section of the water channel is 1.6 m in the streamwise direction, 700 mm in the spanwise direction and 20 mm in the wall-normal direction, corresponding to a channel half-height, h, of 10 mm. Due to the high aspect ratio of the cross-section, the side walls have a negligible effect on the flow at the centreline of the channel flow, and the flow along the centreline of the channel nominally is two-dimensional in the mean [6]. The water channel is constructed using a stainless steel frame with glass on all four sides, providing full optical access to the channel flow. The water channel is powered by a 5.5 kW motor driving a centrifugal water pump. The water from the pump flows into a settling chamber, which holds 200 litres of water and contains four grids and a honeycomb flow straightener to reduce the turbulence level of the inflow. The flow then goes through a 10-to-1 contraction and a boundary layer trip before entering the channel test section. The PIV measurement domain is 1.5 m (150 h) downstream of the trip to ensure a fully-developed channel flow. At this location, the frictional Reynolds number, Re_τ, is estimated to be 1,400 and the viscous length scale, l^+, is estimated to be 8 μm. The field of view of the experiment is in the wall-normal – streamwise direction along the centreline of the channel, which extends the full wall-normal extent of the channel and is 24.5 mm (2.45 h) in the streamwise direction. The field of view is illuminated by an InnoLas Compact 400 PIV lamp pumped Nd:YAG laser, with the flow seeded using hollow glass spheres of 11 μm diameter.

The PIV image pairs were obtained using two Emergent HZ-100-G-M cameras. These cameras have a CMOS sensor measuring 36.1 mm wide and 29.4 mm high, with a total of 103 million (11,276 × 9,200) pixels. As these cameras do not have a double shutter, a beam splitter is used to match the fields of view of the two cameras which capture each of the single-exposed PIV images. The large image sensor of these cameras presents a challenge for camera position calibration, as the error introduced by lens distortion near the corners of the imaging sensor can be of the order of 10 pixels. To avoid unacceptable uncertainties caused by lens calibration, a lensless imaging registration system based on holographic techniques was developed. Unlike conventional imaging, holography belongs to coherent imaging, where the illumination light is a coherent light with a planar wavefront provided by a laser. When a target is placed in the light path, the interference pattern between the scattered light of the camera and the illumination light is recorded by the camera, resulting in the recording of a hologram. Using this technique, it is possible to trace back the incident angle of the imaging light as well as the relative position between the target and each of the two cameras without distortion introduced by a lens. With this method, the mapping of each pixel in the two cameras to the physical coordinates could be obtained with a sub-pixel uncertainty.

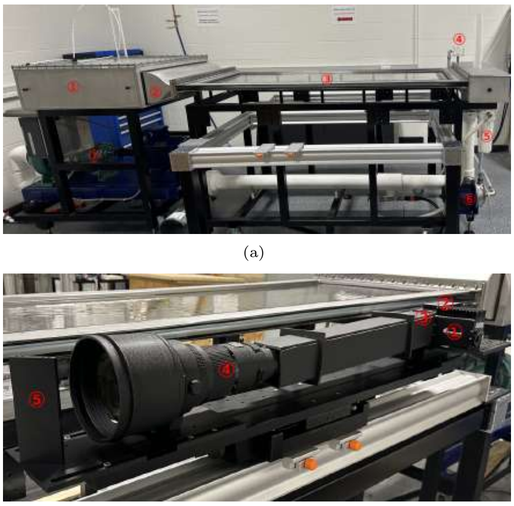

(a)

(b)

Figure 1: (a) A photo of the LTRAC high-speed water channel. 1: settling chamber 2: contraction 3: test section 4: seeding chamber 5: particle filter 6: axillary pump for the filter 7: main pump. (b) A photo of the imaging optical setup. 1: first camera 2: second camera 3: (inside the mount) beam splitter 4: 400mm f/2.8 lens 5: mirror to image inside the channel.

The magnification of the imaging system is 1.47, and the object plane is 350 mm away from the side wall of the water channel, which is longer than the working distance of any available macro lens. Therefore, a telephoto lens was used in the experiment, with the lens located just outside the water channel and the camera positioned about 500 mm away from the lens, as shown in figure 1(b). This optical setup greatly reduces the numerical aperture of the imaging system. Therefore, a large aperture lens, Nikon 400mm f/2.8, is used for the optical PIV imaging system. To increase the signal-to-noise ratio of the PIV images and, at the same time, ensure the measurement volume is adequately seeded, a selective seeding device is used to seed near the central line of the tunnel only. The PIV images are analysed using an in-house multigrid/multipass PIV/PTV algorithm [4], and the PTV velocity vectors are organised into bins that are 0.6 viscous length in height and cover the whole streamwise domain of the measurement. The PTV velocity vectors are corrected for lens distortion using the method described by [5] before being used for statistics calculation.

RESULTS

The velocity statistical profiles are presented below and compared with the profiles from a direct numerical simulation of a similar Reynolds number. Additional results will be presented and discussed at the conference.

REFERENCES

[1] Myoungkyu Lee and Robert D. Moser. Direct numerical simulation of turbulent channel flow up to $Re_\tau \approx 5200$. *Journal of Fluid Mechanics*, 774:395–415, 2015.

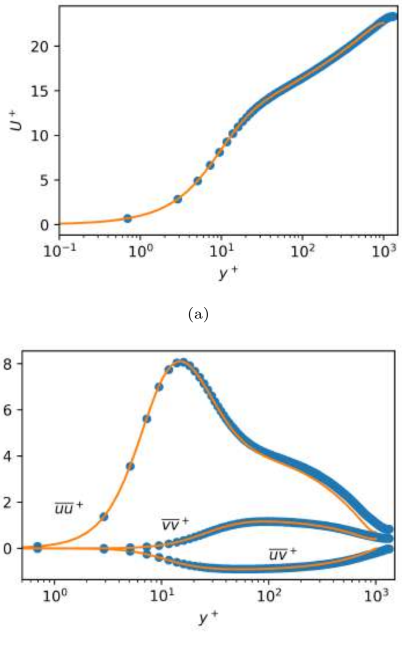

(a)

(b)

Figure 2: — Profile from DNS of $Re_\tau = 1,000$ [1]. ● experimental measurement. (a) mean velocity profile. (b) Reynolds stress profiles.

[2] J. P. Monty and M. S. Chong. Turbulent channel flow: comparison of streamwise velocity data from experiments and direct numerical simulation. *Journal of Fluid Mechanics*, 633:461–474, 8 2009.

[3] M. P. Schultz and K. A. Flack. Reynolds-number scaling of turbulent channel flow. *Physics of Fluids*, 25:025104, 2 2013.

[4] Julio Soria. An investigation of the near wake of a circular cylinder using a video-based digital cross-correlation particle image velocimetry technique. *Experimental Thermal and Fluid Science*, 12:221–233, 1996.

[5] Bihai Sun, Muhammad Shehzad, Daniel Jovic, Christophe Cuvier, Christian Willert, Yasar Ostovan, Jean-Marc Foucaut, Callum Atkinson, and Julio Soria. Distortion correction of two-component two-dimensional piv using a large imaging sensor with application to measurements of a turbulent boundary layer flow at $re_\tau = 2386$. *Experiments in Fluids*, 62:183, 9 2021.

[6] Ricardo Vinuesa, Azad Noorani, Adrián Lozano-Durán, George K. El Khoury, Philipp Schlatter, Paul F. Fischer, and Hassan M. Nagib. Aspect ratio effects in turbulent duct flows studied through direct numerical simulation. *Journal of Turbulence*, 15:677–706, 10 2014.

36

ERCOFTAC
European Drag Reduction and Flow Control Meeting – EDRFCM 2024
September 10$^{\text{th}}$–13$^{\text{th}}$, 2024, Turin, Italy

TOWARDS ADAPTIVE CONTROL OF WALL-BOUNDED TURBULENCE

G. Dacome, M. Kotsonis, W.J. Baars
Faculty of Aerospace Engineering, Delft University of Technology, 2629 HS Delft, The Netherlands

INTRODUCTION

Design and deployment of a real-time controller for engineering flow control applications requires adaptability to the performance envelope of the dynamic plant it is applied to (*e.g.* cruise conditions for an airliner). Adaptive control algorithms can be employed, in this context, to (1) automatically identify the system dynamics, and (2) adapt to slowly-varying conditions in the fluid dynamic system. The Filtered-x Least Mean Squares (Fx-LMS) algorithm is one that has proven itself in the literature both for acoustic noise attenuation [4] and control of convective harmonic flow disturbances [6].

The overarching goal of this work is to build a controller that is able to effectively identify and target large-scale (low-frequency) velocity fluctuations in a turbulent boundary layer (TBL). These space-coherent fluctuations are most intense in the logarithmic region and they are strongly correlated to main skin-friction-drag-producing mechanisms [8]. As such, the intention is to indirectly control (minimize) skin-friction drag, by way of controlling the off-the-wall velocity fluctuations. With the objective of minimizing the controller's form drag and, thus, maximizing net power savings, sensing and actuation hardware need to be embedded in the wall. In particular, it has been shown that wall-pressure can be employed to identify the velocity fluctuations to-be-targeted [1, 9]. In fact, spatio-temporal correlations between streamwise velocity and wall-pressure have revealed low but significant coherence between the low-frequency content of the wall-pressure signal and the velocity in the logarithmic region, which can be attributed to the passage of large-scale motions [3].

Spectrally, turbulence-induced wall-pressure fluctuations are broadband in nature [5] and a complex target for an adaptive controller to identify. Therefore, this paper illustrates the deployment of an adaptive Fx-LMS control algorithm to a TBL, strongly modulated by a Kármán vortex street originating from a wall-parallel spanwise-oriented cylinder. This introduces a harmonic forcing and, thus, a strong degree of coherence to the broadband TBL system. This is taken as a starting point for the development and evaluation of the Fx-LMS algorithm, before generalizing the control framework to broadband turbulence.

EXPERIMENTAL IMPLEMENTATION

Experiments were carried out in an open-return wind tunnel facility (W-Tunnel) at the Delft University of Technology. The facility has a cross-sectional area of $0.6 \times 0.6\,\mathrm{m}^2$ at the inlet of the test section and the freestream velocity was set at $U_\infty = 15\,\mathrm{m/s}$. A test section with a length of 3.75 m is employed, comprising a flexible ceiling configured for a zero-pressure-gradient streamwise development of the flow. At a distance of 2.90 m downstream of the trip (P40-grit sandpaper), the TBL attains a thickness of $\delta = 0.07\,\mathrm{m}$. Further details of the setup can be found in the literature [2].

A coordinate system (x, y, z) is used that has its origin on the wall at the spanwise center of the test section, at a distance of 2.90 m downstream of the trip. To harmonically force the flow, a wall-parallel, spanwise-oriented cylinder was installed, having a diameter of $D = 0.032\,\mathrm{m}$. It was positioned at $x = -7.3D$, with its center line at $y = 1.5D$. A schematic of the experimental setup is presented in fig. 1a.

Input sensors consisted of eight GRAS 46BE quarter-inch free-field CCP microphones, having a nominal sensitivity of 3.6 mV/Pa. Seven of them were integrated in a pinhole-cavity, flush-mounted to the wind tunnel wall at $x = -5.3D$. Additionally, a single microphone was sting-mounted into the freestream flow to monitor acoustic noise and to facilitate real-time noise-removal. This procedure is based on a real-time projection of all eight instantaneous pressure signals onto pre-identified spatial POD modes. Actuators comprise three wall-normal blowing jets triggered simultaneously, activated by fast-acting on/off solenoid valves, with an exit velocity of $v_{\text{jet}} = 0.8U_\infty$. The actuators are situated at $x = 0$. Finally, error sensors are integrated at $x = 4.3D$ and consist of 7 PUI AOM-5035L-HD3 electret microphones. A noise-correction procedure based on POD was also implemented for this downstream array of sensors.

The control loop runs at a frequency of $f_{\text{loop}} = 2.5\,\mathrm{kHz}$ on a Speedgoat Performance real-time target machine and employs the Fx-LMS algorithm (its block diagram is shown in fig. 1b). Further details regarding the implementation of this control logic can be found in the book of Hansen [4] and will be elaborated upon in the full conference contribution.

For assessment of the controlled flow, time-series of the streamwise velocity component were acquired using hot-wire anemometry (HWA). A TSI IFA-300 constant temperature anemometer (CTA) is used, with a standard Dantec 55P15 boundary layer probe. Data were acquired along a wall-normal profile at $x = 2.15D$ for the uncontrolled and controlled flows.

FLOW RESPONSE TO CONTROL

The response of the flow to control is here presented in terms of streamwise velocity spectra along a wall-normal profile at $x = 2.15D$. Pre-multiplied energy spectra of the streamwise velocity component are shown in fig. 2a, in terms of a spectrogram for the uncontrolled flow: $\phi_{uu}(St^*, y/D)$. Here, St^* refers to the characteristic Strouhal number $St^* = fD/U^*$, with $U^* = 12.5\,\mathrm{m/s}$ being the average streamwise velocity at the y-location of the cylinder axis ($y = 2D$) in the clean turbulent boundary layer (*i.e.*, when no cylinder is installed in the test section). The spectrogram in fig. 2a shows a sharp energy increase around $St^* = 0.22$ ($f = 85\,\mathrm{Hz}$). The high-intensity energy is concentrated, as expected, around the upper and lower shear layers of the cylinder wake [7].

The Fx-LMS algorithm identifies the two FIR kernels (see fig. 1b) in real-time after a short convergence time of $\approx 3\,\mathrm{s}$.

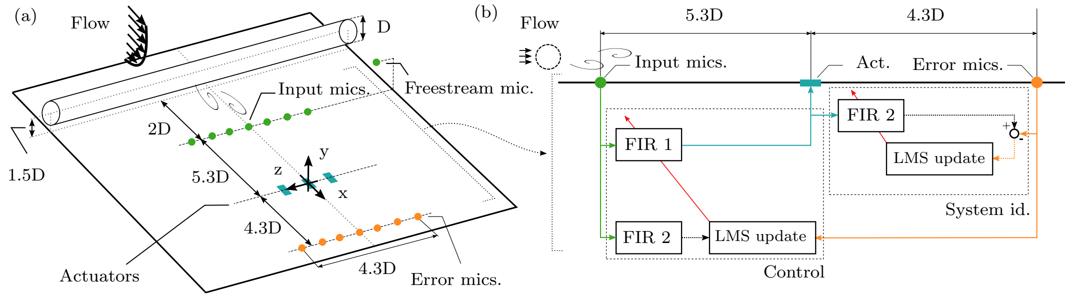

Figure 1: (a) Schematic of the experimental hardware configuration comprising input sensors (green), jet actuators (blue) and error sensors (orange). (b) Fx-LMS control system block diagram, as deployed for the control of cylinder-induced vortex shedding.

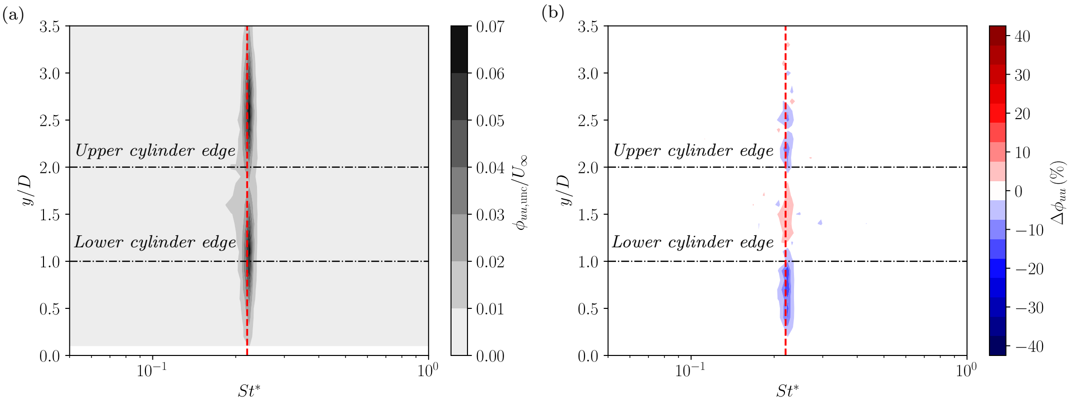

Figure 2: (a) Spectrogram of the uncontrolled flow at $x = 2.15D$, obtained from hot-wire data. (b) Percentage difference in the spectrogram of the controlled flow with respect to the unctrolled case, $\Delta\phi_{uu} = 100 \cdot (\phi_{uu,\mathrm{LMS}} - \phi_{uu,\mathrm{unc}})/\phi_{uu,\mathrm{unc}}$.

Once convergence is achieved, the FIR-kernels are deployed and the effect of the controller on the flow is measured. The percentage difference of the wall-normal spectrogram of the controlled flow, with respect to the uncontrolled case, is presented in fig. 2b. A clear reduction in energy of up to $\approx 39\%$ at $St^* \approx 0.22$ is observed in the region $0.2 \leq y/D \leq 1$. Similar conclusions can be drawn from wall-normal hot-wire velocity profiles acquired at $x = 0$ and $x = 4.3D$, but the results are not presented here for brevity.

Thus far, our results confirm the effective deployment of the Fx-LMS to the cylinder-induced vortex shedding control, as a clear reduction in shedding intensity was measured. In the full conference contribution, a comprehensive set of results will be discussed, touching upon the implementation of the controller, the flow response, and the applicability of the controller to broadband turbulence.

REFERENCES

[1] W. J. Baars, G. Dacome, and M. Lee. Reynolds-number scaling of wall-pressure–velocity correlations in wall-bounded turbulence. *J. Fluid Mech.*, 981:A15, 2024.

[2] G. Dacome, R. Mörsch, M. Kotsonis, and W. J. Baars. Opposition flow control for reducing skin-friction drag of a turbulent boundary layer. *Phys. Rev. Fluids*, 9(6), 2024.

[3] B. Gibeau and S. Ghaemi. Low- and mid-frequency wall-pressure sources in a turbulent boundary layer. *J. Fluid Mech.*, 918:A18, 2021.

[4] C. H. Hansen. *Understanding active noise cancellation.* Taylor & Francis, London, UK, 1st edition, 2001.

[5] J. C. Klewicki, P. J. A. Priyadarshana, and M. M. Metzger. Statistical structure of the fluctuating wall pressure and its in-plane gradients at high Reynolds number. *J. Fluid Mech.*, 609:195–220, 2008.

[6] M. Kotsonis, R. Giepman, S. Hulshoff, and L. Veldhuis. Numerical study of the control of Tollmien–Schlichting waves using plasma actuators. *AIAA J.*, 51(10):2353–2364, 2013.

[7] T. Michelis and M. Kotsonis. Interaction of an off-surface cylinder with separated flow from a bluff body leading edge. *Exp. Therm. and Fl. Sc.*, 63:91–105, 2015.

[8] N. Renard and S. Deck. A theoretical decomposition of mean skin friction generation into physical phenomena across the boundary layer. *J. Fluid Mech.*, 790:339–367, 2016.

[9] C. Sanmiguel Vila and O. Flores. Wall-based identification of coherent structures in wall-bounded turbulence. *J. Phys.: Conf. Series*, 1001 012007, 2018.

37

ERCOFTAC
European Drag Reduction and Flow Control Meeting – EDRFCM 2024
September 10^{th}–13^{th}, 2024, Turin, Italy

EFFECT OF THE WALL-SENSOR AVAILABILITY ON THE FLOW FIELD ESTIMATION WITH 3D-GANS IN TURBULENT WALL-BOUNDED FLOWS

A. Cuéllar
Departamento de Ingeniería Aeroespacial, Universidad Carlos III de Madrid, 28911 Leganés, Spain

A. Ianiro
Departamento de Ingeniería Aeroespacial, Universidad Carlos III de Madrid, 28911 Leganés, Spain

S. Discetti
Departamento de Ingeniería Aeroespacial, Universidad Carlos III de Madrid, 28911 Leganés, Spain

INTRODUCTION

The advancements in flow sensing are crucial for implementing active flow control strategies within turbulent flow layers. In wall-bounded flows, the implementation of non-intrusive sensors within the wall is often the only option available. Linear methods have been to some extent successful in tackling different problems about flow reconstruction within channel flows. In particular, flow estimations from wall-based measurements have yielded accurate results up to the logarithmic layer [2]. The advent of artificial intelligence has opened new avenues for developing methodologies that can capture non-linearities and enhance estimation accuracy. Notably, recent studies have focused on estimating the fluctuation velocity field in wall-parallel planes at various distances from the wall [4, 5, 3]. Generative adversarial networks (GANs) have proven to be particularly effective among the various deep neural network architectures. GANs were able to accurately estimate turbulent flow fields from instantaneous measurements of wall pressure and wall shear stresses, even when only coarse wall measurements were available, in an open channel flow at a Reynolds number $Re_\tau = 180$ [5]. These works performing flow reconstructions in wall-parallel planes have motivated the recent development of 3D-GANs [1], which allow reconstructing the flow field in a three-dimensional region. To do so, this methodology introduces additional complexities to previously developed GANs for planar reconstructions. The approach proposed by Cuéllar et al. [1] is assessed employing Direct Numerical Simulation (DNS) data at with complete wall information. In a practical scenario, however, data might be affected by noise and the available sensor resolution may be lower. The present work will assess these aspects.

MOTIVATION: 3D-GAN

Following Cuéllar et al. [1], a dataset generated from a Direct Numerical Simulation (DNS) of a periodic turbulent channel flow at $Re_\tau = 200$ is leveraged. The simulation domain has dimensions πh (streamwise), $2h$ (wall-normal) and $\pi/2h$ (spanwise), on a grid of $[64\times128\times64]$. The network takes as input $[64\times64]$ mappings of pressure and shear stresses in the streamwise and spanwise directions $[p_w, \tau_{w_x}, \tau_{w_z}]$ measured at the bottom wall of the channel. The network estimates the fluctuation velocities $[u, v, w]$ in the bottom half of the channel in a $[64 \times 64 \times 64]$ grid. The DNS wall and flow data with which the network works are centred and normalized by their standard deviation for each wall-normal coordinate. This innovative approach brings several benefits. Firstly, a single trained network can accurately estimate an entire spatial region, whereas 2D methods often require training multiple networks independently for different wall-normal distances. Furthermore, the integration of 3D convolution layers in the 3D-GAN ensures spatial continuity, a feature lacking in 2D approaches. Besides, despite the 3D-GAN having a higher number of trainable parameters compared to previous 2D GANs, it remains within a similar order of magnitude. This results in a significant reduction in computational resources, as opposed to the need to train 64 separate 2D GANs to achieve comparable estimations.

The 3D representation of the flow enables direct analysis of turbulent patterns. Identifying sweeps and ejections holds particular interest for applications in flow control. The network's capability to perform flow predictions successfully depends not only on the distance from the wall but also on other factors related to wall interactions. The 3D-GAN can reconstruct a wall-attached structure that extends deep towards the centre of the channel with reasonable accuracy, while it may not effectively detect wall-detached events. Thus, the network effectively filters out turbulent coherent structures that lack correlation with the instantaneous sensing at the wall.

METHODOLOGY

This 3D approach introduces the challenge of managing a substantial volume of data, involving $[64 \times 64 \times 3]$ wall inputs per instantaneous frame. Handling such data becomes particularly demanding if the technique is to be applied in scenarios requiring high-frequency data acquisition and processing, such as active control purposes. Moreover, the complexity of deploying a sensor setup with three types of sensors on overlapping grids adds another layer of challenge. Given this situation, a series of cases is proposed in which the network would operate under less ideal conditions, closer to the real conditions that might occur in an experimental application or a prototype based on this methodology. For all these cases, the requirements for estimating the three components of the velocity field in the same domain would be maintained:

- Reduction in the number of sensors by downsampling. The grid that places the sensors in the wall is progressively coarsened, both in the streamwise and spanwise directions.
- Reduction in the number of sensors (as previous point)

with different downsampling factor along each direction to assess the implications of various sampling of scales.

- Reduction in the number of sensors by measuring only one physical quantity, instead of three. This point is combined with the first one, opening several varied possibilities.

- Introduction of noise in the measurements over the cases considered in the first point.

RESULTS & CONCLUSIONS

This study includes an evaluation of the performance of the 3D-GAN under these different challenging scenarios that might be considered towards a real implementation.

One of the main conclusions found in reference [1] was that, even if the performance of the network degrades as one moves away from the wall, structures with a footprint at the wall are still reasonably identified. In relation to this, in this analysis, we show how the network performance has a strong relation with the quality with which these wall patterns are sampled. This may be more important than the number of sensors used *per se.* In figure 1 the error is reported in form of Mean Squared Error on the inner-scaled streamwise velocity fluctuations as a function of the wall distance y. The superscript $^+$ indicates scaling with inner quantities. The case with 32×32 sensors, which is able to capture most of the wall spectra with respect to 64×64 sensors, can provide us with a reconstruction of almost the same quality. When the wall patterns are not so well preserved and there is a substantial loss of scales, as with 16×16 or 8×8 sensors, differences in the error become significant.

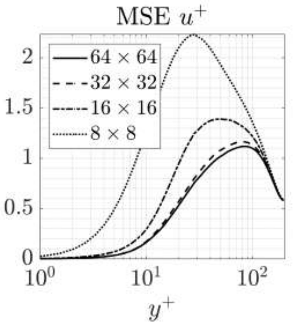

Figure 1: Wall-normal profile of the MSE of the u^+ estimation for cases with different wall-input resolution.

When reconstructions are carried out with just one type of sensor, there is an additional penalty as part of the information is not accessible to the network. The different degrees of correlation of the wall quantities with the flow field affect significantly the network performance. However, the importance of wall patterns and how well they are sensed with the amount of sensors used also plays a very important role, while the scales of each type of wall pattern are different. The patterns of τ_{w_x} are characterized by elongated streaks and are substantially larger than those observed in p_w. Our results show that p_w provides the best performances (except for a small region very close to the wall where τ_{w_x} offers a better correlation) provided that the number of sensors is large (i.e. close to full resolution). However, with downsampled sensors the reconstructions from τ_{w_x} are better than those from p_w, as the τ_{w_x} wall-spectrum is much better preserved. Regarding τ_{w_z}, it offers the worst correlation independently of the resolution employed. However, it is drastically affected by the downsampling, as it has the smallest wall patterns.

The analysis of reconstruction performances in the presence of noise revealed that the error of the reconstructions increased with the level of noise introduced, although surprisingly the effect is more significant for the cases with higher resolution of wall sensor distribution. The additional penalty due to the noise introduced in the measurements is progressively attenuated with downsampling.

The amount of wall information accessible for the network can give us an order of the accuracy of the reconstruction, but there are other elements that can strongly influence its quality. On the one side, we have the wall quantities to which the network has access. The correlation with the flow field is not the same for all of them, element that may limit the network's reconstruction capability. On the other side, the resolution with which the network has access to these quantities can restrain the degree of wall patterns felt by the network, which may alter the real footprint of structures on the wall.

ACKNOWLEDGEMENTS

This contribution has received funding from the Spanish Ministry of Universities under the Formación de Profesorado Universitario (FPU) 2020 programme, and from the European Research Council (ERC) under the European Union's Horizon 2020 research and innovation programme (grant agreement No 949085).

REFERENCES

[1] A. Cuéllar, A. Güemes, A. Ianiro, Ó. Flores, R. Vinuesa, and S. Discetti. Three-dimensional generative adversarial networks for turbulent flow estimation from wall measurements. *J. Fluid Mech.*, doi:10.1017/jfm.2024.432, 2024.

[2] M. P. Encinar and J. Jiménez. Logarithmic-layer turbulence: A view from the wall. *Phys. Rev. Fluids*, 4(11):114603, 2019.

[3] L. Guastoni, A. Güemes, A. Ianiro, S. Discetti, P. Schlatter, H. Azizpour, and R. Vinuesa. Convolutional-network models to predict wall-bounded turbulence from wall quantities. *J. Fluid Mech.*, 928:A27, 2021.

[4] A Güemes, S Discetti, and A Ianiro. Sensing the turbulent large-scale motions with their wall signature. *Phys. Fluids*, 31(12), 2019.

[5] A. Güemes, S. Discetti, A. Ianiro, B. Sirmacek, H. Azizpour, and R. Vinuesa. From coarse wall measurements to turbulent velocity fields through deep learning. *Phys. Fluids*, 33(7), 2021.

 # 38

ERCOFTAC
European Drag Reduction and Flow Control Meeting – EDRFCM 2024
September 10th–13th, 2024, Turin, Italy

TURBULENT CHANNEL FLOW – A MEASUREMENT TECHNIQUE COMPARISON

R. Leister, D. Gatti, B. Frohnapfel, J. Kriegseis
Institute of Fluid Mechanics (ISTM), Karlsruhe Institute of Technology (KIT), 76131 Karlsruhe, Germany

INTRODUCTION

The evaluation of drag reduction in internal flows in experimental set-ups either relies on global pressure drop measurements or on the direct measurement of the wall-shear stress. The latter allows to asses local wall shear stress information, which is particularly interesting for control approaches, where the control effort results in spatially non-uniform near-wall flow conditions. Direct measurements of the skin friction can rely on oil-film interferometry on smooth wall surfaces, which can, however, not be applied in many control scenarios including riblets or plasma-based actuation. In addition, the drag behaviour in non-equilibrium flow conditions is of interest such that a direct evaluation of the skin friction drag is required, since no fitting of the measurement data to a generic velocity profile (which requires outer layer similarity) is applicable.

A variety of techniques exists, that allow the direct measurement of the wall shear stress (cp. [8]). In general, this resorts to a determination of the near-wall mean velocity gradient and the dynamic viscosity. Due to the small spatial scales of near-wall velocity gradients high spatial resolution and the determination of the wall location are of utter importance. In the present contribution we focus on optical measurement methods. For those techniques, a precise localisation of the wall is a non-straightforward, but often an iterative process, where different means exist – from the reflections within the raw data image to the shifting of the extracted velocity profile.

We aim at identifying the measurement technique that enables the best assessment of skin-friction drag along with (possibly simultaneous) flow field measurements across the entire channel flow. To asses the measurement quality in a turbulent channel flow while excluding the challenge of the correct wall localisation, the diagnostic plot introduced by Alfredsson and Örlü [1] is employed. The present contribution takes the findings of several optical measurements conducted at the turbulent channel measurement facility located at ISTM in Karlsruhe and compares them to each other, regarding their suitability and practicability, the retrieved findings and their costs in terms of time and money. The techniques under consideration are *Stereo Particle Image Velocimetry* (Stereo-PIV), *Laser Doppler Velocity Profile Sensor* (LDV-PS), *Defocusing Particle Tracking Velocimetry* (DPTV) and Lagrangian Particle Tracking measurements with the *Shake-the-Box* (STB) method.

EXPERIMENTAL SET-UP AND METHODOLOGY

Figure 1 shows the experimental facility with physical dimensions, where all four measurements techniques came into operation. The coordinate x serves as streamwise direction, while y represents the wall-normal coordinate. The channel dimensions are set to a height H of 25.2 mm (semi channel height $h = 12.6\,\mathrm{mm}$), a width w of 300 mm and an entire length of 4000 mm. As test case a low Reynolds number is chosen, for the possibility to compare with numerical data and to receive a viscous length scale with a certain acceptable spatial extent. As centerline velocity a value of $U_{\mathrm{cl}} = 8.4\,\mathrm{m/s}$ is chosen, which corresponds to a channel Reynolds number $Re_{\mathrm{cl}} = U_{\mathrm{cl}}h/\nu \approx 7,000$. The viscous scaling could be quantified with the velocity $u_\tau = \sqrt{\tau_{\mathrm{w}}/\rho} = 0.42\,\mathrm{m/s}$ and a friction Reynolds number of $Re_\tau \approx 350$. The viscous length scale δ_ν can consequently be stated as $\sqrt{\nu/u_\tau} = 36\,\mu\mathrm{m}$. Given by these parameters we expect a viscous region to be located within the first half millimetre of the wall distance.

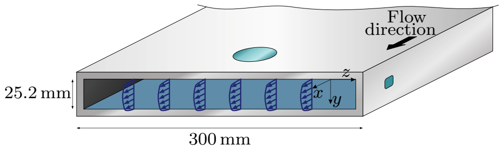

Figure 1: Sketch of the experimental facility with the used coordinate system $\{x, y, z\}$, the physical dimensions and optical accesses.

A window in the top plate with an open diameter of 90 mm, serves as access for the cameras and the LDV-laser, while a window on the side acts as entrance for the laser during PIV and STB measurements. For the Stereo-PIV measurements the cameras were positioned close to the outlet. As seeding fluids di-ethyl-hexyl-sebacate (DEHS) and PIV-light are used, which both lead to a typical droplet diameter in the range of $\approx 1\,\mu\mathrm{m}$. A summary of the technical equipment used for the different experimental campaigns is given in Table 1.

Meas. technique	Equipment
Stereo-PIV [2]	2 × *Photron* SA4 cameras, *Quantronix Darwin Duo* high-speed Laser
LDV-PS [6, 7]	ILA R&D LDV-PS system with Bragg-shift
DPTV [4]	1 × *PCO Edge* 5.5 camera, *Quantel Evergreen* laser
STB [3]	4 × *Phantom* v1840 camera, *Photonics Industries* high speed laser (DM2-100-532-DH)

Table 1: Overview of the different techniques and the employed equipment used for the present comparison. When data were already published, the related reference is cited.

RESULTS

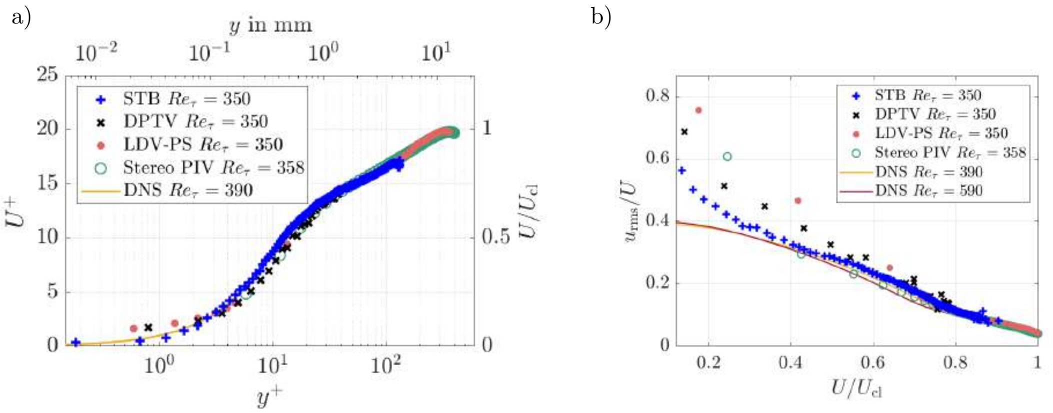

Figure 2: Experimental results: a) ensemble-averaged velocity distribution converted in viscous units with additional physical coordinates on the upper and right axes. b) Diagnostic plot for all compared techniques of ensemble-averaged velocity profiles shown in 2a) and two direct numerical simulations (DNS) [5] as reference.

Figure 2 shows the mean velocity in stream-wise direction u over the wall distance y with a viscous unit normalisation and a diagnostic plot, where the local stream-wise velocity u is normalised with the centerline velocity U_{cl} on the abscissa and the root mean square (rms) of the fluctuations is normalised with the local stream-wise velocity u on the ordinate. Figure 2a) shows that all measurement techniques are able to properly depict the mean flow in viscous units. The achieved plus-unit range of the results demonstrate a general applicability of all considered techniques, since both the logarithmic layer and – at least partially – the viscous sublayer of the turbulent channel flow could be resolved in terms of spatial extent. The STB-technique, due to the large amount of samples, is able to depict statistically-converged data for values of $y^+ = 1$. For the Stereo-PIV measurements the closest spatial point is at $y^+ = 5$, caused by the interrogation-window size, but the technique is able to depict the entire half-channel, including a precise determination of the centerline velocity U_{cl}. Figure 2b) reveals the quality of a precise estimation of the fluctuating movement in a statistical sense. Below $U/U_{\mathrm{cl}} < 0.4$ the results of all experimental techniques reveal an (artificially) increased rms-level, which is caused by an increased contribution of measurement uncertainty close to the wall. The STB-results start to deviate significantly at $U/U_{\mathrm{cl}} < 0.25$. The DPTV-results show an overall slightly increased fluctuating level, which might be accounted for with a finer ensemble-averaging.
The LDV-PS results show velocity-dependent uncertainties, which become particularly noticeable in proximity of the wall where the velocity is low, as already discussed in detail by [7]. This leads in consequence to an comparably early deviation from the DNS data set.

These observations and limitations consequently deserve further investigation so as to uncover their origin and consequences for the evaluation of turbulent channel flows. The presentation will include more detailed data close to the wall to bring these data sets in relation to underlying physical phenomena. Furthermore, a detailed analysis of additionally acquired information for each technique will be given.

REFERENCES

[1] P.H. Alfredsson and R. Örlü. The diagnostic plot—a litmus test for wall bounded turbulence data. *European Journal of Mechanics-B/Fluids*, 29(6):403–406, 2010.

[2] M.T. Hehner, L.H. Von Deyn, J. Serpieri, S. Pasch, T. Reinheimer, D. Gatti, B. Frohnapfel, and J. Kriegseis. Stereo piv measurements of oscillatory plasma forcing in the cross-plane of a channel flow. In *14th International Symposium on Particle Image Velocimetry*. Illinois Institute of Technology (Illinois Tech), 2021.

[3] J. Kriegseis, R. Leister, T. Rockstroh, R. Beslać, and B. Frohnapfel. Turbulent channel flow diagnostics by means of shake-the-box (stb): Flow structures and sublayer profiles. In *21^{st} International Symposium on Application of Laser and Imaging Techniques to Fluid Mechanics, Lissabon, Portugal, 8.-11. Juli 2024*, 2024.

[4] R. Leister, S. Pasch, and J. Kriegseis. Defocusing ptv in a turbulent channel flow - near-wall characteristics. In *15th International Symposium on Particle Image Velocimetry-ISPIV 2023*. California State University, 2023.

[5] R.D. Moser, J. Kim, and N.N. Mansour. Direct numerical simulation of turbulent channel flow up to $Re_\tau = 590$. *Physics of Fluids*, 11(4):943–945, 1999.

[6] S. Pasch, D. Gatti, R. Leister, R. Örlü, B. Frohnapfel, and J. Kriegseis. Measurements in a turbulent channel flow by means of an LDV profile sensor. In *EDRFCM 2022, Paris, France*, 2022.

[7] S. Pasch, R. Leister, D. Gatti, R. Örlü, B. Frohnapfel, and J. Kriegseis. Measurements in a turbulent channel flow by means of an ldv profile sensor. *Flow, Turbulence and Combustion*, 2023.

[8] R. Örlü and R. Vinuesa. Instantaneous wall-shear-stress measurements: advances and application to near-wall extreme events. *Measurement Science and Technology*, 31(11), 2020.

39

ERCOFTAC
European Drag Reduction and Flow Control Meeting – EDRFCM 2024
September 10th–13th, 2024, Turin, Italy

INTERACTION OF TURBULENT BOUNDARY LAYER WITH VISCOELASTIC COATING

G. Voropaiev
Institute of Hydromechanics, NAS of Ukraine, 03057 Kyiv, Ukraine

Ya. Zagumennyi
Institute of Hydromechanics, NAS of Ukraine, 03057 Kyiv, Ukraine

INTRODUCTION

The revealed laws of origin and development of natural disturbances in a laminar boundary layer during the transition process to turbulence have significantly reduced the number of studies on laminar boundary layer control for drag reduction at high Reynolds numbers. Now, most studies aimed at search and development of drag reduction methods for flows around moving objects without separation are devoted specifically to turbulent flow regime. The results of these studies have already been applied to real objects, e.g., Lufthansa aircraft uses structured surfaces based on the Shark Skin Technology for turbulent drag reduction [1].

The studies on dynamic interaction of flow and viscoelastic coating have shown that the dominant parameter describing the coating effect on the turbulent boundary layer characteristics is the equivalence factor between flow velocity and shear wave propagation speed in the coating, $U_0 \sim \sqrt{\mu/\rho}$ [2,3]. So, for flow velocity values greater than 50 m/s, viscoelastic coatings are ineffective, but for those in the range of 20÷25 m/s it is possible to offer a fairly wide range of viscoelastic materials which can satisfy this condition with drag reduction up to 20%. These results were obtained for viscoelastic coatings with constant thickness and high viscosity of the material, when the coating surface oscillations are almost aperiodic, i.e., in a turbulent boundary layer, pulsation energy diffusion in the direction of the surface due to energy dissipation in the viscoelastic coating significantly unloads the layer of constant turbulent stresses. At the same time, the aperiodic waves arising on the surface of a coating with constant thickness propagate both up- and downstream, thus disturbing the flow and making the coating surface dynamically rough.

This report presents numerical results on formation of forced oscillations in a viscoelastic coating with variable thickness under action of a pulsating load and describes the conditions when a directional structure of the wave field can be generated on the coating surface.

PROBLEM STATEMENT

In the frame of the constructed model, conjugation of the fluid and deformable solid mechanics problems is implemented by evaluating the amount of turbulent pulsation energy pumped into the viscoelastic coating, $Y = -p' \cdot u_2$, and the fraction of this energy absorbed by the coating, $Q = D \cdot t$. The difference between these values is the energy returned to the flow by the disturbing surface waves, $E_{surf} = Y - Q$. When $E_{surf} \to 0$, all the pulsation energy perceived by the viscoelastic coating are dissipated, and there is no disturbing effect of the coating on the flow. The principal idea of this study is that the surface waves of the viscoelastic coating not only disturb the flow but can also excite the boundary layer natural disturbances, thereby contributing to filling the turbulence pulsation spectrum with low-frequency components.

The parameters of a local impulse load applied on the viscoelastic coting surface are consistent with the typical space-time scales of the most intense turbulent pulsations and can be approximately determined by the average values of intensity, duration and linear scales of the ‘bursts’ in the turbulent boundary layer: $p'_{avg} \sim K_p \cdot \rho_f \cdot u_*^2$, $t_0 \sim 25\,\nu/u_*^2$, $2l = 100\,\nu/u_*$, where $u_* = \sqrt{\tau_w/\rho_f}$ is the dynamic velocity, τ_w is the shear stress on the surface, $K_p = 2.5 \div 6$ is the Kreichnan parameter connecting the pressure pulsation intensity with the shear stress, ν and ρ_f is the fluid density and kinematic viscosity respectively. The schematic sketch of the problem on unsteady deformation of viscoelastic material under action of turbulent pressure pulsations within a single cell of structured surface with finite length and width and variable thickness is shown in Fig. 1.

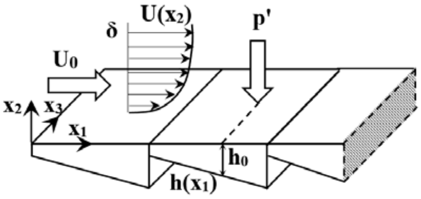

Figure 1. Schematic sketch of the problem

The kinematic and dynamic characteristics of the viscoelastic layer are determined from the solution of the linearized equations of the continuous solid medium movement written in Lagrange variables. The model for viscoelastic medium is based on the hypothesis of instantaneous dependence of stress tensor on the entire time history of changes in strain tensor, which can be formally expressed as an integral relation between stresses and strains [4]. The resulting system of integral-differential equations is solved numerically based on the finite-difference method and iterative procedure of the differential operator splitting by the spatial variables.

NUMERICAL RESULTS

Impulse application of a local load on the surface of viscoelastic layers with constant and variable thickness leads to the formation of unsteady wave motion, the characteristics of which depend on the mechanical and geometric parameters of the coating and the load parameters (Fig. 2). In the case of the viscoelastic coating with variable thickness, a directed surface wave field is formed on the surface of the coating oriented in the direction of its thickening (Fig. 2, b). This situation is similar to the case when an active traveling wave is generated on the surface in the flow direction with the phase speed, $U_{TS}{\sim}0.5U_0$, which can excite the natural disturbances of the boundary layer and significantly affect the laminar-turbulent transition processes [5].

Instantaneous integral values of the perceived, kinetic, potential and dissipated energy components of the viscoelastic layer are in strict instantaneous balance, manifesting a complex unsteady structure of the interacting reflected normal and shear waves (Fig. 3, a). As Fig. 3, b shows, the viscoelastic coating practically stops absorbing the impulse load energy after the reflected normal wave reaches the coating surface. This finding makes enables determining the condition of maximum load energy absorption depending on duration of the load action, local thickness of the viscoelastic coating at the place of its application, and mechanical parameters of the viscoelastic material.

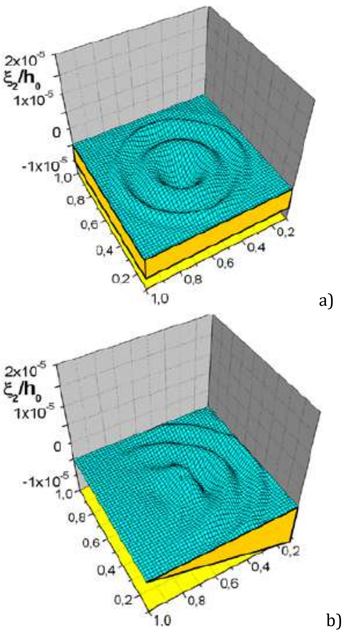

a)

b)

Figure 2. Instantaneous structure of surface deformations of the viscoelastic coatings with constant (a) and variable (b) thickness under action of a local impulse load

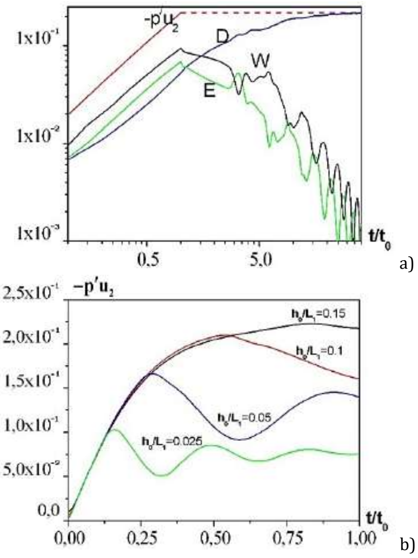

a)

b)

Figure 3. Energy balance in the viscoelastic coatings (a) and amount of impulse loading energy absorbed by the viscoelastic coating depending on its local thickness (b)

CONCLUSION

The constructed numerical model for local interaction of turbulent flow disturbances with a viscoelastic coating demonstrates its absorption capacity for the energy of turbulent boundary layer pulsations, as well as the possibility of generating a directed wave motion of the surface of the coating by changing its structure. It is demonstrated that a directed long-wave field can be formed on the surface of the viscoelastic coating with the proposed structure as a response to turbulent flow pressure pulsations, which can cause a change in the near-wall turbulence spectrum and generation of the propulsive component of thrust.

REFERENCES

[1] S. Fan, X. Han, Y. Tang, Y. Wang, and X. Kong. Shark Skin – An Inspiration for the Development of a Novel and Simple Biomimetic Turbulent Drag Reduction Topology. *Sustainability*. 14:16662, 2022.

[2] G. Voropaev, and C. May. Design of Viscoelastic Coatings to Reduce Turbulent Friction Drag. Patent number 01927412.5-2422-US0140322, 1 March 2001.

[3] C. Zhang, J. Wang, W. Blake, and J. Katz. Deformation of a Compliant Wall in a Turbulent Channel Flow. *J. Fluid Mech*. 823:345–390, 2017.

[4] R. M. Christensen. *An Introduction to Theory of Viscoelasticity*. Academic Press New York and London, 1971.

[5] G. A. Voropaiev, and Ya. V. Zagumennyi. Boundary Layer Perturbations Generated by Locally Deformable Surface. *Int. J. Fluid Mech. Res.*, 46(4):325–335, 2019.

 # 40

ERCOFTAC
European Drag Reduction and Flow Control Meeting – EDRFCM 2024
September 10$^{\text{th}}$–13$^{\text{th}}$, 2024, Turin, Italy

THE ROLE OF ROUGHNESS IN TURBULENT CHANNEL FLOWS OVER ELASTIC WALLS

Morie Koseki[‡]*

M. S. Aswathy[‡]

Marco Edoardo Rosti[‡]
[‡]Complex Fluids and Flows Unit, Okinawa Institute of Science and Technology Graduate University (OIST), 1919-1
Tancha, Onna, Okinawa 904-0495, Japan

INTRODUCTION

Turbulent flow over compliant walls is a complex problem due to the mutual interaction between the deformable walls and turbulence. The presence of the compliant wall has been shown to increase the drag significantly due to the enhancement of the wall-normal fluctuation, leading to a decay in the streamwise coherent structures and increased spanwise coherency [3]. In addition, the wave propagation inside/above the elastic wall can enhance the turbulent intensity while reducing the streamwise disturbances [1, 5].

Compared to the studies on rigid-complex walls, the literature investigating wall elasticity effects remains relatively limited. Existing studies on elastic walls focused mostly on the whole elastic wall effect; however, this can be a combination of many undistinguished effects, i.e., roughness effects (due to the wall deformation by the hydrodynamic force), non-zero wall-normal fluctuations (comes from the wall movement of the elastic wall), and material acceleration (owing to the wave advection). In light of the above observation, we compare results from direct numerical simulations of turbulent flow over elastic and rough walls (shall be detailed later).

WALL CONFIGURATION

We consider elastic and rough walls to understand the interaction effects of wall elasticity. The elastic wall is characterized by the modulus of the transverse elasticity $G/(\rho U_b^2) = 0.5$; the correspondent rough wall is obtained from an instantaneous surface undulation of the former elastic wall, wherein the fluid-solid interaction contribution is eliminated. We consider two such configurations of the rough walls, addressed as Rough 1 and Rough 2 here, corresponding to different instants in time. To evaluate the surface undulations and their dominant features, we report the one-dimensional power spectrum density functions (PSD) of the roughness height along the homogeneous directions (streamwise and spanwise directions) as a function of wavenumber k_i normalized by the computational domain length L_i. From Figure 1, the PSDs of both the elastic and rough walls show a similar distribution, implying similar wall configurations. The undulations do not show any dominant peak along the span, while those along the streamwise direction show a peak at wavenumber $k_x = 5.17/h$. This corresponds to a wavelength $\lambda_x = 2\pi/k_x \approx 1h$. This length scale obtained from the PSD is also consistently observed from the surface visualization.

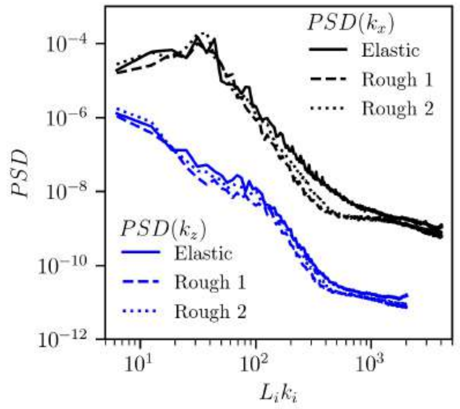

Figure 1: One-dimensional power spectrum density (PSD) as a function of the wavenumber. The magnitude of $PSD(k_z)$ is multiplied by 10^{-2}. The line style represents the different cases: elastic (solid line), Rough 1 (dashed line), and Rough 2 (dotted line). The line color corresponds to the direction of the Fourier transform: streamwise (black) and spanwise (blue).

FORMULATION AND NUMERICAL PROCEDURE

The turbulent flow over complex walls has been simulated by solving the incompressible Navier–Stokes equations. We adopt a neo-Hookean solid satisfying the incompressible Mooney-Rivrin law as a model of the elastic wall. For coupling the two phases, we apply the one-continuum formulation through the volume-of-fluid approach, introduced by [4]. The continuity at the interface is enforced by the velocity and wall-normal traction equality in both phases. The governing equations are discretized and integrated as formulated in [4], and more details and validations of the numerical methods are provided in [3, 4].

All cases have the same computational domain size $6h \times 2.5h \times 3h$, being used with a uniform grid, $1296 \times 540 \times 648$ grid points in streamwise (x), wall-normal (y), and spanwise (z) directions. These settings and related resolutions are similar to [1, 3]. The domain is set such that there is an impermeable rigid wall at the bottom of the channel and a complex wall at the top, whose height is $0.5h$; the interface between fluid and solid is $y = 2.0h$. A constant flow rate condition is imposed

---

*Email for correspondence: morie.koseki@oist.jp with the bulk velocity $U_b = 1$, and the streamwise pressure gradient is calculated at every time step.

RESULTS

We start our analysis by comparing the Reynolds shear stress components with that of a normal channel (represented by symbols) in Figure 2, which shows the streamwise $(\overline{u'u'})$, spanwise $(\overline{w'w'})$, wall-normal $(\overline{v'v'})$, and the shear $(\overline{u'v'})$ components. The thick lines correspond to the elastic walls, and the dashed lines correspond to the rough walls. For both the rough and elastic walls, it can be observed that the magnitude of all components increases, and the distribution becomes more skewed w.r.t the rigid-smooth channel. Despite the Reynolds shear stresses getting strongly enhanced, it should be noted that the mutual fluid-solid interaction has curbed the growth of the streamwise component, with its values comparable to that of the rough channel, thus suggesting a reduction of the streamwise coherent structures in the elastic-wall case.

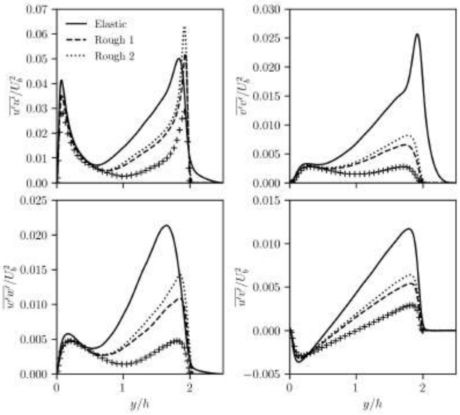

Figure 2: Reynolds shear stress components as a function of the wall-normal direction. The line style is the same as in Figure 1. The symbol represents the normal channel case, from [2]

Next, we look at the instantaneous contour of the streamwise velocity fluctuations at $y = 1.8h$ (position corresponding to the maximum deformation of the elastic wall), shown in Figure 3. While the elastic cases (Figure 3(a)) show dominant spanwise coherency, the rough cases (Figure 3(b, c)) demonstrate organized structures in the streamwise direction. Although the initial wall undulations had equivalent features in the streamwise and spanwise directions, it is evident that the interaction between the fluid and wall for the elastic case played a role in weakening the streamwise fluctuations, corresponding to the fragmented streamwise structures (Figure 3(a)); however, surface roughness does not seem to contribute significantly to the modification of the flow structures (Figure 3(b, c)).

CONCLUSION

We performed turbulent channel flow simulations over elastic and rough walls to understand the mutual interaction effects caused by the elastic wall. The fluid-solid interaction significantly enhances the Reynolds shear stress components except for the streamwise fluctuations. The two-way interaction leads to flow structure alternation regardless of the surface roughness; the flow structures are seen to be more organized along the spanwise direction in the presence of elastic walls, unlike the rough walls, which have streamwise-oriented structures.

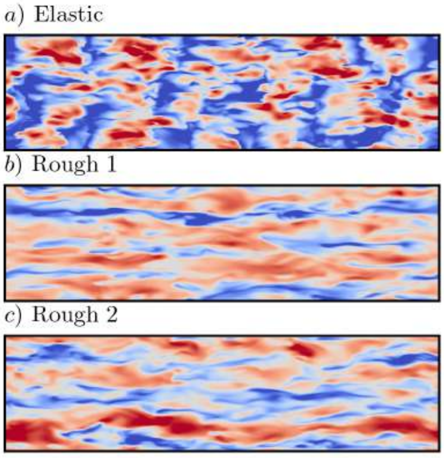

Figure 3: Instantaneous contour of the streamwise velocity fluctuations at $y/h = 1.8$ in the $x - z$ plane. The color represents the range of the velocity fluctuations from -0.35 (blue) to 0.35 (red). The flow direction is from left to right.

REFERENCES

[1] Amir Esteghamatian, Joseph Katz, and Tamer A Zaki. Spatiotemporal characterization of turbulent channel flow with a hyperelastic compliant wall. *Journal of Fluid Mechanics*, 942:A35, 2022.

[2] John Kim, Parviz Moin, and Robert Moser. Turbulence statistics in fully developed channel flow at low reynolds number. *Journal of fluid mechanics*, 177:133–166, 1987.

[3] Marco E Rosti and Luca Brandt. Numerical simulation of turbulent channel flow over a viscous hyper-elastic wall. *Journal of Fluid Mechanics*, 830:708–735, 2017.

[4] Kazuyasu Sugiyama, Satoshi Ii, Shintaro Takeuchi, Shu Takagi, and Yoichiro Matsumoto. A full eulerian finite difference approach for solving fluid–structure coupling problems. *Journal of Computational Physics*, 230(3):596–627, 2011.

[5] Jin Wang, Subhra Shankha Koley, and Joseph Katz. On the interaction of a compliant wall with a turbulent boundary layer. *Journal of Fluid Mechanics*, 899:A20, 2020.

 # 41

ERCOFTAC
European Drag Reduction and Flow Control Meeting – EDRFCM 2024
September 10$^{\text{th}}$–13$^{\text{th}}$, 2024, Turin, Italy

TURBULENT DRAG REDUCTION BY FIBROUS PERMEABLE SUBSTRATES

N. Faure, Z. Lu and R. García-Mayoral
Department of Engineering, University of Cambridge, CB2 1PZ Cambridge, UK

MOTIVATION AND BACKGROUND

The reduction of energy consumption and pollutant emissions are deep and growing concerns for transport applications. This has motivated the investigation of several technologies to reduce turbulent skin friction on vehicle surfaces. One particularly successful example is that of riblets [2], small surface grooves aligned in the direction of the flow. Riblets have been studied extensively and have achieved a reasonable degree of maturity in their design. Optimal riblet shapes can achieve up to 10% reduction in friction but, critically, this much reduction can only be achieved by very specific riblet geometries and under nominal conditions, when riblets are perfectly sharp, with performance degrading quickly as their tips wear out. This work focuses on the new concept streamwise preferential anisotropic permeable substrates [1]. The idea is to exploit optimally the drag-beneficial mechanisms present in riblets, while minimizing the effect of the drag-adverse mechanisms. In particular we study permeable coatings made up of fibers aligned in the streamwise direction, as sketched in figure 1 in comparison with riblets. This arrangement offers less resistance to longitudinal than to transverse flows, like riblets do [6], offsetting the wall-normal turbulent momentum transfer and reducing drag. Our previous numerical studies, which resorted to homogenized models to represent the permeable substrate in direct simulations of the overlying flow, indicated potential drag reductions (DR) of order 20-25% at laboratory Reynolds numbers [4], motivating more detailed exploration of the concept with texture-resolving simulations.

In [4], we modeled the permeable substrates using a macroscopic, homogenized approach, characterizing the flow within using the Darcy-Brinkman equations. These equations are derived from the local volume average to the flow, assuming that viscous effects dominate within the substrate and that the volume average is conducted over length scales much larger than the pore size, yet infinitesimal from a macroscopic perspective. The Darcy-Brinkman equations are sufficiently simple that they can be solved analytically. From these, effective boundary conditions for the overlying turbulence at the substrate/free-flow interface can be obtained and imposed on the direct numerical simulation (DNS) of the overlying turbulent flow. The effective boundary conditions greatly reduced the cost of the simulations, since the grid required to resolve the microscale flow within the substrate would have been much finer than that required to resolve the turbulent scales.

The DNS results indicated that, for small pore size, the drag reduction was directly proportional to the difference between the streamwise and spanwise slip lengths, $\ell_x - \ell_z$ [6], and that the optimum occurred for a fixed value of the wall-normal permeability, $\sqrt{K_y^+} \approx 0.4$, as predicted from a linear-stability model for the onset of Kelvin-Helmholtz like rollers just above the substrate. From the Darcy-Brinkman characterisation of the substrate flow, the streamwise and spanwise slip lengths are essentially equal to the respective permeability length-scales, $\sqrt{K_x}$ and $\sqrt{K_z}$. As a result, the maximum drag reduction in the DNSs was observed to be

$$\mathrm{DR}_{\max} \propto \left(\frac{\ell_x - \ell_z}{\sqrt{K_y}} \right) \approx \left(\frac{\sqrt{K_x} - \sqrt{K_z}}{\sqrt{K_y}} \right) = \left(\phi_{xy} - \phi_{zy} \right), \tag{1}$$

where ϕ_{xy} and ϕ_{zy} are the anisotropy ratios $\sqrt{K_x}/\sqrt{K_y}$ and $\sqrt{K_z}/\sqrt{K_y}$. This suggested that optimal substrates would need to be sparse and highly permeable in the streamwise direction x, but with little permeability in the cross plane y-z.

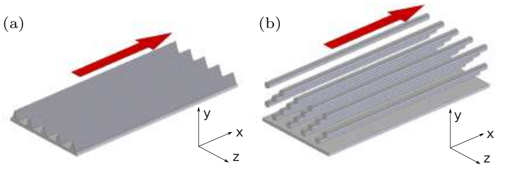

Figure 1: Sketches of drag reducing surfaces. (a) Conventional riblets. (b) Anisotropically permeable coating made up of streamwise-aligned fibers. The red arrows mark the direction of the overlying mean velocity.

The results from [4] showed significant promise and merited further investigation on this concept. In particular, experiments or texture-resolving DNSs were required to gauge whether the modelled boundary conditions were capturing all the relevant physics, and thus producing accurate estimates for the drag reduction.

SLIP LENGTHS

As a first step, we have focused on the actual slip lengths obtained from the texture-resolving computation of the flow within and above the substrate when driven by an overlying tangential shear, and how they compare to those derived from the Darcy-Brinkman model, $\ell_x \approx \sqrt{K_x}$ and $\ell_z \approx \sqrt{K_z}$. As an example, results for the flow in a spanwise-periodic array of fibers are shown in figure 2. The figure compares the velocity field obtained from a texture-resolved computation with that predicted in a Darcy-Brinkman framework. This work shows that the Darcy-Brinkman model yields indeed a good representation of the flow deep within the substrate, but critically it fails at the interface with the free flow, where the requirement that the averaging volume be larger than the pore length scale necessarily breaks down. The flow within is observed to deviate from the Brinkman solution for a depth of the order of the fiber spacing, causing an apparent discontinuity between the macroscale inner flow, as characterized by a Darcy-Brinkman model, and the outer free flow. Even if the thickness of this diverging region is very thin, the resulting slip lengths –and thus the drag reduction– can deviate from the Brinkman predictions by as much as $\sim$30-40%.

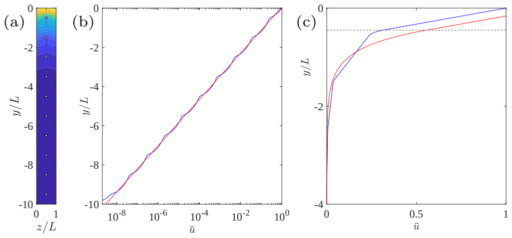

Figure 2: Streamwise velocity driven by an overlying shear for a spanwise-periodic matrix of streamwise-aligned fibres. (a) Velocity field; (b) and (c) —— , spanwise-averaged velocity; —— , Darcy-Brinkman solution with its constants, the permeability and effective viscosity, obtained to best fit the spanwise-averaged flow. In (b), the velocity axis is logarithmic to emphasize the self-similar, exponential character of the solution. In (c), a detail in the vicinity of the interface is shown when the driving shear is imposed far above, resulting in an overprediction of the slip for teh Darcy-Brinkman model.

Microscale computations such as these allow for a quick assessment of the parameters that determine the maximum drag reduction (i.e., the tangential slip lengths) for specific substrate topologies. For the fibres we consider, the slip lengths can be ∼30-40% less than the corresponding permeability lengths, which would need to be accounted for in (1). Other topologies with significant higher interracial sheltering, such as those of [7, 5], would yield slip lengths far smaller compared to the permeability lengths, which explains why those studies did not observe significant reductions in drag.

DIRECT SIMULATIONS WITH RESOLVED SUBSTRATES

Figure 3 shows preliminary DR results from texture-resolved DNSs. Given the high resolution requirements to resolve thin fibres, for this first set of simulations the fibre diameter and layout was selected to keep the cost of simulations moderate. In turn, we expect this to result in a lower drag reduction, given the low anisotropy ratio of the setup. In any event, the results confirm the drag-reducing potential for fibre substrates, and the general trend near and beyond the predicted optimal size, $\sqrt{K_y^+} \gtrsim 0.4$. Simulations at smaller $\sqrt{K_y^+}$, which require a prohibitively expensive refined resolution, are ongoing to complete the DR curve.

This preliminary work shows that fully resolved simulations can capture the features and physical mechanisms that may be missed when using a model for the substrate. In addition to the discontinuity of stresses at the substrate interface, one flow feature that was intrinsically left out in [4] is the effect of texture granularity. As the texture size increases compared to the scales of turbulence, the substrate elements are eventually perceived independently by the turbulent eddies, and their interaction with the flow is no longer simply through their homogenized effect. The effect of this on drag is typically adverse [3]. Figure 4 portrays instantaneous flow fields from the DNS for a drag-increasing substrate with relatively large permeability. The left side panels illustrate the differences between turbulence over a smooth wall, where the footprint of quasi-streamwise vortices dominate, and a permeable surface, where the footptint of Kelvin–Helmholtz rollers dominates. This feature is present in both the modelled- and the resolved-substrate simulations, but the latter shows additionally the signatures of individual texture elements (i.e. of each streamwise-aligned fiber).

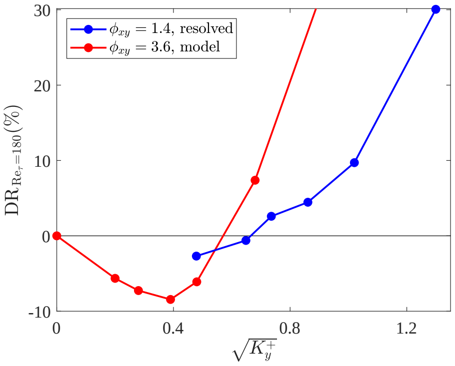

Figure 3: Drag reduction curve from DNSs for a fully resolved fiber coating with anisotropy ratio $\phi_{xy} = \sqrt{K_x/K_y} = 1.4$. Each symbol corresponds to a separate DNS. The curve for a homogenized coating with $\phi_{xy} = 3.6$ from [4] is included for reference.

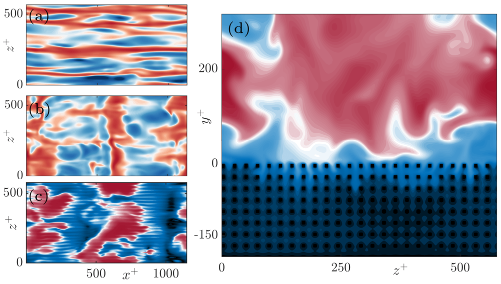

Figure 4: Instantaneous streamwise velocity in planes (a) just above the substrate and (b) normal to the mean-flow direction. (a), smooth wall; (b), coating with $\sqrt{K_y^+} = 1.0$, homogeneous model from [4]; (c) and (d), fully resolved fibers.

REFERENCES

[1] N. Abderrahaman-Elena and R. García-Mayoral. *Phys. Rev. Fluids*, 2(11), 2017.

[2] D. W. Bechert, M. Bruse, W. Hage, J. G. T. Van der Hoeven, and G. Hoppe. *J. Fluid Mech.*, 338:59–87, 1997.

[3] R. García-Mayoral, G. Gómez-de-Segura, and C. T. Fairhall. *Fluid Dyn. Res.*, 51(1):011410, 2019.

[4] G. Gómez-de-Segura and R. García-Mayoral. *J. Fluid Mech.*, 875:124–172, 2019.

[5] S. M. H. Khorasani, M. Luhar, and S. Bagheri. *J. Fluid Mech.*, 984, 2024.

[6] P. Luchini. In *Computational Methods in Applied Sciences '96*, pages 466–470, 1996.

[7] M. Morimoto, R. Aoki, Y. Kuwata, and K. Suga. *Flow Turbul. Combust.*, 113(1):71–92, 2023.

 # 42

ERCOFTAC
European Drag Reduction and Flow Control Meeting – EDRFCM 2024
September 10^{th}–13^{th}, 2024, Turin, Italy

AN AERODYNAMIC DESCRIPTION OF THE FLOW FIELD OVER A LINER WITH GRAZING FLOW

Angelo Paduano, Francesco Scarano
Department of Mechanical and Aerospace Engineering, Politecnico di Torino, Torino 10129, Italy

Damiano Casalino
Department of Flow Physics and Technology, Delft University of Technology, Kluyverweg 1, 2629HS, Delft

Francesco Avallone
Department of Mechanical and Aerospace Engineering, Politecnico di Torino, Torino 10129, Italy

INTRODUCTION

Acoustic liners are crucial for reducing noise in aircraft engines. In Ultra-High Bypass Ratio (UHBR) engines, characterized by larger diameters, shorter nacelles, lower rotational speeds, and reduced jet core velocities with respect to HBR ones, the fan is the primary noise source, generating both tonal noise at the Blade-Passage Frequency (BPF) and broadband noise due to turbulence interaction.

Typically, liners consist of a perforated facesheet, a backing cavity, and a solid backplate, and are configured as Single-Degree-of-Freedom systems to target specific frequencies, dissipating acoustic energy through viscous effects [6].

Although extensive research has been conducted on the noise-damping properties of liners, a significant knowledge gap remains regarding the interaction between aerodynamic and acoustic fields near cavities and its link to increased drag. Research has shown that acoustic liners can increase viscous drag when exposed to high tonal sound levels [7]. Jasinski et al. [4] found that acoustic liners can affect the turbulent flow at certain Reynolds numbers and under high amplitude acoustic excitation, noting unsteady blowing from the perforations overlying the cavities. However, the magnitude was small compared to the mean freestream velocity, suggesting it perturbs the wall layer rather than causing the drag increase. Bento et al. [1] observed that the flow inside a circular cavity creates a pressure force on the downstream edge due to boundary layer impingement. Experiments at NASA's GFIT facility, in the presence of grazing acoustic waves and a turbulent boundary layer, estimated added drag using a static pressure drop approach. They reported a drag increase of 10% to 350% compared to a smooth wall, with most of the total drag stemming from the orifice diameter, plate porosity, and face sheet thickness [3].

Although acoustic liners can affect turbulent coherent structures at the wall, the impact of acoustic waves on these mechanisms and the resulting increase in drag remains poorly understood. Investigating how acoustic waves influence turbulent structures within a boundary layer over lined walls is crucial for optimizing acoustic liners' design to minimize noise and aerodynamic drag.

METHODOLOGY

The commercial software 3DS Simulia PowerFLOW version 6 is adopted. It is based on an extended Lattice Boltzmann Method. A Very Large Eddy Simulation is used, which resolves only the large turbulent scales. It accounts for sub-grid effects using a turbulence model based on two-equation Renormalization Group Theory k-ϵ. This approach differs from the computation of an equivalent eddy viscosity. It dynamically adjusts the Boltzmann model to match the characteristic time scales of turbulent flow. Reynolds stresses are not explicitly added to the governing equations; they arise implicitly from the chaotic exchange of momentum in turbulent flow, where characteristic times are shorter than the slowly varying turbulent flow.

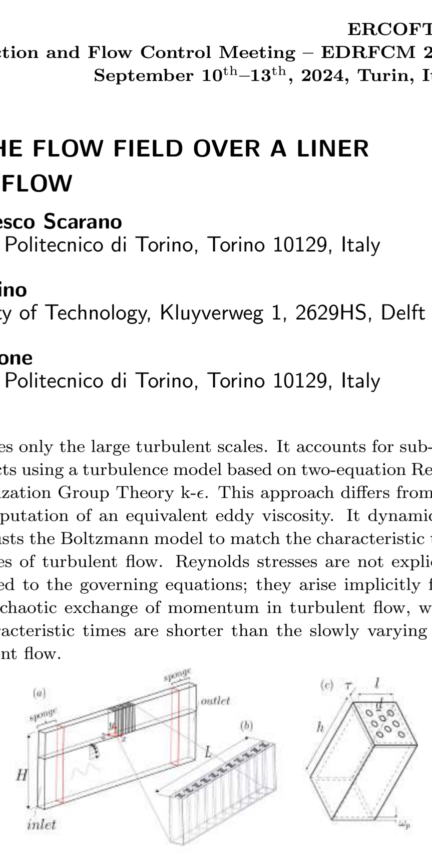

Figure 1: Sketch of the numerical model test section

The computational domain shown in Fig. 1 replicates the UFSC facility [2]. The liner is placed at the top wall of a duct with a rectangular cross-section. Each cavity, with a square cross-section $l = 8.46d$ and depth $h = 34.18d$ ($d = 1.17$ mm corresponds to orifice diameter), has eight orifices, partition walls $w_p = 2.17d$, and a face sheet $\tau = 0.46d$ thick. This resulted in a cavity Percentage of Open Area (POA) equal to 8.75%. The simulation considered a row of eleven cavities, yielding a streamwise length of $L = 116.23d$. A zig-zag trip ($0.21d$ high, 1.71 long) was added upstream at $x = -1367d$ to match the experimental velocity profile [2]. After achieving flow convergence, acoustic waves with an amplitude of 500 Pa and different frequencies were superimposed on the hydrodynamic field. For conciseness, only results at a centerline Mach number equal to 0.32 and $f = 1400$ Hz are presented.

RESULTS

The mean velocity and turbulence intensity profiles are shown in Fig. 2 at two different locations at the centerline of the liner sample: upstream of the cavity array, at x = -0.01 m and downstream of it, at x = 0.140 m. The Clauser chart technique was used to obtain the friction velocity by fitting the mean profiles with the Schlichting equation (k = 0.4, B = 5.5) The upstream friction velocity for the flow-only case was used to non-dimensionalize all statistics in inner units. Velocity

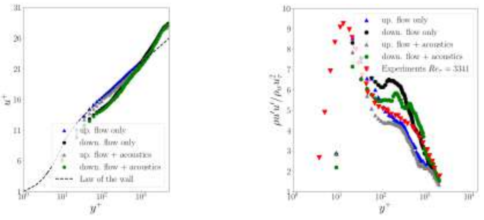

(a) (b)

Figure 2: Mean velocity and standard deviation profiles in wall units

profiles show a downward shift of Δu^+ in the streamwise direction, indicating a decrease in local friction velocity. Figure 2b shows Reynolds stresses in the streamwise direction compared with experimental findings by Vallikivi et al. [8] at a similar Re_τ. Turbulence intensity distribution changes moving in the streamwise direction, with the downstream case showing an outer hump, highlighting that cavities affect boundary layer structures, consistent with previous findings [5]. Differences arise between the case with and without acoustics, with the latter showing a higher outer hump.

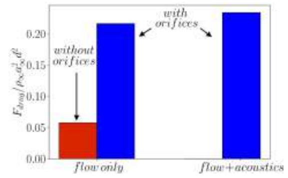

Figure 3: Comparison of drag with and without orifices

Despite reduced skin friction, the integral of forces in the streamwise direction, which includes cavity and orifice walls in the drag estimation, as shown in Fig. 3, results in higher aerodynamic drag in the presence of liners compared to a smooth wall, with differences increasing when an acoustic wave is superimposed. This discrepancy arises from the additional surfaces where the pressure forces are sufficiently large to cause a measurable drag increase in all cases.

Previous studies on cavities and perforated plates revealed that at high Mach number, Kelvin–Helmholtz (KH) instability waves can be generated at the cavity's leading edge and roll up as a vortex-like structure to the trailing edge [7]. The impinging of the vortex results in the generation of high-frequency noise. This is further confirmed by looking at the pressure spectra shown in Fig. 4, where a peak at $f \approx 14000$ Hz is observable both with and without acoustics. Figure 5 shows the Q-criterion visualization of the flow field after filtering with the Spectral Proper Orthogonal decomposition technique with a frequency band centered at $f \approx 14000$ Hz.

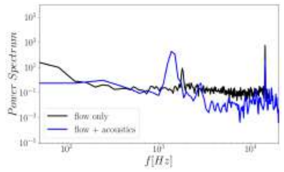

Figure 4: Spectral content of pressure at the center of the channel with and without acoustics

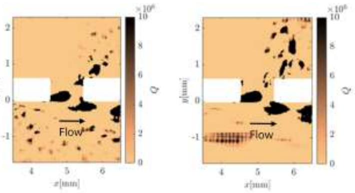

(a) (b)

Figure 5: Q-criterion visualization near the orifice: (a) flow only case, (b) flow + acoustics case

This visualization clearly indicates the presence of vortex-like structures impinging on the downstream edge of the orifice. The continuous impingements of these vortices contribute to higher pressure drag by increasing the pressure forces on the downstream edge of the cavities.

ACKNOWLEDGMENTS

This work is co-funded by the European Union (ERC, LINING, 101075903). Views and opinions expressed are, however those of the author(s) only and do not necessarily reflect those of the European Union (EU) or the European Research Council. Neither the EU nor the granting authority can be held responsible for them.

REFERENCES

[1] H. F. M. Bento, C. P. Vandercreek, F. Avallone, D. Ragni, and M. Snellen. Lattice boltzmann very large eddy simulations of a turbulent flow over covered and uncovered cavities. *Physics of Fluids*, 34, 2022.

[2] L. A. Bonomo, N. T. Quintino, A. M.N. Spillere, J. A. Cordioli, and P. B. Murray. A comparison of in-situ and impedance eduction experimental techniques for acoustic liners with grazing flow and high spl. 2022.

[3] B. M. Howerton and M. G. Jones. Acoustic liner drag: Measurements on novel facesheet perforate geometries. American Institute of Aeronautics and Astronautics Inc, AIAA, 2016.

[4] C. Jasinski and T. Corke. Mechanism for increased viscous drag over porous sheet acoustic liners. *AIAA Journal*, 58:3393–3404, 2020.

[5] F. Scarano, M. C. Jacob, and E. R. Gowree. Drag reduction by means of an array of staggered circular cavities at moderate reynolds numbers. *International Journal of Heat and Fluid Flow*, 102, 2023.

[6] C. K.W. Tam and K. A. Kurbatskii. Microfluid dynamics and acoustics of resonant liners. *AIAA journal*, 38:1331–1339, 2000.

[7] C. K.W. Tam, N. N. Pastouchenko, M. G. Jones, and W. R. Watson. Experimental validation of numerical simulations for an acoustic liner in grazing flow: Self-noise and added drag. *Journal of Sound and Vibration*, 333, 2014.

[8] M. Vallikivi, M. Hultmark, and A. J. Smits. Turbulent boundary layer statistics at very high reynolds number. *Journal of Fluid Mechanics*, 779, 2015.

 # 43

ERCOFTAC
European Drag Reduction and Flow Control Meeting – EDRFCM 2024
September 10th–13th, 2024, Turin, Italy

GLOBAL FRICTION OF HETEROGENEOUS ROUGH SURFACES

C. Schmidt[1], **J. Neuhauser**[1], **D. Gatti**[1], **P. Sujar Garrido**[1, 2], **and B. Frohnapfel**[1]

[1]Institute of Fluid Mechanics, Karlsruhe Institute of Technology, 76131 Karlsruhe, Germany
[2]SimEx/FLOW, Engineering Mechanics, KTH Royal Institute of Technology, SE-100 44 Stockholm, Sweden

INTRODUCTION

Turbulent flows over natural as well as over technical surfaces are often exposed to heterogeneous roughness, a famous example being the flow over a ship hull overgrown with barnacles. The prediction of the related global friction coefficient is of high interest, but remains challenging [1]. In particular, it is not clear how to incorporate roughness heterogeneity into existing predictive frameworks [4]. Classically, global drag prediction relies on the determination of an equivalent sandgrain roughness (and the related roughness function) which is evaluated in the fully rough regime; i.e. a flow regime in which the drag coefficient only depends on the roughness geometry and not on Reynolds number. In order to understand whether the drag over heterogeneous rough surfaces can be predicted with existing tools, reference data for the global drag behaviour is required. To widen the data basis of the friction coefficient of such surfaces, we investigate surfaces with alternating smooth and rough parts in a broad Reynolds number range.

INVESTIGATED SURFACES

In order to initiate a systematic study of heterogeneous rough surfaces we consider the drag of roughness strips aligned in the streamwise direction. The investigated surfaces consist of alternating smooth and rough strips of 4δ width which are made out of P60 grit sandpaper. As depicted in figure 1, the surfaces are produced such that the mean height of the sandpaper is at the same position as the smooth surface part. Similar surfaces with strip width of 1δ and 2δ have previously been investigated by our group [3] and are used to complement the present data set. The geometrical dimensions of all surfaces can be found in table 1.

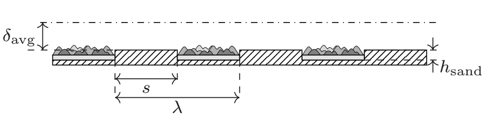

Figure 1: Sketch of the investigated surfaces and the geometric definitions.

name surface	δ_{avg} mm	h_{sand} mm	s mm	λ mm
submerged rough 4 delta	12.692	0.67	50	100
submerged rough 1 delta	12.71	0.67	12.5	25
submerged rough 2 delta	12.66	0.67	25	50

Table 1: Geometrical dimensions of the different surface configurations.

EXPERIMENTAL SET-UP

The experimental investigation of the surfaces is performed in the open-circuit blower wind tunnel depicted in figure 2. The test section has a channel half-height of $\delta = 12.6$ mm and a width of $W = 300$ mm resulting in an aspect ratio of $AR = 12$. The test section has a length of 314δ whereof the last third is equipped symmetrically with the investigated surfaces.

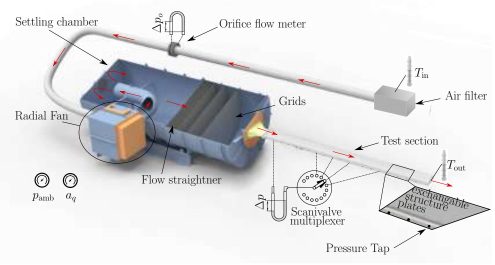

Figure 2: Scheme of the blower wind tunnel with the measurement equipment (adapted from [6]).

The pressure gradient Π along the surface is measured using 21 pressure taps located on both sides of the test section. In conjunction with the mass flow rate $\dot{m}$ measured with an orifice flow meter in the inlet pipe, the bulk Reynolds number Re_b and the global friction coefficient C_f can be calculated by

$$Re_b = \frac{2\delta_{\text{avg}} U_b}{\nu} = \frac{\dot{m}}{\rho \nu W} \tag{1}$$

and

$$C_f = \frac{2\tau_w}{\rho U_b^2} = \frac{8\Pi\rho\delta_{\text{avg}}^3 W^2}{\dot{m}^2}, \tag{2}$$

respectively, with the bulk velocity U_b, and the air's density ρ and kinematic viscosity ν.

RESULTS

Figure 3 includes the results for all three strip widths and also the reference curves for the homogeneous cases, i.e. smooth and homogeneous rough. The smooth-wall reference is in very good agreement with the correlation suggested by Dean [2]. The homogeneous rough curve reaches a quasi-constant value at high Reynolds numbers depicting a fully rough regime for this surface configuration.

Two main observations can be made for the heterogeneous rough surfaces. First, their global drag curves differ even

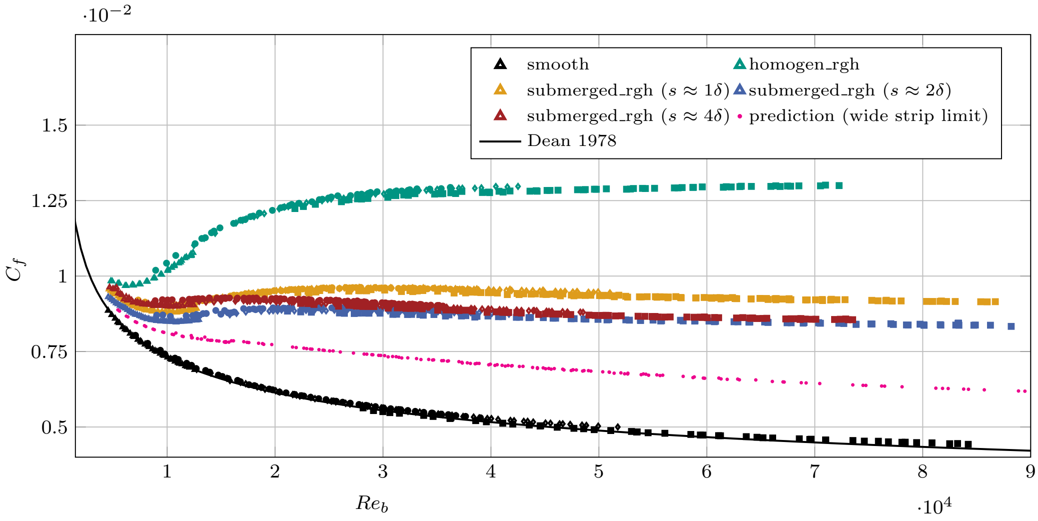

Figure 3: Results for the heterogeneous rough surfaces in comparison with the homogeneous reference cases and the wide strip limit [5].

though all of them have a 50 % surface-coverage with sandpaper. Second, all curves indicate a continuous decline at the highest Reynolds numbers covered by our facility. At relatively low Re_b, which corresponds to the transitionally rough regime of the homogeneous rough surface, the C_f curves of the rough strips reach a flat local maximum. In this Re_b-regime a constant friction factor appears to be present over a limited Reynolds number range in all cases. As no fully rough regime is reached at high Reynolds numbers, no equivalent sandgrain roughness can be defined for the surfaces.

One alternative approach to predict the global drag of the heterogeneous rough surface is the use of an averaging procedure that employs data of the homogeneous smooth and rough case [5]. This model relies on the assumption that the flow above rough and smooth surface parts is in equilibrium with the wall condition, and the related predicted drag curve is added in figure 3. Even though good agreement of the model prediction with DNS results for low Reynolds numbers and small roughness has been shown in previous work [5], the model does not provide a good prediction of the global drag curve of the present P60 sandpaper strips at high Re_b. It also does not capture the intermediate flow regime in which a constant C_f is found for all measured data. Due to the assumption of equilibrium flow conditions, the model is inherently not capable to resolve differences in the strip width. In addition, the prediction clearly underestimates the measured global C_f for all considered cases.

In the conference contribution, the differences between the three measured global drag curves and potential reasons will be discussed in detail. In addition, an improved version of the predictive tool will be presented which can capture the general shape of the global drag curves and allows to distinguish different strip widths.

REFERENCES

[1] D. Chung, N. Hutchins, M. P. Schultz, and K. A. Flack. Predicting the drag of rough surfaces. *Annual Review of Fluid Mechanics*, 53:439–471, 1 2021.

[2] R. B. Dean. Reynolds number dependence of skin friction and other bulk flow variables in two-dimensional rectangular duct flow. *Journal of Fluids Engineering*, 100(2):215–223, June 1978.

[3] B. Frohnapfel, L. von Deyn, J. Yang, J. Neuhauser, A. Stroh, R. Örlü, and D. Gatti. Flow resistance over heterogeneous roughness made of spanwise-alternating sandpaper strips. *Journal of Fluid Mechanics*, 980:A31, 2024.

[4] N. Hutchins, B. Ganapathisubramani, M.P. Schultz, and D.I. Pullin. Defining an equivalent homogeneous roughness length for turbulent boundary layers developing over patchy or heterogeneous surfaces. *Ocean Engineering*, 271:113454, 2023.

[5] J. Neuhauser, K. Schäfer, D. Gatti, and B. Frohnapfel. Simulation of turbulent flow over roughness strips. *Journal of Fluid Mechanics*, 945:A14, 2022.

[6] L. von Deyn, D. Gatti, and B. Frohnapfel. From drag-reducing riblets to drag-increasing ridges. *Journal of Fluid Mechanics*, 951:A16, 2022.

44

ERCOFTAC
European Drag Reduction and Flow Control Meeting – EDRFCM 2024
September 10th–13th, 2024, Turin, Italy

ON THE INTERACTION OF STATIONARY CROSSFLOW INSTABILITIES WITH A WALL-MOUNTED PHONONIC CRYSTAL

A.L. Synodinos, G. Zoppini, T. Michelis, M. Kotsonis
Faculty of Aerospace Engineering,Delft University of Technology, 2629 HS Delft, The Netherlands

INTRODUCTION

Delaying the transition from laminar to turbulent flow can reduce aircraft drag by up to 15%. Therefore, the growth of transitional boundary layer instabilities need to controlled. Various methods have been proposed, including the principle of wave superposition, which capitalizes on their wave nature [4]. Wave superposition can be achieved through either active or passive techniques. Active techniques suffer from issues with adaptability, simplicity, and cost-effectiveness, making passive techniques highly appealing. In the framework of wave superposition, passive flow techniques are often applied by modifying the wall geometry. Dynamic interaction between the fluid and the interface is induced to exploit the wave superposition principle.

Such techniques, have been applied for boundary layer scenarios dominated by Tollmien-Schlichting (TS) waves [1] and Crossflow Instability (CFI) [6]. However, the time modulation of the TS wave makes the application of wave superposition more complex compared to the stationary wave pattern of CFI. Specifically, a streamwise series of Discrete Roughness Elements (DRE) arrays have been employed with optimal amplitude and phase arrangement to attenuate the growth of CFI [6]. Therefore, wave superposition is more readily applied in CFI dominated flows, demonstrating their wave like characteristics. Nevertheless the proposed control technique is highly sensitive to the external disturbances. Hence, other mechanisms from classical wave physics that could be candidates for control are being explored.

A particular mechanism from wave physics, known as Bragg scattering, inherently possesses a dispersive character [2]. This mechanism derives its properties from the periodic repetition of scattering units. When the periodicity of these units is comparable to the wavelength of the incident wave they are designed to control, the effect is observed. Its dispersive wave character, results in the formation on stop-band region, knows as bandgaps, where the waves prevented from propagating due to scattering. In the field of elastic-acoustics, such structures are referred to as phononic crystals (PC) [3].

The objective of this study is to investigate the formation of bandgaps using phononic crystal concepts in transitional fluid flows and to utilize them to suppress wave-like boundary layer instabilities. In this work, CFI is the dominant mode, which is stationary in nature, showing wave-like periodicity in the chordwise direction. Hence, the properties of phononic crystals are characterized by their periodicity and bandgap in the spatial wavelength domain.

To determine whether Bragg scattering is possible in the linear regime of CFI, periodic spanwise-invariant roughness is applied to the wall surface. Thus, a potential PC concept in under investigation. An experimental approach, follows to reveal the physics of BL-PC interaction dominated by stationary CFI.

METHODOLOGY

The measurements presented in this work are performed the Low Turbulence Tunnel (LTT). An in-house designed, constant-chord swept wing model (M3J) is employed [5]. The microroughness is designed as stripes parallel to the leading edge with height of 0.17mm and width 1.4mm. The location of the first strip is set to $x/c_x = 0.125$, while 5 stripes are repeatedly placed with a constant distance (figure 1). The wavelength λ_x of repetition is set to be equal with the dominant mode in the x direction. The configuration S5 corresponds to a repetition of 5 stripes, while the unperturbed configuration is also considered. DRE arrays are applied in both of them at $x/c_x = 0.02$ to provide baseflow BL configurations dominated by the development of a monochromatic CFI mode. Tests are performed on the pressure side of the wing model for a fixed angle of attack $\alpha = -3.4^o$ and Reynolds number $Re_{c_X} = 2.17x10^6$.

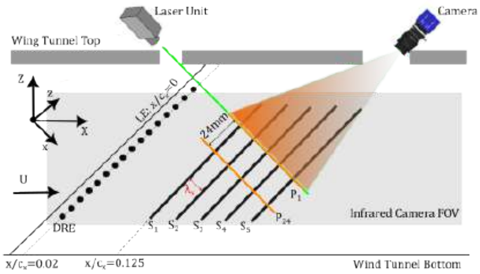

Figure 1: Sketch of PIV experimental setup,roughness configurations and field of view of infrared camera

The global effect of the PC on the BL development is characterized by means of infrared thermography, providing the location and modifications of the BL transition front depending on the applied forcing configuration. In addition, the flow mechanisms dominating the local interaction between the pre-existing CFI and the stripes are locally acquired by high-resolution planar PIV. Specifically, a plane is acquired every 1 mm in the z-direction, covering a total region of 24 mm. Each measurement plane is indicated as P_1 to P_{24}, respectively.

RESULTS

The results presented in this chapter correspond to the forcing case of 5 stripes (S5). In figure 2(a) the transition pattern for the Clean configuration is observed, while figure 2(b) evaluates the effect of the PC configuration on the transition location at $\alpha = -3.4^o$, $Re_{c_X} = 2.17x10^6$. It is clear that the

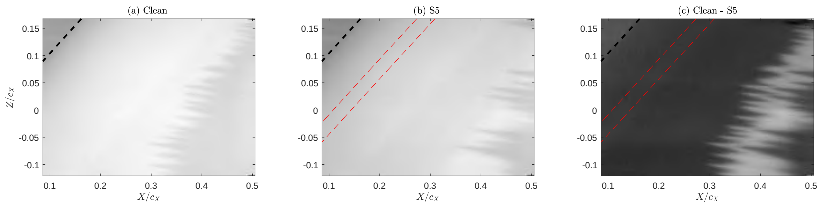

Figure 2: (a,b) Infrared (IR) thermography image of stationary CFI transition pattern at $\alpha = -3.4^o$, $Re_{c_X} = 2.17x10^6$.(a) Clean configuration, (b) S5 configuration, (c) Difference between Clean and S5, with the white region indicating the transition delay. Black dashed line indicates the trailing edge. Red dashed lines denote the location of the first strip and last strip. Freestream direction (X) and vertical direction (Z). Flow comes from the left.

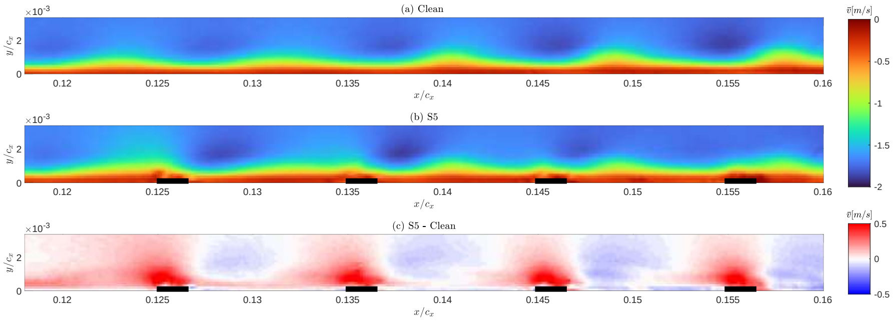

Figure 3: (a,b) Contours of time-averaged $\bar{v}$ velocity for (a) Clean configuration, (b) S5 configuration at $\alpha = -3.4^o$, $Re_{c_X} = 2.17x10^6$. PIV velocity measurements corresponds to the P_1 plane, indicated in figure 1. (c) Difference between the S5 and clean configuration. Black boxes denote the stripes.

presence of stripes, results in delaying the transition of the 3D boundary layer, which is denoted in the white region in figure 2(c). The transition location for the clean configauration takes place at $x_{TR}/c_x = 0.39$ while in the forced S5 configuration occurs at $x_{TR}/c_x = 0.47$, providing a transition delay $\Delta x_{TR}/c_x = 0.08$, corresponding to 8% of the chord.

To understand the mechanism driving the observed transition delay, the BL-PC interaction should be thoroughly examined. In figure 3(a,b), the time-averaged wall-normal velocity $\bar{v}$ contours are provided for the aforementioned cases characterized by the infrared thermography. The PIV velocity contours corresponds to the P_1 plane indicated in figure 1. In figure 3(c) the effect of the PC configuration on the mean boundary layer is isolated by subtracting the Clean configuration. It is observed that PC configuration induce a periodic modulation, on the normal to the wall velocity v.

DISCUSSION AND FULL CONTRIBUTION

A transition delay is observed while unpublished results have shown evidence of wavelength dependence of the phenomenon, which is maximized close to the incoming wavelength of the stationary CFI. This indicates a bandgap behavior for certain wavelengths, attenuating growth compared to the clean configuration. Furthermore, a closer examination reveals that the effect of the PC is the periodic modulation of the wall-normal velocity component. This is equivalent to a periodic modulation of the medium, where the CFI propagates. The aforementioned analysis could serve as potential evidence of the phononic crystal concept. Nevertheless, further investigation is required to reveal the underlying physics. In conclusion, this study is the first indication of bandgap behavior in transitional boundary layer flows. It could pave the way for further employment of PC and metamaterials concepts, relying on wave physics.

REFERENCES

[1] Peter W. Carpenter and Andrew Garrad. The hydrodynamic stability of flow over kramer-type compliant surfaces. part 1. tollmien-schlichting instabilities. *Journal of Fluid Mechanics*, 155:465 – 510, 1985.

[2] Pierre A. Deymier, editor. *Acoustic Metamaterials and Phononic Crystals*, volume 173 of *Springer Series in Solid-State Sciences*. Springer Berlin Heidelberg, Berlin, Heidelberg, 2013.

[3] Mahmoud I. Hussein, Michael J. Leamy, and Massimo Ruzzene. Dynamics of Phononic Materials and Structures: Historical Origins, Recent Progress, and Future Outlook. *Applied Mechanics Reviews*, 66(4):040802, July 2014.

[4] Robert W. Milling. Tollmien-Schlichting wave cancellation. *Physics of Fluids*, 24(5):979–981, May 1981.

[5] J Serpieri and M Kotsonis. Design of a swept wing wind tunnel model for study of cross-flow instability. American Institute of Aeronautics and Astronautics Inc. (AIAA), 2015.

[6] Giulia Zoppini, Theodoros Michelis, Daniele Ragni, and Marios Kotsonis. Cancellation of crossflow instabilities through multiple discrete roughness elements forcing. *Phys. Rev. Fluids*, 7:123902, Dec 2022.

45

ERCOFTAC
European Drag Reduction and Flow Control Meeting – EDRFCM 2024
September 10$^{\mathrm{th}}$–13$^{\mathrm{th}}$, 2024, Turin, Italy

OPTIMAL LAMINAR FLOW CONTROL

G. Li Causi[1], G. Cafiero[1], G. Iuso[1], & J. Serpieri[1]
[1]Department of Mechanical and Aerospace Engineering, Politecnico di Torino, 10129 Turin, Italy

INTRODUCTION

Skin friction drag accounts for about half of the total drag experienced by an airliner in cruise flight. While reducing turbulent flows friction drag is a much studied approach [1], augmenting the portion of laminar flow over the flow-exposed surfaces is also a viable strategy. In the specific, it has been demonstrated that boundary layer (BL) suction from the flow-exposed surfaces is a highly effective flow control technique for delaying BL laminar-turbulent transition. This approach, referred to as laminar flow control (LFC)[2], allows to overcome the limitations of aerodynamic-design based approaches, referred to as natural laminar flow, in delaying the transition process.

Nonetheless, the implementation of LFC is still not very straightforward, due to a few reasons. As per every active control technique, the power needed to pump the BL flow needs to be (considerably) smaller than the power saved by the reduced friction drag. Moreover, suction-based LFC relies on the installation at the flow-exposed surfaces of micro-perforated plates behaving as permeable walls. This is not of straightforward technological realization and it is further challenged in its deployment on aeronautical crafts by atmospheric agents and debris eventually clogging the microscopic holes. Finally, effective and efficient implementation of LFC requires a careful assessment as, while BL suction locally increases the friction drag, the achieved postponement of the transition location shall pay off the initial expenditure. Therefore, a trade-of of the LFC-describing parameters shall be sought after.

METHODOLOGY

This study focuses on utilizing a numerical framework to determine the optimal suction configuration, aiming to maximize the drag reduction within a stationary, incompressible, and two-dimensional flat plate boundary layer flow.

The geometry and boundary conditions (BC) for the numerical simulations were established based on the experiments conducted by [3]. Special care was taken in reproducing the same leading edge geometry, as this plays a critical role for the BL flow receptivity and stability, thus, much influencing the transition position x_t [4]. RANS simulations were conducted using the openFOAM suite, utilizing the γ-Re_θ transitional turbulence model, which incorporates experimental correlations to model the transition process. The boundary conditions recommended by [5] were applied, with suction introduced through the wall BC. The suction velocity v_s is supposed to be uniform and $v_s < 0$ inside the suction region, bounded by the coordinates x_s and x_e which, respectively, denote starting and ending positions of the suction region along the streamwise direction x.

Following a grid convergence study optimized for a free stream velocity $U_\infty = 19\,\mathrm{m/s}$, where the subscript ∞ indicates freestream conditions, the flow wall normal direction y was discretized using 85 points over a height of $0.1\,\mathrm{m}$ with the first cell height of $2\,10^{-5}\,\mathrm{m}$, and a uniform grid spacing of $\Delta x = 5\,\mathrm{mm}$ in the streamwise direction.

The validation of the numerical simulation involved scenarios with and without suction. The results of the CFD simulations were compared to experimental data from [3]. In scenarios without suction (see figure 1), four different plate-length L based Reynolds numbers were tested ranging from $Re_L = 3\,10^6$ to $Re_L = 8\,10^6$. When suction was applied, focus was given to a single Reynolds number flow, with the suction intensity $c_q = -v_s/U_\infty$ ranging from 0% to 0.14%, as shown in figure 2. A good agreement is observed between the numerical and experimental data without suction control and any slight differences could be attributed to uncertainties in the numerical and experimental data, as well as to different definitions of the transition point between the current study and the work of [3]. Conversely, when suction is applied, the agreement is limited to small values of the suction coefficient ($c_q < 2\,10^{-4}$).

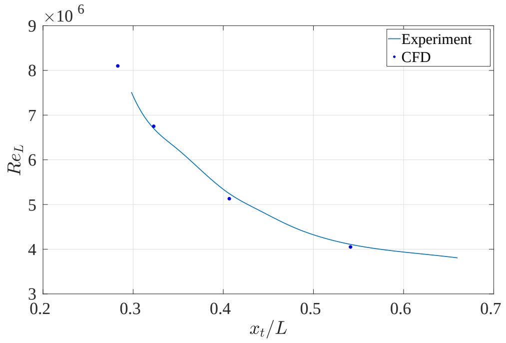

Figure 1: Normalized transition position x_t/L as function of the Reynolds number Re_L; experimental data from [3].

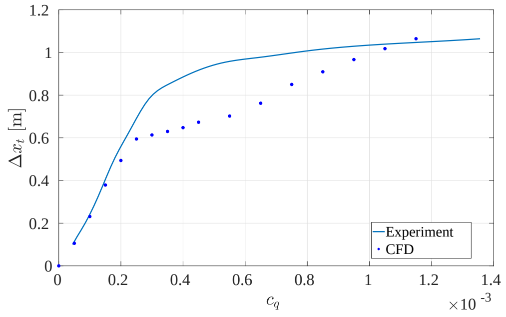

Figure 2: LFC-induced transition position shift Δx_t as a function of c_q; experimental data from [3].

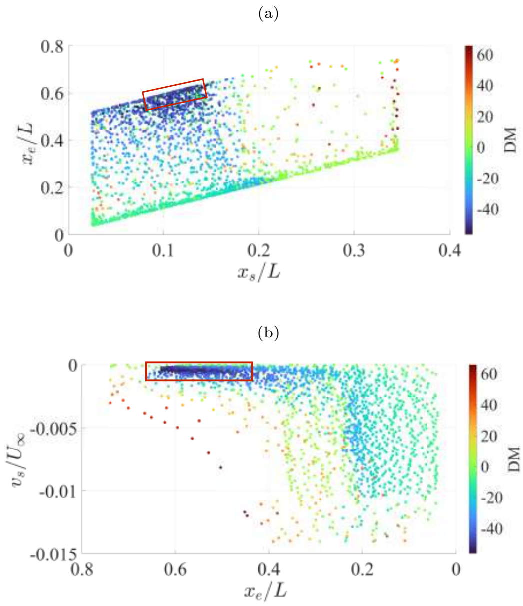

Figure 3: LFC-optimized design space projected on (a) the x_s/L-x_e/L and on (b) the v_s/U_∞-x_e/L plane.

Notably, for these values, the data points nearly align along a line with the same slope as the experimental data.

Upon demonstrating the effectiveness and limitations of the γ-Re_θ closure model, its applicability was leveraged to examine the optimal suction configuration for delaying transition and reducing overall friction drag at a fixed Re_L. The optimization problem was formally articulated as follows:

$$\begin{cases} \min_{\boldsymbol{x}} f(\boldsymbol{x}) \\ h(\boldsymbol{x}) \leq 0 \end{cases} \tag{1}$$

where $f(\boldsymbol{x})$ is the objective function defined as

$$f(\boldsymbol{x}) = \frac{D_f^S - D_f^N}{D_f^N} \times 100 = DM \tag{2}$$

and the constrain is set as $h(\boldsymbol{x}) = -v_s d - 10^{-1} m^3/s$, where $\boldsymbol{x} = [x_s, x_e, v_s]$ is the vector of the design parameters, namely the starting and ending suction position and the wall normal suction velocity, and $d = x_e - x_s$ is the extension of the suction region.

In equation 2, the subscript f indicates that only the friction drag is accounted, while the superscript S refers to the friction drag in the suction case and the N is the flat plate drag in the case of natural transition. When the Drag Modification is negative ($DM < 0$), suction is beneficial as it results in an overall reduction of friction drag. The only constraint imposed (h) accounts for the maximum spilled mass flow during the simulation which was set below 10^{-1} m^3/s; threshold that was extracted from the literature.

The problem stated in equation 1 was tackled using the Matlab Bayesian optimization routine. "Expected Improvement" was selected as acquisition function while an exploration ratio of 0.8 was chosen.

RESULTS

The optimization process evaluated 2250 permutations of the design parameters, showing that, if suction is misplaced, it can be severely counterproductive. In fact, the optimization found LFC configurations increasing of $> 60\%$ the flow drag. On the other hand, beneficial LFC configurations found by the optimization process showed levels of drag reduction above 50% ($DM < -50\%$). These LFC configurations appear in a bounded region of the design space, highlighted by the cluster of dark blue points (further highlighted with red rectangles) in figure 3a and figure 3b. In particular, such amount of drag reduction is reachable when suction operates over a region (d) extending along the streamwise direction for more than 37.5% of the plate length ($d/L > 0.375$) and with a mass flow of about 7.5×10^{-3} m^3/s.

The effect of optimal LFC can be seen, in figure 4, as colormaps of the intermittency function γ within the BL. The effect of the performed suction can be appreciated by the postponement, for the controlled flow, of the upwards deflection of the γ interface.

Further investigations on the effect of LFC on BL flows within pressure distribution fields are ongoing and will be discussed during the presentation.

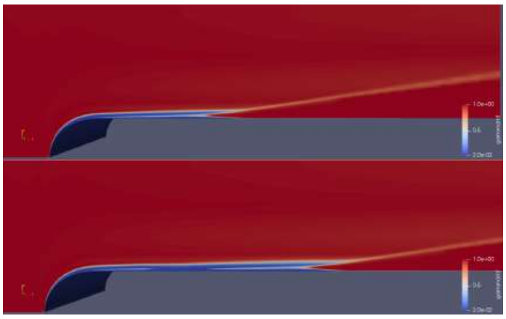

Figure 4: Intermittency γ field: (top figure) natural BL flow, (bottom figure) optimal LFC-controlled BL flow. The y direction is stretched 10:1 against the x direction to improve the figures visibility.

REFERENCES

[1] G. E. Karniadakis and K.-S. Choi. *Annual Review of Fluid Mechanics*, 35:45–62, 2003.

[2] Ronald D Joslin. Aircraft laminar flow control. *Annual review of fluid mechanics*, 30(1):1–29, 1998.

[3] Michelangelo Corelli Grappadelli, Stephan Sattler, Peter Scholz, Rolf Radespiel, and Camli Badrya. Experimental investigations of boundary layer transition on a flat plate with suction. In *AIAA Scitech 2021 Forum*, page 1452, 2021.

[4] Ronald E Hanson, Howard P Buckley, and Philippe Lavoie. Aerodynamic optimization of the flat-plate leading edge for experimental studies of laminar and transitional boundary layers. *Experiments in fluids*, 53:863–871, 2012.

[5] Robin Blair Langtry. A correlation-based transition model using local variables for unstructured parallelized cfd codes. 2006.

46

ERCOFTAC
European Drag Reduction and Flow Control Meeting – EDRFCM 2024
September 10th–13th, 2024, Turin, Italy

Experimental Investigation of Early stage of Turbulent Spot

Haodong Zhu, Kwing-So Choi
Faculty of Engineering, University of Nottingham, University Park, Nottingham NG7 2RD, UK

INTRODUCTION

Turbulent spots, which are significant aggregations of wall turbulence within boundary layers, are observed in many scenarios, particularly during the transition process. As a distinctive turbulent structure, they provide crucial insights into the study of turbulence—a complex issue in fluid mechanics that remains unresolved. In aerodynamics, understanding of the formation and development of turbulent spots can aid reducing air resistance and improving fuel efficiency. Additionally, by controlling the behaviour of turbulent spots, the onset to turbulence can be delayed, thereby reducing frictional drag and enhancing aerodynamic performance.

An isolated turbulent region was firstly discovered by Emmons [1] who named it as the turbulent spot. The existence of turbulent spots was then experimentally confirmed by Schubauer & Klebanoff [2]. Mitchner [3] investigated the generation conditions, propagation characteristics as well as the mutual influences of turbulent spots in the boundary layer flow using the dye flow visualisation. Carlson et al. [4] studied the propagation characteristics of turbulent spots in channel flow through experiments, discovering that the initial shape of turbulent spots is arrow-like, turning concave at the front as they propagate downstream. Gaster & Grant [5] found in their experiments that transient pulses can trigger the initial turbulent spots. In 2021, Wang et al. [6] studied the early development of turbulent spots in a low-turbulence environment. However, this study did not cover very early stages of turbulent spot development, such as when the turbulent spot is still in its 'young' phase, or even before it becomes a turbulent spot.

Here, an experimental investigation was carried out in a low-turbulence wind tunnel to study very early stage of artificially initiated turbulent spots in a laminar boundary layer over a flat plate with two different types of disturbances: wall-normal jet and electric spark. This report aims to further understand the transition process and possible mechanisms by which localised disturbances evolve into turbulent spots through the initial stages of development.

Experimental Setup

Wind tunnel used in this project was a closed-return type at the University of Nottingham. It has an octagonal test section of 0.5 m by 0.5 m in cross section, 3-m long. The maximum speed of this wind tunnel is 15m/s, where the freestream velocity was set to 9 m/s in this experiment with the freestream turbulent intensity of approximately 0.05%. In the test section of the wind tunnel, there is a 20mm diameter hole over a flat plate at 600mm downstream of the leading edge, as shown in Figure 1(a). This hole is used to insert various types of disturbance source. One type of flow disturbance is generated using a loudspeaker, as shown in Figure 1(b). Here, the speaker diaphragm creates a flow that is ejected through a 1mm diameter hole on the test pate, creating a wall-normal jet. Another method to generate the flow disturbances is by using an electric spark, as depicted in the cross-sectional view in Figure 1(c). The experimental setup for the electric spark consists of two needles, where the spark is generated, connected to a DC power source. The gap between the two needles is 1mm, which are positioned 0.5mm from the wall surface.

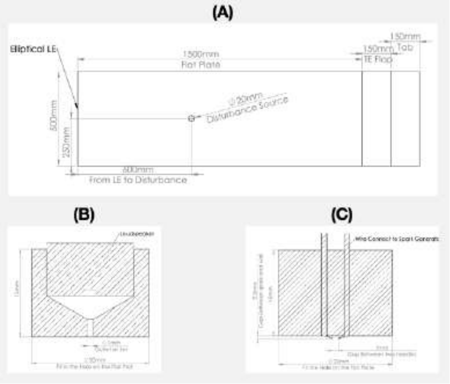

Figure 1. (a) Mounting arrangement of localised disturbance source in the flat plate test section; (b) A mini speaker installed in a small hole on the flat plate; (c) An electric spark generator installed on the flat plate.

After generating the localised disturbance to the laminar boundary layer over the flat plate, the hot-wire anemometry was used to measure the downstream flow field changes. The hot-wire probe was connected to a transverse system which allowed precise movements in all three directions. Here, a laser positioning system was employed to accurately determine the position of the hot-wire probe from the wall.

Results

Two methods of generating the localised disturbances were tested: wall-normal jet and electric spark. In both cases, nearly identical, fully-developed turbulent spots were observed far downstream. For the purpose of this discussion, only the results were selected where the disturbances were just above the threshold, therefore the generated structure did not decay downstream. Observations began just downstream of the localised disturbance. The first observation location was 5mm from the disturbance source, followed by observations at every 20mm downstream. At each observation point, measurements were taken at 30 positions in the wall-normal direction and 40 positions in the spanwise direction. The distance between each measurement point was between 0.125 mm and 0.75 mm, appropriately adjusted based on the size of the local turbulent spot.

Figure 2 illustrates the development of turbulent spots at the centreline position in y-t images. The Fig. 2(a) shows the evolution of turbulent spots generated by a short pulse of wall-normal jet, while Fig. 2(b) depicts those generated by an electric spark. The contours of turbulent spots at various positions are represented by red and blue lines, indicating positive and negative velocity fluctuations, respectively. In the initial stage, the turbulent spots appear small and gradually develop over time. At this point, they are not yet true turbulent spots but rather simple structures formed by an interaction between the wall-normal jet and the laminar boundary layer. Next, the disturbed flow structure expands in both wall-normal and streamwise directions, with increasingly complex contours revealing changes in their internal structure. The structure of the turbulent spot resembles those observed by other researchers. Specifically, a large low-speed region can be seen at positions farther from the wall, which is surrounded by high-speed regions closer to the wall.

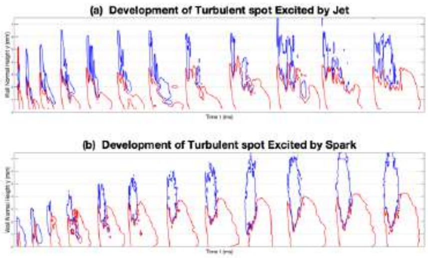

Figure 2. Comparison of the development of turbulent spots with (a) wall normal jet and (b) electric spark depicted by contour of ensemble-averaged x-component velocity fluctuations at 1.76 % (red) and −1.76 % (blue) of the freestream velocity.

Some different structures can be observed, however, due to the difference in generating the localised disturbance in the boundary layer. When using the wall-normal jet, a strong wall-normal jet introduces a large amount of low-speed fluid to positions away from the wall. Thus, in Fig. 2(a) a strong low-speed region can be observed up to y = 6mm early on. In contrast, the electric spark method generates initially weak velocity fluctuations in a cylindrical shape, which are nearly ten times lower than those by the wall-normal jet as shown in Fig. 2(b). Initially the low-speed region can only be observed up to y = 2mm, but the flow structure disturbed by the electric spark develops much quickly downstream by increasing its height faster than that disturbed by the wall-normal jet.

Figure 3 compares the 3-D shapes of early flow structure in z-t contour plots, which were generated 5mm downstream of the disturbance source. Here, it is evident that the early spot has a relatively simpler structure when it is generated by a wall-normal jet. The low-speed region at the top the turbulent spot is due to the wall-normal jet ejected away from the wall. At the same time, a hairpin vortex is formed due to the interaction between the wall-normal jet and the boundary layer. The hairpin vortex helps increase the velocity near the wall due to its downwash, creating the high-speed region near the wall on both sides of the low-speed region. The high-speed region extends longer than the low-speed region as the hairpin vortex stretches downstream.

On the other hand, the initial flow structure generated by the electric spark is quite different. Figure 3 shows that there is no low-speed region in the centre of the structure. This can be understood as follows: the electric spark causes the surrounding air to expand, resulting in an increased downstream velocity in the boundary layer near the wall, but the velocity upstream of the disturbance is decreased at the same time. Since the electric spark is generated close to the wall at y = 0.5 mm, we can observe a high-speed region near the wall, roughly of the width of the electric spark (z = 1mm). In front of this high-speed region, there is a relatively small low-speed region.

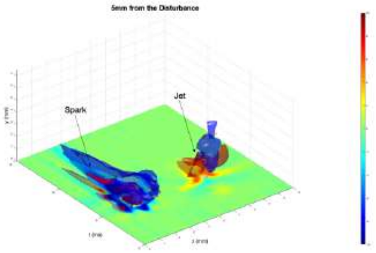

Figure 3. Three-dimensional structure 5 mm downstream of the disturbance source with the electric spark (left) and wall-normal jet (right). The flow structures generated by these disturbances are depicted by iso-surfaces of ensemble-averaged x-component velocity fluctuations at 2.5 % (red) and −2.5 % (blue) of the freestream velocity, and a corresponding colour contour slices at y = 1 mm, whose velocity magnitude is shown in the colour bar.

Conclusion

We have studied the very early development turbulent spots from two different localised disturbance sources. The intensity of these disturbance was set just above the threshold needed to form a turbulent spot downstream without decay. We found that the late stages of evolution leading to the final structure of the turbulent spots were very similar to each other. However, there were significant differences in the turbulent spot structure in the very initial stages. With a wall-normal jet disturbance, a distinct hairpin vortex structure was observed, whose secondary and subsidiary vortices dictated the subsequent evolution to the turbulent spot. With an electric spark disturbance, a high-speed region was observed near the wall, roughly of the width of the electric spark. Meanwhile, there was relatively small low-speed region observed.

Future research should focus on a better understanding of the impact of the electric spark on the surrounding flow field and more detailed observations of the evolution process near the disturbance source.

REFERENCES

[1] Emmons H W. The laminar-turbulent transition in a boundary layer-Part I. Journal of the Aeronautical Sciences, 18(7), 490-498, 1951.

[2] Schubauer G B, Klebanoff P S. Contributions on the mechanics of boundary-layer transition. NACA Tech. Note, TN 3489, 1955.

[3] Mitchner M. Propagation of turbulence from an instantaneous point disturbance[J]. Journal of the Aeronautical Sciences, 21(5), 350-351, 1954.

[4] Carlson D R, Widnall S E, Peeters M F. A flow-visualization study of transition in plane Poiseuille flow. Journal of Fluid Mechanics, 121, 487-505, 1982.

[5] Gaster M, Grant I. An experimental investigation of the formation and development of a wave packet in a laminar boundary layer. Proceedings of the Royal Society of London. A. Mathematical and Physical Sciences, 347, 253-269, 1975.

[6] Wang Y X, Choi K-S, Gaster M, et al. Early development of artificially initiated turbulent spots. Journal of Fluid Mechanics, 916, 2021.

 # 47

ERCOFTAC
European Drag Reduction and Flow Control Meeting – EDRFCM 2024
September 10th–13th, 2024, Turin, Italy

TRANSITION CONTROL OF HYPERSONIC BOUNDARY LAYER VIA NON-UNIFORM WALL TEMPERATURE

L. Boscagli, G. Rigas, P. Bruce
Department of Aeronautics, Imperial College London, SW7 2AZ London, UK

O. Marxen
School of Mechanical Engineering Sciences, University of Surrey, GU2 7XH Guildford, UK

INTRODUCTION

The development of aerospace technologies that travel with a flight Mach number (M_∞) well above sonic is challenged by complex aerothermodynamic behaviours. This flight regime is typically referred to as hypersonic. Boundary layer instability and transition can significantly affect the flight envelope and operability limits of hypersonic vehicles [4]. For laminar hypersonic boundary layers, an important non dimensional parameter is the relative Mach number $\overline{M}$, which is defined based on the velocity of the flow (u) relative to the phase speed (c_{ph}) of the hydrodynamic instability within the boundary layer. When $\overline{M}^2 > 1$, the compressible counterpart of the Rayleigh's equation admits multiple wave-like solutions, also referred to as higher Mack modes [5]. For a flight Mach number between 4 and 6, a two-dimensional instability mode (second Mack mode) plays an important role within the initial linear transition stage.

For hypersonic regime several numerical and experimental studies have determined and quantified the beneficial effect of roughness elements on transition delay [6, 3]. However, the implementation in a real flight scenario is challenged by the long exposure to high heat fluxes which can adversely affect the shape of the control device and erode the potential benefits, increasing drag and heat flux. Theoretical and computational work [8, 9] showed that it is possible to reduce the growth rate of the second Mack mode and delay transition to turbulence through the generation of steady streaks. Recent work [7] has shown that the generation of streaks is possible via a non-uniform spanwise surface temperature distribution, and a practical implementation can be achieved through smart-surfaces with different thermal characteristics. The method is highly tuneable and promises notable improvement in the aero-thermal-structural efficiency of hypersonic technologies.

In this work, numerical simulations of a hypersonic boundary layer over a flat plate are used to assess the effect of the manipulation of the surface temperature distribution on second Mack mode.

METHODS

Three dimensional, time-dependent Direct Numerical Simulations (DNS, [6]) of the compressible Navier-Stokes equations for a calorically perfect gas are used to assess the effect of a spanwise non-uniform surface temperature on the amplification and growth rate of the second Mack mode. The boundary condition for the non-dimensional wall temperature (T_w) is formulated as

$$T_w = T_{w,initial}\left(1 + A_{T_w}\sin\left(\frac{2\pi}{\lambda_z}z\right)\right), \qquad (1)$$

where the temperature is expressed relative to the freestream static temperature ($\tilde{T}_\infty$), and $T_{w,initial}$ refers to the baseline (uncontrolled) uniform case; λ_z is the width of the computational domain, which corresponds to the fundamental harmonic of the streak, and A_{T_w} is used to control the amplitude of the hot/cold patches (Fig. 1). A wall normal momentum perturbation (actuator, Fig. 1) is introduced slightly downstream of the domain inflow to trigger boundary layer instabilities. Linear stability theory (LST, [5]) is used to select the appropriate range of temporal (ω) and spatial frequencies to excite the second Mack mode, as well as to determine the streamwise bounds of the computational domain ($[x_s, x_e]$, Fig. 1). The amplitude of the perturbation is sufficiently small to avoid bypass of the linear regime. Sponge regions are used at the inflow, outflow and upper boundary of the computational domain to damp the solution to a self-similar laminar state, which is also used to initialize the computations. Periodic boundary conditions are used in the spanwise direction.

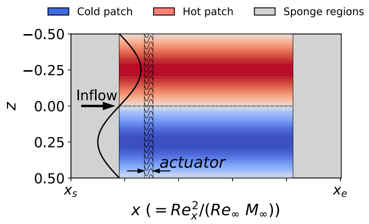

Figure 1: Schematic of the streamwise (x) and spanwise (z) arrangement of the computational domain, and blowing and suction (actuator) and wall temperature boundary conditions.

The equations are discretized on a spatially structured, curvilinear grid, and a time-accurate solution is achieved through a 6^{th} order compact finite difference scheme within the interior nodes of the domain and with an explicit 3^{rd} order Runge-Kutta time-stepping method [6]. In the streamwise direction there are approximately 22 points per wavelength of the second Mack mode. In the wall normal direction 211 points are used with grid stretching near the wall to resolve the boundary layer with a minimum of 85 points. In the spanwise direction 13 grid points are used. For time-accuracy, the second Mack mode is resolved with approximately 600 timesteps per fundamental period ($2\pi/\omega$).

RESULTS

The operating conditions are based on previous work [7], with $M_\infty = 6$, $\tilde{T}_{w,\infty} = 216.7$K and unit Reynolds number based on the free stream speed $\tilde{Re}_\infty \approx 11 \times 10^6 1/\mathrm{m}$. A cold flat plate is used as a baseline (uncontrolled) case, with $T_w = T_{w,initial} = 3$. For this case, the maximum growth rate (σ) of the second Mack mode occurs at approximately $Re_x \approx 2500$ (Fig. 2a), and it manifests with a typical phase speed $c_{ph} \approx 0.9$, and rope-like signature in the fluctuations of the streamwise density gradient (Fig. 2b). The agreement between LST and DNS (Fig. 2a) confirms the appropriate selection of the time-space characteristics of the wall-normal momentum perturbation to trigger the second Mack mode.

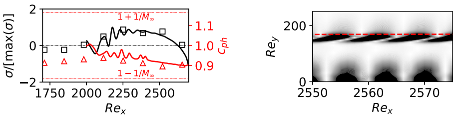

(a) (b)

Figure 2: (a) Second Mack mode growth rate (σ, black) and non-dimensional phase speed (c_{ph}, red) based on DNS (lines) and LST (markers); DNS data computed from wall static pressure fluctuations. (b) DNS time snapshot of streamwise density gradient fluctuations; red dashed line: $u = 0.999$. Uniform ($T_w = 3$) case.

For the controlled configuration, the amplitude of the spanwise temperature variation is set to $A_{T_w} = 0.3$ for both the hot and cold patch, such that a left/right symmetric configuration is investigated. For the controlled case, the maximum ($T_w = 4$) and minimum ($T_w = 2$) wall temperature (Fig. 3a) is approximately 58% and 29% the adiabatic wall temperature, respectively. The streaks' amplitude (As_u,[1]) undergoes a noticeable growth from the start of the non-uniform wall temperature distribution to the end of the computational domain (Fig. 3b).

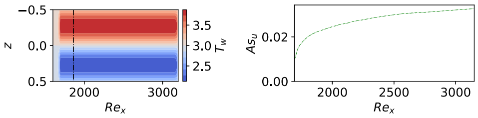

(a) (b)

Figure 3: (a) Wall temperature and (b) streaks amplitude distributions for the controlled case. Black dot-dashed line in (a) marks the end of the actuator region.

The manipulation of the surface temperature distribution to generate streaks leads to spanwise asymmetry in the flow for the controlled case (Fig. 4). This is mostly driven by the different effect of heating and cooling on second Mack mode [5], and the implications will be further discussed during the meeting.

A frequency (f) and spanwise wavenumber (k) decomposition of the primitive variables is used to determine the amplitude of the perturbations due to the steady streaks, $(f, k) = (0, \pm 1)$, second Mack mode, $(f, k) = (1, 0)$, and nonlinear interactions, $(f, k) = (1, \pm 1)$. For this case, the contribution of the second Mack mode dominates the amplitude of the unsteady perturbations. The Chu's energy (E^{fk}_{Chu},[2]) is used to track the evolution of the boundary layer instabilities, and it is normalized with the value downstream of the actuator region ($E^{fk}_{Chu,0}$) to determine the amplification factor. For this case study, the control method leads to approximately 37% reduction in the second Mack mode (linear) amplification (Fig. 5). While more investigations are required for different

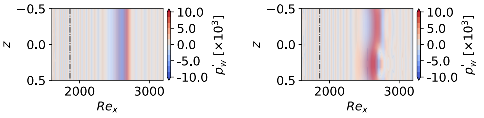

(a) (b)

Figure 4: Effect of control method on instantaneous, non-dimensional wall static pressure fluctuations (p'_w). (a) Uniform T_w (no control); (b) spanwise non-uniform T_w (with control). Black dot-dashed line marks the end of the actuator region.

operating conditions and configurations to determine the net effect on transition to turbulence, the control method looks promising and highly tuneable.

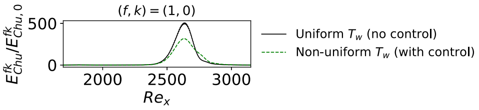

Figure 5: Effect of control method on second Mack mode amplification.

REFERENCES

[1] P. Andersson, L. Brandt, A. Bottaro, and D. S. Henningson. On the breakdown of boundary layer streaks. *J. Fluid Mech.*, 428:29–60, 2001.

[2] B.-T. Chu. On the energy transfer to small disturbances in fluid flow (part i). *Acta Mech.*, 1(3):215–234, 1965.

[3] K. D. Fong, X. Wang, Y. Huang, X. Zhong, G. R. McKiernan, R. A. Fisher, and S. P. Schneider. Second mode suppression in hypersonic boundary layer by roughness: Design and experiments. *AIAA J.*, 53:3138–3143, 2015.

[4] T. C. Lin. Influence of laminar boundary-layer transition on entry vehicle designs. *J. Spacecraft Rockets*, 45(2):165–175, 2008.

[5] L. M. Mack. Linear stability theory and the problem of supersonic boundary-layer transition. *AIAA J.*, 13:278–289, 1975.

[6] O. Marxen, G. Iaccarino, and E. S.G. Shaqfeh. Disturbance evolution in a mach 4.8 boundary layer with two-dimensional roughness-induced separation and shock. *J. Fluid Mech.*, 648:435–469, 4 2010.

[7] K. Ozawa, C. Xia, G. Rigas, and P. J. Bruce. Passive control of high-speed boundary layer transition using non-uniform surface temperature distributions. Number AIAA 2023-0849. AIAA SCITECH 2023 Forum, January 2023.

[8] P. Paredes, M. M. Choudhari, and F. Li. Transition due to streamwise streaks in a supersonic flat plate boundary layer. *Phys. Rev. Fluids*, 1, 12 2016.

[9] J. Ren, S. Fu, and A. Hanifi. Stabilization of the hypersonic boundary layer by finite-amplitude streaks. *Phys. Fluids*, 28, 2 2016.

48

ERCOFTAC
European Drag Reduction and Flow Control Meeting – EDRFCM 2024
September 10^{th}–13^{th}, 2024, Turin, Italy

INFLUENCE OF SHALLOW GAPS ON COMPRESSIBLE BOUNDARY-LAYER TRANSITION

J. A. Franco*,†, Y. Heinritz, S. Hein*
*Institute of Aerodynamics and Flow Technology, German Aerospace Center (DLR), 37073 Göttingen, Germany.
†Universidad Politécnica de Madrid, Plaza Cardenal Cisneros 3, E-28040 Madrid, Spain.

INTRODUCTION

The aviation industry is constantly demanding further increase in the fuel efficiency of aircraft, *e.g.* by a reduction in drag. One of the most promising technologies is the use of *laminar wings*, i.e. wings in which the laminar properties of the incoming flow extend along the wing surface much longer that on current wing designs [2]. Unfortunately, the different components of the wing introduce unavoidable surface imperfections, such as steps, gaps, humps, etc. These irregularities might lead to an upstream displacement of the expected laminar-turbulent transition location compared with a clean configuration (i.e. without surface irregularities).

The depth D^* of these surface irregularities is typically of the same order as the local boundary-layer displacement thickness δ_c^* where the imperfection is placed (x_c^*). The wall imperfections introduce locally large streamwise gradients in the flow. Standard numerical approaches for linear stability analysis, such as *Local Stability Analysis (LST)*, or *Parabolized Stability Equations (PSE)* cannot handle these highly non-parallel flow features that arise in the vicinity of the surface imperfections. Alternatively, techniques such that *Harmonic Linearized Navier-Stokes (HLNS)* equations or *Direct Numerical Simulations (DNS)* are able to deal with large streamwise variations. However, the computational cost, in terms of number of grid points required in streamwise direction, limits the use of HLNS or DNS for parametric studies. In between *low-cost* approaches (LST, PSE) and *high-fidelity* methods (HLNS, DNS), the *Adaptive Harmonic Linearized Navier-Stokes (AHLNS)* equations [1] has arisen as a very powerful tool for parametric studies when two-dimensional (2D) surface imperfections are present.

THE AHLNS METHODOLOGY

The *Adaptive Harmonic Linearized Navier-Stokes (AHLNS)* equations describe the linear evolution of the flow instabilities that trigger typically the laminar-turbulent transition in low-turbulence scenarios, i.e. Tollmien-Schlichting (TS) waves and Crossflow (CF) vortices. The flow instabilities are represented by a *wave-like* expression in x-direction:

$$\tilde{\mathbf{q}}(x,y,z,t)=\hat{\mathbf{q}}(x,y)e^{i\int \alpha(x')dx'+\beta z-\omega t} \qquad (1)$$

This representation of the convective instabilities (TS/CF) is identical for PSE and AHLNS. Here, α, β, and ω stand for the streamwise wavenumber, spanwise wavenumber, and circular frequency of the disturbances $\tilde{\mathbf{q}}$, respectively. Therefore, the coupling between both approaches is straightforward (see Fig. 1). Methodologies such as HLNS and DNS describe the flow instabilities in streamwise x-direction by an amplitude function $\hat{\mathbf{q}}$ only. As a consequence, the number of grid points in x-direction required by the AHLNS method is about one or two orders of magnitude smaller than HLNS or DNS approaches. In contrast to PSE, the AHLNS equations represent a fully-elliptic system, similar to HLNS or DNS. However, it cannot be solved by a marching procedure (as PSE) [4].

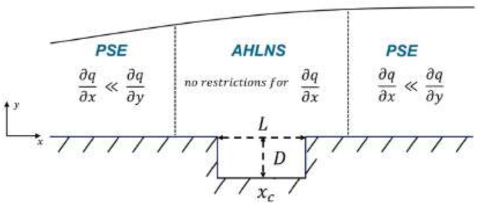

Figure 1: Sketch of the multi-zonal technique for boundary-layer instability analysis in the presence of a rectangular gap. The vertical dashed lines represent the inflow and outflow locations for AHLNS computations. Magnitude $\mathbf{q}$ holds for both base flow quantities $\bar{\mathbf{q}}$ and amplitude function of the disturbances $\hat{\mathbf{q}}$. Nondimensional parameters L, D, and x_c stand for the length, depth and x-location of the center of the gap, respectively. Flow direction is from left to right.

SHALLOW GAPS

We study the influence of a rectangular shallow gap (i.e. gaps whose length L^* is significantly larger than its depth D^*) on the boundary-layer transition of a two-dimensional compressible laminar flow on a semi-infinite flat plate. The Mach number of the incoming flow is fixed to $Ma_\infty = 0.5$. Parameters L^* and D^* are made nondimensional with δ_c^*. A total number of nine rectangular gaps are analysed. The nondimensional gap length L takes values of $L = 50$, 100, and 150. The nondimensional gap depth D takes values of $D = 0.4$ (*small*), 0.8 (*medium*), and 1.0 (*large*). Figure 2 shows the nondimensional steady laminar base flow pressure contours $\bar{p}$ and streamlines for *large* gaps, varying the length L. Other parameters, such as unit Reynolds number and x-position of the gap x_c, remain fixed.

According to the criteria of Sinha *et al.* [3], shallow cavities can be split into *open* or *closed*. Shallow open cavity flows are such that there is a single recirculation bubble within the gap area (Fig. 2-a)). Shallow closed cavity flows are such that there are two individual separation bubbles: a relatively large bubble at the upstream face of the gap, and a much smaller one at the downstream side (Fig. 2-b), -c)). One aim of the

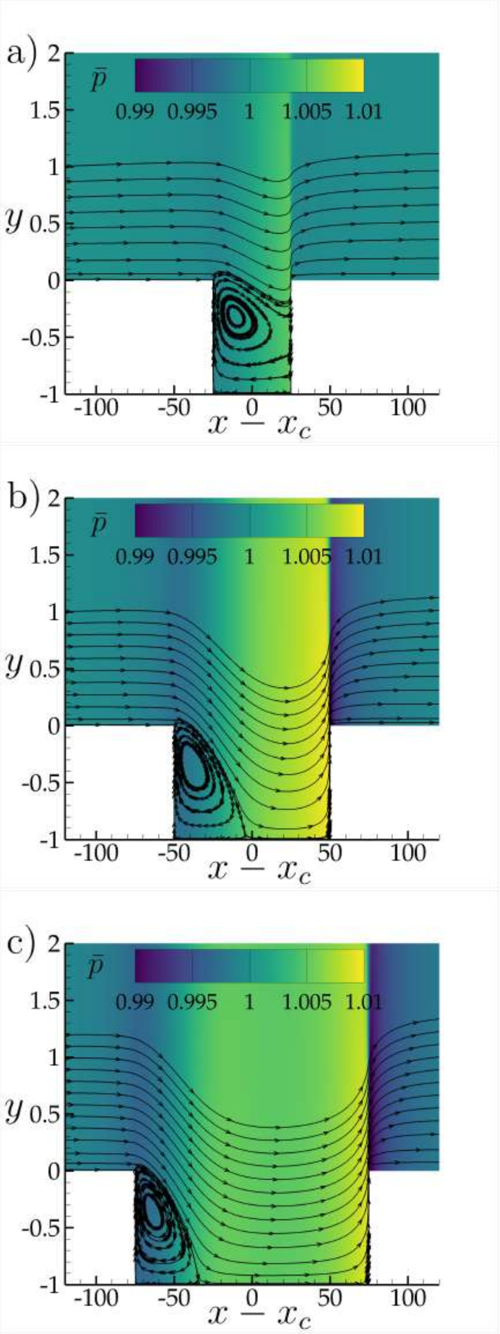

Figure 2: Steady laminar base flow pressure $\bar{p}$ contours and streamlines for cases: a) $D10\_L50$, b) $D10\_L100$, c) $D10\_L150$. Flow direction is from left to right. Axes are not to scale.

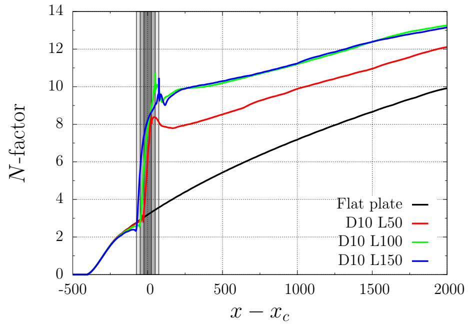

Figure 3: Effect of gap length L on N-factor envelope for gaps with $D = 1.0$. The three grey areas indicate the position and length (50, 100, 150) of the gap. The black curve for a flat plate is added as reference.

present study is to relate the base flow structure *open/closed* with the boundary-layer instability characteristics in order to enhance the current knowledge about these types of flows.

The accumulated growth and decay of each TS wave is computed via the individual n-factor curve using the multi-zonal approach shown in Fig. 1. The envelope of all n-factor curves considered for a particular gap defines the N-factor envelope curve. As an example, Fig. 3 collects the N-factor envelope curves for the three gaps described in Fig. 2.

CONCLUSIONS

An outcome of the investigation is that, for the current flow configuration, if two different shallow *closed* gaps have similar pressure gradients along the gap and the area of the separated flow is approximately the same, then the values of the N-factor envelope curve for both gaps practically coincide. This result explains why, for shallow *closed* gaps, variations in length have no effect in the corresponding N-factor envelope curves. On the other hand, reducing the length of the gap such that the flow structure inside the gap changes from *closed* to *open* leads to a significant decrease in the destabilizing effect of the gap on the expected transition location. Figure 3 describes visually this outcome of the investigation.

Other aspects, such as the variation of the depth D (from *small* to *large*) while the length L is kept constant, will be discussed in the talk.

REFERENCES

[1] J. A. Franco and S. Hein. Adaptive harmonic linearized Navier-Stokes equations used for boundary-layer instability analysis in the presence of large streamwise gradients. *AIAA Paper 2018-1548*, 2018.

[2] J. Reneaux. Overview on drag reduction technologies for civil transport aircraft. *ECCOMAS*, 2004.

[3] S. N. Sinha, A. K. Gupta, and M. M. Oberai. Laminar separating flow over backsteps and cavities. II-Cavities. *AIAA Journal*, 20(3):370–375, 1982.

[4] F. Tocci, J. A. Franco, S. Hein, G. Chauvat, and A. Hanifi. The effect of 2D surface irregularities on laminar-turbulent transition: A comparison of numerical methodologies. *New Results in Numerical and Experimental Fluid Mechanics*, XIII:246–256, 2021.

 # 49

ERCOFTAC
European Drag Reduction and Flow Control Meeting – EDRFCM 2024
September 10th–13th, 2024, Turin, Italy

PIV MEASUREMENTS ON A WING WITH UNIFORM BLOWING

G. Fahland[1], D. Wöllstein[1], R. Leister[1], B. Frohnapfel[1] & J. Serpieri[2]
[1]Institute of Fluid Mechanics (ISTM), Karlsruhe Institute of Technology (KIT), 76131 Karlsruhe, Germany
[2]Department of Mechanical and Aerospace Engineering, Politecnico di Torino, 10129 Turin, Italy

INTRODUCTION

Uniform blowing in turbulent boundary layers is a flow control scheme that offers the prospect of large friction drag reduction [7, 8]. Theoretical [4], numerical [5] and experimental investigations [1] have been conducted to investigate the influence of this control on other drag components in a more practical flow scenario than flat plate boundary layers, in particular on airfoils. One open issue in the related comparison of experimental and numerical data is the boundary condition for wall-normal blowing. While uniformity is assumed in theoretical considerations and directly enforced in numerical simulations, its experimental realization clearly has practical limitations. The present study therefore compares experimental data of the flow measured over an airfoil model with numerical data obtained with an idealized uniform blowing boundary condition.

METHODOLOGY

The airfoil model is mounted in the open jet return-type wind tunnel at ISTM [3]. The control surface is located on the airfoil's pressure side (PS). It is made from a perforated titanium sheet metal of thickness $t = 1\,\mathrm{mm}$, hole diameter of $d_\mathrm{h} = 60\,\mu\mathrm{m}$ and an open area ratio of $A_\mathrm{hole}/A_\mathrm{control} = 10\,\%$. It is supported by a frame that separates the control area, along the streamwise direction, in seven spanwise-extending strips. The control mass flux is monitored and regulated for each strip separately. The control intensity $c_\mathrm{q} = v_\mathrm{BLC}/U_\infty$ depends on the wall-normal velocity and the free stream (wind tunnel) velocity U_∞. Planar Particle Image Velocimetry (PIV) measurements are conducted with a light sheet perpendicular to the airfoil's surface as indicated in the test rig set-up shown in Fig. 1. Table 1 provides the specifications of the PIV hardware. The camera is mounted outside the free jet of the wind tunnel with a working distance of $k \approx 700\,\mathrm{mm}$. Eleven Fields of View (FOV) are examined by traversing the camera along the airfoil surface in the streamwise direction, such that the boundary layer on the PS can be investigated in the interval of $X/c = [66, 89]\,\%$ in the airfoil-conform coordinates. At each FOV, an image series of $n_\mathrm{tot} = 410$ images is recorded alongside of analog measurements from the aerodynamic balance and pressure taps to measure integral lift and drag synchronously. The integral quantities are required to calculate the wind tunnel corrections [2], which provide the information on the infinite freestream angle of attack α_aero which corresponds to the geometric angle of attack α_geom of the experiment.

The recorded grey-scale images are investigated in a three-step process. First, each raw image is scanned for the wall position that is estimated from a brightness peak search and approximated within each FOV by a third-order polynomial fit to account for the wall curvature. The images are then filtered using Proper Orthogonal Decomposition (POD) to reduce the light scattered from the wall [6]. In the second step, a commercially available code (*PIVview2C*) is used to conduct the PIV processing. A multigrid/multipass approach is used with a final interrogation area size of $8\,\mathrm{px} \times 32\,\mathrm{px}$ (wall-normal × wall-parallel) with a $50\,\%$ overlap in both directions. The corresponding datapoint step size is $4\,\mathrm{px} \times 16\,\mathrm{px} \mathrel{\widehat{=}} 0.037\,\mathrm{mm} \times 0.149\,\mathrm{mm}$ along the wall-normal and streamwise directions, respectively. In the third step, the velocity fields obtained with *PIVview2C* are treated for further processing. The velocity fields are normalized with the wind-tunnel velocity to account for low frequency ($< 1\,\mathrm{Hz}$) wind-tunnel velocity fluctuations and ambient conditions such as density. Static pixel locking close to the wall is the most pronounced problem of the presented data despite the raw image treatment with POD. Therefore, a velocity threshold of $u/U_\infty = 3\,\%$ is introduced, below which an instantaneous velocity is discarded from temporal averaging. This is possible as no backflow events are expected for the present campaign. This also provides an indicator function for data quality: The number of snapshots used for temporal average n_avg compared to the total number of snapshots $n_\mathrm{tot} = 410$ indicates threshold violation to provide information on data uncertainty.

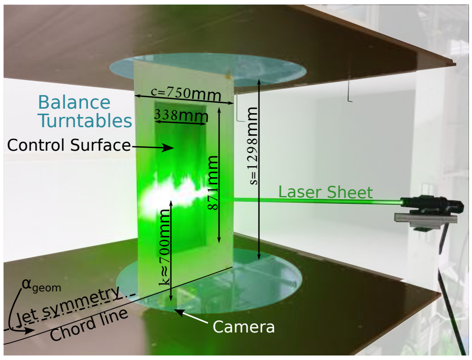

Figure 1: Test rig schematic with PIV setup

PIVLIGHT	water-based seeding	
PIVlight30	particle diameter	$d_p = 1.2\,\mu\mathrm{m}$
	response time	$t_p \approx 4.4\,\mu\mathrm{s}$
Evergreen	Wave length	532 nm
	Power	200 mJ
Nikon f/4D I	Focal length	200 mm
F-ED Nikkor	Teleplus HD 2.0X DGX	×2
PCO Edge	Sensor	sCMOS
	Resolution	2560 x 2160
2D-Target	Scaling	$107.4\ \frac{\mathrm{Pixel}}{\mathrm{mm}}$

Table 1: PIV measurement hardware for measurements in wall-normal plane of the turbulent boundary layer

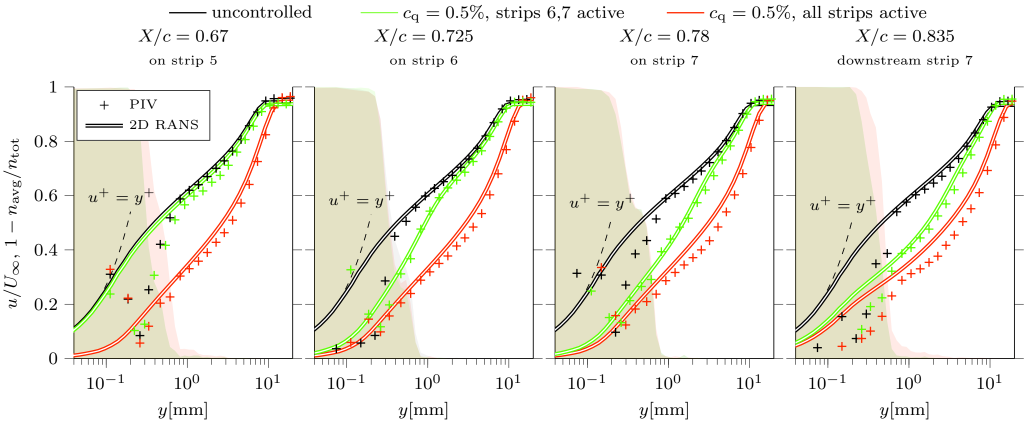

Figure 2: Time-averaged wall-parallel velocity u normalized by the wind tunnel velocity U_∞ displayed by lines and markers. Opaque fields show the ratio of excluded snapshots $1 - n_{\text{avg.}}/n_{\text{tot}}$ of the average as a function of wall distance y. Opaque fields are color-coded with the respective case colors (▨: uncontrolled; 🟩: strips 6, 7 active; 🟥: all strips active). $\alpha_{\text{geom}} = 4°$, $\alpha_{\text{aero}} = 1.09°$, chord Reynolds number $Re_c = 1.5$Mio, $v_{\text{BLC}} = 15.9\,\frac{\text{cm}}{\text{s}}$, $U_\infty = 31.8\,\frac{\text{m}}{\text{s}}$

RESULTS

The boundary layer velocity profiles of four streamwise stations and three different configurations for a geometrical angle of attack $\alpha_{\text{geom}} = 4°$ are shown in Figure 2. The uncontrolled configuration (in black) describes the case where control is completely inactive and the surface-averaged wall-normal velocity $v_{\text{BLC}} = 0$. The agreement of the boundary layer velocity profile with 2D Reynolds-Averaged Navier-Stokes (RANS) simulations at the same lift conditions (identical to the angle of attack in an infinite freestream $\alpha_{\text{aero}} = 1.09°$) is good down to a wall distance of about $y \gtrapprox 0.6\,\text{mm}$. This coincides with the distance where the number of snapshots excluded for the temporal average $(1 - \frac{n_{\text{avg}}}{n_{\text{tot}}})$ rises abruptly, presumably due to "locking" to static wall reflections. This implies that the boundary layer conditions of the 2D numerical case and the 3D wind tunnel experiment match well and the properties of the perforated surface are close to an unaltered smooth wall. This also implies the good agreement of the integral quantities, which are not the topic of the data presented here but are required to find the 2D freestream case corresponding to the 3D experiment using wind tunnel corrections [2].

The modified boundary layer profiles (green and red curves) show the expected reduction of wall-parallel velocity due to the applied control. The case with blowing applied to all spanwise strips (+) shows that the boundary layer has already thickened significantly compared to the uncontrolled case when it reaches the area investigated by PIV. The case with partial control (+) captures the effect that the start of the control has on the boundary layer profiles. Overall, the good agreement of experimental and numerical results persists for the controlled cases. This leads to the conclusion that the discrete blowing in the experiment has a limited impact on the boundary layer development compared to the uniform blowing defined in numerical studies, at least for the close-to-zero pressure gradient present at this angle of attack. Therefore, RANS simulations with idealized homogeneous blowing boundary conditions can be used as a tool to investigate this particular flow control method.

The presentation will include more detailed data on the boundary layer measurements both for controlled and uncontrolled cases as well as further information on flow uniformity and data quality.

REFERENCES

[1] K. Eto, Y. Kondo, K. Fukagata, and N. Tokugawa. Assessment of Friction Drag Reduction on a Clark-Y Airfoil by Uniform Blowing. *AIAA Journal*, 57(7):2774–2782, 2019.

[2] B. F. R. Ewald, editor. *Wind tunnel wall correction - La correction des effets de paroi en soufflerie.* Number 336 in AGARDOGRAPH. AGARD, Neuilly sur Seine, 1998. DOI.

[3] G. Fahland. User Manual for the Göttinger Windtunnel at ISTM. User Manual V1.3.0.eng, Institute of Fluid Mechanics (ISTM), Karlsruhe Institute of Technology, Karlsruhe, Germany, 2024. doi.org/10.5445/IR/1000162981.

[4] G. Fahland, M. Atzori, A. Frede, A. Stroh, B. Frohnapfel, and D. Gatti. Drag Assessment for Boundary Layer Control Schemes with Mass Injection. *Flow, Turbulence and Combustion*, (Progress in Flow Control and Drag Reduction), 2023.

[5] G. Fahland, A. Stroh, B. Frohnapfel, M. Atzori, R. Vinuesa, P. Schlatter, and D. Gatti. Investigation of Blowing and Suction for Turbulent Flow Control on Airfoils. *AIAA Journal*, 59(11):4422–4436, July 2021. DOI 10.2514/1.J060211.

[6] M.A. Mendez, M. Raiola, A. Masullo, S. Discetti, A. Ianiro, R. Theunissen, and J.-M. Buchlin. POD-based background removal for particle image velocimetry. *Experimental Thermal and Fluid Science*, 80:181–192, January 2017.

[7] J. Park and H. Choi. Effects of uniform blowing or suction from a spanwise slot on a turbulent boundary layer flow. *Physics of Fluids*, 11(10):3095–3105, October 1999.

[8] A. Stroh, Y. Hasegawa, P. Schlatter, and B. Frohnapfel. Global effect of local skin friction drag reduction in spatially developing turbulent boundary layer. *Journal of Fluid Mechanics*, 805:303–321, October 2016.

50

ERCOFTAC
European Drag Reduction and Flow Control Meeting – EDRFCM 2024
September 10$^{\text{th}}$–13$^{\text{th}}$, 2024, Turin, Italy

PARAMETRIC STUDY OF HOMOGENEOUS BLOWING AND SUCTION ON THE TRANSONIC AIRFOIL RAE2822

A. Frede, D. Gatti
Institute of Fluid Mechanics, Karlsruhe Institute of Technology, 76131 Karlsruhe, Germany

INTRODUCTION

Civil aviation is responsible for about 3% of the global CO_2 emissions [4]. A decrease in the total drag of an airplane leads to an increase in efficiency and thus a reduction of fuel consumption and emissions. Viscous losses related to the skin friction at the surfaces are responsible for roughly half of the overall drag, thus reducing them promises potentially large performance improvements.

One method to achieve a skin-friction drag reduction is the control of the turbulent boundary layer. Active flow control requires additional energy compared to passive methods but promises a higher drag reduction. One active control method is wall-normal homogeneous blowing and suction. A small mass flow rate is injected or extracted from the flow to control the turbulent boundary layer formation and thus the drag generation. Early investigations of Prandtl and Beck [7] on a flat plate showed that suction can prevent the boundary layer from separation. Later studies showed the great potential of this control technique which results in a friction drag reduction of up to 50% in the subsonic and up to 80% in the transonic regime [5]. So far most studies considered the zero-pressure gradient boundary layer or other canonical flows. If an airfoil is considered the geometry is more complex and thus skin-friction drag is not the only drag component anymore. Fahland et al. [3] investigated the effect of homogeneous blowing and suction on a NACA4412, where none of the addressed configurations resulted in a drag reduction when the costs of the actuation are taken into account. A Bayesian optimization of the flow control on a NACA4412 in the incompressible regime showed, that there indeed are blowing and suction distributions where a drag reduction is reached, especially in high lift configurations [6]. When considering civil aviation the flow around the airfoil becomes transonic, which leads to the occurrence of a weak shock wave on the suction side of the airfoil. The occurrence of such a nonlinear effect leads to changes in the flow and thus affects the potential for homogeneous blowing and suction to generate a drag reduction.

In the present study, the effect of uniform blowing and suction on the aerodynamic efficiency as well as the effect on the shock characteristics are investigated via a parametric study of the transonic airfoil RAE2822.

METHODOLOGY

The flow around the transonic airfoil RAE2822 is simulated via Reynolds-Averaged Navier-Stokes equations (RANS). The simulations are conducted with the open source solver SU2 [1] with a density-based steady-state solver. As a turbulence model, the $k-\omega-$SST model was employed. At $x/c = 0.1$, with c as the chord length, a fixed transition via a semi-explicit scalar source is implemented. The grid consists of hexahedral cells and has a 2D block pattern. The C-radius is $50c$ and the outlet distance is $75c$. A validation of the RANS data with well-resolved LES simulation is being performed.

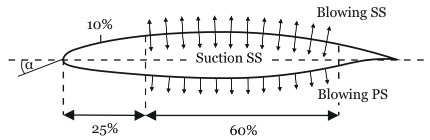

Figure 1: Sketch of the control areas and the configurations.

The surface of the airfoil where no control takes place is simulated as adiabatic walls with the no-slip condition. In the areas where control takes place a homogeneous wall-normal mass flow is prescribed. The control regime spans from 25% up to 85% of the chord length. Three different control configurations are investigated: blowing on the suction side, blowing on the pressure side and suction on the suction side. All configurations are studied individually and no combination of different configurations is considered. A sketch of the airfoil and the control configurations is shown in figure 1.

Since fluid is expelled in or removed from the system the costs e.g. accelerating the fluid which is blown into the system need to be taken into account when the overall drag component is calculated. For the analysis of the results of the parametric study the inclusive drag $c_{D,inc}$ is considered

$$c_{D,inc} = \begin{cases} c_{D,body} = c_{D,wake} + c_{BLC} & \text{for suction} \\ c_{D,wake} = c_{D,body} + c_{BLC} & \text{for blowing} \end{cases} \tag{1}$$

with the body $c_{D,body}$ and the wake drag $c_{D,wake}$. The boundary layer penalty is calculated from

$$c_{BLC} = \left| 2 \frac{u_{BLC}}{U_\infty} \frac{l_{BLC}}{c} \frac{\rho_{BLC}}{\rho_\infty} \right| \tag{2}$$

with the velocity magnitude of the control fluid u_{BLC} and the freestream flow U_∞, the length of the control area l_{BLC} and the density of the control fluid ρ_{BLC} and freestream fluid ρ_∞. For a detailed description of the concept of the inclusive drag see Fahland et al. [2].

The boundary layer penalty accounts for the costs that result from the non-zero mass flow, additionally, the power that is required to run the active control needs to be considered in the final analysis.

The simulations for the parametric study are conducted at a constant Reynolds number of $Re = 5 \cdot 10^6$. The Mach number is varied between the subsonic regime ($Ma = 0.6$) up to the transonic regime ($Ma = 0.729$). A maximum control magnitude of $\dot{m}_{BLC} = 3\%\dot{m}_\infty$ is chosen with the free-stream mass flow of $\dot{m}_\infty = U_\infty c \rho_\infty$, while the angle of attack is varied between $\alpha = -1^\circ$ to 3°.

The free-stream parameters selected in this study are chosen to represent a cruise flight scenario at an altitude of 11km.

The free-stream temperature of $T_\infty = -53.5°\mathrm{C}$, the viscosity of $\mu_\infty = 1.449 \cdot 10^{-5} \frac{\mathrm{kg}}{\mathrm{ms}}$ and the Mach number are prescribed, while the ideal gas law is used to determine the density and pressure from the given parameters.

RESULTS

In the parametric study, three different control configurations are studied. Figure 2 shows the pressure coefficient for the three different configurations at a transonic Mach number of $Ma = 0.725$, an angle of attack of $\alpha = 2.31°$ and a control magnitude of $\dot{m}_{BLC} = 0.1\%\dot{m}_\infty$.

The uncontrolled reference case is covered by the red curve. For blowing on the suction side a strong effect of the active control on the shock characteristics can be observed. The shock position is shifted towards the leading edge and the shock magnitude is decreased. This leads to a reduction of the lift coefficient c_l compared to the uncontrolled case. As already observed in previous investigations blowing leads to a reduction of the friction drag, which is also seen in the present results. Under consideration of the increased pressure drag and the boundary layer penalty, the inclusive drag increased and a decrease of the efficiency is observed. The opposite effect can be observed for suction on the suction side, the shock is shifted towards the trailing edge and it is increased in magnitude. In this case, an increase in c_l is present. Additionally, the growth in magnitude also leads to an increase in the drag coefficient. Overall, an increase in the efficiency of suction on the suction side was observed. Blowing on the pressure side does not influence the position or magnitude of the shock.

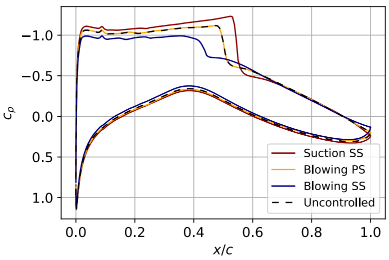

Figure 2: Pressure coefficient for the three control configurations and the uncontrolled reference case for $\dot{m}_{BLC} = 0.1\%\dot{m}_\infty$, $\alpha = 2.31°$ and $Ma = 0.725$.

The parametric study showed cases where an increase in the efficiency at a constant angle of attack is observed. For a better comparison of the effect, these cases are analysed in more detail and are rerun at a constant lift coefficient. An increase in efficiency was mainly observed for the cases with suction on the suction side at low control magnitudes. Promising cases are observed throughout the whole investigated Mach number and angle of attack regime. The most promising case of suction on the suction side is at $Ma = 0.725$ and $\dot{m}_{BLC} = 0.1\%\dot{m}_\infty$ at $c_l = 0.897$. Compared to the uncontrolled case an efficiency increase of 22.29% is observed for suction on the suction side. As already mentioned above, additional energy is needed for active control, which is not taken into account so far. Since the air intake or dumping of fluid is not explicitly defined in the investigated system, a worst-case estimation of the costs is made. Even under consideration of the costs, an increase in the efficiency of 17% is observed.

DISCUSSION

As already studied in the previous literature blowing leads to a reduction of the friction drag of up to 40% for a transonic case with a medium mass flow rate. When the inclusive drag is calculated and thus the pressure drag as well as the boundary layer penalty are included, an increase in the total drag is observed. When considering the inclusive drag the only control configuration which leads to a decrease in the inclusive drag and thus an increase in the efficiency is suction on the suction with a low control magnitude. The presence of the non-linear effect of the shock, whose characteristics are strongly affected by the active flow control, leads to the positive effects of the control which are not observed in the subsonic regime. Taking into account the energy that is needed to run the control results in a higher drag coefficient. Even though the assumptions which are made to get an estimation of the costs reflect a worst-case scenario, configurations with a maximum increase in the efficiency of 17% are found.

The results of the parametric study show that the active flow control of wall-normal homogeneous blowing and suction has potential, especially suction on the suction side at low control magnitudes in the transonic regime. Considering the non-optimal estimation of the costs and no targeted optimization is made, the potential of the control might be even larger.

In the conference talk the results of the study will be presented in detail with a focus on the cases where an increase in efficiency is observed and on validation via scale-resolving simulations. This includes a discussion of the simulation results and a more detailed look at the assumptions made to estimate the cost of the control.

REFERENCES

[1] T. Economon, F. Palacios, S. Copeland, T. Lukaczyk, and J. Alonso. SU2: An open-source suite for multiphysics simulation and design. *AIAA Journal*, 54(3):828–846, 2015.

[2] G. Fahland, M. Atzori, A. Frede, A. Stroh, B. Frohnapfel, and D. Gatti. Drag assessment for boundary layer control schemes with mass injection. *Flow, Turbulence and Combustion*, accepted for publication, 2023.

[3] G. Fahland, A. Stroh, B. Frohnapfel, M. Atzori, R. Vinuesa, P. Schlatter, and D. Gatti. Investigation of blowing and suction for turbulent flow control on airfoils. *AIAA Journal*, 59(11):4422–4436, 2021.

[4] B. Graver, K. Zhang, and D. Rutherford. Emissions from commercial aviation, 2018. In *International Council on Clean Transportation*. 2019.

[5] D. Hwang. Review of research into the concept of the microblowing technique for turbulent skin friction reduction. *Progress in Aerospace Sciences*, 40(8):559–575, 2004.

[6] F. Mallor, G. Semprini-Cesari, T. Mukha, S. Rezaeiravesh, and P. Schlatter. Bayesian optimization of wall-normal blowing and suction-based flow control of a naca 4412 wing profile. *Flow, Turbulence and Combustion*, pages 1–26, 2023.

[7] L. Prandtl and A. Betz, editors. *Ergebnisse der Aerodynamischen Versuchsanstalt zu Göttingen - IV. Lieferung*, volume 7 of *Göttinger Klassiker der Strömungmechanik*. Göttingen University Press, Göttingen, 1932.

ERCOFTAC
European Drag Reduction and Flow Control Meeting – EDRFCM 2024
September 10th–13th, 2024, Turin, Italy

A BAYESIAN OPTIMIZATION FRAMEWORK FOR OPTIMIZING GLOBAL SKIN-FRICTION DRAG REDUCTION VIA WALL BLOWING

Xiaonan Chen
School of Engineering, Newcastle University, NE1 7RU Newcastle upon Tyne, UK

Mike Diessner
School of Computing, Newcastle University, NE1 7RU Newcastle upon Tyne, UK

Kevin J. Wilson
School of Mathematics, Statistics and Physics, Newcastle University, NE1 7RU Newcastle upon Tyne, UK

Richard D. Whalley
School of Engineering, Newcastle University, NE1 7RU Newcastle upon Tyne, UK

INTRODUCTION

Turbulent boundary layer generated skin-friction drag is prevalent on the surface of high-speed moving trains, airplanes, and ships, which results in significant extra energy consumption. Controlling the turbulent flow to reduce the skin-friction drag is of great engineering and economic interest. In real-world scenarios, the aforementioned vehicles do not always operate at a constant speed and under constant environmental conditions. Therefore, it becomes necessary to identify different sets of control strategies for a range of Reynolds number cases in order to maximize drag reduction. To address varying Reynolds number conditions, low-amplitude wall blowing as an active flow control technique [1], which can achieve a long-lasting skin-friction drag reduction effect in the streamwise direction, appears to be a feasible choice in the present study. Since the drag reduction effect depends on multidimensional control parameters, including blowing amplitude, frequency, angle, duty cycle, and wavelengths in both the streamwise and spanwise directions, using a machine learning framework to optimize the control strategy could be a potential approach to solving this kind of complex N-dimensional problem. Several previous simulation works [2] applied an easy-to-use Bayesian optimization framework (NUBO, Newcastle University Bayesian Optimization [3]) to optimize the control parameters of low-amplitude wall-normal blowing in a turbulent boundary layer flow. In the present study, we aim to employ the same optimization framework, NUBO, to achieve maximal local drag reduction across a large range of Reynolds numbers. This is the first attempt at using NUBO in a wind tunnel as part of a physical fluid dynamics experiment. Once NUBO is proven to work well with our experimental system, it will be applied to optimize more control parameters in further investigations.

EXPERIMENTAL SETUP

The experiment was performed in the boundary layer wind tunnel facility located in Newcastle University. The schematic of the experimental setup is shown in Figure 1. To promote the transition to turbulence, a tripping zigzag with a height of 1.5 mm and a width of 10 mm was installed 100 mm downstream of the tip of the flat plate. The origin of the coordinate system is set at the centre of the tripping zigzag. Throughout the paper, we use x, y, and z to refer to the streamwise, wall-normal, and spanwise directions, respectively. The microblowing rig is embedded in the wall with the blowing region set at $x = 475$ mm to $x = 830$ mm. To obtain the skin-friction distribution in the turbulent boundary layer with and without the flow control, a hot-wire probe with a diameter of 0.5 um and a length of 1.25 mm was employed to measure the near-wall mean velocity profile at several different streamwise positions as shown in Figure 1. Here, the skin-friction was estimated by a linear-fit technique [4]. To optimize the flow control strategy for each Reynolds number, the skin-friction coefficient with a corresponding set of control parameters was sent to NUBO as an initial input. From this NUBO generated the next set of control parameters. After a series of iterations, the measured skin-friction coefficient should approach a constant value, indicating that NUBO has found the optimal control parameters for this Reynolds number. For further information regarding of NUBO and its validation, please refer to [5].

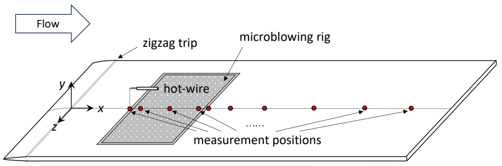

Figure 1: Schematic of wind tunnel experiment setup.

GLOBAL SKIN-FRICTION DRAG REDUCTION

Figure 2 (a) and (b) show the streamwise distribution of the skin-friction coefficients measured with and without flow control, under high and low Reynolds number conditions, respectively. For both cases, the skin-friction coefficient decreases gradually with increasing streamwise positions in the absence of control, exhibiting classic characteristics of a canonical turbulent boundary layer. For the flow control cases, the skin-friction coefficient decreases significantly from the region where wall-normal blowing begins and gradually recovers to match the non-blowing case downstream of the blowing region. This result implies that the wall-normal blowing used in this study has achieved a long-lasting drag reduction effect in the streamwise direction. With the increase in the intensity of wall-normal blowing, the reduction in the global skin-friction coefficient becomes more remarkable. To evaluate the skin-friction drag reduction effect, the global skin-friction drag reduction was calculated. The maximum global drag reductions achieved for high and low Reynolds numbers are 37.2% and 15.8%, respectively.

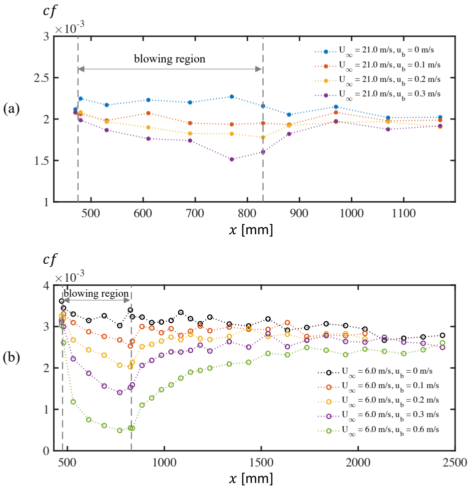

Figure 2: Streamwise skin-friction coefficient distribution with and without flow control. (a) measured at $U_\infty = 21.0$ m/s; (b) measured at $U_\infty = 6.0$ m/s.

OPTIMIZING WALL BLOWING WITH NUBO

The first experiment using NUBO to optimize one-dimensional control parameters under a range of randomly changing wind speeds to obtain the minimum local friction velocity was conducted to assess the applicability of NUBO. At the beginning of the experiment, a local friction velocity with a corresponding blowing amplitude and a freestream velocity were sent to NUBO to generate the next set of experimental conditions. As shown in Figure 3, the colored dots represent the friction velocities measured at $X = 835$ mm under 60 sets of randomly decided freestream velocities and flow control conditions provided by NUBO. The black circles represent the friction velocities measured without flow-control at the same streamwise position for comparison. For no blowing cases, the friction velocity increases linearly with the increase in freestream speed. For cases with blowing, all measured friction velocity values exist under the fitting curve for the no-blowing case. In the experiment, after a series of iterations, NUBO consistently recommended a high blowing amplitude for each randomly determined freestream velocity, as indicated by the yellow dots in Figure 3. This outcome suggests that NUBO progressively identified the optimal control strategy to achieve the lowest local friction velocity across various freestream velocities.

CONCLUSION AND OUTLOOK

We experimentally achieved a reduction in global skin-friction drag reduction in turbulent boundary layers using low-amplitude wall blowing. The initial results indicate that

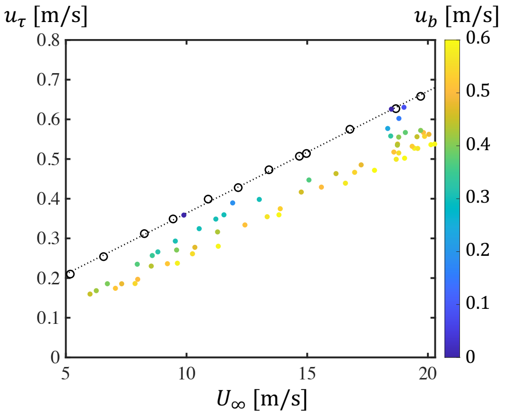

Figure 3: Friction velocities measured at $X = 835$ mm under different freestream velocities and flow control conditions as provided by NUBO. Black and colored symbols represent the results measured without and with flow-control, respectively.

our blowing rig can indeed generate uniform blowing and adjust the blowing intensity as we anticipated, leading to drag reduction at different levels. The maximum global drag reductions achieved for high and low Reynolds numbers are 37.2% and 15.8%, respectively. We have also attempted the first optimization experiment using NUBO to obtain the lowest local friction velocity across various freestream velocities. As expected, NUBO quickly found the optimal control strategy, which involved blowing at a high amplitude within the parameter bounds. While we have achieved drag reduction only through varying intensities of uniform wall-normal blowing, we have plans for further modifications. Control parameters, including blowing amplitude, frequency, angle, duty cycle, and wavelength will be explored and optimized with NUBO in subsequent experiments to achieve both global skin-friction drag reduction and net energy savings. We plan to conduct a direct numerical simulation (DNS) to validate our experimental results and provide detailed flow field information for further analysis to understand the mechanism behind the relationship between control parameters and drag reduction, providing insights for refined design in turbulent boundary layer control. The corresponding results will be presented in future work.

REFERENCES

[1] V. I. Kornilov and A. V. Boiko. *AIAA Journal*, 50(3):724–732, 2012.

[2] O. A. Mahfoze, A. Moody, A. Wynn, R. D. Whalley, and S. Laizet. *Physical Review Fluids*, 4(9):094601, 2019.

[3] M. Diessner, K. J. Wilson, and R. D. Whalley. *arXiv preprint arXiv:2305.06709*, pages 1–21 [submitted to Journal of Statistical Software], 2023.

[4] N. Hutchins and K. Choi. *Progress in Aerospace Sciences*, 38(4-5):421–446, 2002.

[5] M. Diessner, J. O'Connor, A. Wynn, S. Laizet, Y. Guan, K. J. Wilson, and R. D. Whalley. *Frontiers in Applied Mathematics and Statistics*, 8, 2022.

52

ERCOFTAC
European Drag Reduction and Flow Control Meeting – EDRFCM 2024
September 10$^{\text{th}}$–13$^{\text{th}}$, 2024, Turin, Italy

CHARACTERIZATION OF THE WAKE OF A ROAD VEHICLE TO IMPROVE AERODYNAMIC PERFORMANCES

A. Abed-Meraim, P-Y. Passaggia, A. Kourta
Univ. Orléans INSA-CVL, PRISME UR 4229, F45072, France

STATE OF THE ART

Flaps have shown promising potential in reducing aerodynamic drag on canonical models [2] (up to 15%), both as passive and active devices. On the Ahmed body, which amounts to the majority of the studies, flaps were extensively used as a mean for flow control. Their effects on the dynamics of the flow depends on the configuration. When mounted horizontally, they are seen to reduce the size of the recirculation region. Also, flaps appear to delay the flow detachment (cavity) thus increasing the base pressure. These studies [2] [3] [5] have shown that longer flaps result in better drag reduction [5], and this effect is linked to an increase of base pressure and a longer recirculation region.

However, flaps have yet to demonstrate their effectiveness in reducing drag for realistic car models [4]. This difference between simplified and real models towards drag reduction calls for a complete characterization of the wake of a realistic road vehicle in order to identify the mechanisms that contribute to the drag. It is therefore crucial to verify whether the drag mechanisms identified for the Ahmed body [3] [5] are still relevant for a more realistic car model.

This study will focus on defining the wake topology and identify the key contributors to the drag by means of a momentum budget on a selected number of interfaces, such as the recirculation region interface (RRI). Finally, based on the wake characterization, a wide range of flaps' configurations have been tested, but the drag reduction obtained is very small compared to square-back Ahmed Body used in idealized conditions. However, such strategies may still prove to be relevant in the presence of variable atmospheric conditions where the yaw and free-stream turbulence impact the wake.

EXPERIMENTAL SETUP

A representative car model of a Citroën C4 was tested in the Malavard wind tunnel of the PRISME Laboratory in Orléans (Figure 1). It is a 1/5th scale with a length of $L = 1074$ mm, a width of $W = 437$ mm and a maximum height of $H = 352$ mm (which will be used as the main length scale). This model is set on a rotating platform that is connected to a three-component aerodynamic balance that measures forces with an uncertainty of 0.2 N. The rear of the car is equipped with 92 pressure sensors (running at 150 Hz) which provide information on the base pressure contribution to the drag. A planar Stereo Particle Image Velocimetry (SPIV) system, acquired at a frequency of 15 Hz, allowed for measuring the three components of the velocity over the full recirculation region. In addition, hot-wire anemometry (performed at 60 kHz) is used to obtain the local temporal dynamics. The free-stream velocity used in this study is $U_\infty = 20$ - $30\ m/s$ ($Re = HU_\infty/\nu = 5 - 7 \times 10^5$, where ν is the kinematic viscosity).

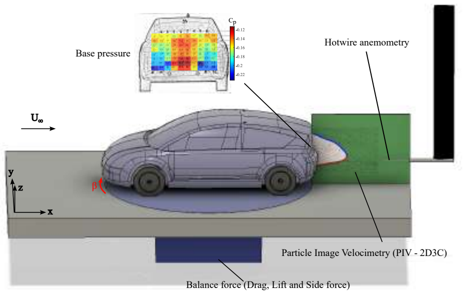

Figure 1: Illustration of the experimental setup, highlighting the overall measurement techniques used to characterize the wake of

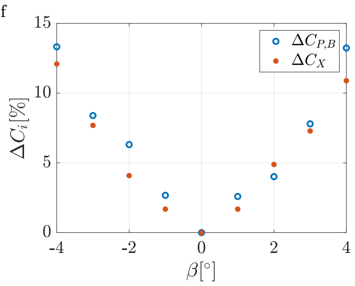

Figure 2: Evolution of both drag and base pressure coefficient with respect to yaw angle

DRAG MEASUREMENTS

Realistic driving conditions require a constant correction of the trajectory of the vehicle, which translates in a range of yaw angles between 1° to 4°. The aerodynamics forces were measured with respect to the yaw, and Figure 2 shows the evolution of drag and base pressure with respect to different yaw angles. The base pressure coefficient is defined as

$$C_{P,B} = \frac{1}{S}\iint \frac{2(P - P_\infty)}{\rho U_\infty^2}\mathrm{d}S. \qquad (1)$$

The distribution of the force coefficients are symmetrical around the 0 degree yaw angle, consistent with the literature [1]. The drag difference for these angles ranges from 5% to 10%, which ought to be taken into account in the design process. The aim is to obtain an efficient drag reduction solution taking into account the yaw angle of the vehicle, which can be adapted dynamically [2]. In fact, a small yaw angle changes the topology of the wake by breaking its symmetry [1]. Also, it can be observed that base pressure and drag evolve sim-

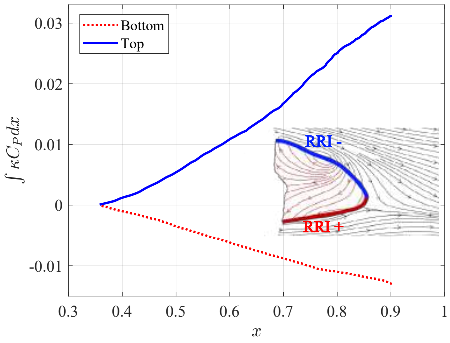

Figure 3: Contribution of pressure in the momentum budget on the recirculation region interface

ilarly, making base pressure the main factor to the increase of drag when subjected to a yaw angle. Also, for this model, base pressure amounts to 61% of the total drag whereas it represents 82% for the Ahmed body, which is attributed to the difference of geometry.

MOMENTUM BUDGET

The Recirculation Region Interface (RRI), characterized by the surface where horizontal velocity is null in the near wake, separates the mass exchanges between the recirculation region and the outer flow bounded by the shear layers. It is a valuable tool as it offers a systematic topological method to measure parameters such as the recirculation length and to integrate the momentum equation, thereby deriving an equation that relates aerodynamic drag to flow quantities in a budget (each RRI is depicted in colour in Figure 3). Specifically, the momentum budget links wake characteristics (mean and turbulent flow) to the base pressure

$$\begin{aligned} C_{P,B} = & \int_{RRI+} [\kappa(C_P + 2\overline{u'^2}) - \overline{u'w'}]\mathrm{d}x \\ & - \int_{RRI-} [\kappa(C_P + 2\overline{u'^2}) - \overline{u'w'}]\mathrm{d}x, \end{aligned} \tag{2}$$

where $C_{P,B}$ is the base-pressure coefficient, C_P the pressure coefficient, and $\overline{u'^2}$, $\overline{u'w'}$ are the normal and shear stress components. Figure 3 shows the cumulative integral of pressure along the RRI while being conducted for all the elements mentioned for the momentum budget. The turbulent terms, globally contribute to the decrease of the base pressure along the RRI. The normal-stress term seems to increase the pressure, thus providing a net thrust, but it is negligible, as its contribution to the base pressure coefficient is 5%. As for the shear stress, it contributes to approximately 40% of the base pressure drag. Moreover, the pressure term is responsible for 60% of the contribution in the RRI. These results were also observed on the Ahmed body [5], both in simulations and experiments.

EFFECT OF THE FLAPS ON MEAN QUANTITIES

Following the momentum budget results, two vertical flaps were positioned at the location where flow separation occurs. Because pressure is mainly governed by the mean flow, using static flaps should allow for reducing drag similar to the Ahmed body [5]. Note that the positive angle means that the flap is oriented toward the base of the body, and the negative angles towards the outside. Also, both flaps will always have the same angle in this experiment. The evolution of the aerodynamics coefficients with regard to the flaps angle shows that, for positive values, drag is reduced up to 2.4%, consistent with full-scale wind tunnel measurements, for a slightly different car model [4]. Moreover, the length of the flap scales with drag reduction. Preliminary results, show that the recirculation region extends further downstream, thus resulting in an increase of base pressure up to 15%. However, it was found that increasing the base pressure using the longest flaps does not necessarily lead to drag reduction. For instance, the best drag reduction led to 1 to 2% improvement. Moreover, the largest base pressure increase did not lead to the best drag reduction, which implies additional drag from the flap themselves. Further details will be provided during the presentation using the momentum budget given in eq.(2) along the horizontal plane.

CONCLUSION

This study demonstrates the reliability of the model used, which shares very similar features to full-scale models. This allowed for the characterization of the wake and the identification of key mechanisms contributing to drag. A momentum budget conducted on the RRI, linking base pressure to the flow's physics, shows that turbulence contributes for 40% of base pressure coefficient mainly on the lower part of the interface, while the mean flow (i.e. obtained from pressure) is responsible for 60%. Finally, although flaps reduce drag, there is little to be gained in controlling the mean flow of an optimized geometry. These results contradict the conclusions obtained with the Ahmed body, suggesting the need for further investigation.

From the identification of key mechanisms that contribute to drag, an in depth study of turbulence needs to be conducted and its sensitivity analysed in the presence of free stream turbulence.

REFERENCES

[1] G. Bonnavion, O. Cadot, A. Évrard, V. Herbert, S. Parpais, R. Vigneron, and J. Délery. On multistabilities of real car's wake. *J. Wind Eng. Indus. Aero.*, 164:22–33, 2017.

[2] A. Cembalo, P. Coirault, J. Borée, C. Dumand, and G. Mercère. Active control of road vehicle's drag for varying upstream flow conditions using a Recursive Subspace based Predictive Control methodology, 2024. arXiv:2404.04652.

[3] M. Grandemange, A. Mary, M. Gohlke, and O. Cadot. Effect on drag of the flow orientation at the base separation of a simplified blunt road vehicle. *Exp. Fluids*, 54(5):1529, 2013.

[4] S. Sebben, L. Sterken, and T. Wölken. Characterization of the rear wake of a SUV with extensions and without extensions. *Proc. Inst. Mech. Eng., Part D: J. Auto. Eng.*, 231(9):1294–1302, 2017.

[5] W. Zeidan, N. Mazellier, E. Guilmineau, P-Y. Passaggia, and A. Kourta. A near-wake survey of an Ahmed body comparing low- & high-fidelity numerical models with experiments. *Euro. J. Mech. - B/Fluids*, 101:195–208, 2023.

 # 53

ERCOFTAC
European Drag Reduction and Flow Control Meeting – EDRFCM 2024
September 10$^{\mathrm{th}}$–13$^{\mathrm{th}}$, 2024, Turin, Italy

WAKE ASYMMETRY BEHIND A WALL-MOUNTED HEMISPHERE

Liu Jiaxin
Fluid Mechanics Key Laboratory of Education Ministry, Beihang University, Beijing 100191, China

Zhu Yichen
Fluid Mechanics Key Laboratory of Education Ministry, Beihang University, Beijing 100191, China

Wang Jinjun
Fluid Mechanics Key Laboratory of Education Ministry, Beihang University, Beijing 100191, China

INTRODUCTION

The flow around a surface-mounted hemisphere is a fundamental issue in fluid dynamics for its widely practical engineering applications; for example, one of the classic uses of the hemispherical shape in aircraft is as a beam director. In general, extending a protuberance into the flow around an aircraft is often accompanied by adverse aerodynamic issues such as massively separated flow and wake vortex shedding. Although the hemisphere has simple geometry, the flow over it is highly unsteady and three-dimensional and has various flow structures, which may create structural issues from the cyclic loading associated with highly unsteady flows. However, reasonable application of the surface-mounted hemisphere in the aircraft could improve the flow field characteristics, delay the separation, and reduce the aerodynamic resistance. Meanwhile, hemisphere protuberance can be used as an alternative approach to artificially generating hairpin vortices (HV) in the laminar boundary layer, which has been proven to have characteristics very similar to the typical HVs generated in turbulent boundary layers [7, 3]. In short, studying the flow around the hemisphere has great significance for understanding the dynamics of hairpin vortices and promoting its engineering applications in flow control.

While many important structures in typical cross-sections have been revealed, the dynamics characteristics over a hemisphere investigated from the experimental measurements are deficient. Previous studies reported symmetric shedding patterns in the hemispherical wake at low Reynolds numbers [1, 6] and asymmetric shedding patterns at high Reynolds numbers [2, 5], but the coexistence of these two patterns has barely been observed, and likewise, the mechanism of asymmetric patterns lacks clear explanations. The objective of the present study is to further investigat the near wake of a hemisphere using advanced experimental techniques.

EXPERIMENTAL SET-UP

Time-resolved tomographic particle image velocimetry was employed to measure the flow field around a 10mm height hemisphere completely immersed in a laminar boundary layer. Figure 1 illustrates the schematic of the experimental model and set-up. The flat plate of dimensions 500 mm × 15 mm × 1500 mm (height × thickness × length) was placed vertically in the channel with a 5:1 semi-elliptical profile to ensure a subsequent laminar flow field, and the distance between the center of the hemisphere and the leading edge of the plate was 300 mm. The incoming freestream velocity was set to $U_\infty = 154.8mm/s$, and the Reynolds number based on the hemisphere height is 1530 ($Re_h = U_\infty h/\nu$, where ν is the kinematic viscosity of the fluid). The field of view was approximately $12h\times$ $8h\times$ $2h$, and the three-dimensional and three-component velocity fields are calculated using multi-pass correlation analysis with window deformation with final interrogation volume size is 48 × 48 × 48 voxels with 75% overlap, giving the vector pitch of 0.576 mm.

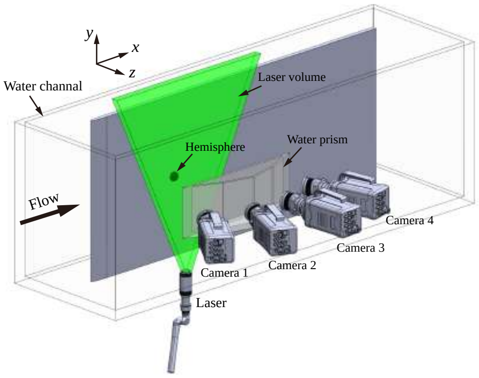

Figure 1: Sketch of the tomographic PIV configuration.

RESULTS AND DISCUSSION

In the wake of the hemisphere, a new asymmetric shedding pattern is observed in the present study. In contrast to the canonical shedding pattern exhibiting discrete HV with spanwise symmetrical distribution, the asymmetric pattern manifests alternating lateral inclinations of the HVs, which is analogous to the phenomenon observed in wall-mounted prismatic wake [4]. However, unlike the transformation of the wake from the symmetric to the asymmetric shedding pattern with increasing Reynolds number reported before, the coexistence of the two shedding patterns was observed experimentally in the hemispherical wake at the current Reynolds number for the first time. Figure 2 gives three typical instantaneous flow fields around a hemisphere. The symmetric distribution shown in Figure 2a is consistent with our previous observations at lower Reynolds numbers [6], while Figure 2b, c clearly display the deflections of HV towards the positive and negative y-axis during convecting downstream, respectively.

Natrually, the low-speed region under the head portions of HVs similarly oscillates laterally with it. It is worth noting that asymmetric oscillations occur intermittently in the near wake rather than in a regularly periodic manner.

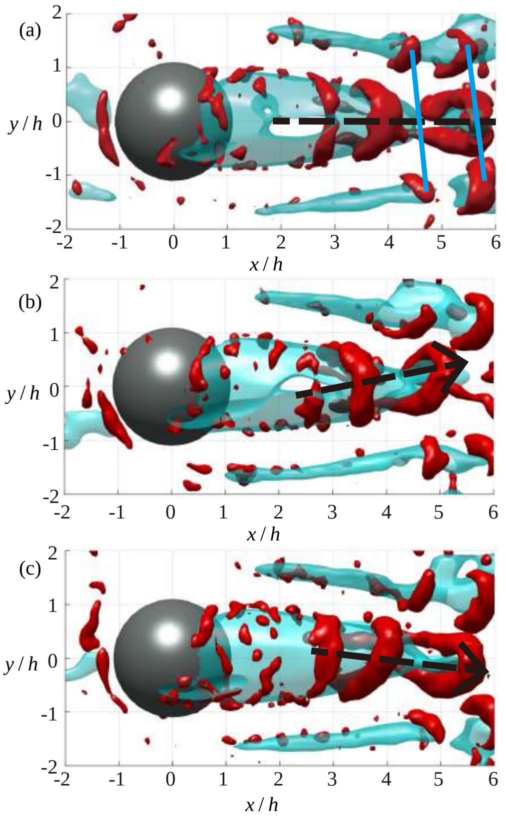

Figure 2: Three typical instantaneous flow fields with isosurfaces of $Q/(U_\infty/h)^2 = 4.4$, and the blue transparent isosurfaces of $u/U_\infty = 0.35$ depict the low-speed region behind the hemisphere.

Two distinct low-speed regions appear on each side of the hemisphere, due mainly to upwash motions induced by the re-oriented standing vortices, which push the low-momentum fluid near the wall upwards. The low-momentum fluid interacts with the external high-momentum flow to form strong shear layers, which further roll up to form the arch-shape vortices, referred to as side hairpin vortices (SHV). As shown in Figure 2, SHVs resemble bridges straddling the low-speed region on either side of the wake. Surprisingly, SHV structures are not symmetric along the spanwise direction in the present work (indicated by the blue lines in figure 2), but rather formed and shed alternately regardless of the shedding pattern of HVs in the middle of the wake.

Figrue 3 gives the correlation coefficient between the streamwise velocity fluctuations of two spanwise symmetric locations at different flow locations. One is at $x = 3.3$, where the SHV has not yet rolled up, and the other is at $x = 5.1$, where SHVs have been completely formed and shed downstream. Their common maximunms are reached when $\Delta t/T_{SHV} = 0.17$, where the T_{SHV} represents the period of SHV shedding. This indicates that there is always a phase difference of $\pi/3$ between the two low-speed regions on both sides of the hemisphere. Therefore, it is suggested that there are spanwise asymmetric perturbations contained in the low-speed region on both sides, and these perturbations are transported from upstream to downstream, leading to asymmetric shedding of SHVs.

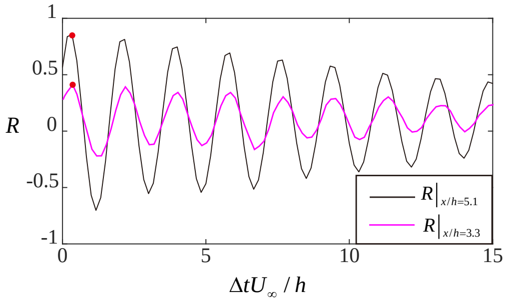

Figure 3: Temporal cross-correlation of the streamwise velocity fluctuations at two spanwise symmetric locations at different streamwise location, denoted as black ($x/h = 5.1$, $y/h = \pm 1.35$, $z/h = 0.8$) and magenta lines ($x/h = 3.3$, $y/h = \pm 1.58$, $z/h = 0.8$), respectively.

REFERENCES

[1] M. S. Acarlar and C. R. Smith. A study of hairpin vortices in a laminar boundary layer. Part 1. Hairpin vortices generated by a hemisphere protuberance. *J. Fluid Mech.*, 175:1–43, 1987.

[2] Yong Cao and Tetsuro Tamura. Large-eddy simulation study of Reynolds number effects on the flow around a wall-mounted hemisphere in a boundary layer. *Physics of Fluids*, 32(2):025109, 2020.

[3] Tian-da Gao, Jiao Sun, Wen-yi Chen, Ying Fan, and Yantao Zhang. Experimental investigation on the effect of particles on large scale vortices of an isolated hemispherical roughness element. *Physics of Fluids*, 33(6):063308, 2021.

[4] Shubham Goswami and Arman Hemmati. Mechanisms of wake asymmetry and secondary structures behind low aspect-ratio wall-mounted prisms. *J. Fluid Mech.*, 950:A31, 2022.

[5] Jiahua Li, Xiang Qiu, Yu Shao, Haoxuan Liu, Yuan Fu, Yizhou Tao, and Yulu Liu. Turbulent coherent structures in channel flow with a wall-mounted hemisphere. *AIP Advances*, 12(3):035006, 2022.

[6] Jiaxin Liu, Jinjun Wang, Yichen Zhu, and Chong Pan. Vortex dynamics in the near wake of a surface-mounted hemisphere. *Physics of Fluids*, 36(1):013619, 2024.

[7] J. Zhou, R. J. Adrian, S. Balachandar, and T. M. Kendall. Mechanisms for generating coherent packets of hairpin vortices in channel flow. *J. Fluid Mech.*, 387:353–396, 1999.

 # 54

ERCOFTAC
European Drag Reduction and Flow Control Meeting – EDRFCM 2024
September 10$^{\mathrm{th}}$–13$^{\mathrm{th}}$, 2024, Turin, Italy

CONTROL OF FLOW SEPARATION VIA CORIOLIS ACCELERATION IN FLAPPING FLIGHT

Yekaterina Goodwin
Department of Aeronautics, Imperial College London, SW7 2AZ, London, United Kingdom

Georgios Rigas
Department of Aeronautics, Imperial College London, SW7 2AZ, London, United Kingdom

Jonathan F. Morrison
Department of Aeronautics, Imperial College London, SW7 2AZ, London, United Kingdom

INTRODUCTION

Leading edge vorticity generation [1] is a key unsteady mechanism for delaying stall and promoting flow attachment at high angles of attack. We present an investigation into control of this unsteady structure by taking inspiration from flapping flight, exhibited as the primary form of locomotion for tens of thousands of vertebrate and millions of invertebrate species [2]. Wind tunnel investigations of flapping flight are often complex, however, due to the difficulty of working with live specimens and the challenge of building robotics capable of capturing the wide ranging kinematics observed in nature. We have designed a novel experimental method for investigation of flapping flight dynamics in a wind tunnel, using a 6-axis articulated robotic arm, offering a programmable platform to explore a wide range of flight kinematics and the corresponding large parameter space. With this approach, we parameterise the flapping profile with respect to Rossby number to investigate attachment of leading edge vorticity (LEV) on the wing. The formation of LEVs strongly depends on Rossby number, which quantifies centripetal and Coriolis accelerations, for stability which can be varied via the radius of revolution of the stroke R [3]. We explore this relationship at higher Reynolds numbers in the freestream, by controlling the radius of revolution for a figure-of-8 flapping wing path, with the goal of exploring novel methods of separation control exploiting unsteady flight dynamics for this setup.

THE MODEL

The model for this study is a flat plate, with a 150 mm chord c and 325 mm span b, actuated by a six-axes ABB IRB140 industrial robot, mounted outside the tunnel test section with the wing connected via a beam to the robot flange. The wing is mounted at its quarter chord and is positioned in the center of the test section $\pm b/4$. Procedures for flapping are written in RAPID code on the robot controller, performing a simple figure-of-8 path with the pitch angle varying from $-30°$ to $30°$; the stroke path is shown in Figure 1. The origin point for rotation varies from negative infinity (pure translation) to the wing root (pure revolution), as shown in Figure 2. The parameter space explored by the experiment series covers $Re_c = 16,000$ (defined based on the chord, freestream velocity and wingtip velocity) and advance ratio $J = 7.25$; within this, the Rossby number is varied from $Ro = 12.8 - 31.0$, with an infinite Rossby number case representing pure translation of the stroke. A significant advantage of the chosen method is the ability to change the radius of revolution by simply editing code without having to swap out or change any physical characteristics of the setup itself, allowing a full parameterised study.

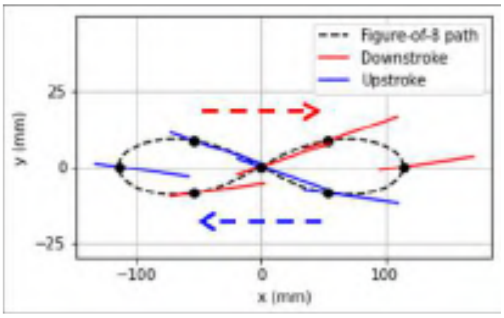

Figure 1: The wingtip motion of the plate, showing rotation about the quarter-chord as the path is swept out. The freestream is from left to right. The axes are not to scale.

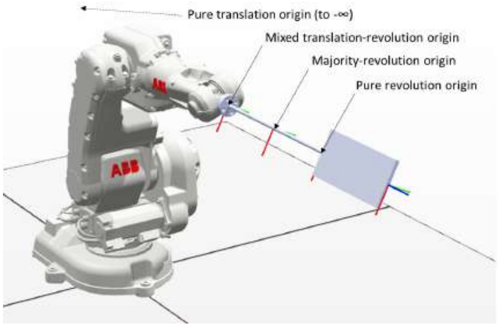

Figure 2: The ABB IRB140 robot simulation with the origins of rotation shown. At the half span $b/2$, the pure translation origin gives $Ro = \infty$, mixed translation-revolution $Ro = 23.11$, majority-revolution $Ro = 16.8$ and pure revolution $Ro = 7.92$. Note that the plate was fixed at the quarter chord for the experiments.

EXPERIMENTAL METHODOLOGY

The flow fields for the various procedures were captured using translational single-shot stereo-PIV, at $y/b = 0.25, 0.5$ and 0.75. The measurements are time resolved, capturing the full recursive stroke path 8 times in succession with an acquisition frequency of 250 Hz. In order to move the acquisition plane, the robot itself was used to adjust the position of the plate, rather than moving the optics, providing a time saving solution to capturing multiple stereo-PIV planes without having to change the acquisition setup. Experiments were carried out in the T1 Wind Tunnel at Imperial College London with a tunnel speed of 1.5 m/s. The full setup is shown in Figure 3, with the acquired PIV plane locations shown in Figure 4.

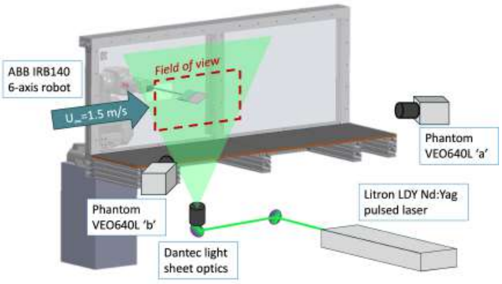

Figure 3: The experimental setup, shown via a streamwise cross section of the T1 wind tunnel.

RESULTS

Controlling the radius of revolution R for hovering flight has previously been shown at Reynolds numbers in the range $110 - 1400$ to stabilise the attachment of leading edge vorticity [3]. An initial inspection of our vorticity fields at higher Reynolds numbers, with freestream velocity, shows that leading edge vorticity generated at the start of the upstroke and downstroke stays coherent for longer when the radius of revolution is minimised, confirming that LEV stability scales with $1/Ro$ as seen in previous experimental work in the field [3]. Of particular interest in this study is the LEV bursting (a Reynolds number dependent effect) vs shedding (a Rossby number dependent effect) interaction, where a loss in coherence of the LEV does not necessarily indicate separation of the flow from the flat plate [3] - an analysis of this behaviour for these data will be presented. Figure 5 shows a possible example of this bursting and subsequent shedding behaviour of the leading edge vorticity for the translation case. We will then further analyse the spectral properties of the flowfields, inspecting both snapshot POD and spectral analysis of the modes, to investigate our previously observed energy transfer between the harmonics of the attached structures with respect to Rossby number.

ACKNOWLEDGEMENTS

This work is funded by the President's PhD Scholarships at Imperial College London.

REFERENCES

[1] Charles P. Ellington, Coen van den Berg, Alexander P. Willmott, and Adrian L. R. Thomas. Leading-edge vortices in insect flight. *Nature*, 384:626–630, 12 1996.

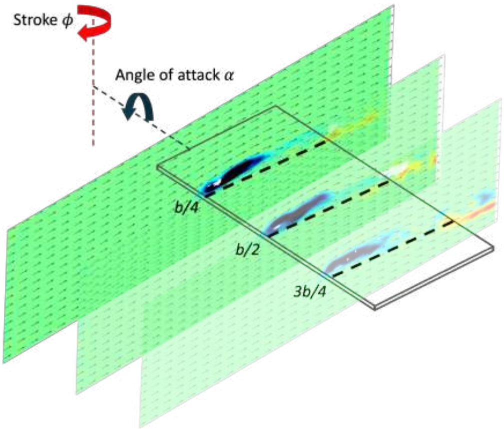

Figure 4: The three PIV planes gathered for each procedure; a snapshot of the results for the majority-revolution stroke is shown. In these vorticity fields, the LEV (dark blue, clockwise) and trailing edge vorticity (red, anticlockwise) is clearly observed.

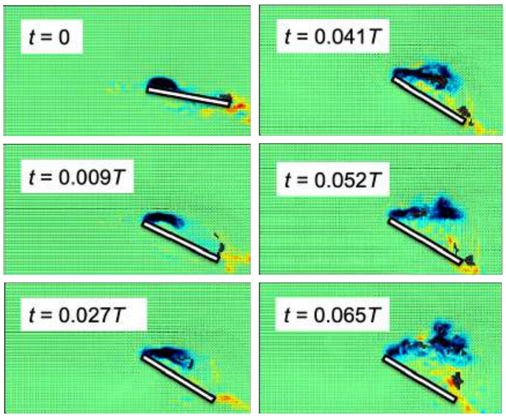

Figure 5: Plot of vorticity for the translation case, where T is the time period of the complete stroke. The plate position is superimposed on top; an LEV (dark blue) is shown forming, bursting and separating.

[2] W. Jetz, G. H. Thomas, J. B. Joy, K. Hartmann, and A. O. Mooers. The global diversity of birds in space and time. *Nature*, 491(7424):444–448, 11 2012.

[3] David Lentink and Michael H. Dickinson. Rotational accelerations stabilize leading edge vortices on revolving fly wings. *Journal of Experimental Biology*, 212(16):2705–2719, 08 2009.

55

ERCOFTAC
European Drag Reduction and Flow Control Meeting – EDRFCM 2024
September 10$^{\text{th}}$–13$^{\text{th}}$, 2024, Turin, Italy

TURBULENT BOUNDARY LAYER SEPARATION CONTROL USING MICRO ROTATING CYLINDRICAL VORTEX GENERATORS

Yongxiang Wu, Ulrich Rist and Christoph Wenzel
Institute of Aerodynamics and Gas Dynamics, University of Stuttgart, 70569 Stuttgart, Germany

INTRODUCTION

Turbulent boundary-layer separation from a curved surface is characterized by complicated phenomena including spatially and temporally irregular separation and reattachment lines, strong interaction with the outer flow and interaction between pressure and velocity fluctuations [1]. Understanding and controlling its onset, development and reattachment with corresponding control mechanisms impacts all related practical applications.

Starting in Prandtl's time, continuous attempts were undertaken to investigate the capabilities of many active/passive means for boundary-layer separation control. Passive control methods such as vortex generators are effective in energizing the boundary layer by generating streamwise elongated vortices through the lift-up mechanism [5], where high-momentum fluid is pulled towards the wall and low-momentum fluid is pushed away from the wall. Active control strategies, on the other side, are flexible in adapting to various operating conditions by adjusting the input for the actuators [2]. Flow separation is controlled through the mechanisms of either directly energizing the flow by injecting high-momentum fluid, e.g. by blowing/suction or synthetic jets [3], or inducing high-momentum flow with actuators such as vortex- or plasma-actuators [7]. While passive control strategies are preferred for their simplicity and no extra energy requirements, active control methods are favoured for their flexibility and controllability. The most promising direction for providing a robust boundary-layer separation control is the so-called micro vortex generators (MVGs) in the form of either surface protrusions [6] or fluidic injection [4]. As shown by [6], the most efficient mechanism to reduce flow separation is based on mixing low- and high-momentum fluid between the near wall region and the outer region. The height of the vortex generators, effective for separation control, was found to be $0.2 \sim k/\delta \sim 0.8$, where k is the vortex generator height and δ is the boundary-layer thickness. Such micro-devices' success is ascribed to the basic mechanism that strong vortices are generated close to the wall. The non-linear mechanisms amplify the vortices into the macro scales, thus energizing the boundary layer.

The current work investigates a specific form of micro vortex generator for turbulent boundary-layer separation control: micro rotating cylindrical vortex generators (mRCVGs). Figure 1(a) shows a setup with a counter-rotating pair of the mRCVGs embedded in a boundary layer. The rotation strength is quantified as the relative tangential velocity at the top of the cylinder to the incoming local mean velocity $\bar{u}(y = k)$, i.e $\Omega_u = \Omega D/2\bar{u}(k)$, where Ω is the angular velocity and D the cylinder diameter. A laminar baseflow induced by the counter-rotating mRCVGs with $\Omega_u = 0.2$ is shown in Figure 1(b), where a high-speed streak is brought into the boundary layer.

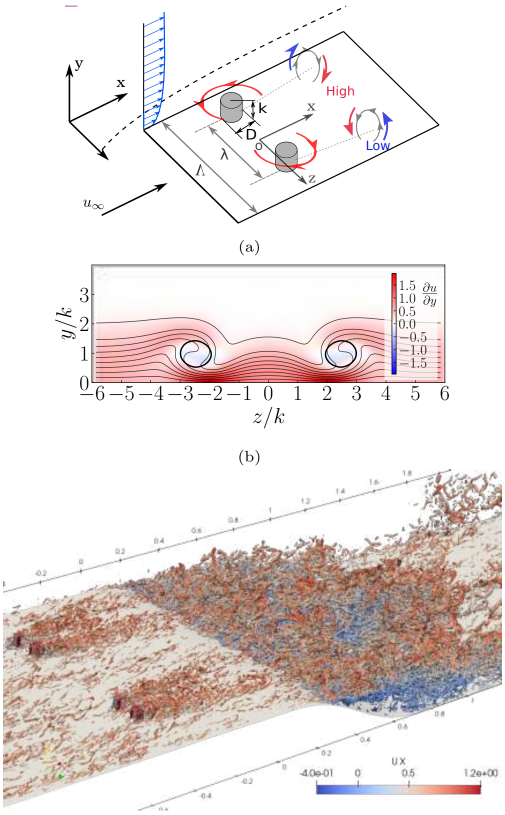

(a)

(b)

(c)

Figure 1: (a): Numerical setup of counter-rotating vortex generators embedded in a flat-plate boundary layer. (b): Slices of the laminar baseflow induced by counter-rotating mRCVGs with $\Omega_u = 0.2$. Thin solid lines are isolines of $u/u_\infty = 0.1 \sim 0.95$. Thick black lines visualize vortex cores employing $\lambda_2 = -5$. (c): Isocontours of λ_2 coloured by streamwise velocity for instantaneous turbulent flow field induced by counter-rotating mRCVGs with $\eta = 0.5$ and $\Omega_u = 1$.

In our previous study [10, 11], it is found that the induced high-speed streak is capable of delaying and controlling the Tollmien-Schlichting instabilities [9, 12]. The current investigation will focus on the mRCVGs-induced streamwise vortices and their potential to control a turbulent boundary separation bubble over a curved ramp.

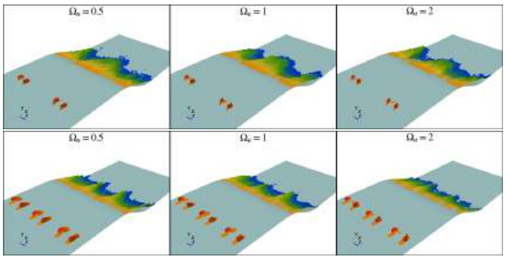

Figure 2: Isocontour of $u = 0$ coloured by wall-normal coordinate y, visualizing the temporal averaged separation bubble. Top row: $\eta = 0.5$, bottom row: $\eta = 1$.

Re_θ	$\eta = D/k$	λ	Λ	Ω_u
1000	0.5	2	12	0.5, 1, 2
1000	1	2.8	8	0.5, 1, 2

Table 1: Parameters of setups

NUMERICAL METHOD

Numerical investigations are performed with the k-equation model LES approach. A digital filtering synthetic eddy method (SEM) [8] is used to generate an unsteady, turbulent inlet flow with $Re_\theta = 300$. After some induction distance, a fully developed turbulent flow at $Re_\theta \approx 400$ can be obtained. The mRCVGs are placed at a streamwise station $Re_\theta = 1000$. The spatial resolution for the general grid over the flat plate is $x^+ \times y^+_{min} \times z^+ = 15 \times 1 \times 12$, which is further reduced to $r^+ \textit{(radial)} \times \phi^+ \textit{(circumferential)} = 1.1 \times 3.7$ for the grids around the cylinder. The sampling time is two times longer and the domain size is even bigger, however, the CPU hours used in the LES simulation (0.66×10^5 hours) is two orders of magnitude lower than that of a DNS. The solver used is *pimpleFoam* in its *piso* mode which solves the incompressible N-S equations by using a Pressure-Implicit with Splitting of Operators (PISO) algorithm. The pressure equation is solved by the Geometric Algebraic Multi-Grid (GAMG) solver and the velocity equation by the Preconditioned Bi-Conjugate Gradient (PBiCG) solver.

RESULTS AND DISCUSSIONS

Figure 1(c) shows a snapshot of the instantaneous vortices of the turbulent boundary layer with counter-rotating mRCVGs with aspect ratio $\eta = D/k = 0.5$ and rotation rate $\Omega_u = 1$. In contrast to the laminar case, the induced streamwise vortices break into large and small coherent structures. Even so, the broken vortex is still effective in pulling down the high-speed fluid from outside of the boundary layer.

Figure 2 shows the control effects of two set-ups of counter-rotating mRCVGs with different aspect ratios, spanwise spacings and rotation rates. The set-up parameters are shown in Table 1. The separation bubble appears to be suppressed as the rotation rate increases. The suppression effect is more evident in the wake region of the mRCVGs since high-velocity streaks are supposed to be induced in the middle of the mRCVGs and therefore the turbulent boundary layer is energized.

For unveiling possible unsteady mechanisms behind the above-observed separation suppression and spatial-temporal characteristics of the turbulent separation bubble with and without the control of mRCVGs, two-point auto-correlation and dynamic mode decomposition analysis of the turbulent flow will be presented in the meeting contribution. In addition, the interaction between the mRCVGs-induced coherent structures and the unsteady separation bubble over the curved backward ramp will be discussed.

REFERENCES

[1] M. Breuer, N. Peller, C. Rapp, and M. Manhart. Flow over periodic hills–numerical and experimental study in a wide range of reynolds numbers. *Comput Fluids*, 38(2):433–457, 2009.

[2] Louis N Cattafesta III and Mark Sheplak. Actuators for active flow control. *Annu. Rev. Fluid Mech.*, 43:247–272, 2011.

[3] A. Glezer and M. Amitay. Synthetic jets. *Ann. Rev. Fluid Mech.*, 34(1):503–529, 2002.

[4] Kursat Kara, Daegyoum Kim, and Philip J Morris. Flow-separation control using sweeping jet actuator. *AIAA J.*, 56(11):4604–4613, 2018.

[5] MT Landahl. A note on an algebraic instability of inviscid parallel shear flows. *J. Fluid Mech.*, 98(2):243–251, 1980.

[6] J. Lin. Control of turbulent boundary-layer separation using micro-vortex generators. In *30th Fluid Dynamics Conference*, page 3404, 1999.

[7] J. Lin. Review of research on low-profile vortex generators to control boundary-layer separation. *Prog. Aerosp. Sci.*, 38(4-5):389–420, 2002.

[8] R Poletto, T Craft, and A Revell. A new divergence free synthetic eddy method for the reproduction of inlet flow conditions for les. *Flow, turbulence and combustion*, 91(3):519–539, 2013.

[9] T. Römer, K. Schulz, Y. Wu, C. Wenzel, and U. Rist. Delay of laminar–turbulent transition by counter-rotating cylindrical roughness elements in a laminar flat plate boundary layer. *Exp Fluid.*, 64:42, 2 2023.

[10] Y. Wu, G. Axtmann, and U. Rist. Linear stability analysis of a boundary layer with rotating wall-normal cylindrical roughness elements. *J. Fluid Mech.*, 915:A132, 2021.

[11] Y. Wu, T. Römer, G. Axtmann, and U. Rist. Transition mechanisms in a boundary layer controlled by rotating wall-normal cylindrical roughness elements. *J. Fluid Mech.*, 945:A20, 2022.

[12] Y. Wu, C. Wenzel, and U. Rist. Control of laminar-turbulent transition using counter-rotating cylindrical roughness pairs. In *Dillmann A., Heller G., Krämer E., Wagner C., Julien W. (eds) New Results in Numerical and Experimental Fluid Mechanics XIV.*, Notes on Numerical Fluid Mechanics and Multidisciplinary Design, pages 402–411. Springer, Cham, 2024.

 # 56

European Drag Reduction and Flow Control Meeting – EDRFCM 2024
September 10–13 2024, Turin, Italy

THE STATE OF TURBULENCE IN A PIPE FLOW WITH DRAG REDUCTION

E. Gallorini
Dipartimento di Scienze e Tecnologie Aerospaziali, Politecnico di Milano, via La Masa 34, 20156 Milano, Italy,
D. Massaro
SimEx/FLOW, Engineering Mechanics, KTH Royal Institute of Technology, SE-100 44 Stockholm, Sweden
P. Schlatter
Institute of Fluid Mechanics (LSTM), Friedrich–Alexander–Universität (FAU) Erlangen–Nürnberg, DE-91058 Erlangen, Germany
M. Quadrio
Dipartimento di Scienze e Tecnologie Aerospaziali, Politecnico di Milano, via La Masa 34, 20156 Milano, Italy,

INTRODUCTION

Since their introduction [5], streamwise traveling waves of spanwise wall velocity (StTW) have been an efficient approach to reducing drag in wall-bounded flows such as channel flow or pipe flow. The drag-reducing effect of StTW has been confirmed experimentally for the first time by [1], where a discrete counterpart of the continuous sinusoidal wave was used. Drag reduction figures represented in figure 1 were obtained. The figure plots drag reduction in a pipe flow for a wave experimentally discretized by three discrete segments ($s = 3$), with the streamwise wavenumber fixed at $k_x^+ = 0.0082$ (where the superscript $^+$ stands for viscous units of the reference case) and compares them to the original channel flow data obtained by DNS. Here, $R = 1 - \frac{C_f}{C_{f,0}}$ is the drag reduction, and C_f and $C_{f,0}$ are the friction coefficients measured respectively in the actuated and reference cases.

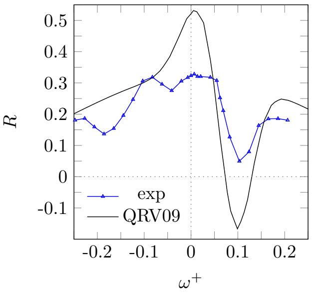

Figure 1: Drag reduction R experimentally measured for StTW in [1] in the pipe flow (blue triangles), compared at the same value of k^+ to available DNS information for StTW from the DNS study of [5] in the planar geometry (continuous black line).

The experimental and the numerical curves are not identical. The experiments show wiggles absent in the simulations and with the maximum drag reduction limited to $R \sim 0.3$. These effects, already noticed in [1], have been recently discussed in [3], which focused on the discrete nature of the control, which explains the wiggles observed in the experiment. The higher drag reduction observed in the simulations has been attributed to a state of partial relaminarization that could not be reached in the experimental facility. The present work intends to explore this last topic further, by studying how StTW affect the flow state. In particular, since flow relaminarization is obtained at (bulk) Reynolds numbers that are much higher than the usual ones around which transition to turbulence in pipes is observed [2], we ask the question whether Re is enough to characterize the transition process in a controlled pipe flow.

METHODOLOGY

Direct numerical simulations (DNS) of a turbulent pipe flow modified by StTW are carried out to study how skin friction modifications alter the flow state. Navier–Stokes equations are written in non-dimensional form and in cylindrical coordinates, for the primitive variables pressure p and velocity $\boldsymbol{u}$, as described in [3]. Temporal discretization is based on a partially implicit scheme with a combination of the implicit Crank-Nicholson scheme for the linear terms and a three-substeps, low-storage Runge–Kutta scheme for the convective terms. Regarding spatial discretization, the homogeneous streamwise and azimuthal directions x and θ call for a spectral discretization, naturally enforcing the required periodic boundary conditions with the computational efficiency of the pseudo-spectral approach. Compact, fourth-order accurate finite differences are used to discretize differential operators in the radial direction. The azimuthal resolution would increase above the required level as the pipe axis is approached, with expensive requirements on the timestep to satisfy the CFL conditions. The present numerical method, as described in [3], works around this issue by gradually truncating the Fourier series in θ direction as the radial coordinate approaches the center of the channel, such that the azimthal resolution remains approximately constant with the radial coordinate. The pipe studied in this set of numerical experiments has a length $L_x = 30D$, being D the pipe diameter. This extended dimension, compared to work on similar topics, has been chosen to make sure that the phenomena are not constrained by the domain length. To duplicate the experiment, the simulations are run at a constant flow rate, with a bulk Reynolds number $Re_b = \frac{U_b D}{\nu} = 4900$ and a reference friction Reynolds number $Re_\tau = \frac{u_\tau R}{\nu} = 169$. StTW are applied by explicitly imposing a Dirichlet condition for the azimuthal velocity of the type

$u_\theta(x,t) = A\sin(k_x x - \omega t)$, being A, k_x and ω the control amplitude, wave-length and frequency. Several simulations in different positions of the $k_x - \omega$ plane are performed, while $A = 0.5$ ($A^+ = 14.5$). As k_x is changed, the length of the domain is slightly enlarged/contracted to always accommodate an integer number of waves.

RESULTS

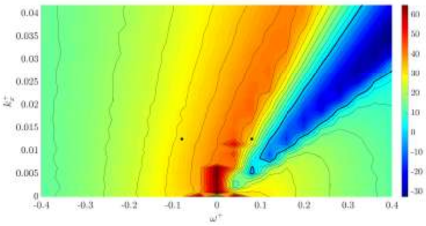

Figure 2: Map of friction drag reduction (percentage) in the $\omega - k_x$ plane for $A = 0.5$ and $Re_b = 4900$. Contours are spaced by 5% intervals, with the zero level indicated by thick lines. The two dots, at the same R, correspond to the two flows considered later in figure 3.

We first explore the $\omega - k_x$ parameter space by performing approximately 700 DNS for different combinations of k_x and ω. The data are organized in a drag reduction map as in [5] and plotted in figure 2. The simulation outcomes in terms of drag reduction resemble those of the plane channel flow, and exhibit, as expected, regions of high drag reduction and drag increase at similar frequencies and wavelengths. In the present case, the maximum drag reduction is obtained at low wavenumbers where a complete relaminarization of the flow is obtained, corresponding to a drag reduction of $\mathcal{R} = 65\%$.

All the cases are at $Re_b = 4900$, and it is known [2] that this is well above the transitional regime in the natural pipe flow. Here, however, the picture is complicated by the presence of the drag-reducing forcing, possibly leading to a state of spatially-localized turbulence observed in [3] and also typical of the natural pipe flow but at much lower Re_b. One might surmise that, since the StTW alter the one-to-one relationship between Re_b and Re_τ of the natural pipe flow, perhaps Re_τ is a better indicator for transition.

To describe the flow state, we compute at any time instant the integral of the cross-stream turbulent kinetic energy q across the cross-section A of the pipe:

$$q(x,t) = \int_A (u_r^2 + u_\theta^2)\, dA, \qquad (1)$$

which is an acknowledged indicator of turbulence [4]. In fact q is useful to emphasize where along the pipe axis turbulent puffs develop, and where a nearly laminar flow exists.

We show the spatio-temporal evolution of $q(x,t)$ for two cases, identified with dots in figure 2. These have the same $k_x^+ = 0.0126$; the two frequencies $\omega^+ = \pm 0.08$ yield a similar amount of $\mathcal{R} \sim 31\%$, hence the same value of friction Reynolds number Re_τ.

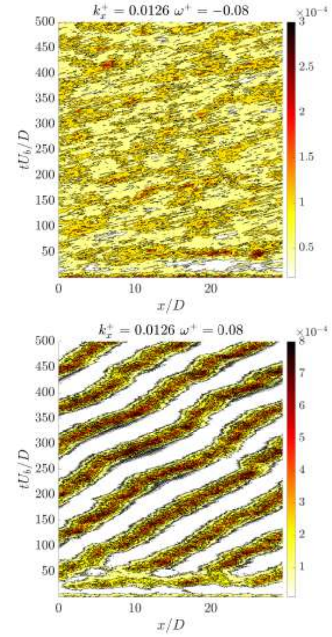

Figure 3: Space-time contour plot of $q/(AU_b^2)$ in a reference frame moving with a convection velocity $U_c = U_b$, for the two cases with $k_x^+ = 0.0126$ and $\omega^+ = \pm 0.08$. Flow is from left to right.

Figure 3 represents the evolution of $q(x,t)$ over the periodic pipe with time. The two cases have the same friction and bulk Reynolds numbers, yet the flow behavior is different. With the backward-traveling wave (top panel), turbulence reduces compared to the reference case, but the flow is turbulent everywhere during the whole simulation. With the forward-traveling wave (bottom panel), instead, turbulence is localized in highly energetic spots, while the regions inbetween are quiescent and nearly laminar. This is often observed in transitional pipe flows, and closely resembles the puff structures observed in pipe flow experiments [2]. Note that here these transient phenomena appear at $Re_b = 4900$, that is well beyond the critical value (around $Re_b = 2000$) identified in previous work to sustain turbulence [2]. Hence, the global bulk and friction Reynolds numbers are insufficient to identify the flow regime in a pipe under the action of drag-reducing control. Further research is ongoing to clarify if and how local friction affects the localized state of turbulence.

REFERENCES

[1] F. Auteri, A. Baron, M. Belan, G. Campanardi, and M. Quadrio. Experimental assessment of drag reduction by traveling waves in a turbulent pipe flow. *Physics of Fluids*, 22(11):115103/14, 2010.

[2] M. Avila, D. Barkley, and B. Hof. Transition to Turbulence in Pipe Flow. *Annual Review of Fluid Mechanics*, 55(1):575–602, 2023.

[3] E. Gallorini and M. Quadrio. Spatial discretization effects in spanwise forcing for turbulent drag reduction. *Journal of Fluid Mechanics*, 982:A11, March 2024.

[4] D. Moxey and D. Barkley. Distinct large-scale turbulent-laminar states in transitional pipe flow. *Proceedings of the National Academy of Sciences*, 107(18):8091–8096, May 2010.

[5] M. Quadrio, P. Ricco, and C. Viotti. Streamwise-traveling waves of spanwise wall velocity for turbulent drag reduction. *Journal of Fluid Mechanics*, 627:161–178, 2009.

57

ERCOFTAC
European Drag Reduction and Flow Control Meeting – EDRFCM 2024
September 10th–13th, 2024, Turin, Italy

ONSET OF POLYMERIC DRAG REDUCTION AT DIFFERENT REYNOLDS AND WEISENBERG NUMBERS

Lukas Brandfellner
Doctoral College Advanced Functional Materials, University Vienna, 1090 Vienna, Austria

Alexander Bismarck
Institute of Materials Chemistry and Research, University Vienna, 1090 Vienna, Austria

Hans Werner Müller
Institute of Materials Chemistry and Research, University Vienna, 1090 Vienna, Austria

High molecular weight polymers can act as drag reducing agents. Dimensionless numbers used to describe the flow of solutions containing these polymers are the Reynolds number (Re), Weisenber number (Wi) and Fanning friction factor (f). Re is the ratio of inertia forces to viscous force governing the flow, Wi the ratio of the timescales of polymer relaxation and of the flow and f the ratio of the local shear stress and the local kinetic energy density. Drag reduction (DR) is calculated by comparing f of the polymer solution with f of the pure solvent at the same Re, while Wi provides additional insight into the polymer behaviour.

In a given polymer solvent system Wi is directly proportional to Re. In pipe flow different flow regimes can be observed with increasing Re. Depending on the relation of Wi and Re a polymer solution either transitions from laminar flow directly to turbulent drag reduction flow (f differs from f of the pure solvent) or an additional turbulent regime is encountered in between (pre-onset turbulent flow, f following the Prandtl-Kármán law). Eventually the flow transitions from intermediate DR to maximum DR as described by Virk's asymptote, [1]. The regime boundaries depend on polymer and solution properties.

We performed long term degradation experiments in a pipe flow facility [2], using polyacrylamide (PAAm) as drag reducing agent. Some of these experiments were presented in [3]. Starting from different initial molecular weights, polymer degradation caused the molecular weight of PAAm samples to decrease and altered their weight distribution. The degradation was monitored by measurements of DR, molecular weight and viscosity. Changes in flow regimes were forced by varying Re in the flow facility. The degradation induced changes in DR were fitted by an exponential decay function depending on the total length the solution travelled through the flow facility (distance). The Re dependence of the friction factor was as linear interpolation between the Prandtl-Kármán law (no DR) and Virk's asymptote (max. DR). Combining these fits we received a surface in the Prandtl-Kármán plot describing the behaviour of one degradation experiment as shown in Figure 1. This analysis allowed to derive the onset of DR at any point of degradation in the long-term experiment.

Wi was calculated as the product of shear rate at the onset of DR and polymer relaxation time, with the shear rate being derived directly from f and Re. Polymer relaxation was calculated based on Oldroyd-B using the weight average molecular weight (M_w) and the viscosity contribution of the polymer as in [4].

In the Re-Wi plane the DR onset points were clustered along two lines, corresponding to two different transitions, shown in Figure 2. A transition from pre-onset turbulent flow to the intermediate DR regime was found at Wi between 0.5 and 1 independent of Re. [5] reported a constant Wi of 0.5 for this onset. Another cluster showed an increasing Re at onset with increasing Wi for higher Wi. The trend is similar to that described for the laminar flow - DR-flow transition with increasing Re by [6].

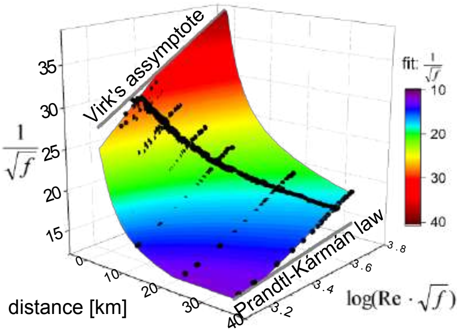

Figure 1. Extrapolation of Fanning friction factors measured in pipe flow taken from [2]. Each black point corresponds to a flow experiment.

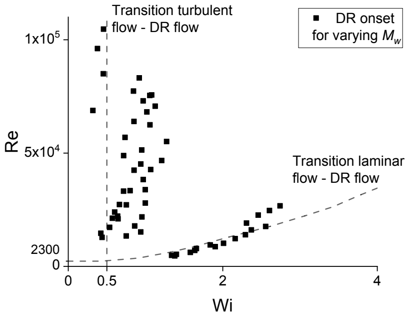

Figure 2. DR onset of solutions of PAAm with varying molecular weight in comparison with transitions reported in [4] and [5].

REFERENCES

[1] P. S. Virk. Drag reduction fundamentals. *AIChE J.*, 21:625-656, 1975.

[2] H. W. Müller, L. Brandfellner, A. Bismarck. Long-term degradation of high molar mass poly(ethylene oxide) in a turbulent pilot-scale pipe flow. *Phys. Fluids* 35:023102, 2023.

[3] L. Brandfellner, E. Muratspahić, A. Bismarck and H. W. Müller. Quantitative description of polymer drag reduction: Effect of polyacrylamide molecular weight distributions. *J. Non-Newtonian Fluid Mech.*, 325:105185, 2024.

[4] A. Zell, S. Giera, S. Rafaïb and C. Wagnera. Is there a relation between the relaxation time measured in CaBER experiments and the first normal stress coefficient? *J. Non-Newtonian Fluid Mech.*, 165:1265–1274, 2010.

[5] B. E. Owolabi, D. J. C. Dennis and R. J. Poole. Turbulent drag reduction by polymer additives in parallel-shear flows. *J. Fluid Mech.*, 827:R4, 2017.

[6] L. Xi. Turbulent drag reduction by polymer additives: Fundamentals and recent advances. *Phys. Fluids*, 31:121302, 2019.

58

ERCOFTAC
European Drag Reduction and Flow Control Meeting – EDRFCM 2024
September 10th–13th, 2024, Turin, Italy

STUDY OF DRAG REDUCTION CAPABILITY OF MACROSCALE CORRUGATED SURFACE IN TURBULENT CHANNEL FLOW

M. A. Razzak

Temasek Laboratories, National University of Singapore, Singapore

B. C. Khoo

Temasek Laboratories, National University of Singapore, Singapore

CMJ Tay
Temasek Laboratories, National University of Singapore, Singapore

INTRODUCTION

This study intends to investigate innovative surface modifications in the form of macroscale corrugated surface with the aim of reducing the turbulent skin friction drag in channel flow. It was reported by Razzak et al. (2019;2020) by performing numerical simulations, that carefully designed macroscale corrugated surfaces reduce skin friction drag in Taylor Couette flow. On the other hand, in vehicle and industrial applications, the drag reduction technique would be applied on channel flow or the external turbulent boundary-layer flow over the surface of the body. However, there is a fundamental resemblance between these types of flows which makes it plausible that the modified surface geometry will yield drag reduction also for the turbulent channel or boundary layer flow. Another reason for the potential success of the usage of macro scale corrugated surface in Taylor Couette flow is that the corrugated surface has been shown to produce naturally occurring oscillating spanwise flow, resembling the effect of spanwise wall-oscillations, an active flow control technique (yielding drag reduction of up to 50%). Interestingly, the oscillating spanwise flow reported by Razzak et al. (2019;2020;2023) occurs naturally and does not need any external power or a complex system otherwise used in the application of spanwise wall oscillation of drag reduction. Besides, the ease in maintenance and manufacturing of macroscale corrugated surface will overcome limitation of conventional drag reduction techniques such as riblets, complaint coating, superhydrophobic surfaces etc. Therefore, if it is possible to trigger and enhance the emergence of naturally occurring oscillating spanwise flow by the means of surface manipulation, a more effective and practical drag reduction technique can be achieved, and this might be a breakthrough achievement in enhancing energy efficiency and reducing carbon emission. These have motivated us to investigate the generation of naturally occurring oscillating spanwise flow by the means of surface manipulation in the form of macroscale corrugated surface and its corresponding influence on skin friction drag reduction in turbulent channel flow. The schematic diagram of macroscale corrugated surface in channel flow is shown in Figure 1.

To fulfill the objective of this study, Large Eddy Simulations (LES) has been performed at Re_τ=550 after being validated against the DNS study of Lee & Moser (2015) involving a turbulent channel flow with smooth walls shown in Figure 2. Following this, numerical simulations of macroscale corrugated surfaces in turbulent channel flow has been performed for amplitude to wavelength ratios (A/λ) of 0.125, 0.075, 0.05, 0.025 and 0.0125 and a half channel height to wavelength ratio (h/ λ) of 2.5. The streamline patterns associated with the mean flow structures in the plane normal to the flow shown in Figure 3 indicates that a pair of counter rotating vortices appears in each wavelength of the macroscale corrugated surface which results in the formation of ejection at the peak and sweep at the valley. Besides, As A/λ decreases, formation of spanwise secondary flow is observed between the counter rotating vortices shown in Figures 3 b-c. These contribute to suppressing the strength of sweeps and enhancing ejections attributed to reduced wall shear stress at the peak regions (i.e., ejection region) and slightly higher wall shear stress in the valley regions (i.e., sweeping). This combined effect results in lower wall shear stress in the macroscale corrugated surface compared to that of smooth surfaces for all A/λ. Despite the reduction in wall shear stress for all the ratios of A/λ, the net drag is found to be higher in macroscale corrugated surface for A/λ ≥ 0.06. This is related to the higher percentage increase in surface area than the percentage reduction in wall shear stress. For A/λ <0.06, net drag reduction is observed, and maximum drag reduction is found to be 2% at A/λ=0.025 as shown in Figure 4. Further studies will be carried out to enhance the strength of spanwise secondary flow and its corresponding influence on skin friction drag reduction.

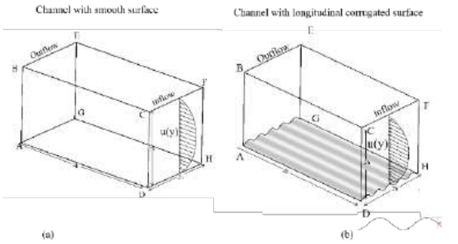

Figure 1: Schematic diagram of channel flow configuration (a) channel flow with smooth surface (b channel flow with longitudinal corrugated surface.

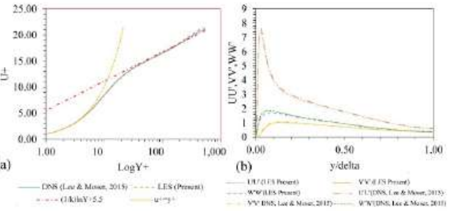

Figure 2: Comparison of LES results agains DNS of Lee & Moser (2015) for smooth channel at Re_τ =550 (a) Comparison of normalized mean streamwise velocity profile between LES and DNS (b) Comparison of normalized Reynolds stress between LES and DNS.

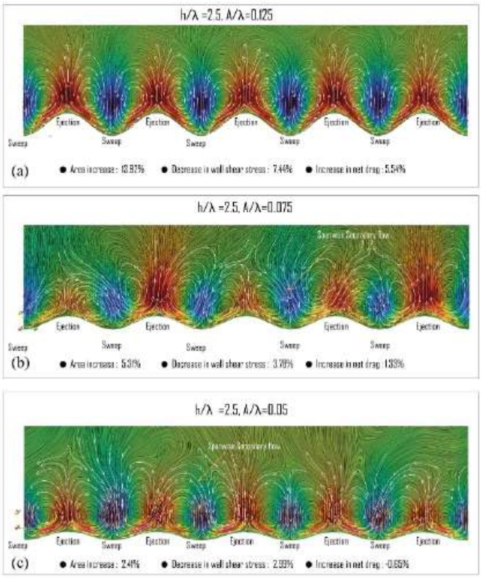

Figure 3: Streamline pattern associated with mean flow structures at plane normal to flow where contour shows mean wall normal velocity for channel with macroscale corrugated surface (a) mean flow structure for A/λ=0.25 (b) mean flow structure for A/λ=0.075 (c) mean flow structure for A/λ=0.05.

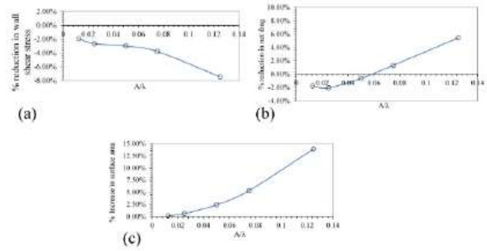

Figure 4: (a) Change in percentage reduction in wall shear stress with A/λ (b) Change in percentage net drag reduction with A/λ (c) Change in percentage increase in surface area of corrugated surface with A/λ

REFERENCES

Razzak, M. A., Khoo, B.C. & Lua, K.B., "Numerical study on wide gap Taylor Couette flow with flow transition". *Physics of Fluids, 31*(11) (2019).

Razzak, M. A., Khoo, B.C. & Lua, K.B., "Numerical study of Taylor Couette flow with longitudinal corrugated surface". *Physics of Fluids, 32(5)* (2020).

Razzak, M. A., Khoo, B.C., Lua, K.B, C. M. J. Tay; "Drag reduction study of naturally occurring oscillating axial flow induced by helical corrugated surface in Taylor–Couette flow". Physics of Fluids, 35 (8) (2023).

Lee, M and Robert Moser, D., "Direct numerical simulation of turbulent channel flow up to Re_{tau} = 5200". *Journal of Fluid Mechanics*, 774(2015).

59

ERCOFTAC
European Drag Reduction and Flow Control Meeting – EDRFCM 2024
September 10th–13th, 2024, Turin, Italy

DRAG REDUCTION OF A DOWNSTREAM CYLINDER WITH A FLEXIBLE FIN IN THE WAKE GENERATED BY AN UPSTREAM CYLINDER

Min Jae Kang
Department of Mechanical Engineering, Ulsan National Institute of Science and Technology, 44919 Ulsan, South Korea

Young Dal Jeong
Department of Mechanical Engineering, Ulsan National Institute of Science and Technology, 44919 Ulsan, South Korea

Jae Hwa Lee
Department of Mechanical Engineering, Ulsan National Institute of Science and Technology, 44919 Ulsan, South Korea

INTRODUCTION

The circular cylinder has often been found to be arranged with another one in many engineering fields, e.g., supporting columns of offshore plants and wind turbines. The flow around the two cylinders in tandem configuration, as the simplest arrangement, has been investigated to evaluate fluid dynamics related to the multiple cylinders. The drag acting on the downstream cylinder in the wake of the upstream cylinder was determined by the value of *G/D* [1], where *D* and *G* are the cylinder diameter and center-to-center distance between two adjacent cylinders, respectively. When the value of *G/D* was small, the drag acting on the downstream cylinder was reduced by the presence of the upstream cylinder, which was due to a decrease in the positive pressure at the stagnation point by no vortices in the gap region between the two cylinders (i.e., vortex shedding was only formed behind the downstream cylinder). However, when the value of *G/D* was large, distinct vortices were shed from the upstream and downstream cylinders, respectively, indicating the increased positive stagnation pressure of the downstream cylinder. As a result, the downstream cylinder experienced a sudden increase in drag at a large value of *G/D*.

The dependency of the drag acting on the downstream cylinder on the value of *G/D* suggests that arranging two cylinders at small *G/D* is favorable for the cylindrical structure design. However, it is difficult to arrange the two cylinders with small *G/D* due to constraints related to operational efficiency or structural stability. To overcome this challenge, we consider the attachment of a flexible fin to the downstream cylinder to reduce the drag on the downstream cylinder in the wake of the upstream cylinder when the value of *G/D* is large.

NUMERICAL METHOD

The motions of a two-dimensional incompressible viscous fluid flow are governed by the Naver-Stokes and continuity equations:

$$\frac{\partial \boldsymbol{u}}{\partial t} + \boldsymbol{u} \cdot \nabla \boldsymbol{u} = -\nabla p + \frac{1}{Re}\nabla^2 \boldsymbol{u} + \sum \boldsymbol{f}_j \qquad (1)$$

$$\nabla \cdot \boldsymbol{u} = 0 \qquad (2)$$

where $\boldsymbol{u}$ is the velocity vector, p is the pressure, t is time and $\boldsymbol{f}_j$ is the Eulerian momentum force to enforce the no-slip boundary condition along the immersed boundary [2]. In addition, Re is the Reynolds number defined as $Re = \rho_f U_\infty D/\mu$, where U_∞ is the freestream velocity, ρ_f is the fluid density and μ is the dynamic viscosity. In Eq. (1), j is the index number, where $j = 1$, 2 and 3 denote the upstream cylinder, downstream cylinder and a flexible fin, respectively. The upstream and downstream cylinders are located at (x/D, y/D) = (0, 0) and (G/D, 0), where x and y are streamwise and cross-stream distances from the origin. The flexible fin is attached to the base point of the downstream cylinder.

The motion of the inextensible flexible fin (j = 3) is governed as follows [2]:

$$\frac{\partial^2 \boldsymbol{X}_3}{\partial t^2} = \frac{\partial}{\partial s_3}\left(T\frac{\partial \boldsymbol{X}_3}{\partial s_3}\right) - \frac{\partial^2}{\partial s_3^2}\left(\gamma\frac{\partial^2 \boldsymbol{X}_3}{\partial s_3^2}\right) - \boldsymbol{F}_3 \qquad (3)$$

$$\frac{\partial \boldsymbol{X}_3}{\partial s_3} \cdot \frac{\partial \boldsymbol{X}_3}{\partial s_3} = 1 \qquad (4)$$

where s is the Lagrangian variable, s_3 ranges from 0 to L, L is the length of the fin, γ is the bending rigidity, $\boldsymbol{X} = [X(s), Y(s)]$ is the position vector, T is the tension force and $\boldsymbol{F}$ is the Lagrangian force exerted on the flexible fin by the surrounding flow.

The clamped and free-end boundary conditions are applied at the leading and trailing edges of the flexible fin, respectively. The momentum forcing term $\boldsymbol{F}_j$ in Eq. (3) is derived using a feedback law,

$$\boldsymbol{F}_j = \alpha\int_0^t (\boldsymbol{U}_{ibj} - \boldsymbol{U}_j)dt' + \beta(\boldsymbol{U}_{ibj} - \boldsymbol{U}_j) \qquad (5)$$

where α and β are large negative free constants. In Eq. (5), $\boldsymbol{U}_j = \partial \boldsymbol{X}_j/\partial t$ is the velocity of the structure and $\boldsymbol{U}_{ibj}$ is the velocity of the immersed boundary.

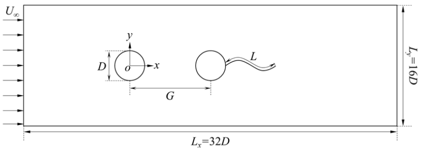

Figure 1. Schematic of the computational domain with two tandem cylinders-flexible fin system

Figure 1 presents a schematic of the two tandem cylinders with a flexible fin attached to the base point of the downstream cylinder. The Reynolds number is fixed at 100 in the present study.

RESULTS AND DISCUSSION

The numerical simulations of the two tandem cylinders with a flexible fin are performed to explore the drag variation on the downstream cylinder with the flexible fin in the wake of the upstream cylinder when *L/D* and *γ* are systematically varied. In the present study, we consider two values of *G/D* = 4 and 8. Figure 2 shows the drag ratio ($\overline{C_{D,total}} / \overline{C_{D,ref}}$, where $\overline{C_{D,total}}$ is the time-averaged total drag acting on the downstream cylinder-flexible fin system and $\overline{C_{D,ref}}$ is that on a pure downstream cylinder without a fin) on a 2-D parameter space (*L/D*, *γ*). The fluttering motions of the fin are classified into three distinct modes, which are superimposed in Figure 2: the limit-cycle flapping mode (open square), the chaotic flapping mode (closed diamond), and the deflected mode (open circle). When *G/D* = 4 in Figure 2(a), the limit-cycle flapping mode is predicted in small *L/D* and *γ*. As *L/D* and *γ* increase, it is transitioned to the deflected mode. In the intermediate range between the limit-cycle flapping mode and the deflected mode, the chaotic flapping mode arises. Compared to the variation for *G/D* = 4, the deflected mode is more dominant when *G/D* = 8 in Figure 2(b). In the limit-cycle flapping and the chaotic flapping modes, the drag acting on the downstream cylinder is reduced by the presence of the flexible fin compared to that on the pure downstream cylinder without the fin. The maximum drag reduction of 42.5% is found at (*L/D*, *γ*) = (1.5, 0.1) when *G/D* = 4. In the deflected mode, the drag is larger than that on the pure downstream cylinder, and a maximum is observed at (*L/D*, *γ*) = (1.9, 0.1) when *G/D* = 8.

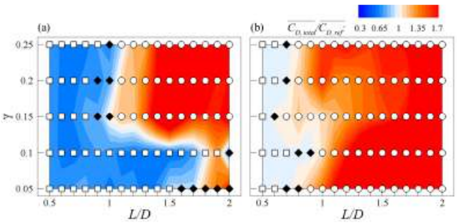

Figure 2. Contours of the drag ratio ($\overline{C_{D,total}} / \overline{C_{D,ref}}$) and regime diagram of the flapping mode on a map of (*L/D*, *γ*) when (a) *G/D* = 4 and (b) *G/D* = 8: (□) the limit-cycle flapping mode, (♦) the chaotic flapping mode and (○) the deflected mode.

To analyze the drag reduction mechanism of the downstream cylinder when the flexible fin is attached, the instantaneous vorticity (ω_z) and time-averaged pressure contours for representative cases are shown in Figure 3. The vorticity and pressure contours for the pure tandem cylinder without the fin are included for comparison in Figure 3(a). When no flexible fin is attached, strong vortical structures are observed behind the downstream cylinder, resulting in a low negative base pressure acting on the downstream cylinder. In the limit-cycle flapping and chaotic flapping modes when the flexible fin is attached in Figures 3(b) and (c), the vortices from the downstream cylinder are highly suppressed by the fin (see the solid and dashed lines). The suppressed vortices lead to recovery in the negative base pressure, indicating the drag reduction. However, when the flapping state is in the deflected mode, a strong recirculation is predicted behind the deflected fin. As a result, the drag on the downstream-flexible fin system increases compared to that on the pure downstream cylinder without the fin.

The present study achieves the maximum drag reduction of 42.5% in the cylinder-flexible fin system, demonstrating superior drag reduction performance compared to the cylinder-rigid fin system reported in a previous study [3]. In the EDRFCM 2024, we will show the enhanced drag reduction performance further by applying an active pitching motion to a flexible fin.

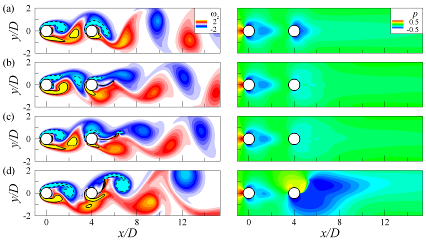

Figure 3. Instantaneous vorticity (ω_z) and time-averaged pressure contours: (a) pure tandem cylinder without the fin, (b) *G/D* = 4, *L/D* = 1.5 and *γ* = 0.1 in the limit-cycle flapping mode, (c) *G/D* = 4, *L/D* = 2 and *γ* = 0.1 in the chaotic flapping mode, and (d) *G/D* = 4, *L/D* = 1.5 and *γ* = 0.2 in the deflected mode. In the figure, the solid and dashed lines indicate ω_z = ±2.

ACKNOWLEDGEMENTS

This work was supported by the National Research Foundation of Korea (NRF) funded by the Ministry of Education (Grant No. NRF-2022R1I1A2054865) and was also funded by the Korea Meteorological Administration Research and Development Program (Grant No. RS-2024-00404042).

REFERENCES

[1] B. Sharman, F.S. Lien, L. Davidson, and C. Norberg. Numerical predictions of low Reynolds number flows over two tandem circular cylinders. *Int. J. Numer. Meth. Fluids*. 47:423–447, 2005.

[2] W.-X. Huang, S.J. Shin, and H.J. Sung. Simulation of flexible filaments in a uniform flow by the immersed boundary method. *J. Comput. Phys*. 226:2206-2228, 2008.

[3] P. Sikdar, S.M. Dash, and K.P. Sinhamahapatra. A numerical study on the drag reduction and wake regime control of the tandem circular cylinders using splitter plates. *J. Comput. Sci*. 66:101927, 2023.

60

ERCOFTAC
European Drag Reduction and Flow Control Meeting – EDRFCM 2024
September 10th–13th, 2024, Turin, Italy

A PARTICLE IMAGE VELOCIMETRY STUDY OF AERODYNAMICALLY-SHAPED VORTEX GENERATOR IN ZERO PRESSURE GRADIENT BOUNDARY LAYER

S.H. Bin Mohamed Noor, X. Liu, B. Zang, M. Azarpeyvand
School of Civil, Aerospace and Design Engineering, University of Bristol, Bristol BS8 1TR,
United Kingdom.

INTRODUCTION

The implementation of Vortex Generators (VGs) has emerged as a promising technique in aeronautical engineering, demonstrating significant enhancements in stall delay and prevention across various applications. Both experimental and numerical investigations attest to the efficacy and versatility of VGs in aerodynamic improvements. For instance, experimental studies by Hansen et al on a DU-91-W2-250 aerofoil revealed a substantial enhancement of up to 32.6% in the maximum lift coefficient ($C_{L,max}$)and an increase in the stall angle of attack (α_{stall}) by 3 degrees [1]. Similarly, numerical simulations conducted by Wang et al. on an NREL S809 aerofoil reported a remarkable 48.64% increase in $C_{L,max}$ and a 2-degree delay in α_{stall} [2]. Moreover, Dima et al. explored the impact of VGs on commercial and supersonic aircraft, noting significant enhancements in lift and aerodynamic efficiency for commercial models, albeit observing adverse effects on supersonic transport due to vortex interactions [3]. Beyond stall delay and prevention, VGs have been employed effectively for flow control purposes. Martinez et al. implemented VGs on wind turbine blades, resulting in improved torque generation and effective mitigation of side-flow effects on the outboard blade span [4]. Kerho et al. investigated VG types to control laminar separation bubbles, promoting flow transition [5]. Further research has explored VG optimization strategies to balance geometric and aerodynamic parameters. Godard and Stanislas, Fouatih et al., Li et al., and Zhen et al. proposed various optimization techniques on VGs, demonstrating improved performance in flow control, such as delay of flow separation [6-8]. In particular, a more recent study by Mariani and Neves [9] investigated the effects of aerofoil profile and tumble angle of VGs on a flying-wing concept and reported significant enhancements in aerodynamic performance metrics if the appropriate parameters were selected. Specifically, increases in lift coefficient by 2.45% and 3.86%, coupled with reductions in drag coefficient by 2.58% and 3.32%, were observed at an angle of attack (α) of 16° when utilizing optimized parameters in both co-rotating and counter-rotating VG configurations. Moreover, these configurations raised the stall angle (αstall) from 13° to 16° and 15°, respectively. These findings underscore the effectiveness of optimized VG setups in advancing overall aerodynamic performance. However, Mariani and Neves only carried out steady-state RANS to evaluate the performance; the exact modifications to the flow dynamics and the resulting performance enhancement were not explored in detail. Moreover, their main purpose was to investigate the performance of different specifications of vortex generators (VGs). A deeper study of the flow dynamics is needed to understand the physical mechanisms of the VGs. As such, the present paper aims to undertake detailed flow measurements by investigating the flow development in the wake of the VGs. Two planes of interest were investigated. The first plane is positioned in the middle between two adjacent VGs to visualize the effect of the interactions between each vane and its neighbour. The second plane is located at the wake of the toed-in VG. Notably, the tumble angle has never been thoroughly studied, making this research essential for a comprehensive understanding of its impact on flow dynamics and performance. The present study will permit us to investigate the direct effect of vortex generation from the tumble angle.

VORTEX GENERATOR DESIGNS

In this paper, following the study from [9], the VGs are tailored to the S1233 aerofoil, with additional specifications including an upper to lower surface ratio of 0.15. The chord length (C) in Fig. 1, is set at 46.515 mm (where C = 1.329H), with a maximum thickness of 9 mm and a height of H = 35 mm (where H = 1.4δ), determined based on a boundary layer thickness (δ) of 25 mm established during PIV experiments. The VGs are designed with three distinct tumble angles (ρ): 0 °, 15 °, and -8°. They were also configured under two conditions: co-rotation and counter-rotation, each has a skew angles (β) of 13° as an optimized design [9]. In the co-rotation setup, the periodicity (D) was set at 146.58 mm (where D = 4.188H). Meanwhile, in the counter-rotation setup, the pair spacing (λ) was 76.3 mm (where λ = 2.18H), and the periodicity (D) was 172.9 mm (where D = 4.94H). For this experimental series, 6 configurations resulting from these parameters were fabricated using 3D printing. These six models are named M1 (ρ=0°), M2 (ρ=15°) and M3 (ρ=-8°) for Co-Rotation set up, and M4(ρ=0°), M5 (ρ =15°) and M6 (ρ =-8°) for Counter Rotation set up.

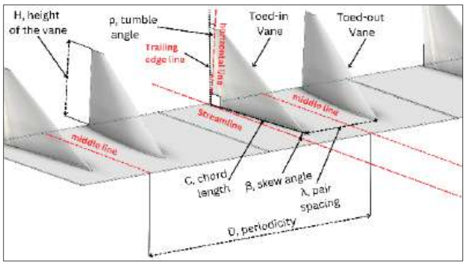

Figure 1. Vortex generator parameters.

EXPERIMENT SET UP

The experiments were conducted in a subsonic, low turbulence wind tunnel, with a test section approximately 0.8 m x 0.6 m in dimensions and extending 1.6 m in length. The airspeed during experiments is set at 15 m/s, with a low turbulence intensity of 0.05%. A 1m-long flat plate with an elliptic leading-edge was mounted in the test section to allow development of a turbulent boundary layer, as shown in Fig. 2. To obtain the desired boundary layer thickness of δ=25mm at the location of the VGs, a porous tripping device was affixed close to the leading edge of the flat plate, The VGs, printed from additive manufacturing were placed at approximately 600mm downstream of the plate. The flow field in the wake of the VGs were then captured by planar particle-image velocimetry at two streamwise planes, namely the wake plane immediately behind the trailing-edge of the VG and the mid-plane in between the two VGs, as can be seen in Fig. 2. The PIV images were sampled at a rate of 250Hz and a total of 2000 image pairs were captured and subsequently post-processed using multi-pass cross-correlation algorithms in LaVision DaVis 10. The field-of-view of the measurement was approximately 172mm × 172mm with a final interrogation window size of 0.336mm × 0.336mm.

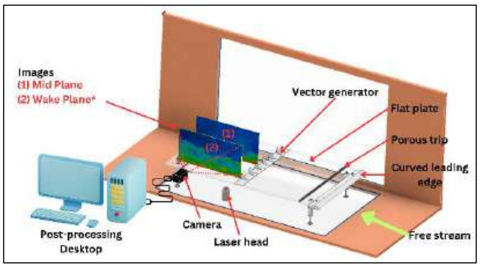

Figure 2. PIV experiment set up. The (2) wake plane* in the schematic is off-set for a better viewing.

RESULTS & DISCUSSION

To have a firsthand knowledge of the turbulence development immediately behind the VGs, Fig. 3 shows the turbulent kinetic energy (TKE) plots for models M4 (ρ=0°), M5 (ρ=15°), and M6 (ρ=-8°) respectively at both the wake and mid planes. The three models presented here are in the Co-Rotation set-up. From this preliminary analysis, it is demonstrated experimentally that a tumble angle of ρ=-8° yields the highest TKE. Increased TKE signifies heightened velocity fluctuations and turbulence contents within the flow, which possibly indicates enhanced mixing in the near wake of the VGs fluid motion. In the context of passive flow control applications, flow separation typically occurs when the boundary layer lacks sufficient energy to remain attached to the surface. Elevated TKE levels can supply the necessary kinetic energy to the boundary layer, thereby either aiding the flow to remain attached to the wall or facilitating its re-attachment after flow separation takes place.

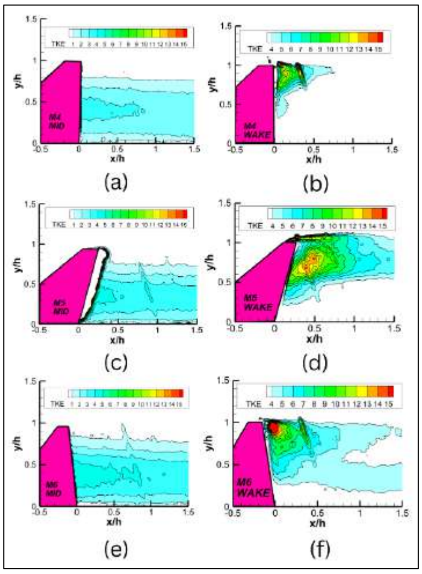

Figure 3. TKE plots for (a) M4 middle plane, (b) M4 wake plane, (c) M5 middle plane, (d) M5 wake plane, (e) M6 middle plane and (f) M6 wake plane.

PROSPECTIVE WORK

In the full paper, more analyses on the effect of VG arrangement (counter- and co-rotating) will be presented, together with other turbulence statistics and flow modes from proper orthogonal decomposition.

REFERENCES

[1] Hansen, M. O. L., Velte, C. M., Øye, S., Hansen, R., Sørensen, N. N., Madsen, J., & Mikkelsen, R. (2016). Wind Energy, 19(3), 563–567.
[2] Wang, H., Zhang, B., Qiu, Q., & Xu, X. (2017). Energy, 118, 1210–1221.
[3] Dima, C., Manor, D., Carter, R.L. In : 32nd Aerospace Sciences Meeting & Exhibit. Reno, NV, 1994.
[4] Martinez Suarez, J., Flaszynski, P., & Doerffer, P. (2018). Wind Energy, 21(11), 1202–1215.
[5] Kerho, M., Hutcherson, S., Blackwelder, R. F., & Liebeck, R. H. (1993). Journal of Aircraft, 30(3), 315–319.
[6] Godard, G., & Stanislas, M. (2006). Aerospace Science and Technology, 10(3), 181–191.
[7] Fouatih, O. M., Medale, M., Imine, O., & Imine, B. (2016). European Journal of Mechanics, B/Fluids, 56, 82–96.
[8] Li, X., Yang, K., & Wang, X. (2019). Energies, 12(5).
[9] Raffaelo Mariani and Carlos Neves, AIAA SCITECH 2024 Forum, Jan. 2024.

 # 61

ERCOFTAC
European Drag Reduction and Flow Control Meeting – EDRFCM 2024
September 10$^{\text{th}}$–13$^{\text{th}}$, 2024, Turin, Italy

DEEP REINFORCEMENT LEARNING FOR LOW-SPEED STREAKS CONTROL IN TURBULENT FLOWS

G. M. Cavallazzi, A. Pinelli
Department of Engineering, City, University of London, London, UK

INTRODUCTION

Streamwise traveling waves of spanwise velocity (STW) are an active Drag Reduction (DR) method capable of reducing the Skin-Friction Coefficient (C_f) by up to 45% [4]. These waves are implemented as boundary conditions in Direct Numerical Simulations (DNS) codes by imposing the instantaneous value of the spanwise component of the velocity (w) at the wall.

$$w\left(x,0,z,t\right) = A\sin\left(\lambda z - \omega t\right) \tag{1}$$

In this work we consider a more dynamic behaviour of the STW by allowing the wave pulsation (ω) to change over time.

$$w\left(x,0,z,t\right) = A\sin\left(\lambda z - \omega\left(t\right)t\right) \tag{2}$$

With this modification and by targeting the maximisation/minimisation of specific cost functions we aim at further exploring the mechanisms that govern turbulence regeneration cycle at the wall.

The time variation of ω is obtained as the outcome of the interaction of the DNS environment and an active control based on a Deep Reinforcement Learning (DRL) algorithm [2]. The action that DRL gives as output to control the system is ω, which is selected by a policy that the DRL algorithm tries to learn by using a specific set of data that represents a proxy of the actual flow state. In this case, the data consists of a 2D snapshot of streamwise velocity u sampled on a plane parallel to the wall located at $y^+ = 15$ [6]. Concerning the selected cost function, a natural choice could be related with high rewards associated with low C_f values. In this study we take a different approach aiming at understanding the nature of the wall regenerating cycle. As a first case we tried to promote velocity streaks characterised by straight patterns (i.e. aligned with the mean flow direction) and measure its impact on wall turbulence by exploring typical integral values (e.g. the C_f) and the velocity fluctuations distributions.

The methodology we used to promote the appearance of straight streaks is based on the definition of the reward function $r \in [-1,1]$. In particular, the turbulent kinetic energy (E_k) and the energy of the straight streaks (E_{ks}), defined as

$$E_{ks} = \frac{1}{L_x L_z \delta}\int_0^{L_x}\int_0^{L_z}\int_0^{\delta}\left(u'\right)^2 dxdydz, \tag{3}$$

are computed in a volume that contains the low-speed streaks [3]. Their difference, corresponding to the energy of the non-coherent fluctuating field, is rewarded when moving towards low values following the definition

$$r = 2^{(E_k - E_{ks})/b} - 1. \tag{4}$$

Here, b is an adjustable parameter. The policy, and therefore the pulsation $\omega\left(t\right)$, are updated every $\Delta t^+ = 10$.

The DRL policy that we have used is DDPG (included in the Stable-baselines3 Python libraries [5]) and the DNS environment is the open source incompressible Navier-Stokes solver CaNS [1]. The DRL-DNS communication occurs via the message passing interface library.

RESULTS

The training of the neural network led to a strategy that maintains the streaks straighter, with a higher energy compared to the standard STW, for a longer time. Such configurations are not observed in non-actuated cases or with STW, and they correspond to a non-negligible (yet, not optimal) drag reduction, as can be seen in figure 3.

FIGURES

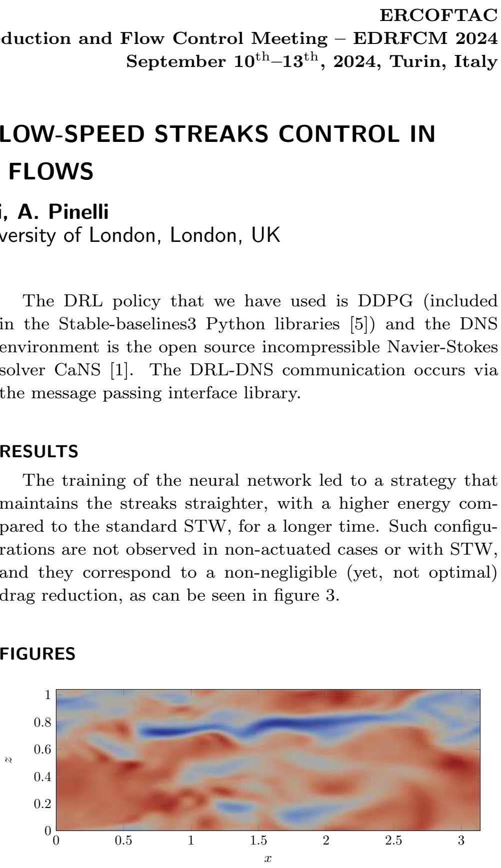

Figure 1: Non-actuated field of streamwise velocity at its minimum value of E_{ks}/E_k The field, as in figure 2, is displayed at $y^+ = 15$.

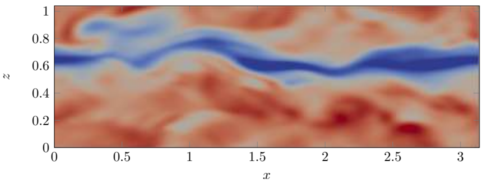

Figure 2: Actuated field at its minimum value of E_{ks}/E_k. A tidier configuration, unreachable without control, is available.

NEXT DEVELOPMENTS

Current improvements to the present study consist in further generalising the boundary conditions by adding more waveforms to the spanwise velocity component of the wall

$$w\left(x,0,z,t\right) = \sum_{k=-N_s/2}^{N_s/2} A_k(t)e^{i2\pi kx/L_x} \tag{5}$$

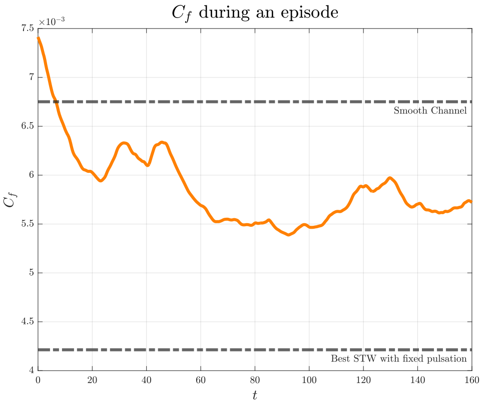

Figure 3: History of C_f during an episode. Almost half of the DR is achieved by simply promoting configurations with straighter streaks.

and therefore the action space can increase from dimension 1 to N_s, potentially unleashing new strategies inaccessible with a single control parameter.

We will also consider different types of rewards to explore the causality of events in the regeneration cycle. In particular, we are now considering the minimisation of the energy content of the 4^{th} quadrant events that are believed to be one of the drivers of velocity streaks instabilities.

The enlarged action space and testing new rewards will add further complexity to the overall methodology. Indeed, it is anticipated that the training of the neural network will take longer and that further calibration of the process will need to be considered. i.e. the time period between successive actions and the duration of the averaging of the integral quantity considered for the reward.

REFERENCES

[1] Pedro Costa. A FFT-based finite-difference solver for massively-parallel direct numerical simulations of turbulent flows. *Computers & Mathematics with Applications*, 76(8):1853–1862, October 2018.

[2] Paul Garnier, Jonathan Viquerat, Jean Rabault, Aurélien Larcher, Alexander Kuhnle, and Elie Hachem. A review on deep reinforcement learning for fluid mechanics. *Computers & Fluids*, 225:104973, July 2021.

[3] Javier Jiménez and Alfredo Pinelli. The autonomous cycle of near-wall turbulence. *Journal of Fluid Mechanics*, 389:335–359, June 1999.

[4] Maurizio Quadrio, Pierre Ricco, and Claudio Viotti. Streamwise-travelling waves of spanwise wall velocity for turbulent drag reduction. *Journal of Fluid Mechanics*, 627:161–178, May 2009.

[5] Antonin Raffin, Ashley Hill, Adam Gleave, Anssi Kanervisto, Maximilian Ernestus, and Noah Dormann. Stable-Baselines3: Reliable Reinforcement Learning Implementations.

[6] Takahiro Sonoda, Zhuchen Liu, Toshitaka Itoh, and Yosuke Hasegawa. Reinforcement learning of control strategies for reducing skin friction drag in a fully developed turbulent channel flow. *Journal of Fluid Mechanics*, 960:A30, April 2023.

 # 62

ERCOFTAC
European Drag Reduction and Flow Control Meeting – EDRFCM 2024
September 10th–13th, 2024, Turin, Italy

BAYESIAN OPTIMIZATION OF AN OPPOSITION CONTROL STRATEGY IN A FULLY TURBULENT CHANNEL FLOW

E. Saccaggi[1] & G. M. Di Cicca[1]

[1]Department of Mechanical and Aerospace Engineering, Politecnico di Torino, 10129, Turin, Italy

INTRODUCTION

The significance of drag reduction becomes essential to diminish both energy consumption and pollutant emissions in modern transportation systems. Skin friction stands out as a crucial contributor to drag, accounting for as much as 55% of the total drag for commercial aircraft.

Choi et al. [2] found that by using blowing and suction to counteract wall-normal velocities in a turbulent channel flow, skin friction reduction up to 25% can be achieved.

Rebbeck and Choi [8] demonstrated through wind tunnel experiments that real-time opposition control, using a wall-normal jet to block high-speed fluid during sweep events, can effectively reduce skin friction drag in the turbulent boundary layer.

Bayesian optimization has proven to be an effective tool for optimizing the actuation parameters in flow control strategies aimed at reducing drag in turbulent flows. Mahfoze et al. [5] applied Bayesian optimization to determine the optimal amplitude and coverage parameters for wall-normal blowing control in a zero-pressure gradient turbulent boundary layer, achieving significant skin-friction reductions.

The present study investigates a real-time opposition control strategy to reduce skin friction drag in a fully turbulent channel flow. The actuation parameters were optimized through a Bayesian algorithm.

EXPERIMENTAL SETUP

Experiments were conducted in an 8-meter-long duct with a 7 cm x 30 cm rectangular cross-section. The flow is characterized by a Reynolds number based on the friction velocity $Re_\tau = 420$.

Two hot-wire probes connected to Dantec 55M10 CTA Standard Bridge anemometers, were used. The front probe is positioned 65 viscous units upstream of the control point and 15 viscous units from the wall. Following the work of Rebbeck and Choi [7], sweep events were detected using the velocity gradient technique applied to the longitudinal component of the velocity, measured by the front probe. The gradient was computed from the hot wire anemometer analog voltage output signal and a comparator device identified sweep events when the gradient exceeded a given threshold. The threshold level has been set to ensure that both the gradient and the VITA techniques (see Blackwelder and Kaplan [1]) detected a comparable number of events. For the VITA technique, the parameters used were a threshold value of $k = 1.2$ and an averaging time $T^+ \approx 10$.

A detected sweep event triggers a TTL signal which is sent to an Arduino Uno Rev3 microcontroller, introducing with the latter a delay to account for the convection time and the actuator response. The delayed TTL signal triggers a signal generator to produce a sine wave, which is then amplified to drive a loudspeaker that emits a jet through a 1 mm orifice.

The control parameters (voltage amplitude, frequency, and delay) were optimized via a Bayesian algorithm to maximize velocity reduction, measured by the rear probe positioned at $x^+ = 76$ and $y^+ = 15$. The rear probe was mounted on a 2-axis movable stand to allow movements in the streamwise and wall-normal directions.

Both probes were calibrated in situ. Data were collected using a National Instruments board with a sample rate of 10 kHz.

A workstation is connected to both the microcontroller and the signal generator to automatically adjust the actuation parameters. Data post-processing and the Bayesian optimization algorithm are executed on a laptop connected to the workstation via Ethernet. The communication is allowed by a TCP protocol and a Python-based server-client setup.

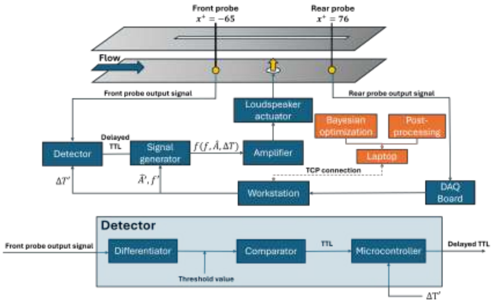

Figure 1: Schematic of the control system. The signal from the upstream probe is used to trigger the actuation. The signal coming from the downstream probe allows the optimization of the control strategy.

CONTROL PARAMETERS OPTIMIZATION

A closed-loop control logic was implemented through a Bayesian optimization algorithm. Bayesian optimization is well suited for minimizing functions expensive to evaluate, and for handling stochastic noise in the function evaluation. The algorithm is constituted of two main components: a Bayesian statistical model to build a surrogate for the objective function and an acquisition function to determine the next point to sample. The statistical model, a Gaussian process, provides a Bayesian posterior distribution for potential values of the cost function $\mathcal{J}(\psi)$ at any candidate point ψ, which is updated with each new observation of $\mathcal{J}$. The acquisition function assesses the value that would be generated by evaluating the objective function at a new point $\psi_{n+1} = \psi$, leveraging the posterior distribution which is formed after observing n data points. According to [3, 6], the posterior distribution is defined as:

$$\mathcal{J}(\psi)\,|\mathcal{J}(\psi_{1:n}) \approx \mathcal{N}\left(\mu_n(\psi), \sigma_n^2(\psi)\right), \tag{1}$$

where: $\sigma_n^2(\psi)$ is the posterior variance which is equal to the prior covariance $\Sigma_0(\psi,\psi)$ minus a term representing the variance reduction from observing $\mathcal{J}(\psi_{1:n})$; $\mu_n(\psi)$ is the posterior mean that is a weighted average of the prior mean $\mu_0(\psi)$ and an estimate derived from the data $\mathcal{J}(\psi_{1:n})$ having the weights dependent on the kernel $\Sigma_0(\psi,\psi')$. ψ and ψ' are two candidate points in the input space.

A measure of the longitudinal local mean velocity reduction, and thus of the control effectiveness, can be obtained through the difference in areas between the uncontrolled and controlled cases. This difference is depicted in figure 2 for the best triplet ψ_{opt}. The cost function is written for a generic ψ_i:

$$\mathcal{J}(\psi_i) = -\frac{A_{\text{nc}} - A_{\text{c}}(\psi_i)}{A_{\text{nc}}}, \tag{2}$$

where the generic area in either, controlled or uncontrolled cases, is:

$$A = \int_{t_m}^{t_w} u^+ dt, \tag{3}$$

u^+ is the fluctuating component of the streamwise velocity in wall units, t_m is the time in correspondence of the first minimum peak, t_w is a time window that was selected to ensure the robustness of the cost function, ψ is a triplet consisting of voltage amplitude, frequency, and delay. The episode length was set to 120 seconds, during which the voltage amplitude, frequency, and delay were kept constant. This duration was calibrated to ensure approximately 800 events for statistical analysis.

The optimization intervals were $60 \div 100$ Hz, $50 \div 75$ mVpp and $0.15 \div 6$ s for frequency, amplitude and delay, respectively. These intervals were chosen to take into account both equipment limitations and operational reasons. To explore the space before optimizing, 32 points were sampled using the Sobol' sequence which is a quasi-random low-discrepancy sequence [9]. The kernel used was obtained by multiplying a constant kernel with the Màtern kernel [4] and then by adding a white noise kernel to account for measurement noise. Expected Improvement was used as the acquisition function.

RESULTS

Figure 2 shows the conditionally averaged sweep events in the uncontrolled and controlled case for the optimal triplet (ψ_{opt}). A reward of 54% was achieved for this configuration. A survey was also conducted at various downstream coordinates for the same control parameters. It is noteworthy that the effect of the control persists for approximately 500 viscous units, albeit with reduced intensity.

The posterior mean μ_n is represented in figure 3 as a function of frequency and delay by keeping constant the amplitude to 60 mVpp. It can be observed that low actuation frequencies and low delay times produce a positive impact on the control.

ACKNOWLEDGEMENT

This abstract is part of the project PNRR-NGEU which has received funding from the MUR – DM 118/2023.

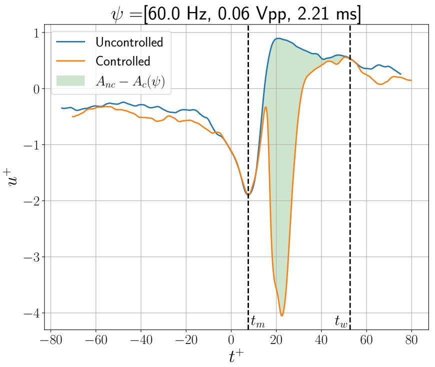

Figure 2: Conditionally averaged sweep events for the controlled case with ψ_{opt} and uncontrolled case at $x^+ = 76$ and $y^+ = 15$. The area difference is highlighted in green.

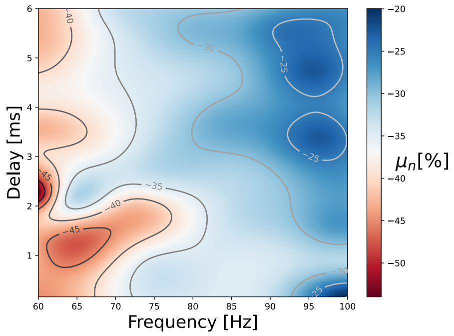

Figure 3: Posterior mean μ_n for different delay times and frequencies. The amplitude is kept constant to 60 mVpp.

REFERENCES

[1] R. F. Blackwelder and R. E. Kaplan. *J. Fluid Mech.*, 76(1):89–112, 1976.

[2] H. Choi, P. Moin, and J. Kim. *J. Fluid Mech.*, 75:262, 1994.

[3] P. I. Frazier, July 2018. arXiv:1807.02811.

[4] M. S. Handcock and M. L. Stein. *Technometrics*, 35(4):403–410, 1993.

[5] O. A. Mahfoze, A. Moody, A. Wynn, R. D. Whalley, and S. Laizet. *Phys. Rev. Fluids*, 4:094601, Sep 2019.

[6] C. E. Rasmussen and C. K. I. Williams. The MIT Press, November 2005.

[7] H. Rebbeck and K. S. Choi. *Phys. Fluids*, 13(8):2142–2145, 08 2001.

[8] H. Rebbeck and K. S. Choi. *Phys. Fluids*, 18:035103, 2006.

[9] I.M. Sobol'. *U.S.S.R Comput. Maths. Math. Phys.*, 7(4):86–112, 1967.

 # 63

ERCOFTAC
European Drag Reduction and Flow Control Meeting – EDRFCM 2024
September 10$^{\text{th}}$–13$^{\text{th}}$, 2024, Turin, Italy

BLUFF BODY WAKE CONTROLLED WITH DEEP REINFORCEMENT LEARNING

E. Amico[1], J. Serpieri[1], G. Iuso[1], & G. Cafiero[1]
[1]Department of Mechanical and Aerospace Engineering, Politecnico di Torino, 10129 Turin, Italy

INTRODUCTION

Reducing aerodynamic drag in vehicles is essential to lower pollutants, fuel consumption, and costs. A $7-10\%$ reduction in drag can decrease fuel consumption by $2.7-5.2\%$ [1]. This is increasingly important for electric vehicles to maximize their range. At high speeds, city cars face significant aerodynamic drag, making up about 80% of total drag at 130 km/h compared to 50% at 50 km/h [2]. Due to limited geometric optimization and regulatory constraints, drag reduction is challenging.

Active flow control holds promise for minimizing drag in commercial vehicles. Deep Reinforcement Learning (DRL) has become a crucial advancement in fluid dynamics and control theory, particularly effective for closed-loop flow control [3]. DRL uses AI and neural networks to manage complex flow environments, learning optimal control policies through interaction and rewards, without needing explicit knowledge of flow physics [4].

METHODOLOGY

This study examines the wake topology of a bluff body, representative of a commercial vehicle, manipulated by different control laws for pulsed jets located at the edges of the model's rear base. Parameters were identified using a Deep Reinforcement Learning (DRL) algorithm trained to reduce the drag while considering the energy budget.

Related to the study currently presented, Amico et al. [5] trained different DRL agents to obtain forcing conditions leading to the drag reduction scenario of the same commercial road vehicle by means of 4 pulsed jets, one per edge of the model base, with adjustable exit velocity (U_j) and pulsation frequency (f_j).

The agent's training is conducted using two distinct state definitions, as outlined in Table 1. The state is characterized by the distribution of the pressure coefficient Cp on the base of the model.

$$Cp = \frac{<p> - <p_\infty>}{0.5 \cdot \rho \cdot U_\infty^2} \tag{1}$$

where the subscript ∞ indicates freestream conditions and the symbol $<>$ indicates the time-averaged value.

Subsequently, this definition is expanded by incorporating fluctuating pressure (p') via Cp_{RMS}.

$$Cp_{RMS} = \frac{\sqrt{<p'^2>}}{0.5 \cdot \rho \cdot {U_\infty}^2} \tag{2}$$

A first agent was trained to maximize a reward (r) defined as

$$r = Cd_0 - Cd = \Delta Cd \tag{3}$$

where Cd and Cd_0 are the drag coefficients in the forced and unforced conditions, respectively.

	State	Reward
Case 1	Cp	ΔCd
Case 2	Cp+Cp_{RMS}	ΔCd

Table 1: Summary of the state and the reward definitions.

The model used is a 3D printed square-back road vehicle typically employed as heavy-duty vehicle, with length (L), width (W) and height (H) equal to 412 mm, 170 mm and 200 mm, respectively. The forcing is obtained by four air jets slits located along the edges of the model's base.

Velocity field measurements were conducted in the vehicle wake using Planar Particle Image Velocimetry (PIV) and Stereoscopic Particle Image Velocimetry (sPIV), as shown in Figure 1. PIV results indicate that significant drag reduction shortens the recirculating flow bubble in the streamwise direction, symmetrizes the wake, and improves pressure recovery at the model's base (compare Figures 1 and 2). When considering the energy budget, the changes are smaller due to reduced actuation.

This study builds on previous work (Amico, 2022) by offering insights into wake topologies for active flow control strategies to reduce pressure drag.

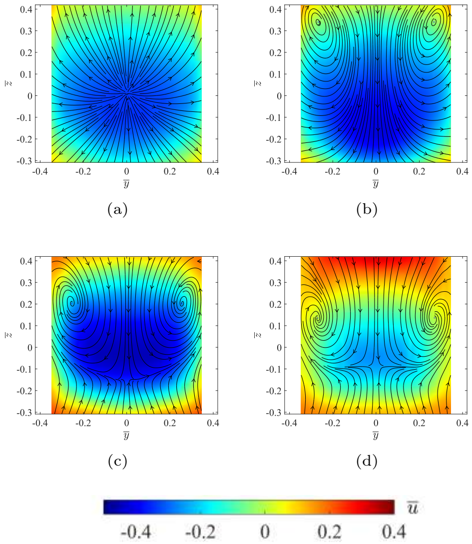

(a) (b)

(c) (d)

Figure 1: Colormaps of streamwise time-averaged velocity $\overline{u}$ fields at $\overline{x} = 0.15(a)$, $0.4(b)$, $0.6(c)$, $0.8(d)$, view from downstream, with overlaid $v-w$ streamlines (in black), for the unforced condition.

RESULTS

A substantial pressure recovery at the base of the model characterizes the conditions that achieve significant drag reduction. The extent of the recirculating region, measured as $max(x/W)_{\overline{u}(x/w)\leq 0}$, is shortened compared to the unforced case, with $\overline{B}_L$ values decreasing from 0.8 to 0.5 and 0.6.

The model shown in Figures 3b and 3c depicts the wake configuration, when maximum drag reduction is achieved. It is evident that the C-pillar has moved upwards and the recirculation bubble has compressed towards the base of the model, resulting in better pressure recovery. The interaction between the underbody flow and the recirculation bubble creates a vortex structure that develops in the direction of the flow.

In Case 1, a noticeable upward shift of the C-pillar and the compression of the bubble towards the model's base are evident, resulting in increased pressure recovery. Additionally, in Case 2, the formation of flow structures due to the interaction between the top jet and the recirculation bubble is observed. From the analyses conducted, it becomes clear that the agent can identify the condition of maximum drag reduction, marked by wake symmetrization, and can achieve this configuration using different control strategies. Specifically, in Case 2, the agent replaces the flow reduction from the side jet with the synchronized activation of the top jet.

These findings suggest that flow injection from the bottom jet is effective to achieve drag reduction (approximately 10%), as it advances the closure of the recirculating zone by shifting the interaction between the shear layers generated by the top and bottom model edges further upstream. However, this approach demands significant energy consumption. Moreover, while describing the flow topology found by the DRL agent for the different rewards, gives insights on how actively-controlled wake flows should appear to reduce their pressure drag.

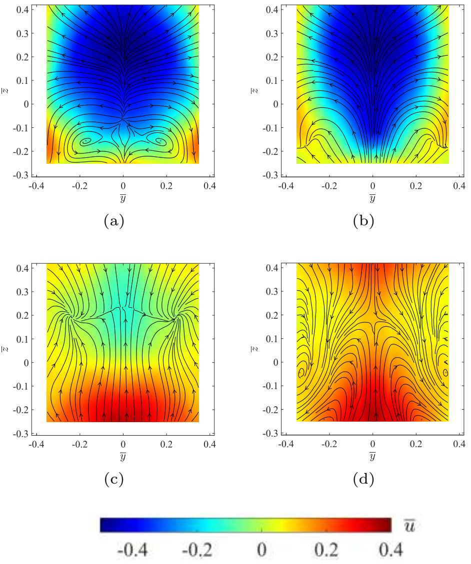

(a) (b)

(c) (d)

Figure 2: Colormaps of streamwise time-averaged velocity $\overline{u}$ fields at $\overline{x} = 0.15(a)$, $0.4(b)$, $0.6(c)$, $0.8(d)$, view from downstream, with $v - w$ streamlines (in black), for Case 1.

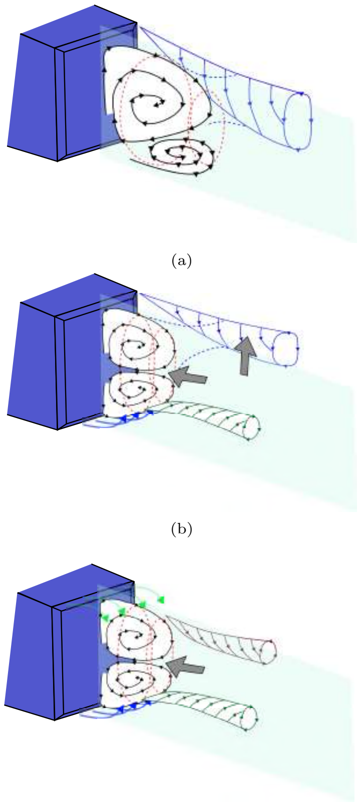

(a)

(b)

(c)

Figure 3: Schematic representation of the wake for Baseline Case (a) and forced case under maximum drag reduction conditions (b and c).

REFERENCES

[1] Zulfaa Mohamed-Kassim and Antonio Filippone. *Transportation Research Part D: Transport and Environment*, 15:275–284, 7 2010. 10.1016/J.TRD.2010.02.010.

[2] Patrick Gilliéron and Azeddine Kourta. *Experiments in Fluids*, 48:1–16, 4 2009. 10.1007/s00348-009-0705-7.

[3] Colin Vignon, Jean Rabault, Joel Vasanth, Francisco Alcántara-Ávila, Mikael Mortensen, and Ricardo Vinuesa. *Physics of Fluids*, 35, 6 2023. 10.1063/5.0153181.

[4] Dixia Fan, Liu Yang, Zhicheng Wang, Michael S Triantafyllou, and George Em Karniadakis. *Proceedings of the National Academy of Sciences*, 117:26091–26098, 10 2020. 10.1073/pnas.2004939117.

[5] Enrico Amico, Gioacchino Cafiero, and Gaetano Iuso. *Physics of Fluids*, 34:105126, 10 2022. 10.1063/5.0108387.

64

ERCOFTAC
European Drag Reduction and Flow Control Meeting – EDRFCM 2024
September 10th–13th, 2024, Turin, Italy

EFFECT OF SYNTHETIC JET ON MULTI-ELEMENT AIRFOIL LIFT ENHANCEMENT

Qi-Ming Wang
Fluid Mechanics Key Laboratory of Education Ministry, Beihang University, Beijing 100191, China

Zhe Li
Fluid Mechanics Key Laboratory of Education Ministry, Beihang University, Beijing 100191, China

Li-Hao Feng*
Fluid Mechanics Key Laboratory of Education Ministry, Beihang University, Beijing 100191, China

*Email: lhfeng@buaa.edu.cn

INTRODUCTION

Modern airliners release lifting devices such as the slat and flap during takeoff and landing to increase the wing curvature, which in turn increases the lift and improves takeoff and landing performance [1]. At this point, the wing can be simplified to a multi-element airfoil. However, significant deflection of the trailing-edge flaps can lead to flow separation and affect the lift enhancement effect. Therefore, suppressing flow separation through flow control techniques to achieve lift enhancement has significant engineering application value.

Previous studies have found that continuous jets [2,3] and sweeping jets [4,5] applied at the leading edge of multi-element wings can enhance the lift. However, these active flow control methods typically require air sources, often solved through engine bleed air, which inevitably leads to engine power loss. Synthetic jets manipulate flow by generating vortices through periodic blowing and suction. Compared to traditional jet control methods, synthetic jets do not require an external air supply, offering advantages such as compact structure, low energy consumption, rapid response, and high efficiency [6].

This work investigates the control effect of a synthetic jet array on lift enhancement of the multi-element wing through wind tunnel experiments. The control mechanisms behind flow separation suppression and lift enhancement are revealed.

EXPERIMENTAL SETUP

The experiment was conducted in an open return low-speed wind tunnel with an elliptical test section measuring 1.45 meters in length, featuring a 1.02 m × 0.76 m inlet. Figure 1(a) illustrates the schematic diagram of the multi-element airfoil model, which comprises components such as the slat, main wing, synthetic jet array, and cover. The wingspan was 400 mm, and the chord length of the airfoil was 200 mm. The synthetic jet array included six piezoelectric-driven actuators, consisting of an actuator cavity, actuator middle plate, O-ring silicone, piezoelectric diaphragm, and jet exit. The jet outlets were located at the leading edge of the flap, with dimensions of 1 mm × 44 mm and spaced 58 mm apart. The jet direction was tangential to the wing surface. Every two actuators were driven by one ATA-214 high-voltage amplifier with a maximum output of 400 $V_{\text{p-p}}$ at 300 mA, as shown in Figure 1(b). An AFG1062 function generator was used to generate the sinusoidal input signal that was concurrently monitored by a SDS1102X oscilloscope.

The model was installed vertically in the test section of the wind tunnel with the pivot in connection with a force transducer. Two end plates parallel to the free stream were horizontally installed in proximity to the ends of the airfoil model, minimizing the impact of the end effect on the flow in the midspan area. Under the free-stream velocity U_∞ of 10 m/s, the Reynolds number based on the chord was $Re = 1.3 \times 10^5$.

Velocity measurements were conducted via two-dimensional particle image velocimetry (PIV). The PIV system comprised a Beamtech Vlite-Hi-527-50 high-speed double-pulsed laser and a high-speed CMOS camera. The particle images of the investigated flow fields were captured by the camera in the double-exposure mode. The camera resolution was set to 2048 × 2048 pixels to store over 10800 particle images corresponding to 5400 image pairs in each sampling. The measured field of view was about 150 mm × 150 mm, resulting in a magnification of 0.073 mm/pixel. The sampling frequency of the image pairs was set to 500 Hz with a straddling time of 100 μs, ensuring that the maximum particle displacement remained below 16 pixels.

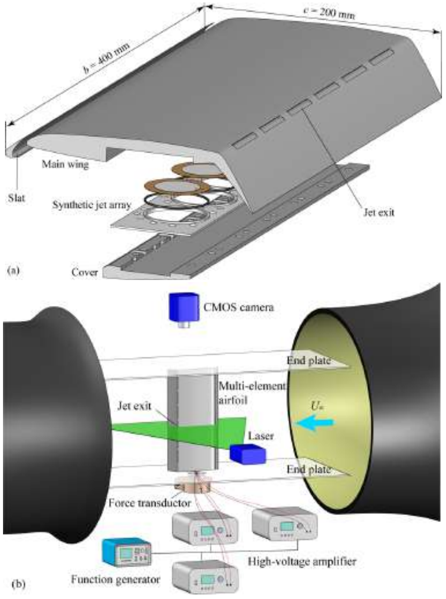

Figure 1. Schematic diagram of (a) the multi-element airfoil model, (b) experimental setup.

RESULTS

During the experiments, synthetic jets were generated at an applied voltage of 300 Vp-p. The jet exit velocity was measured by placing a single hot wire in the major-axis plane of the exit with the sampling frequency of 20 kHz for 10 s. Based on the measurement of the jet velocity over a range of frequencies, the highest velocity value was chosen at the excitation frequency of f_e = 1 kHz. The jet exit velocity was phase-averaged and interpolated by a spline fit over a period of the actuator operation, as shown in Figure 2(a). The fitting result displays an approximately sinusoidal distribution corresponding to the peak velocity at the jet exit u_p = 71.4 m/s and the average exit velocity U_j = 18.6 m/s. In addition, Figure 2b presents the power spectral density (PSD) of the instantaneous jet exit velocity, in which the profound peaks are detected at the excitation frequency of 1 kHz and its high-order frequency components.

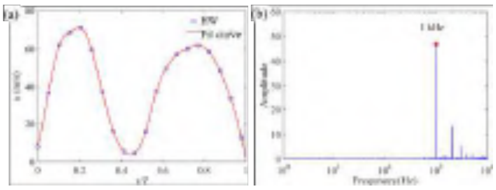

Figure 2. Synthetic jet characteristics at the exit: (a) phase-averaged jet exit velocity at f_e = 1 kHz and $V_{\text{p-p}}$ = 300 V, (b) power spectral density (PSD) of instantaneous jet exit velocity.

Figure 3 displays the variations of lift coefficient and lift-drag polar of the baseline airfoil over the range of 0°-40° in comparison to the controlled case. Stall and a sudden drop in lift coefficient are observed for the baseline airfoil after α = 24°. The synthetic jet significantly increases lift both before and after stall, resulting in an improvement of the lift performance before α = 38°, with the maximum lift coefficient increasing by 11.5%. Additionally, the lift-drag polar curve is shifted upward overall after control. Synthetic jets can significantly improve the lift-to-drag ratio at smaller (α < 14°) and larger (α > 24°) angles of attack. At the same lift coefficient where it is the maximum lift coefficient for the baseline case, the drag coefficient of the airfoil under synthetic jet control is reduced by 13.8%.

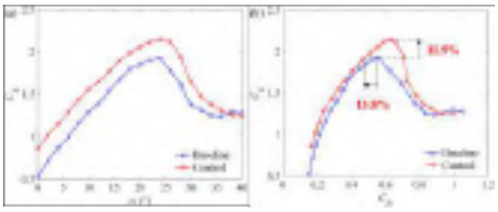

Figure 3. Variations of (a)lift coefficient and (b) lift-drag polar for the baseline and controlled airfoils.

Figure 4 depicts the time-averaged velocity field with and without control for the case of α = 16°, and 24°, respectively. At α = 16°, the flow separation point coincides with the jet orifice. Two counter-rotating vortices originating from the upper and lower surfaces can be observed in the recirculation zone. After applying control, the separated flow on the flap surface reattaches, and flow separation is completely suppressed. The velocity on the upper surface significantly increases, while the airflow velocity on the lower surface decreases. Thus, the lift is enhanced. As the angle of attack increases to α = 24°, the separation point moves upstream of the jet orifice, and the scale of the recirculation zone further increases, with the main flow structure primarily consisting of the vortex shedding from the upper surface. Although the jet orifice is submerged within the recirculation zone at this point, the separated shear layer remains within the disturbance range of the synthetic jet. After control, the separation point shifts from upstream of the flap to the middle of the flap, reducing the size of the recirculation zone and suppressing flow separation. Additionally, the airflow velocity near the orifice significantly increases, indicating that the synthetic jet can inject momentum into the recirculation zone. Therefore, the synthetic jet reduces the size of the recirculation zone and suppresses flow separation through both mixing and momentum injection, thereby achieving lift enhancement.

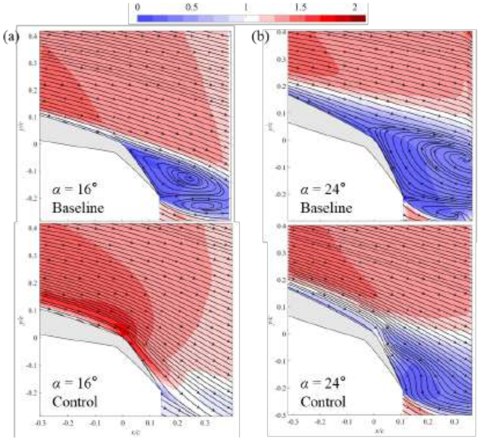

Figure 4. Time-averaged velocity field with and without control at (a) α = 16°, (b) α = 24°.

CONCLUSIONS

This work investigates the aerodynamic control effects of a synthetic jet array on a multi-element airfoil through wind tunnel experiments. The results indicate that synthetic jets can increase the lift of the airfoil and improve the lift-to-drag ratio, with the lift enhancement persisting beyond the stall. The control mechanism was revealed by flow field analysis. Synthetic jets reduce the scale of the recirculation zone and suppress flow separation on the flap through mixing and momentum injection, thereby increasing lift.

REFERENCES

[1] K. C. Peter. *High-lift systems on commercial subsonic airliners*. NASA-CR-4746, 1996.

[2] R. Radespiel, M. Burnazzi, M. Casper, and P. Scholz. Active flow control for high lift with steady blowing. *The Aeronautical Journal*, 120(1223):171-200, 2016.

[3] M. Burnazzi, R. Radespiel. Assessment of leading-edge devices for stall delay on an airfoil with active circulation control. *Council of European Aerospace Societies Aeronautical Journal*, 5: 359-385, 2014.

[4] J. C. Lin, L. P. Melton, J. A. Hannon, et al. Testing of high-lift common research model with integrated active flow control. *Journal of Aircraft*, 57(6): 1121-1133, 2020.

[5] M. DeSalvo, E. Whalen, and A. Glezer. High-lift performance enhancement using active flow control. *AIAA Journal*, 58(10): 4228-4242, 2020.

[6] J. J. Wang and L. H. Feng. *Flow control techniques and applications*. Cambridge University Press, 2018.